Heat and Mass Exchanger Design for Inter-seasonal Liquid Absorption Heat Storage

Benjamin Fumey, Swiss Diploma Engineer

Faculty of Architecture and the Built Environment

of the University of Ulster

A thesis submitted for the degree of

Doctor of Philosophy

June 2020

I confirm that the word count of this thesis is less than 100,000 words.

Acknowledgement

This thesis is part of the ongoing research at Empa, The Swiss Federal Institute of Material Science and Technology, in the area of liquid sorption heat storage, in which the author has been involved since 2011. My thanks goes to Peter Richner, deputy heat of Empa, for supporting my ambition to write this thesis. In this work, substantial support by Robert Weber and Luca Baldini from the Empa Urban Energy Systems Lab is gratefully acknowledged, the many discussion have been very supportive and valuable. Further support from Andreas Borgschulte from the Empa Advanced Analytical Technologies Lab is gratefully acknowledged. It was by his advice, assistance and experience that the Raman based mass diffusion analysis as well as the neutron imaging study at the Paul Scherrer Institutes (PSI), Swiss Spallation Neutron Source Facility were made possible. At which point assistance by Pavel Trtik and Anders Kaestner from PSI is also gratefully recognised. In the timeframe of the herein reported work the author was able to design, built and operat a diversity of testing facilities. This was substantially supported by the Empa internal mechanical design lab and mechanical workshop. This is where the ideas were turned into professional mechanical drawings and on to components well fitting for the task. The author's thanks goes to all those involved. In addition support in the automation, commissioning and operation of these test setups is gratefully accredited to Sascha Stoller, Reto Fricker and Ralf Knechtle as well as several young men carrying out their Swiss civilian service (alternative to army service) and students performing internship studies. A hardy thanks to all involved.

A special thanks goes to Philip Griffith and Neil Hewitt for paving the way for me to be able to accomplish this thesis at Ulster University Belfast Campus. Thank you Philip, for your time and support towards making this possible, I hope we will have further collaborations.

I also do not want to neglect to thank my wife Damaris and my children, who have been very supportive and encouraging, thank you. I thank my heavenly Father for his creation and guidance in my life.

This research work was financially supported by the Swiss Innovation Agency Innosuisse grant Nr. 1155002545 and is part of the Swiss Competence Centre for Energy Research SCCER HaE. Further funding was received from the Swiss Federal Office of Energy SFOE grant Nr. SI/ 501605-01.

Abstract

Sorption heat storage gives perspective for renewable space heating in buildings. Benefits put forth are, loss free storage over time and increased energy density exceeding that of hot water storage. Critical performance parameters in this application are: gross temperature lift, volumetric power density and volumetric energy density. Heat and mass transport in light of these parameters is a challenge holding back this technology from commercialisation. In this thesis, an effective heat and mass exchanger design for liquid absorption heat storage with aqueous sodium hydroxide for compact inter-seasonal heat storage is presented.

In this work, global sorption heat storage performance parameters and operating temperatures were defined, followed by a categorisation of sorption heat storage process types and analysis of performance potential. The closed transported process with single pass and true counterflow was found favourable.

Mass transport was recognised as the dominant boundary in this process, and detailed analysis from milligram to kilogram scale was undertaken. Still film absorption measurements showed the need for extended exposure time for sufficient absorbent exchange (energy capacity). Hereto a novel vertically installed spiral finned tube heat and mass exchanger was developed. Highly temporally and spatially resolved analysis of the mass diffusion in thin absorbent film as present on the spiral finned tube was undertaken with Raman spectroscopy. Mass diffusion in the film was found to be the limiting parameter, indicating that there is potential for improved mass flux through mixing. Visual evaluation of absorption and mass transport was carried out with neutron imaging. In this approach, strong concentration stratification due to buoyancy force was detected. A method towards engaging this buoyancy movement for increased absorption kinetics was found by flooded spiral finned heat and mass exchanger. The functionality of this advanced approach was extensively examined on the lab test bench and good performance was found.

Table of content

Nomenclature

A: Area [m^2]

b: Molecular size constant in the Stokes-Einstein equation [-].

c_p: specific heat capacity [J g^{-1} K^{-1}]

D: Mass diffusion coefficient [m^2 s^{-1}]

H: enthalpy [J g^{-1}]

j: chemical current, mass diffusion [mol m^{-2} s^{-1}]

k_B: Bolzmann constant (1.38064352 J K^{-1})

L: Length/depth [m]

m: mass [g]

$\dot{m}$: Mass flow rate [g s^{-1}]

M: Molar mass [g mol^{-1}]

$\dot{M}$: Molar mass flow rate [mol^{-1} s^{-1}]

P: Power [W]

p: Pressure [kPa], [mbar]

Q: Energy [J]

$\dot{q}$: thermal diffusion [K m^{-2} s^{-1}]

r: radius [m]

T: Time [s]

T_0: the time at which the absorption process is started [s]

$T_{1/2}$: the time at which half the absorption process is completed [s]

V: Volume [m^3]

X: weight per cent [wt%]

β: coefficient of thermal expansion [-]

β*: coefficient of concentration change [-]

η: dynamic viscosity [Pa s]

Θ: absolute temperature [K]

ϑ: Temperature [°C]

λ: Thermal diffusion coefficient [m^2 s^{-1}]

v: kinematic viscosity [m^2 s^{-1}],

ρ: density [kg m^{-3}]

σ: coefficient in Hertz-Knudsen equation [-]

τ: half time, the time to reach half the concentration change [s], $\tau = T_{1/2} - T_0$

Abbreviations

GTL: Gross temperature lift [K]

GTLD: Gross temperature lift in desorption [K]

GTLS: Gross temperature lift in sorption [K]

H2O: Water

HTF: Heat transfer fluid

min: Minute

NaOH: Sodium hydroxide

TE: Thermal effectivity [K/K]

WBT: wet bulb temperature

Non-dimensional Parameters

Ra: Rayleigh number

Gr: Grashof number

Re: Reynolds number

Subscripts

0: process starting condition

1: Process one

2: Process two

a: Absorption

ate: Sorbate

b: bulk

C: Charging

c: Condensation

d: Desorption

D: Discharging

e: Evapoation

ent: Sorbent

exp: Experimental

htf: Heat transfer fluid

i or in: In

int: interface

m: mol

max: Maximum

min: Minimum

o or out: Out

PC: Phase change

s: sorbent

SE: Stokes-Einstein equation

si: Sink

so: Source

sol: solution

v: Vapour

1. Introduction

This research set out to develop a heat and mass exchanger for the application of inter-seasonal thermal storage with liquid absorbent. Included are both, application relevant aspects of heat storage for building space heating such as relevant operating temperatures, as well as material characterisation, for example mass diffusion. The objective has been to unite these sides to develop an effective heat and mass exchanger for the inter-seasonal application.

A short overview of thermal storage with an extended classification, is followed by an in-depth analysis of the sorption heat storage operation. Process description and discussion of important basic performance parameters is followed by a categorisation and thorough account of the basic system processes. It is recognised that in parallel to the applied material, the chosen process strongly affects performance.

In order to be able to evaluate material, component and system performance, as well as assess performance improvement, clearly defined operation temperatures are of upmost importance. For this reason, application relevant temperatures are defined for both the charging and discharging operation.

Specific application, benefits and challenges of liquid sorption heat storage are discussed. There are various liquid sorbents commonly considered. A closer look in respect to the inter-seasonal performance boundaries, especially storage price, shows that many of these do not meet the requirements.

On a component level, the conflicts with conventional tube bundle falling film heat and mass exchangers is examined. It is recognised that novel heat and mass exchanger designs are required in order to be able to fully achieve the required performance criterion. Preliminary tests in absorption and desorption under application specific conditions on a bulk scale (sorbent gram level) in a tray type absorber are followed by the design of a novel spiral finned tube heat and mass exchanger. This is tested in a lab scale test

bench setup (sorbent kilogram level). It is found that operation is substantially improved in respect to temperature gain and energy capacity, nevertheless, volume specific power is low. In the following chapters experimental studies with the goal to understand power limitations in respect to mass transport are presented, with a focus to overcome restrictions. These are; Raman spectroscopy for mass diffusion analysis and neutron imaging for visual absorption analysis.

From the result of this work, steps towards adapting the spiral finned tube heat and mass exchanger are undertaken. Substantial improvement in volumetric power density is achieved while keeping to the temperature gain and volumetric energy density requirements.

The upgraded spiral finned tube heat and mass exchanger was extensively tested under the defined application specific conditions and good performance was found. Based on this improved vertically installed spiral finned tube heat and mass exchanger, upscaling can be followed by implementing a respective number of tubes in parallel. Such an inter-seasonal heat storage system would then consist of the heat and mass exchanger component (power unit) connected to the working fluid storage tanks (energy unit). In this way, a power and energy independent system scaling is possible, able to fit within a diverse of applications in buildings.

1.1. Framework of this thesis

Research in the field of absorption-based heat storage with sodium hydroxide commenced in 2006 at the Empa Building Technology Lab with initial work performed by Robert Weber including a first *proof of function* system based on tray type heat and mass exchangers as described in Weber and Dorer (2008). In 2011 the author of this thesis joined the research team. From 2011 to 2015 development work was continued by Robert Weber and the author, in collaboration with the Swiss Institute for solar Technology (SPF) in the frame of the EU Horizon 2020 funded project COMTES (Fumey et al. 2014a, 2014b, 2014c, 2015a 2015b, 2015c, 2016). In this project, a tube bundle falling film heat and mass exchanger was designed by

SPF (Daguenet-Frick et al. 2014). In this thesis the continued work, post COMTES project, is presented.

1.2. Thermal energy storage[1]

Thermal energy storage is an important enabler for the utilisation of renewable energy as well as waste energy. It can be applied on a time scale from hours and days up to several months, in the latter case it is referred to as long-term or inter-seasonal thermal energy storage used for seasonal thermal energy shifting (Rommel et al. 2016, Bales 2006a). This is an important asset for renewable heating of buildings (IEA SHC Task 32, IEA SHC Task 42, van Helden et al. 2016, IEA Energy technology perspective report) as well as sector coupling (IEA ECES Annex 35 Flexible Sector Coupling), by joining the electric and thermal energy sectors through storage systems, which are integrated for the extended use of renewable energy. Research activities in the field of inter-seasonal thermal energy storage have increased in the past years and a broad range of system designs employing different storage materials and concepts have been evaluated, tested and in some cases brought to the market. Principal criteria for long-term thermal energy storage are among others, high energy density, low thermal loss during storage time and low investment cost. The last mentioned is a critical factor, due to the low number of cycles and thus low overall energy turnover leading to high energy capacity cost as noted by Rathgeber et al (2016). The discipline of long-term thermal energy storage is divided into sensible, latent, and sorption thermal energy storage involving adsorption, liquid absorption and solid absorption with hydration and hydroxide reaction. Both sensible and latent storage systems suffer continuous heat loss, a substantial challenge for long-term storage applications. This is countered by large scale sensible storage systems (Kabus and Wolfgramm 2009) and supercooling in latent systems as reported by Dannemand et al. (2016) and Englmair et al. (2018).

[1] This section basis on the published work:
Fumey B., Weber R., Baldini L., Sorption based long-term thermal energy storage – Process classification and analysis of performance limitations: A review, Renewable and Sustainable Energy Reviews 111, 2019, 57–74

In figure 1 the categorisation of thermal energy storage technologies is shown, extended from work done by Zondag (2015). A strong focus in research is set on the so called compact thermal energy storage, involving latent and sorption technologies (IEA SHC Task 58/ECES Annex 33).

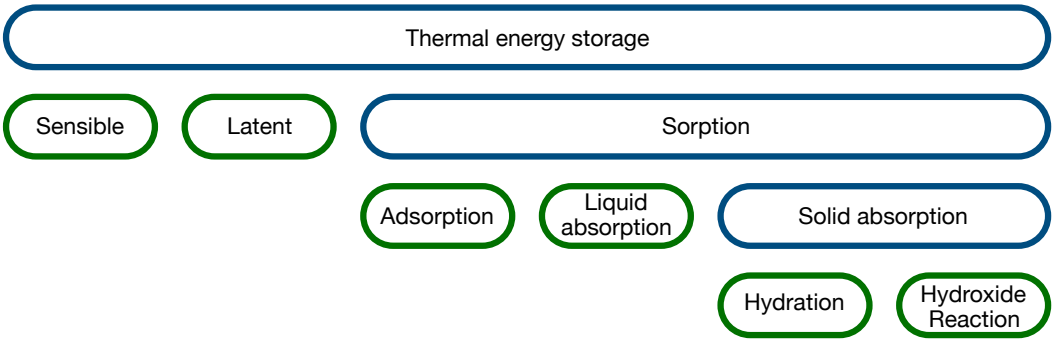

Figure 1: Thermal storage categorisation, extended from Zondag (2015).

1.3. Sensible heat storage

In sensible thermal storage, storage density is derived from the specific heat of the material and the respective temperature change (Faninger 2004, Fernandes et al, 2012).

$$Q = m \times c_p \times \Delta\Theta, \text{ Equation 1}$$

Where *Q* [J] is the stored energy, *m* [g] is the material mass, *ΔΘ* [K] the temperature difference between charged and discharged state and c_p [J g^{-1} K^{-1}] is the specific heat capacity of the material.

Examples of sensible thermal storage materials are: water, thermal oil, molten salt, rock bed, concrete, fire brick, etc (Bauer et al. 2010, Zhao et al. 2011, Dincer and Rosen 2002, Zondag et al. 2015). Sensible storage systems include small and large in-house water tanks, large outdoor or underground water tanks, bore hole heat exchanger fields, large aquifer rock formations etc. (Raab et al. 2004, Lottner et al. 2000, Kabus and Wolfgramm 2009, Schmidt et al. 2004, Drake Landing Solar Community 2012, Colclough et al. 2011, Clarke et al. 2014, Griffiths and Colclough 2015).

Sensible heat storage has a relatively low storage capacity and suffers continuous heat loss. For this reason, inter-seasonal storage is challenging, and large volumes are required.

1.4. Latent heat storage

Latent heat storage systems, often referred to as phase change material thermal energy storage systems serve both as sensible and latent thermal storage. The phase change is engaged in order to increase thermal capacity in contrast to the solely sensible heat storage (Hasnain 1998, Kenisarin 2010, Regin et al. 2008, Reddy et al. 2018, Abhat 1983). Apart from the supercooling effect, a characteristic employed for long term storage where a material remains liquid below its melting/solidification temperature (Englmair et al. 2020), continuous heat or cold loss is encountered in phase change materials during storage time. In charging, heat above melting temperature is supplied to the storage unit and the phase change material is liquefied. In discharging, the reverse process takes place, and the phase change material solidifies, releasing heat at the respective solidification temperature. Phase change material thermal energy storage systems are generally characterised by a narrower temperature range for a given storage capacity, compared to storage systems based purely on sensible heat, taking advantage of the phase change enthalpy rather than the material specific heat capacity. This is potentially beneficial since reduced temperature difference to the ambient decreases the thermal loss during storage periods and the moderate storage temperature improves charging efficiency such as from a solar collector or compression heat pumps where applicable. Examples of phase change materials are ice, paraffins, fatty acids, salt hydrates, nitrate salts and sugar alcohols (Abhat 1983, Zalba et al. 2003, Farid et al. 2004, Nielsen 2003).

In the phase change material thermal energy storage system, sensible heat storage capacity can be estimated according to equation 1, and latent heat storage capacity is calculated according to:

$$Q = m \times \Delta H_{PC}, \textit{ Equation 2}$$

Where ΔH_{PC} [J g^{-1}] is the phase change enthalpy, melting or solidification.

Phase change material heat storage utilising supercooling allows combined short-term and long-term heat storage. The short-term storage makes use of the specific heat of the phase change material in liquid phase and the long-term heat storage makes use of the phase change enthalpy as reported by Englmair et al. (2020).

1.5. Sorption heat storage

Sorption heat storage, also referred to as thermo-chemical material energy storage is an umbrella term that covers adsorption as well as liquid and solid absorption processes, generally also including hydration and hydroxide reactions as shown in the categorisation in figure 1 on page 16. In this heat storage approach, the concept of a reversible decomposition reaction process involving both thermophysical and thermochemical bonds (Vasiliev and Kulakov 2003, Inglezakis and Poulopoulos 2006) in a bi-directional temperature swing process is followed. This takes into account the aggregate change of the sorbate through evaporation and condensation (Garg et al. 1985, Zondag 2015, Paksoy 2007, Kawasaki et al. 1999, Boman et al. 2017a, Aristov 2013, N'Tsoukpoe et al. 2013, Cabeza et al. 2017). In the action of adsorption, sorbate in its gaseous phase is adhered to a solid surface. Both Van der Waals physisorption forces and chemisorption based on valency forces are involved (Wang et al. 2009, Sriviastava et al. 1998, Inglezakis and Poulopoulos 2006). Absorption on the other hand, is the process by which a gas enters a solid or liquid also referred to as hydration [Inglezakis and Poulopoulos 2006, Armstrong et al. 2007, Sriviastava et al. 1998, Perry 2007], and a concentration difference with different hydration states results. Appropriate adsorbents, such as zeolites, have a large surface area where water vapour is bonded. Due to this, a major challenge is the very low thermal conductivity of the adsorbents owing to the high material porosity. This is a challenge also found in composite, salt impregnated adsorbents such as zeolites or vermiculites (de Jong et al. 2014). Liquid absorbents do not suffer the same challenge in thermal conductivity, nevertheless due to the liquid state, the active surface area for absorption is substan-

tially lower compared to adsorbents and thus the rate of absorbate uptake is reduced.

Application of sorption thermal storage, has the prospect of high energy density and lossless storage over time making it attractive for compact inter-seasonal heat storage (Paksoy 2007, Bales 2005, Kato 2007). It is important to note that sensible heat is not accumulated, but the potential to regain heat at a later point in time and at serviceable, elevated temperature is stored in a reversible process. Thus, it functions as a chemically driven heat pump accessing heat from a low temperature source. In the heat storage (charging) process, the sorbent temperature is increased, and sorbate is evaporated therefrom. The sorbate vapour is either condensed at a respective lower temperature and the heat released to the ambient, or the sorbate is directly ejected to the ambient. This is a possible approach if the sorbate is water. In the heat release (discharging) process, the opposite takes place. Sorbate is evaporated by means of low temperature heat source from the ambient or directly sourced from the air and adhered to the sorbent. As a result the sorbate aggregate state changes and the heat of condensation is released to the sorbent (Paksoy 2007, Perry 2007, Kawasaki et al. 1999). Dependent on the sorbent material and the state of charge, a temperature increase from the evaporator or partial vapour pressure equivalent temperature results. Further explanation is followed in chapter 2.1.1. “Gross temperature lift” on page 23.

The reaction scheme for the sorption heat storage processes can be represented as follows:

Step 1:

$$A(x+y)B_{(l\ or\ s)} + heat \rightleftharpoons A(x)B_{(l\ or\ s)} + (y)B_{(g)},\ Equation\ 3$$

Step 2:

$$(y)B_{(g)} \rightleftharpoons (y)B_{(l)} + heat,\ Equation\ 4$$

Where *A* is the sorbent and *B* the sorbate, with x representing the remaining bound sorbate in charged condition and y symbolising the exchanged sorbate between charged and discharged order. The sorbent and sorbate mix-

ture *A(x+y)B* can be either in liquid or solid aggregate state. In the charing process, the mixture *A(x+y)B* (for example aqueous sodium hydroxide or zeolite containing water) is heated and part of the sorbate $(y)B_{(g)}$ (in the examples part of the water content) is evaporated. In systems open to the ambient air, this vapour is directly released. In closed systems, step 2 is followed, whereby the vapour is condensed and only the condensing heat is released to the ambient. In discharging the inverse process is followed. Heat is employed to change the phase of the liquid sorbate $(y)B_{(l)}$ to gas $(y)B_{(g)}$ in the closed systems or $(y)B_{(g)}$ is sourced from the ambient. This gaseous sorbent $(y)B_{(g)}$ is then sorbed by the sorbent and sorbate mixture *A(x)B resulting in the increase of sorbate concentration in the mixture A(x+y)B* and releasing the heat of condensation of the sorbate. Lossless storage is achieved by preventing recombination of sorbent and sorbate during storage time.

2. Sorption heat storage for buildings[2]

The inter-seasonal thermal energy storage system challenges pointed to in literature are; choice of the best process (open or closed) and heat and mass exchanger design (Hadorn 2006, Zondag 2015).

These two criteria are followed as a guideline in this work. The major focus is placed on the heat and mass exchanger development which, in turn is dependent on the choice of process.

In order to design and evaluate systems and components, guidelines are required. To date such globally agreed guidelines have been missing. Substantial work in the frame of the combined IEA SHC task 58 and ECES annex 33 towards system categorisation, performance evaluation and application conditions has been carried out by the author as subtask leader. In this chapter these boundary conditions for the domestic application of sorption heat storage technology are elaborated. Herein, an analysis of the major storage performance parameters is presented, followed by a categorisation of sorption heat storage systems, with pros and cons discussed and concluded with a study of application specific temperatures for the building internal heat storage. Understanding these boundary conditions is an important step towards the effective design of a successfully operational inter-seasonal heat storage system. Without these, it is impossible to clearly evaluate progress, and it is the absence of these guidelines that has led to many erroneous claims of storage capacity at both material as well as component and system level.

2.1. Performance parameters

In literature the following suggested criteria for choice of sorption materials are found (Perry 2007, Bales 2006a, ASHRAE 2005, Wongsuwan et al. 2001, Rathgeber et al 2016):

[2] This section basis on the published work:
Fumey B., Weber R., Baldini L., Sorption based long-term thermal energy storage – Process classification and analysis of performance limitations: A review, Renewable and Sustainable Energy Reviews 111, 2019, 57–74

- Desorption and sorption temperatures fitting to specific application
- High affinity of sorbent to sorbate – (affecting both temperature gain as well as volumetric charge and discharge power)
- High specific volumetric uptake of sorbate on sorbent – (affecting volumetric energy storage density)
- Substantially higher volatility of sorbate than sorbent – (for good separation through evaporation)
- Good mass and heat transfer characteristics – (affecting temperature gain and charge and discharge power)
- Good chemical and mechanical stability – (affecting cycle stability)
- Favourable life cycle properties such as ecology and embodied emissions – (positively affecting sustainability)
- Low material price – (affecting economic viability)

Other criteria considered are corrosiveness, toxicity and moderate operation pressure. Nevertheless, these issues are disputable and appropriate coating and system engineering solutions may be found to mitigate potential negative impact on performance, longevity or acceptance. In this list, material price is again stated and recognised as a decisive parameter, which must be given high priority when choosing a storage material.

Three basic specifications of performance for sorption heat storage can be derived from the list. These are: temperature gain, also referred to as gross temperature lift (GTL), volumetric charge and discharge power density, and volumetric energy storage density. It is the unique composition of gross temperature lift, power and energy density, required in sorption heat storage systems compared to other sorption machines that make their design highly challenging. This is due to the fact that, high concentration change from charged to discharged state (energy) leads to operation close to the equilibrium state, in turn substantially reducing the sorption driving force (power).

When looking at the performance criteria in respect to development scale, milligram material to megagram material, it can be noted that not all performance categories can effectively be evaluated on all levels. Gross temperature lift and energy density are measures that can be assessed on

all scales, from milligram material tests, for example with Differential Scanning Calorimetry (DSC) or Thermogravimetric analysis (TGA) to demonstrator system operation on the megagram scale. Power on the other hand is more dependent on the interaction of sorption material with the heat and mass exchanger, and directly dependent on the heat and mass exchange kinetics.

Performance of all parameters is strongly linked to operation conditions, namely operating temperatures. For this reason, chapter 2.4 “Application temperatures” on page 39 is dedicated to the clear definition of available and required temperatures both in sorption and desorption for the building application.

2.1.1. Gross temperature lift

Gross temperature lift is a term referring to the temperature gained in sorption and required in desorption between the sorbent material and the vapour pressure equivalent temperature. In the closed operating process this is the evaporating or the condensing temperature, in the open process it refers to the partial vapour pressure equivalent temperature. Adiabatic gross temperature lift is conditioned on the equilibrium state between sorbate pressure and sorbent composition temperature as well as the vapour pressure and is given in degree Kelvin (K). Measurement of gross temperature lift can be applied along the complete scale from material to component and system, as a means of evaluating material suitability as well as for the analysis of performance reduction along the scales (Fumey et al. 2019). In figure 2, a diagram for simple evaluation and comparison is shown, with the gross temperature lift on the x-axis vs. the mass fraction on the y-axis. Values for the liquid sorbent aqueous sodium hydroxide, based on a water vapour pressure of 6.5 mbar (1°C evaporating temperature) are included. In discharging (absorption), operating values along the scale from material to system will be on or above the equilibrium curve, meaning resulting temperatures are lower than equilibrium and concentration greater. In charging (desorption) on the other hand, values will be on or below the line, thus required temperatures are greater than equilibrium. Diversion from equilibrium is

linked to heat and mass exchange kinetics. For example, temperature gradient between sorbent and heat transfer fluid will led to loss in gross temperature lift.

This visualisation is a simple way to determine how close to the theoretical maximum (adiabatic state) the gross temperature lift is. In this way, it can be used to visualise degradation in gross temperature lift performance along the scale from material to system level.

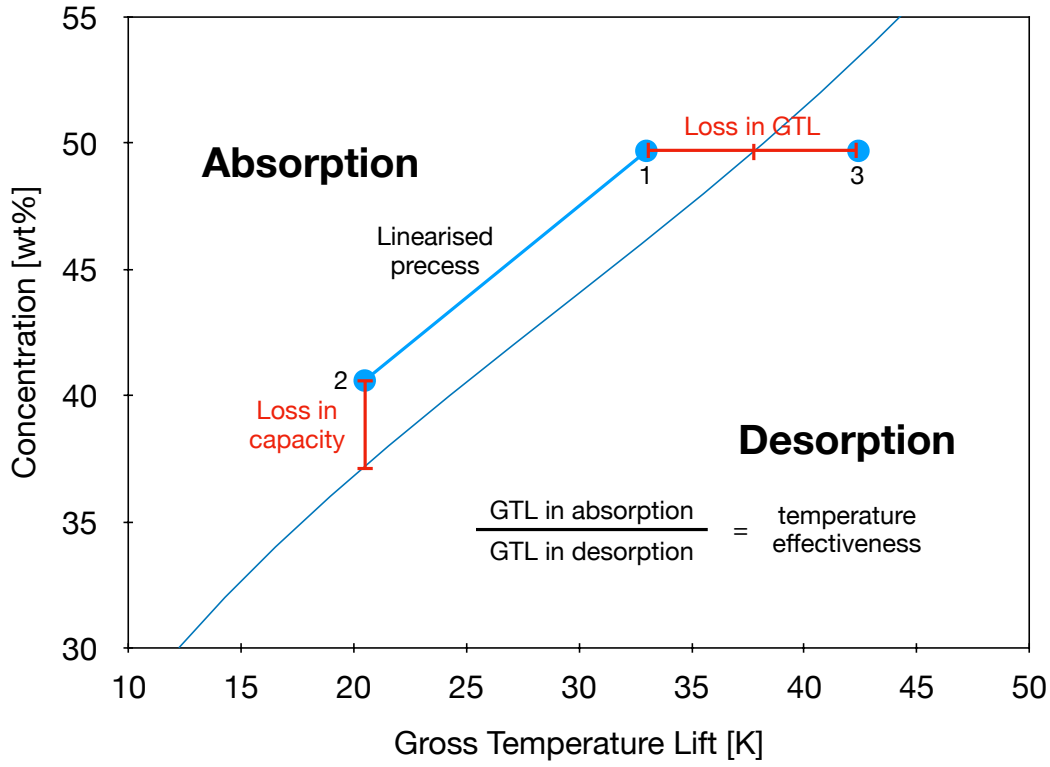

Figure 2: Diagram showing concentration vs. gross temperature lift, for evaluation along the development scale. The blue line is the calculated adiabatic equilibrium curve for aqueous sodium hydroxide at 6.5 mbar vapour pressure, based on work by Olsson et al (1997). The light blue dots 1 and 3 indicate the gross temperature lift in absorption and desorption respectively based on the starting and resulting condensation. Good performance is close to the equilibrium line. The horizontal red line shows the loss in gross temperature lift between desorption, absorption and the equilibrium line. The light blue dot 2 shows the final concentration at the minimum gross temperature lift. Indicated with the red vertical line, is the capacity loss due to the deviation from the adiabatic state.

2.1.2. Temperature effectiveness

A measure of temperature effectiveness (TE) can be derived based on the gross temperature lift using the ratio between gross temperature lift in sorption (GTLS) and gross temperature lift in desorption (GTLD). Temperature effectiveness can be used as a method to describe how well the system takes advantage of the full potential of the employed storage material. This approach enables; simple comparison along the development scale (evaluation of performance drop along the scale), easy performance assessment of heat and mass exchanger design variations and provides a sound basis for comparison between varying systems (development lines). In addition, this evaluation provides grounds for comparing basic system process categories. System process categorisation is further elaborated on in chapter 2.2. “Sorption heat storage system categorisation” on page 30 with a temperature effectivity evaluation in chapter 2.3. “Performance evaluation of reported systems ” on page 36. When comparing systems evaluated under varying testing conditions, it must be noted that a slight operation dependency remains, based on the sorbate vapour pressure. Even so, this approach is substantially more robust in comparing the diversity of reported systems than resorting to reported output temperature, power and / or energy density. In as far as the vapour pressure remains constant both in desorption and sorption, theoretical temperature effectiveness without temperature drop is unity. Figure 3 illustrates the deviation from unity due to the difference in vapour pressure in the charging and discharging process. Shown is the vapour pressure vs. temperature diagrams for various aqueous sodium hydroxide concentrations. In the diagrams the theoretical gross temperature lift at 1 kPa is compared to the equivalent at 10 kPa vapour pressure. It can be seen that at greater sorbent vapour pressure the gross temperature lift increases, noted by the red circled line. This difference is thermodynamically based and results is an unavoidable loss since charging occurs at greater temperature and resulting pressure, than discharging.

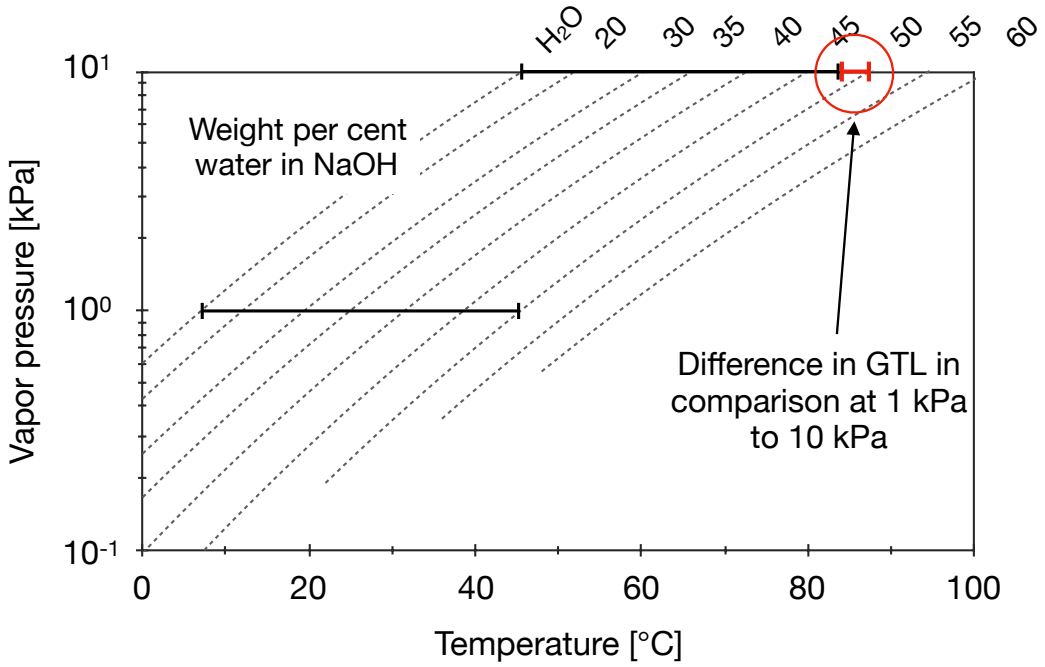

Figure 3: Vapour pressure vs. temperature of aqueous sodium hydroxide (Fumey et al. 2015a). Indicated is the thermodynamically based difference, noted in red, between gross temperature lift from water to 50 wt% concentration at the vapour pressure of 1 kPa and 10 kPa respectively. Since charging is performed at elevated condensing temperature (pressure) to discharging. This loss can not be omitted.

In the application as long-term thermal storage, the vapour pressure in desorption is typically greater than the respective pressure in sorption, see the chapter 2.4. “Application temperatures” on page 39 for further clarification. Thus the result is that the adiabatic gross temperature lift in sorption is smaller than the equivalent in desorption and temperature effectiveness is less than unity. This is an unavoidable loss in gross temperature lift, due to the application as heat storage. Its specific degree depends on the sorption material and the operational conditions.

2.1.3. Volumetric charge/discharge power

In the design of a sorption heat storage system it is important that a certain application dependent volumetric specific power output is reached. Measure is given in watt per cubic metre (W m^{-3}). Due to the interlinked

process of mass and heat transport, the evaluation of power is complex and very much dependent on the heat and mass exchanger design. In sorption-based heat storage, on a process level, power and energy capacity are strictly interlinked, since substantial reduction of sorption driving force (power) is encountered as equilibrium (maximum energy density) is approached. Representational power performance can thus only be measured under application specific conditions, including specific components (heat and mass exchanger) and realistic temperatures as well as in light of reaching high storage capacity, thus with reference to the deviation from the equilibrium line (figure 2, page 24). For this reason, evaluation and comparison of power is only possible on the component and system scale. On the gram scale or in specific analysis of mass or heat transport on the milligram scale, possible indications of power performance and methods of optimising heat and mass exchanger can be reached. Such work is followed in later chapters with Raman spectroscopy, neutron imaging and bulk scale evaluation of the absorption and desorption process.

Looking at the varying system processes, especially transported and fixed, see chapter 2.2 “Sorption heat storage categorisation” on page 30 further difficulty in respect to the volume reference arises. In fixed bed systems both volumetric specific power and energy is referenced to the storage or if segmented the storage segment volume. In transported processes on the other hand, the volume of the converter unit (heat and mass exchanger) is taken. In a transported process with continuous flow of sorbent, generally found with liquid sorbents, constant power output is achieved. In fixed process designs on the other hand, power is not continuous and the question of power definition, peak, average or other variation, occurs. For this reason, the declaration of volume specific power is challenging, and further work will be required to approach a clear more global definition. In this thesis reference will be made to the specific heat and mass exchanger volume, that is the volume of tubes required, not to be confused with the actual volume of the heat and mass exchanger unit.

2.1.4. Energy density

The third criteria, energy density, is closely related to the gross temperature lift. Energy density is based on the change of mass fraction between charged and discharged sorbent composition as well as solution or reaction enthalpy. In the heat storage application, reference to storage volume is more fitting than storage weight, since, for the use as stationary long-term heat storage, volumetric rather than gravimetric capacity is key. The unit of measurement is thus joule per cubic meter (J m^{-3} or Wh m^{-3}). From the gross temperature lift equilibrium diagram (figure 2 page 24), theoretical sorbate mass change can be determined, on the basis of which, the heat exchange in the form of sorbate vapour, as well as heat released by solution, can be derived. Shortcomings in reaching the material adiabatic gross temperature lift will provide explanation for lack of reaching the maximum theoretical energy densities. As discussed in the volumetric power discussion, the reference to volume is challenging, though in respect to energy density the reference is slightly different. There are two basic approaches to indicating the volumetric energy density, one includes the setup, components and system, while the other refers only to material volume. Reference to material is more uniformly applicable since prototype systems generally follow a spacious built design and it is not the scientist's discipline to optimise and compact design. Nevertheless, reference to material can be misleading when considering the required volume in buildings. For this reason, when making reference to material volume, allusion should be made to the material state of maximum volume, providing better indication of potentially required system volume. This depends on the sorption composition material and basic system approach, see chapter 2.2 "Sorption heat storage system categorisation on page 30. For fixed bed open systems, maximum volume is in the sorbed state due to the sorbent volume increase in sorption. For fixed closed systems, maximum volume is under sorbed condition with addition of the sorbate volume, due to the additional sorbate storage required in desorbed state. For transported open systems, again the desorbed state is key. In transported closed systems due to the sorbate storage, it is under charged

condition that maximum volume occurs, in as far as the volume of the separated materials is greater than in combined state. An additional challenge at the system design level in this approach is the demand for separate storage volume for both charged and discharged sorbent composition, thus practically doubling the storage volume and introducing a high degree of unoccupied volume. Solutions with multiple tank arrays with the possibility of using tanks for charged as well as discharged sorbent, or tanks with membrane separated compartments can substantially reduce the problematics of excess volume. In the continuation of this work, the volumetric energy density will be referenced to the maximum state of volume, being both absorbent and adsorbate in its separated (charged) state, thus assuming no dead volume.

In the past, many review papers on compact thermal energy storage have erroneously followed the practice of comparing power and energy density of various technologies and proof of concept systems as reported in the respective publications (N'Tsoukpoe et al, 2009, Kuznik et al. 2018, Palomba et al. 2018, Solé et al. 2015, Yu et al. 2013, Abedin and Rosen 2011). As has been shown in this section, this approach is highly misleading, due to the substantial dependency of both volumetric energy storage density and volumetric charge and discharge power density on operating conditions and definition of volume (Scapino et al. 2017a).

2.2. Sorption heat storage system categorisation

Sorption heat storage systems focussed on in research and reported in literature can be classified into the process variations open versus closed as reported by Bales (2005) and fixed versus transported as pointed to by Zondag (2015). The former refers to material contact to the ambient air and the latter deals with sorbent material handling. A similar process classification is found proposed by Scapino et al. (2017b), reference is made to open, closed and liquid. In this section categorisation and process evaluation are performed.

To date, the choice of process, heat and mass exchanger design as well as specific system design is largely based on the choice of sorbent material. Sorbents that react with CO_2, are hazardous or easily airborne, are studied in closed systems (N'Tsoukpoe et al. 2013), and non-hazardous mainly solid materials are often employed in open systems for reason of their simplicity (Kerskes et al. 2013). Solid sorbents are primarily studied in fixed systems with some work done on agitated transported processes (Zondag et al. 2013) and transported sorbent systems are largely used for liquids (N'Tsoukpoe et al. 2013, Weber and Dorer 2008). Figure 4 illustrates the four basic sorption heat storage processes as defined, separating open and closed horizontally and fixed and transported vertically (Fumey et al. 2019). Illustrations are numbered for further reference. In the following subchapters the varying processes are described and benefits as well as drawbacks discussed.

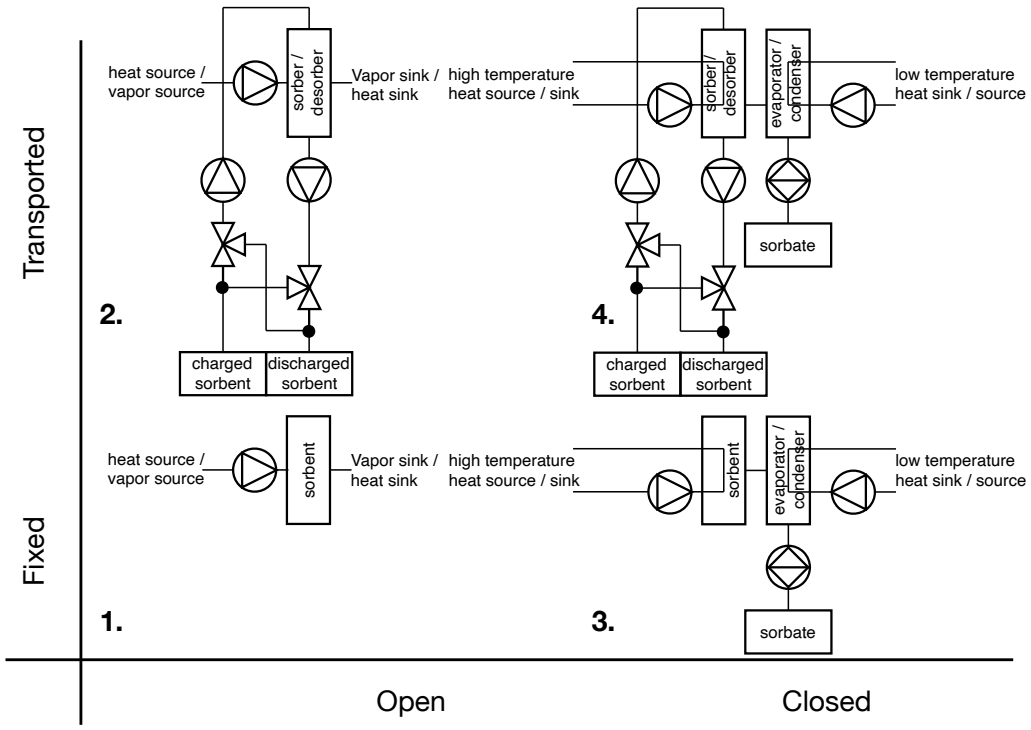

Figure 4: Illustration of basic sorption thermal energy storage processes (Fumey et al. 2019).

2.2.1. Open process

The open process (illustration 1 and 3 in figure 4) operates solely with water as sorbate at atmospheric pressure. Sorbate (water vapour) is released to and sourced from the atmosphere dependent on the relative vapour pressure and sorbent temperature (Kerskes et al. 2011). This is illustrated by the pump symbol sourcing sorbate from the ambient. Systems based on the open process consist of a sorption and desorption heat and mass exchanger and a sorbent storage unit (Zondag et al. 2015). These systems do not have an evaporator and condenser unit or sorbate storage (Weber et al. 2016) and do not require vacuum or pressure compliance (Kerskes et al. 2011). Thus, respective system complexity and volume are reduced. Discharge power directly depends on the given partial vapour pressure of sorbate in the ambient air (van Alebeek et al. 2018). This is generally low due to the low ambient temperature during the heating season. For this reason, high volumetric air flow is required to reach adequate humidity supply (Tatsidjodoung et al. 2016). This corresponds to a large thermal mass of inert carrier gas flow, limiting effective sorption gross temperature lift, discharge power and discharge efficiency through effected cooling (Zondag et al. 2015). In order to improve performance, air to air heat exchangers for heat recovery (Zondag et al. 2013) and air humidifiers are employed (Tatsidjodoung et al. 2016), leading to an increase in complexity, system volume and cost. To increase vapour mass transport in the supply air, water is sprayed into the air stream bringing about an air temperature reduction at increased relative humidity. A general challenge in the open process is fouling on the sorbent material by airborne pollutants, bringing about a decline in temperature gain and power losses over time (Perry 2007).

2.2.2. Closed process

In the closed process (illustration 2 and 4 in figure 4 on page 30) the sorbate and sorbent are not in direct contact with the atmosphere and the sorbate is stored separately (Zondag et al. 2015). Thus, the open process exchanges heat and matter, while the closed process exchanges only heat

with its surroundings. Closed systems consist of a sorption and desorption part as well as an evaporator and condenser part of the heat and mass exchanger, and sorbent and sorbate storage vessels (Fumey et al. 2017). They operate under sorbate atmosphere generally below atmospheric pressure, require good sealing (Zondag et al. 2015) and are highly sensitive to the presence of non-condensing gases (Weber and Dorer 2008, de Boer et al. 2004). Closed systems reject heat to, and source it from, the ambient, typically the ground or the air (Zondag et al. 2015) and are not bound to water as sorbate. Even so, water is often used due to its high phase change enthalpy from liquid to gas as well as generally high solubility in, and high affinity to, the respective sorbents (Boman et al. 2017b). Sorbent and sorbate are stored in separated vessels and the sensible part of the thermal energy employed for material separation is released to the atmosphere (Zondag et al. 2015). In sorption, the system output temperature is dependent on the low temperature heat source supplied to the evaporator and the sorbent material based gross temperature lift. In liquid sorbents gross temperature lift is dependent on sorbent mass fraction and in solids it is dependent on the level of hydration.

In order to simplify comparison of closed and open systems in respect to vapour pressure and temperature gain, it is favourable to convert a given partial water vapour pressure in air to its respective vapour pressure equivalent temperature. This corresponds to the respective evaporation temperature in a closed system. Since this temperature is always lower than the ambient temperature, sink and source temperature is greater for closed systems than open systems. Thus, closed systems potentially require higher desorption temperatures but also release higher output temperatures than open systems (Hauer 2008). This is most critical in the heat release in sorption, where it is important to reach high output temperature and maximum state of discharge. In this respect, closed systems are superior for the task of heating in buildings.

2.2.3. Fixed process

In the fixed bed process (illustration 1 and 2 in figure 4 on page 30) the sorbent is kept stationary and often combined with the heat and mass exchanger (Köll et al. 2017). No separate storage vessels are required (Solé et al. 2015), but a direct interdependence of desorption and sorption power and storage capacity on the system level results (Zondag 2015). This is the most frequently followed process approach with solid sorbents (Solé et al. 2015, van Alebeek et al. 2018). In the design of a fixed bed system it is important to know how sorption and desorption transitions progress through the bed (Perry 2007, Zondag et al. 2008). This introduces the factors time and space into the analysis, leading to a dynamic character. Practical aspects such as mass transport, thermal conduction, dispersion phenomena at bed scale and volume change are important parameters to be considered (Perry 2007). Fixed bed systems generally suffer high pressure drop through the bed, reducing potential sorption gross temperature lift and requiring high parasitic power consumption (Baghapour et al. 2018). In the desorption process, the complete sorbent bed is heated and has to be maintained at a material specific desorption temperature in order to reach the desired charged state (Mette et al. 2006). In sorption the same process is followed. Through sorption based heat release, the complete bed is heated to the sorption temperature (Zondag et al. 2008, Jaehnig et al. 2006). It follows that high thermal capacity of the material leads to system capacity loss. The sorption process is maintained until the output temperature drops below the minimum required output temperature, referred to as thermal breakthrough. The achievable storage density decreases drastically, when the thermal breakthrough temperature is increased (Hauer 2008). In non-continuous sorption, sorbate mass transfer during inactive periods may occur and lead to the establishment of a new homogeneous state of charge at a lower potential sorption gross temperature lift and thus lower maximum output temperature in continued discharge (Kerskes et al. 2011). Segmentation of storage vessels is employed in order to reduce issues with partial discharge (Kerskes et al. 2011), as well as enable discharge below breakthrough

threshold by connecting segments in series (de Jong et al. 2016). Complexity in fixed bed application is increased when used for heat storage purposes through heat recovery, compared to other fixed bed striping processes. In the design of heat exchangers two approaches are followed, integrated including direct air heating (Weber et al. 2016, Tatsidjodoung et al. 2016, Krönauer et al. 2015) and separated (Zondag 2015). Integrated heat exchangers are placed inside the fixed bed, while separated heat exchangers are positioned separate from the sorbent downstream from the sorbent supply. In both approaches, mean temperature results. This temperature is substantially lower than the maximum temperature that can be reached based on the mass fraction specific sorption gross temperature lift.

2.2.4. Transported process

In the transported process (illustration 3 and 4 in figure 4 page 29) the heat and mass exchanger unit is separated from the sorbent storage (N'Tsoukpoe et al. 2009). Thus, separate storage vessels and means of sorbent transportation are required (Solé et al. 2015, Fumey et al. 2017). In this approach, heating power and thermal energy capacity on a system level are separated and can be individually designed and scaled for a specific application (Zondag 2015). Due to the sorbent transport and continuous supply of fresh sorbent a system level steady state operation can be reached in the heat and mass exchanger (Perry 2007), leading to continuous desorption or sorption with steady temperature and power profiles. This is in strong contrast to the fixed approach with dynamic profiles in the sorbent bed. Reaction processes are thus reduced to a fraction of the total storage material (Mette et al. 2012a). Sorbent transport parameters, such as viscosity and wetting behaviour for liquids (Boman et al. 2017b) and grain size, material stability and flowability for solids (Zondag et al. 2008) are important. Liquids are beneficial due to their simple transport by pumping (N'Tsoukpoe et al. 2009, Fumey et al. 2017). For solids three basic reactor types are discussed, fluidised bed, extruder reactor and bulk flow reactor (Zondag et al. 2008, Mette et al. 2012b). In the design of the heat and mass exchanger two characteristics are of significant benefit: sorbent single pass and counter flow.

Recirculation of partly discharged sorbent, as typically employed in liquid sorbent chillers for good wetting, will lead to substantial reduction of the maximum discharge temperature due to mixing of fresh and partly discharged sorbent. Counterflow of sorbent and heat transport fluid is important for optimal heat exchange from sorbent to heat transport fluid. In this way maximum output temperature is reached due to continuous contact of heat transport fluid to fully charged sorbent and maximum discharge is enabled through cooling the sorbent to the minimum heat transfer fluid temperature.

Considerations of best heat and mass exchanger design in terms of sorbent velocity, vessel height, contact area of sorbent to sorbate and heat transfer fluid, exposure time and sorbent flow distribution is important for optimum sorption kinetics both for liquid and solid sorbents. Due to the single pass requirement, slow flow with good liquid wetting or solid contact for improved thermal conductivity and high sorption surface area is key (Fumey et al. 2017). Residence time and hence, the heat and mass exchanger holdup, are important design features in order to enable a close fit to temperature and vapour pressure equilibrium for maximum storage capacity. It follows, that for heat storage, a heat and mass exchanger is designed on the basis of sufficient sorbent holdup or exposure time rather than on the basis of high mass transfer rate for maximum power density.

In comparing fixed systems to transported systems it can be concluded that, in as far as single pass and counter flow is followed, transported systems are superior, since the desorption gross temperature lift is reduced and the sorption gross temperature lift increased, thus also the temperature effectivity improved. In addition, since in the sorption process, the desorbed sorbent temperature is below the required minimum output temperature greater sorbate uptake and thus higher energy density is reached (Zondag et al. 2008). Fixed systems are discharged to the heat transport fluid output temperature and maximum sorption gross temperature lift is not reached due to bulk thermal capacity and internal mixing of heat from sorbent at varying mass fraction. Transported systems on the other hand are dis-

charged to the heat transport input temperature, which is naturally lower than the output temperature (Kerskes et al. 2011). Thus, fixed systems are sensitive in capacity to the output temperature (Hauer 2008) while transported systems are not (Fumey et al. 2015a) in as far as they reach the required temperature. For both fixed and transported systems capacity decreases if the heat transport fluid input temperature increases in respect to the sorbate evaporation temperature. A further overview of the process advantages and disadvantages is found in (Fumey et al. 2019).

2.3. Performance evaluation of reported systems

Temperature effectiveness as a measure of comparison between sorption systems was introduced in chapter 2.1.2. “Temperature effectiveness” on page 24. The approach benefits from non-confinement to a specific material, system approach or testing procedure. In table 1 examples from literature are categorised according to the basic sorption thermal energy storage processes and compared based on the gross temperature lift in desorption as well as absorption and the resulting temperature effectiveness. Interestingly, it is found that many tests are performed at material ideal temperatures rather than realistic application temperatures, an issue paid attention to in chapter 2.4. “Application temperatures” on page 39. Since some reports provide insufficient indication of water vapour pressure or equivalent temperature, these were assumed and thus indicated in brackets.

Table 1: Overview of the evaluated systems including sorbent and sorbate materials, with desorption gross temperature lift, sorption gross temperature lift and temperature effectiveness as the ratio of absorption gross temperature lift to desorption gross temperature lift. In several of the open systems the ambient vapour pressure was not declared. In order to complete the list, an ambient temperature of 25 °C and 55% relative humidity, resulting in a condensing temperature of 15°C is assumed. Values based on assumptions are in brackets (Fumey et al. 2019).

System	Sorbent	Sorbate	GTL_D [K]	GTL_S [K]	TE [-]	Author
Open Fixed	zeolite Na-X	water	(165)	43	0.26	Johannes et al. 2015
	zeolite 13X	water	(165)	44	0.27	Tatsidjodoung et al. 2016
	$SrBr_2$	water	62	19	0.31	Michel et al. 2014
	zeolite 13XBF	water	172	42	0.24	Weber et al. 2016
	activated alumina / LiCl	water	(95)	27	0.28	Zhang et al. 2017
	zeolite 13X	water	120	21	0.18	Aydin et al. 2016
	zeolite 13X	water	(175)	20	0.11	Gaeini et al. 2017
Open Transported	CaCl2 and zeolite	water	173	50	0.29	Nonnen et al. 2016
Closed Fixed	zeolite 5A	water	83	30	0.36	Finck et al. 2014
	zeolite 13XBF	water	163	25	0.15	Köll et al. 2017
	AQSOA FAM Z02	water	60	25	0.42	Palomba et al. 2017
	LiCl / expanded graphite	water	67	22	0.33	Zhao et al. 2016
	MnCl2-CaCl2	ammonia	136	47.4	0.35	Jiang et al. 2017
	LiCl/vermiculite	water	60	24.5	0.41	Brancato et al. 2018
	MnCl2	ammonia	154	35	0.23	Yan et al. 2018
Closed-Transported	NaOH	water	55	23	0.42	Fumey et al. 2017
	LiBr	water	55	22	0.40	Zhang et al. 2014
	KCOOH	water	43	12	0.28	Le Pierrès et al. 2017

From table 1 it can be seen that there are substantial performance differences of the systems in terms of temperature effectiveness. A performance tendency based on the choice of basic system can be observed. Looking at the open fixed systems, those requiring a desorption gross tem-

perature lift above 100K, show a low temperature effectiveness from 0.11 to 0.27 These are systems based on zeolite, which is the most studied solid material for inter-seasonal heat storage. In this comparison, these systems are generally larger scale, containing more storage material and are more developed towards the application. This, and the fact that zeolite due to its inherent high porosity is a very poor thermal conductor may lead to these low ratios. The systems with desorption gross temperature lift below 100K also have higher temperature effectiveness between 0.28 to 0.31. These work with salt impregnated materials and are generally at a smaller scale. Comparing the open fixed system results to the open transported system result, all but one temperature effectiveness is lower. This points to the tendency of better performance in transported systems due to the continuous process with introduction of fresh sorbent in order to reach high sorption gross temperature lift. There is a variation of performance in the closed fixed system, again with zeolite-based systems requiring substantially greater desorption gross temperature lift and having lower temperature effectiveness. In part, this has to do with the size of the system as with the open fixed design. Comparing only the zeolite-based systems, thus providing a more common ground, it can be concluded that closed fixed systems perform better than open fixed ones and the open transported system reaches a higher temperature effectiveness than the closed fixed system. The comparison cannot be continued to the closed transported approach, since there is no known closed transported system based on zeolite. The closed transported systems are all based on liquid sorbents since these can easily be pumped for transportation. Temperature effectiveness is generally higher in this approach in comparison to all other process options. In general, it is important to note that a desorption gross temperature lift beyond 60K (more strictly specified in chapter 2.4.2. “Charging temperatures” on page 42) is not realistic with conventional solar thermal systems or domestic heat pumps, thus to a lesser degree applicable in building integrated inter-seasonal heat storage systems.

This evaluation of reported systems based on the temperature effectivity supports the conclusion in chapter 2.2. “Sorption heat storage system categorisation” that, performance of the storage material, and hence the exploitation of its potential, is dependent on the process design. The transported approach is favoured for fixed beds and the closed system approach performs better than the open one. Overall, the closed and transported system approach is seen to have the highest performance potential in terms of temperature effectiveness and will be followed and further discussed in chapter 6. “Heat and mass exchanger design” on page 79.

2.4. Application temperatures

When considering application specific temperatures for sorption heat storage systems, both source and sink need to be specified in charging and discharging. In this chapter these required temperatures are defined as a guideline for the development of sorption heat storage systems for buildings.

2.4.1. Allocation of relevant temperatures

In order to define the operating temperatures, it is important to first clarify the allocation of the relevant temperatures and their relation, after which the specific temperature values can be defined. To assist this, a uniform thermal storage system schematic is created and shown in figure 5, showing both a heat source and a sink in charging and discharging. In the illustration, the left side of the system boundary box is considered to be the building connection and the right side is termed ambient denoting the secondary low temperature source and sink which may be air, water or ground. The allocation of the specific temperatures is shown in the schematics. The square indicates system boundaries.

There are two levels of temperature allocation to be considered; system and material. Starting from the system periphery, both, input and output temperatures of the source and sink are relevant. On the building side, this results in the four temperatures; charging source in ($\vartheta_{D/so/i}$), charging source

out ($\vartheta_{C/so/o}$), discharging sink in ($\vartheta_{D/si/i}$), and discharging sink out ($\vartheta_{D/si/o}$), for sorption heat storage systems. An additional four temperatures are required on the ambient side. These are; charging sink in ($\vartheta_{C/si/i}$), charging sink out ($\vartheta_{C/si/o}$), discharging source in ($\vartheta_{D/so/i}$), and discharging source out ($\vartheta_{D/so/o}$). These temperatures are directly applicable for component and system performance evaluation and are based on available and required temperatures in operation. Inside the system boundary the material temperatures are significant. Again, four temperatures are important. These are: charging sorbent temperature ($\vartheta_{C/ent}$), charging sorbate temperature ($\vartheta_{C/ate}$), discharging sorbent temperature ($\vartheta_{C/ent}$) and discharging sorbate temperature ($\vartheta_{D/ate}$). In operation with counter-flow of sorbent to heat transfer fluid additional two temperatures must be included, these are the charging sorbent out temperature ($\vartheta_{C/ent/o}$) and the discharging sorbent in temperature ($\vartheta_{D/ent/i}$). This is due to the particular functionality where the sorbent is cooled below the output-based temperature to an input dependent temperature.

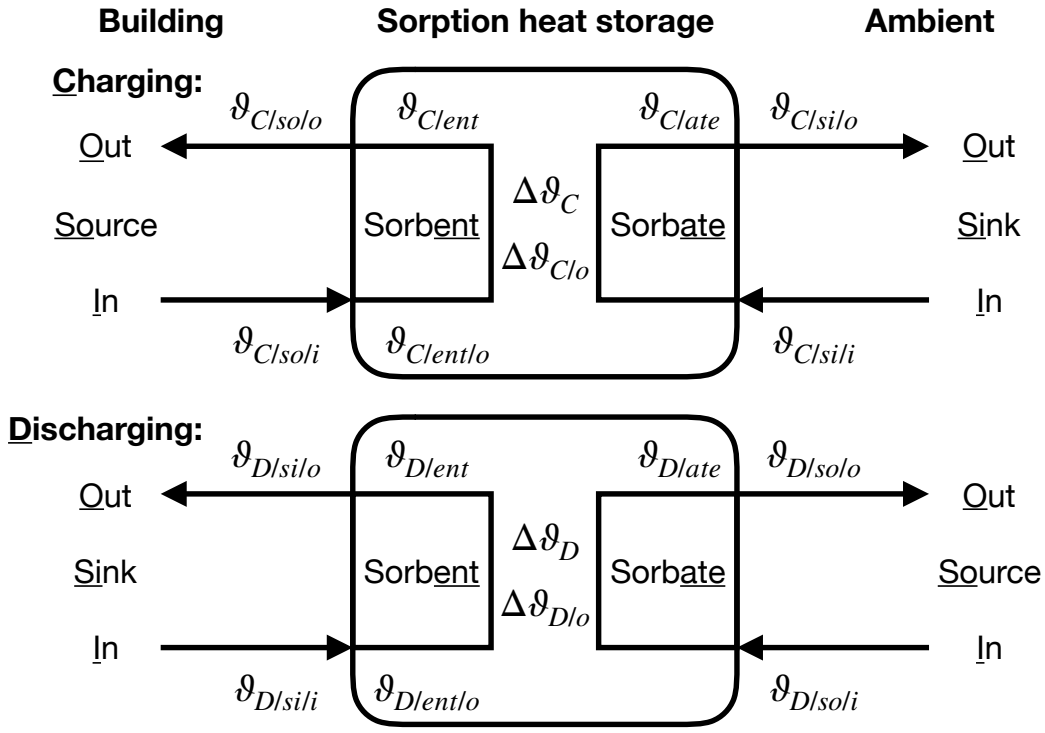

Figure 5: Uniform thermal storage system schematics, indicating the evaluation relevant temperatures. The origins of the temperature subscript abbreviations are pointed to through underscore in the respective denotations.

It is important to note that the material temperatures are not equal to the system boundary temperatures and are either higher or lower depending on the direction of heat transport in charging and discharging mode. For this study, a general temperature difference of 3K is taken between the heat transport fluid and the storage material in order to define material temperatures. This is an optimistic assumption and especially for solid sorbents in packed bed processes this low temperature difference may be challenging to reach. The material temperatures are indicative for material testing under application specific conditions, serving as a prelude for potential system performance. In the diagram in figure 5, further notation is made on the temperature difference between the sorbent and sorbate temperature. This is the gross temperature lift required in charging and reached in discharging. As previously noted, in the application as heat storage in buildings, where the ambient sink temperature is greater than the respective ambient source temperature, gross temperature lift in discharging will always be lower than in charging and thus temperature effectiveness will be less than unity.

The source and sink heat transport fluid can be either liquid, in the form of water, thermal oil, glycol solution, etc., or it can be air, as is the case of an open sorption system. In this instance, relative humidity or its partial vapour pressure respective temperature is an important additional parameter to be specified. These temperatures are indicated in brackets.

The relations between the specified temperatures in both charging and discharging are as follows.

Source side charging:

$$\vartheta_{C/so/i} > \vartheta_{C/so/o} > \vartheta_{C/ent}, \textit{ Equation 5}$$

And:

$$\vartheta_{C/ent/i} > \vartheta_{C/ent}, \textit{ Equation 6}$$

($\vartheta_{C/ent/i}$ is only relevant in a counter flow heat exchange process, the subscript i is in reference to the sorbent flow direction which is opposite to the indicated heat transport fluid direction)

Sink side charging:

$$\vartheta_{C/si/i} < \vartheta_{C/si/o} < \vartheta_{C/ate}, \textit{ Equation 7}$$

In addition:

$$\Delta\vartheta_{C/o} = \vartheta_{C/ent/o} - \vartheta_{C/ate}, \textit{ Equation 8}$$

$$\Delta\vartheta_{C} = \vartheta_{C/ent} - \vartheta_{C/ate}, \textit{ Equation 9}$$

And:

$$\Delta\vartheta_{C/o} > \Delta\vartheta_{C}, \textit{ Equation 10}$$

Source side discharging:

$$\vartheta_{D/so/i} > \vartheta_{D/so/o} > \vartheta_{D/ate}, \textit{ Equation 11}$$

(note that source and sink side switch)

Sink side discharging:

$$\vartheta_{D/si/i} < \vartheta_{D/si/o} < \vartheta_{D/ent}, \textit{ Equation 12}$$

And:

$$\vartheta_{D/ent/o} < \vartheta_{D/ent}, \textit{ Equation 13}$$

($\vartheta_{D/ent/o}$ is only relevant in a counter flow heat exchange process, the subscript o is in reference to the sorbent flow direction which is opposite to the indicated heat transport fluid direction)

In addition:

$$\Delta\vartheta_{D/o} = \vartheta_{D/ent/o} - \vartheta_{D/ate}, \textit{ Equation 14}$$

$$\Delta\vartheta_{D} = \vartheta_{D/ent} - \vartheta_{D/ate}, \textit{ Equation 15}$$

And:

$$\Delta\vartheta_{D/o} < \Delta\vartheta_{D}, \textit{ Equation 16}$$

In the following section, temperature values for the building application are defined.

2.4.2. Charging temperatures

In domestic application, there are conventionally two main renewable energy sources to be considered; solar thermal and solar electric. To date, the more widespread approach for heat storage systems is thermal supply from solar thermal collectors. For building integrated glycol or water based solar collector systems, the system temperature is limited, due to the hot water storage tank, to a maximum of 95°C. This is regulated by the EN 12897[3] standard. Beyond thermal charging, there is the prospect of electrical charging. The benefit in electric charging is found in the increased access of renewable energy in the form of own and grid-sourced photovoltaic (PV) electricity, as well as wind and other renewable sources. This provides a means for storage supported sector coupling between electricity and heat. Electric charging can be performed with direct resistive heating, microwave-based heating as reported by Zettl and Lachner (2015) or alternatively by electrically driven compression heat pump. With resistive heating very high temperatures can be reached and limitations are bound by the employed materials. Nevertheless, higher efficiency can be achieved by using a compression heat pump, at the cost of decreased charging temperature. For this reason, $\vartheta_{C/so/i}$ is set to 95°C with 200_R°C noted with a subscript capital R, indicating possible electric resistive charging. In resistive heating, heating coils are directly integrated into the storage, thus a value for $\vartheta_{C/so/o}$ is not included. In operating with a heat transport fluid, $\vartheta_{C/so/o}$ is taken to be 3K lower than $\vartheta_{C/so/i}$, a condition adopted from the EN 14511-2[4] standard. This standard is well fitted to this application and is further used to define temperatures in discharging.

The ambient sink temperature relevant for charging can also be taken from the EN 14511-2 standard by referring to the standard rating conditions

[3] “Water supply –Specification for indirectly heated unvented (closed) storage water heaters”

[4] “Air conditioners, liquid chilling packages and heat pumps for space heating and cooling and process chillers, with electrically driven compressors - Part 2: Test conditions”

in cooling mode for air-cooled multi-split systems. The input temperature $\vartheta_{C/si/i}$ is 30°C with wet bulb temperature (WBT) 24°C, taken as the partial vapour pressure equivalent temperature and $\vartheta_{C/si/o}$ is 35°C. In the standard, no partial vapour pressure equivalent temperature value for $\vartheta_{C/si/o}$ is provided, since in compression heat pumps no mass is exchanged. In an open process sorption system on the other hand the $\vartheta_{C/si/o}$ wet bulb temperature is relevant. In order to encourage uniform testing across the varying processes, it is thus suggested that the outbound air is saturated and $\vartheta_{C/si/o}$ wet bulb temperature is also equal to 35°C. In the case of heat release to the ground by means of geothermal heat exchanger, a temperature reduction by 10K is proposed, thus $\vartheta_{C/si/i}$ is 20°C and $\vartheta_{C/si/o}$ is 25°C. Figure 6 shows the uniform thermal storage system schematics with the relevant heat charging temperatures.

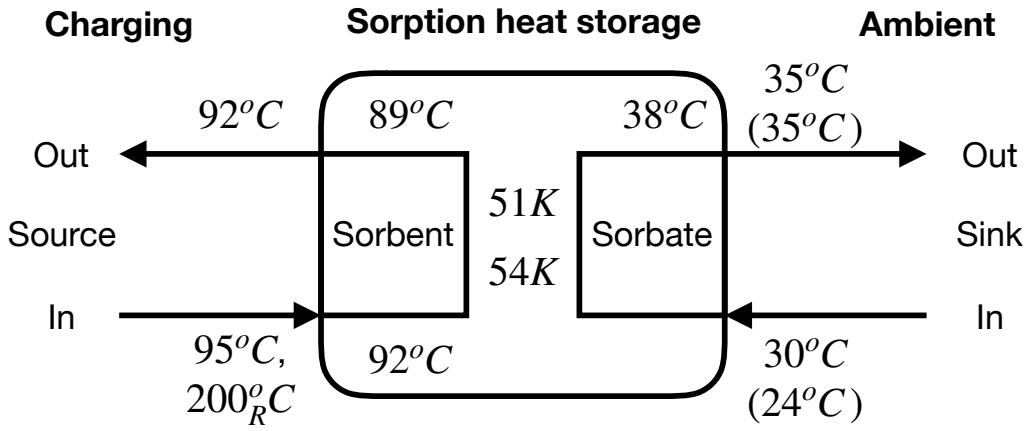

Figure 6: Uniform thermal storage system schematics with relevant heat charging temperatures indicated. Wet bulb temperatures are indicated in brackets.

2.4.3. Discharging temperatures

In the discharging process there are two varying applications to be observed, space heating, and preparation of domestic hot water. Again, the EN 14511-2 standard is a good resort for space heating and for domestic hot

water the EN 16147[5] standard and the CEN/TR 16355[6] recommendation are appropriate.

In EN 14511-2, heating systems with water distribution are subcategorised into low, medium and high temperature. Low temperature refers to under floor heating, requiring 35°C source temperature with 30°C return temperature. Medium and high temperature applications feature radiators for heat release. The required temperatures are 45°C and 55°C as source with 40°C and 47°C return respectively. The input temperature for air heating systems is 20°C with a wet bulb temperature of 15°C. The output temperature is not defined, nevertheless, a temperature well above 22°C must be reached in order to conform to the comfort temperature of 22°C stated in the EN 15251[7] standard. In order to provide a minimised temperature profile to be followed, these temperatures are reduced to a single supply and return temperature. Since the starting point for solar based heating or solar assisted heating is a good low temperature heat distribution and a well-insulated building, it is reasonable to assume the availability of under floor heat distribution. The output temperature is thus set to 35°C and the input to 25°C for both water and air systems. These temperatures for space heating are shown in figure 7.

In preparation of domestic hot water, there is an increasing awareness concerning the growth of bacteria, especially legionella, in the domestic hot water supply. Temperatures between 25°C and 50°C encourage legionella growth. For this reason, according to CEN/TR 16355, it is recommended that within 30s after fully opening a draw-off fitting the water temperature should not be less than 60°C. Specific profiles for testing of heat pumps for domestic hot water are given in the EN 16147 standard. In order to enable a simple initial evaluation of heat storage material and components $\vartheta_{D/si/i}$ is

[5] “Heat pumps with electrically driven compressors - Testing, performance rating and requirements for marking of domestic hot water units”

[6] “Recommendations for prevention of Legionella growth in installations inside buildings conveying water for human consumption”

[7] “Indoor environmental input parameters for design and assessment of energy performance of buildings addressing indoor air quality, thermal environment, lighting and acoustics”

proposed to be 25°C, this can be an average temperature of the discharged domestic hot water tank or the heating water return temperature from a fresh hot water station and $\vartheta_{D/si/o}$ should be 65°C, a temperature slightly greater than the draw-off temperature, accounting for transport loss. The source temperatures are equal to those for the space heating temperatures. In a system application if the heat storage is not able to supply hot water at 65°C this final increase must be reached by other means, for example direct resistive heating.

Temperatures for the low temperature heat source in discharging can also be taken from the EN 14511-2 standard. Three varying heat sources are provided; Air source, water sources and brine source. Air source temperatures are 7°C (WBT 6°C), 2°C (WBT 1°C), -7°C (WBT -8°C) and -15°C (WBT NaN) with reference at 7°C. Water source temperatures are 10°C and 15°C with reference at 10°C. And, brine source temperatures are 5°C, 0°C and -5°C with reference at 0°C. Since subzero temperatures are not applicable for sorbent systems operating with evaporation of water and open systems require both dry and wet bulb temperatures, it is suggested to use 7°C (WBT 6°C) as global input temperature with output temperature 4°C (WBT 4°C) coherent to the 3K input to output temperature difference followed for discharging source temperature in the standard. Figures 7 and 8 show the defined testing temperatures for discharging for space heating and domestic hot water. Since temperatures above 0°C are required for evaporating water during discharging, it is generally necessary to resort to heat supplied from a geothermal heat exchanger. This is a practical disadvantage, limiting application and increasing storage price.

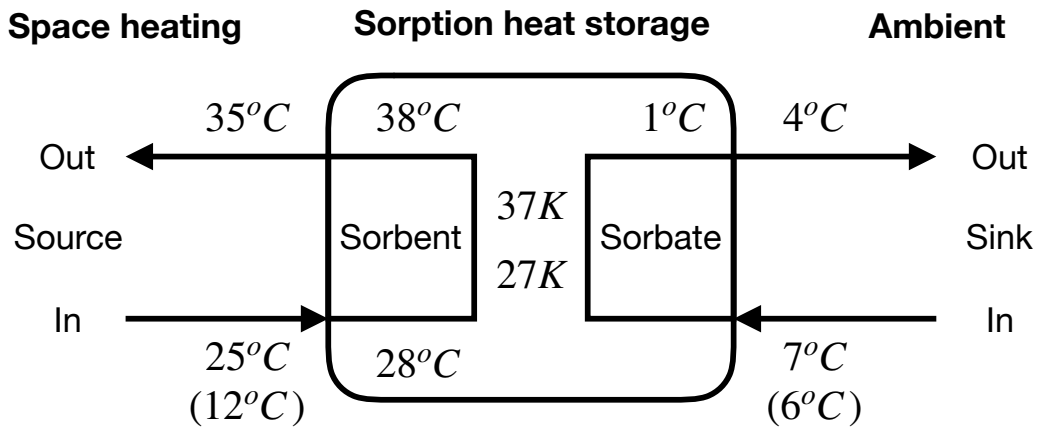

Figure 7: Uniform thermal storage system schematics with relevant space heating discharging temperatures indicated. Wet bulb temperatures are indicated in brackets.

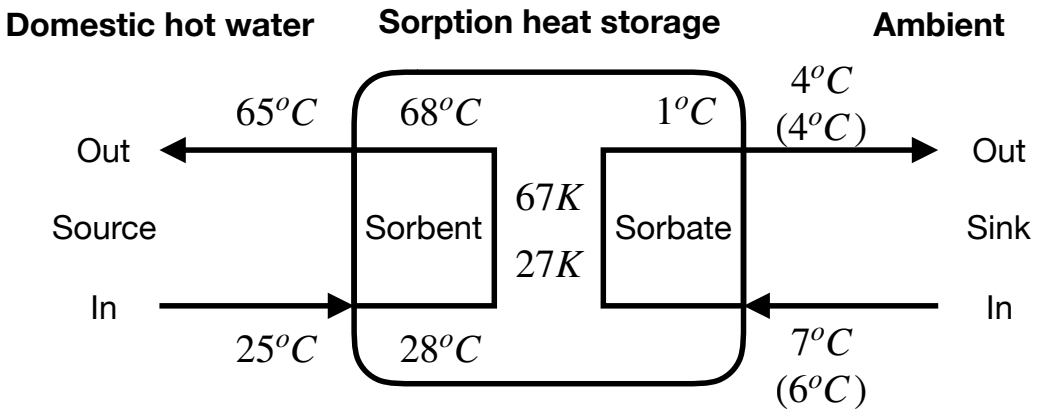

Figure 8: Uniform thermal storage system schematics with relevant domestic hot water discharging temperatures indicated. Wet bulb temperatures are indicated in brackets.

In respect to the domestic hot water profile it must be noted that in charging a maximum gross temperature lift of 51K or 54K, if true counter flow is followed, can be reached. Nevertheless, in order to achieve a temperature output of 65°C for domestic hot water, a gross temperature lift of 67K is required in discharging. This cannot be reached, since the evaporator temperature and wet bulb temperatures are substantially lower in discharging than in charging. Thus, it is clearly shown that with realistic building application specific temperatures, it is not possible to supply domestic hot wa-

ter directly from a single step sorption heat storage system. This does not signify that sorption heat storage cannot assist the production of domestic hot water, nevertheless, further measures are required on a system level.

Clear indications of the benefits of true counter flow heat exchange are also shown in the results, since greater gross temperature lift can be reached in charging and lower gross temperature lift is reached in discharging, thus greater sorbent exchange is reached, providing higher volumetric energy capacity.

With this definition of available and required source and sink temperatures for building application, it is now possible to evaluate performance of varying materials, components and systems. Materials can be compared both in respect to theoretical gross temperature lift and energy density, while on the level of components and systems comparison can also include power.

3. Closed transported liquid absorption heat storage[8]

In the inter-seasonal heat storage process categorisation and discussion, it is shown that closed transported system show substantial benefits compared to the other schemes, in respect to all three performance parameters, especially if a true counterflow process is followed. Sorbent transport on the other hand is more straightforward with liquids rather than solid particles. For this reason, in the continuation of this work focus is set on closed, transported sorption storage based on liquid sorbent.

Liquid absorption generally involves the absorption of water vapour in hygroscopic salt solutions and the absorption of gasses like ammonia vapour into water. In the process, the weight concentration of the absorbent in the solution of absorbent and absorbate, referred to as absorbent solution, is alternated from high in charged stage to reduced in discharged state and vice versa.

Many material studies on the potential of absorption heat storage have been performed (N'Tsoukpoe et al. 2009, Zhang et al. 2014), and proof of concepts or demonstrators have been attempted for working pairs such as, aqueous lithium chloride (Bales 2006b, Bales 2008), aqueous lithium bromide (N'Tsoukpoe et al. 2013, Zhang et al 2014), aqueous sodium hydroxide (Fumey et al. 2014a, Weber and Dorer 2008, Weber 2010]) and aqueous calcium chloride (Quinnell et al. 2011, Le Pierrès et al. 2011). When evaluating possible absorbents and taking material price and maximum temperature gain (gross temperature lift) into consideration, it is found that the price for lithium bromide and lithium chloride does not permit inter-seasonal storage

[8] This section basis on the published works:
Fumey B., Weber R., Baldini L., Sorption based long-term thermal energy storage – Process classification and analysis of performance limitations: A review, Renewable and Sustainable Energy Reviews 111, 2019, 57–74
Fumey B., Weber R., Baldini L., Liquid sorption heat storage – A proof of concept based on lab measurements with a novel spiral fined heat and mass exchanger design, Applied Energy, 200, 2017, 215-25.

and the gross temperature lift of calcium chloride is low, thus concludes that sodium hydroxide remains as a potential liquid absorbent.

3.1. General system description

Inter-seasonal sorption heat storage systems based on liquid absorbents operate on the same concept as absorption cooling machines or heat transformers. Figure 9 provides a simple illustration of the process based on the uniform thermal storage system schematic, complemented with the respective schematic illustration in the vapour pressure vs. temperature diagram. Illustrations are numbered for reference. The process consists in general of four heat and mass exchangers; absorber, desorber, evaporator and condenser. The absorber and desorber are in contact with the absorbent and the evaporator and condenser are in contact with the absorbate. The desorption and condensation process are at elevated pressures to the evaporation and absorption process. In the cooling and heat transformer application illustrated in figure 9 Nr. 1, the absorbent is continuously circulated from absorber to desorber and the absorbate is condensed on the condenser, pumped to the evaporator and again evaporated. In the cooling machine, the point of interest is the evaporator and in the heat transformer it is the absorber. In sorption heat storage the same concept is followed, nevertheless not with continuous circulation of the absorbent, but with intermittent storage as shown in figure 9 Nr. 2. A seasonally shifted process of desorption and condensation in summer and evaporation and absorption in winter is followed. In general, it is thus proposed that desorber and absorber as well as condenser and evaporator can be combined respectively, as shown in figure 9 Nr. 3. This may lead to a reduction of components and improvement of power and energy density.

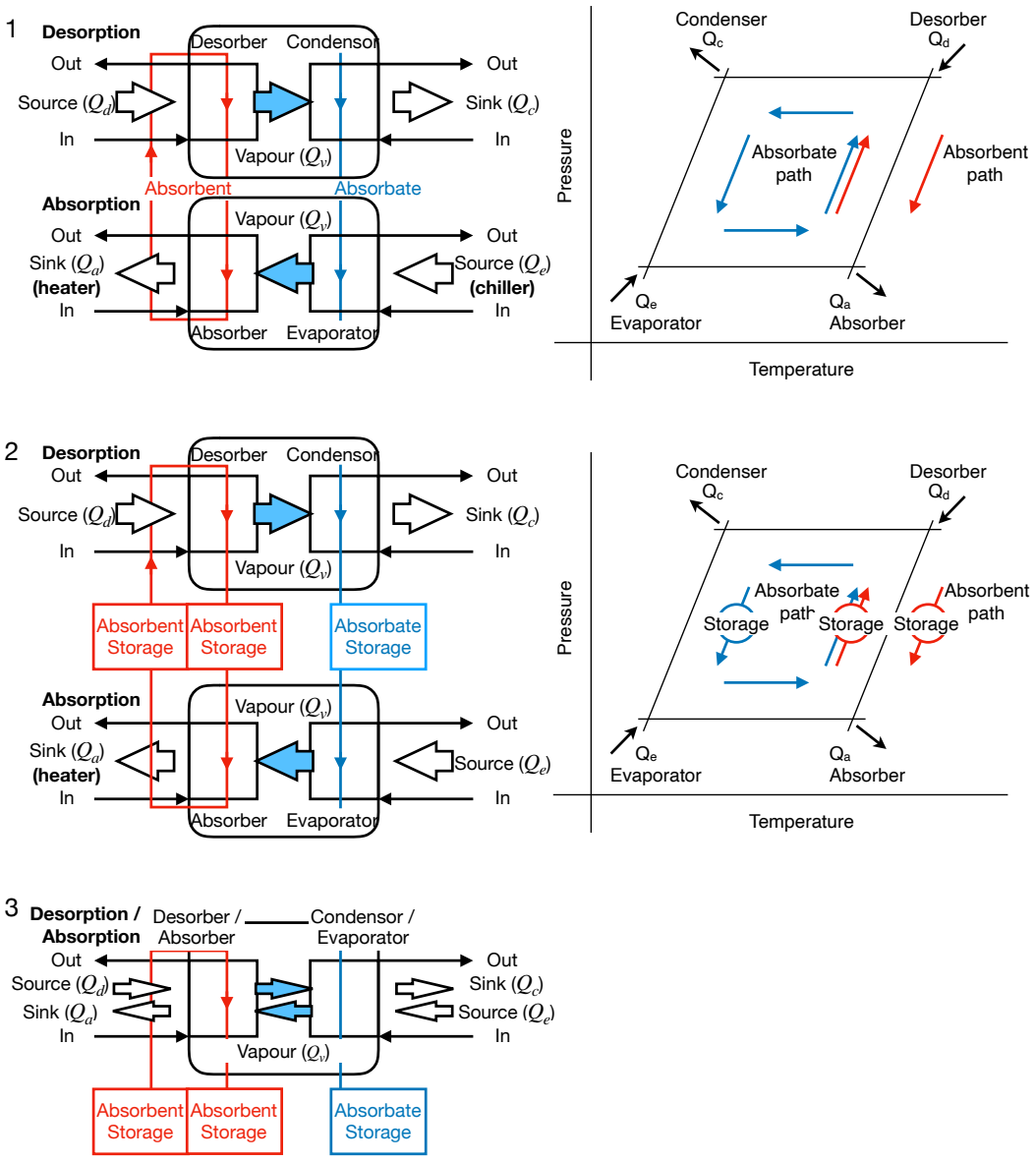

Figure 9: Illustration of the similarities of liquid sorption cooling machines and transformer (position 1), to liquid sorption heat storage (position 2 and 3), based on the uniform thermal storage system schematic, and the process illustration in the vapour pressure vs. temperature diagram.

Many published absorbent material studies show good potential, but absorbent based inter-seasonal heat storage demonstrators perform poorly. Even though there are market ready, absorption cooling machines, heat pumps and dehumidifiers (Kessling et al. 1998a, Kessling et al. 1998b), no mature long-term heat storage systems exist (N'Tsoukpoe et al. 2009). It is found that operation frequently suffers from low absorbate mass difference

between desorption and absorption processes. For example, the demonstrator system with LiBr described by Zhang et al. (2014), reached only a low energy capacity due to the low concentration change from 61.8wt% to 56.9wt%, even though absorbent recirculation was followed for better heat and mass exchanger wetting, with the consequence of reduced gross temperature lift. The system described by N'Tsoukpoe et al. (2013) proved to have no significant heat release at all. As highlighted in chapter 2.1 "Performance parameters" on page 21, in the absorption heat storage, the final capacity is directly linked to the absorbate exchange between desorption and absorption process.

Despite the fact that, the process of absorption and desorption in the heat storage application is comparable to the absorption heat pump or chiller, the actual operation differs strongly. In chillers and transformers, charging and discharging occur continuously and large change in absorbent solution concentration between absorption and desorption process is not of primary importance. Thus, high absorbent solution flow for optimal wetting as required for example in the tube bundle falling film heat and mass exchanger, can be reached. In the heat storage approach on the other hand, a continuous but not full cycle process is at work (Fumey et al. 2014c, Weber and Dorer 2008). This is on account of its role as storage as illustrated in figure 9. In this application it is of significant importance that a high absorbent concentration difference is reached between absorption and desorption process. As previously pointed to, this directly affects the heat storage energy density. In addition, owing to the dependence of the output temperature to the concentration of absorbent in the absorbent solution, complete absorption must occur in one process step and recirculation is not permissible by reason of absorbent concentration reduction in the solution. Consequently, high absorbent solution flow for optimal wetting of the heat and mass exchanger is not possible.

The problem of low absorbate exchange in absorption heat storage demonstrators primarily results from adopting heat and mass exchanger designs from absorption heat pumps, which commonly rely on liquid falling film

tube bundle type heat and mass exchangers (Ibarra-Bahena and Romero 2014, Daguenet-Frick 2014, Srikhirin et al. 2001).

3.2. Process of charing and discharging

In absorption, the discharge or heat release process, liquid absorbate is evaporated by means of employing a low temperature heat source, for example a ground source heat exchanger. This absorbate in turn condenses on the charged liquid absorbent solution due to the reduced vapour pressure on the liquid surface. From the absorbate phase change and the respective heat release, and to a minor part from absorbent and absorbate mixing (solution), the sorbent surface temperature increases and reaches a concentration, vapour pressure and temperature equilibrium state. Heat and absorbate mass transport into the absorbent and heat release to the heat transport fluid in the heat and mass exchanger enables further mass uptake, at lower temperature, due to the increase of absorbate in the absorbent solution. In desorption, the charging or heat uptake process, the inverse process is followed. The absorbent solution with high sorbate content (discharged state) is heated and absorbate is evaporated from the sorbent solution surface and separately condensed and the heat of condensation is discarded to the ambient. Through evaporation, the sorbent surface is cooled and the absorbate concentration is reduced thus again an equilibrium state is reached. Further heat and sorbate mass transport to the surface again enables desorption (absorbent evaporation). Both absorbent solution with high absorbent content and absorbate are separately stored in their liquid state for later release of serviceable heat through absorption.

As with all sorption heat storage processes, heat is not stored in its sensible form, but the potential to regain heat at increased temperatures from a low temperature heat source is accumulated. The approach benefits from lossless storage of this potential and improved thermal energy density in comparison to sensible heat storage. Specific benefits of the liquid absorption heat storage are the possibility of separating storage vessels and heat and mass exchanger (conversion unit) owing to the liquid state of both

absorbent solution and absorbate. This enables a separation of converter unit (power) and storage unit (energy) on a system level and thus may lead to; a reduction of components, improvement of energy density, improved heat transfer, flexibility in storage design as well as enabling a continuous process in charging and discharging which is often not possible with solid adsorbents. Figure 10 shows an illustration of the absorption process in blue and desorption process in red. Illustrated are two chambers serving as absorber and desorber as well as evaporator and condenser. Chamber one is in contact with aqueous sodium hydroxide and chamber two with water.

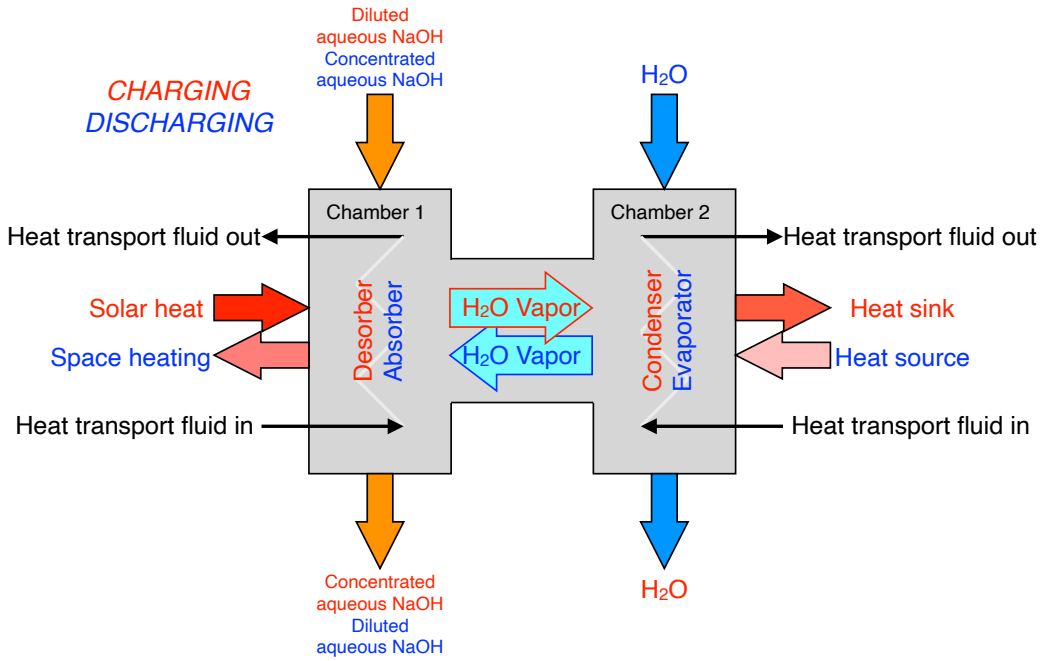

Figure 10: Illustration of the adsorption and desorption process.

4. Aqueous sodium hydroxide

In this work focus is placed on aqueous sodium hydroxide (NaOH) for reasons previously stated in the introduction to chapter 3., “Closed transported liquid absorption heat storage” on page 49. In this chapter relevant material parameters and theoretical performance of gross temperature lift and energy density according to the application temperatures from chapter 2.4., “Application temperatures” on page 39 is discussed.

Sodium hydroxide is highly soluble in water and aqueous sodium hydroxide has a reduced water vapour pressure in comparison to water. The working pair - sodium hydroxide and water - can thus be used as an absorbent in a chemical heat pump process for heating as well as cooling. Due to its high reactivity with carbon dioxide as well as the inherently low active surface area compared to solid highly porous adsorbents, the closed process is required to prevent carbonisation and reduce mass transport interference, resistance from non-condensing gases, in the gas phase. Since aqueous sodium hydroxide solutions smaller or equal to 50wt% sodium hydroxide in water are liquid at room temperature (see Appendix A., “Solubility” on page 202), the transported process can easily be applied in as far as the 50wt% limit is not exceeded. Operation at sub-ambient pressures, water vapour pressure, through removal of non-condensing gases, further enables ample evaporation of water for increased power density, even at low evaporation temperatures. Sodium hydroxide is a common base and a major inorganic, utilised in a diversity of industries. The majority of its production is used in the manufacture of chemicals, such as propylene oxide and sodium salts, however, the pulp and paper, soap and detergent, and textile industries are also great areas of application. Electrolysis of sodium chloride accounts for most of today’s installed capacity for sodium hydroxide.

4.1. Material Characteristic

Sodium hydroxide, also known as caustic soda, lye, white caustic or sodium hydrate, is a very strong odourless base. Anhydrous sodium hydrox-

ide has a white, waxy, opaque crystal structure and in its aqueous form, diluted in water, it is a transparent liquid. sodium hydroxide has a molar mass of 39.9971g mol^{-1}, its anhydrous density is 2.13g cm^{-3} and in aqueous solution at 50wt% and 30wt% it is 1.525g cm^{-3} and 1.328g cm^{-3} respectively. It is highly soluble in water (418g l^{-1} at 0°C, 1110 g l^{-1} at 20°C, 3370 g l^{-1} at 100°C) and lesser so in methanol and ethanol. The melting point is at 318°C and the boiling point is 1388°C. Sodium hydroxide has an unlimited shelf life, but since it reacts strongly with carbon dioxide (CO_2), forming sodium carbonate, contact to air should be prevented. Sodium hydroxide is highly corrosive and contact with its solutions can readily decompose proteins and lipids in living tissues, which consequently causes chemical burns and may induce permanent blindness upon contact with eyes. Annual production of sodium hydroxide is approximately 70 million metric tonnes (www.essentialchemicalindustry.org 2020). The price per metric tonne of anhydrous material is approximately US$ 280 (www.intratec.us 2020) and the price for aqueous solution at 50wt% is US$ 140 per metric tonne (yosemite.epa.gov 2020). Amongst others, producing companies are Solvay Chemicals International SA, DOW and Oxychem.

Aqueous sodium hydroxide is a well-known and characterised chemical. Its properties have been studied in detail and reported by Olsson et al. (1997) and Alexandrov (2005). In appendix A “Aqueous sodium hydroxide” on page 186, important characteristics of aqueous sodium hydroxide for absorption heat storage are provided. When considering the characteristics of aqueous sodium hydroxide in light of the absorption heat storage application, there are two levels to be looked at. These are performance in respect to temperature and energy capacity on one side and on the other side performance in respect to power. Theoretical temperature and energy capacity performance is solely dependent on the water vapour pressure on aqueous solutions of sodium hydroxide. Practical performance thereof depends on heat and mass transport kinetics (power) and exposure time (heat and mass exchanger design). Power on the other side is dependent on parameters such as viscosity, material density, thermal conductivity, and solubility, as well as preferable heat and mass exchanger design (heat transport). Viscosi-

ty for example, effects both flow regime in the heat and mass exchanger as well as the kinetics of mass transport of water into or out of the aqueous sodium hydroxide solution in absorption or desorption respectively. Thermal conductivity is a further important parameter in respect to kinetics, since mass and heat transport are strongly interlinked processes.

Additional important practical parameters for operation are; the concentration and temperature-based solidification curve, the boiling temperature, the specific mass and the physical, chemical and thermal stability of the material. In the case of aqueous sodium hydroxide it is recognised that concentration beyond 50 wt% sodium hydroxide in water is not practicable due to the potential of solidification at room temperature. This is a restriction that limits both energy density, and to a greater degree gross temperature lift. Due to the substantially higher boiling temperature of sodium hydroxide compared to water, good separation through evaporation is possible and a carry-along of sodium hydroxide is not expected due to the considerably greater mass of sodium hydroxide compared to water. Sodium hydroxide is a very stable chemical, as indicated by its unlimited shelf life. For this reason and due to its low price application in inter-seasonal heat storage appears fitting.

4.2. Temperature and energy density

The vapour pressure of the aqueous sodium hydroxide solution is an important parameter to identify the temperature and energy performance potential. Figure 11 shows the pressure vs. temperature diagram of varying aqueous sodium hydroxide concentrations calculated according to Olsson et al. (1997). By positioning operating points, provided from chapter 2.4. “Application temperatures” on page 39, in absorption as well as desorption, theoretical temperature performance and change in concentration, which in turn enables calculation of material-based energy density, shown in figure 12 on page 60, can be made.

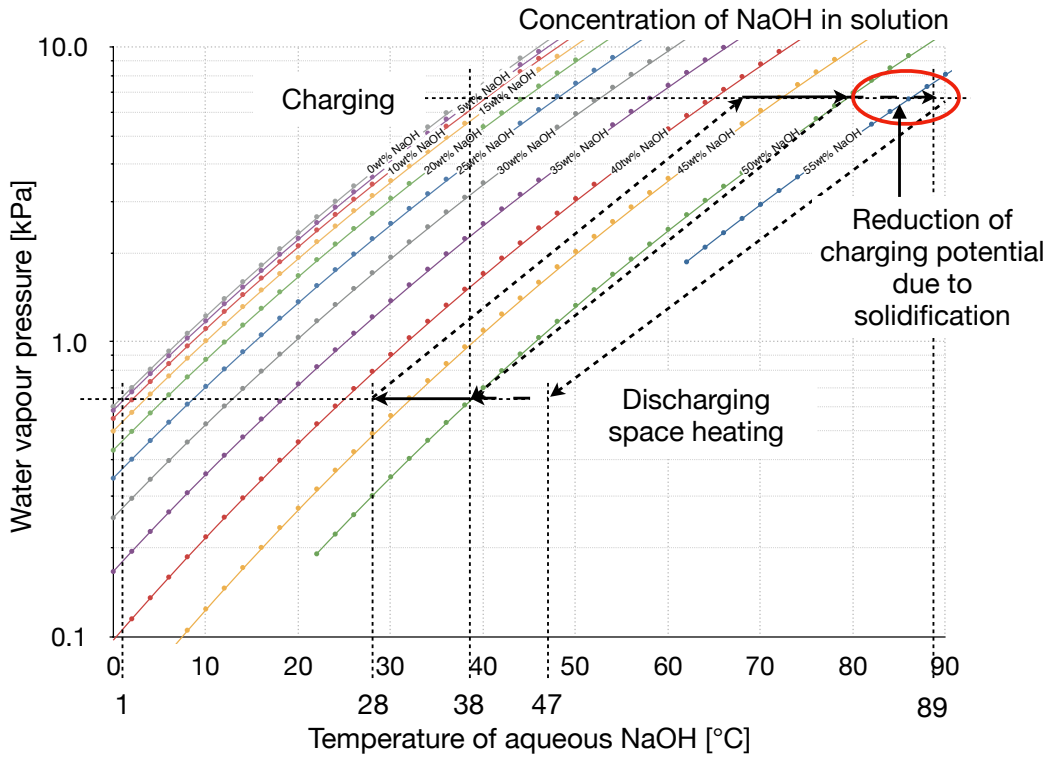

Figure 11: Vapour vs. temperature diagram of aqueous sodium hydroxide. Indicated is the charging and discharging process based on the realistic temperature profile for space heating. The complete available temperature scope can not be utilised as noted with the red circle, due to the risk of solidification at concentration greater than 50wt% and room temperature, see Appendix A. "Solubility" on page 202 [Fumey et al. 2015a].

Since aqueous sodium hydroxide can be employed as a liquid absorbent, counter flow of absorbent to heat transport fluid is possible and the lower absorbent temperature can be applied in absorption, thus reaching greater material exploitation (Fumey et al. 2017). Figure 11 shows the operating process in charging as well as discharging, in the absorbate vapour pressure vs. absorbent temperature diagram, based on the elaborated realistic temperature profile. Starting at the water vapour condensing temperature of $\vartheta_{C/ate}$ = 38°C, the vapour pressure reaches 69.7mbar, as indicated with the respective fine dashed lines. By heating the aqueous sodium hydroxide to its maximum temperature of $\vartheta_{C/ent/o}$ = 89°C the sodium hydroxide concentration in the solution at equilibrium state, reaches approximately

57wt%. In the liquid absorbent process, this concentration is too high, due to the risk of crystallisation at room temperatures as seen in the solidification line provided in appendix A. “Solubility” on page 202. For this reason, the concentration is kept at 50wt% in order to prevent issues with process failure from crystal clogging. The absorption heat storage based operated with liquid aqueous sodium hydroxide is thus not able to use the full charging potential of the available realistic temperature profile. This has a negative effect on both gross temperature lift and energy capacity. By limiting to 50wt%, with an evaporating temperature of $\vartheta_{D/ate}$ = 1°C, the maximum sorbent material temperature is $\vartheta_{D/ent/o}$ = 38°C, which is just the required sorbent temperature for floor heating. If maximum charging could be reached, the maximum absorbent temperature would be 47°C. Since counter flow is followed, the sorbent can be cooled down to $\vartheta_{D/ent}$ = 28°C and a concentration difference between 50wt% and approximately 42wt% is reached. This results in a maximum storage capacity of approximately 0.62GJ m^{-3} (172kW h m^{-3}) in respect to the volume taken to include the sorbent volume in its charged state and the sorbate volume as shown in Figure 12.

In the concentration gradient from 50wt% down to 40wt% there is a continuous change from a mixture of the hydration state 3.5 and 2 towards 4 and 3.5 in solution, see appendix A. “Solubility” on page 202. For this reason, there is a continuous absorption and heat release process at hand, at varying temperature, dependent on the absorbent concentration. This is different to many solid salt absorption processes where hydration is not a continuous process, resulting in heat release at only specific temperatures (Roelands et al. 2015, Trausel et al 2014).

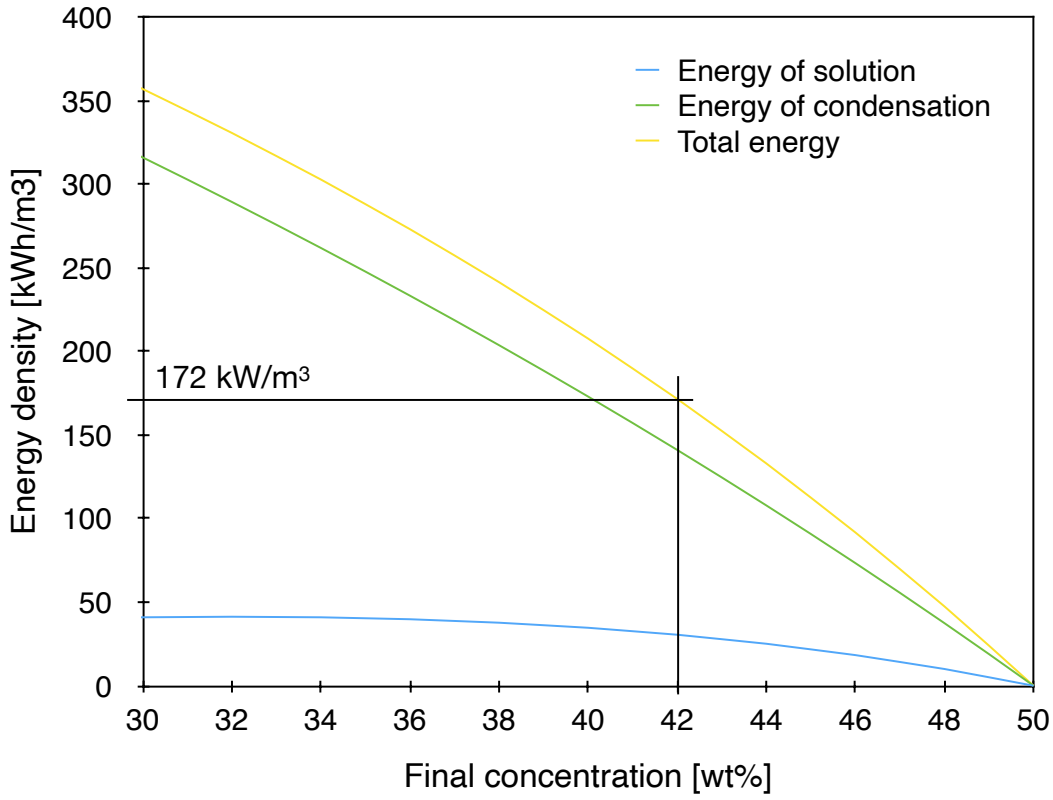

Figure 12: Diagram showing the theoretical energy density of solution (blue), the theoretical energy density of condensation (green) and the total energy density (yellow). The specific energy density is calculated in respect to the volume of charged sorbent at 50wt% and the required sorbate to reach a specific concentration change. Energy of solution is taken from Appendix A. "Heat of solution" and energy of condensation is based on the water vapour mass uptake multiplied by its condensation enthalpy.

Based on a good characterisation of the material in respect to vapour pressure, temperature and concentration equilibrium, as well as the defined application specific temperature profile, a good initial evaluation of the maximum material temperature and energy density performance can be made. This is now followed by material testing based on the application specific temperatures, at which stage kinetic behaviour in the form of heat and mass transfer may further reduce final capacity and give indication towards appropriate design of components. In a final step, components and systems are tested according to the defined heat transfer fluid temperatures. At

which point, heat transport losses are critical, reduction thereof will lead to improved storage capacity and vice versa.

4.3. Power

Power is a performance parameter more difficult to assess on the material level, and relevant values can only be provided on the components and system scale. Power is affected both by the interlinked heat and mass transport kinetics as well as the active area, or when referring to the volumetric power, the specific volumetric active area. Aqueous sodium hydroxide has a good thermal conductivity, see appendix A. “Thermal conductivity” on page 207, as liquids generally do. Its low water vapour pressure further encourages rapid vapour condensation on the sorbent surface. On the other hand, due to the high viscosity, mass transport of the sorbate (condensed water) into the aqueous sodium hydroxide solution is generally slow, since rate of mass transport is directly dependent on viscosity (see equation 30, page 75). High viscosity brings forth another practical design challenge in respect of reaching high volumetric specific active area. Since viscosity and surface tension are high, aqueous sodium hydroxide tends to accumulate, substantially reducing both contact to sorbate vapour and contact to heat exchanger and so further reducing specific power (see equation 26, page 69). For this reason it is of upmost importance to find a practical design that prevents accumulation of absorbent and to understand the process of mass transport in absorption and desorption.

Thus, in the continuation of this work, chapters 5 to 10, focus is set on understanding the process of mass transport of water into aqueous sodium hydroxide under application specific conditions. The following chapters are dedicated to these activities. A bulk scale setup was designed and built in order to measure water uptake and release on an absorbent still film to understand kinetic behaviour. An experimental apparatus was built to measure mass transport in absorbent film with Raman spectroscopy, in order to detect transport resistance and a further testing facility was built to visualise water uptake on aqueous sodium hydroxide with neutron imaging in order to

study potential for inducing absorbent mixing for improved mass transport. For application true practical evaluation, a lab scale heat and mass exchanger was built to enable extensive testing of potential heat and mass exchanger designs.

Not included in this performance evaluation of aqueous sodium hydroxide for absorption heat storage is efficiency. In addition to the defined operating temperatures this requires definition of the storage temperature. Process efficiency losses are due to non-recoverable temperatures, such as the temperature difference between the water vapour of as low as 1°C and the absorbent temperature of possibly 20°C in absorption to the minimum absorbent temperature of 28°C. This naturally further reduces the storage capacity but is not advanced in this study.

4.4. Corrosion

Sodium hydroxide is well known and frequently used as strong lye. Its imposed elevated chemical stress at high concentration and / or temperature on many materials has been thoroughly studied. Plastics such as polypropylene or polytetrafluorethylene show good resistivity to concentrated aqueous sodium hydroxide and application in storage tanks at room temperature is well fitting. Nevertheless, in the heat and mass exchanger, due to the low operating pressures and concerns for mechanical strength at elevated temperatures, application of plastics is not considered ideal. A further uncertainty therein is the risk of outgassing of plastics under these conditions. For this reason, diversion to appropriated metals is required.

As a rule of thumb, all standard stainless steels are resistant to general corrosion by all concentrations of aqueous sodium hydroxide up to about $65^{o}C$ (Davies 1997). The resistance to general corrosion in aqueous sodium hydroxide is almost directly proportional to the nickel content. However, stainless steels may be subject to stress corrosion cracking, intergranular attack and localised or pitting corrosion. Nickel based alloys are more resistant, but not totally immune to these forms of corrosion (Davies 1997).

An important parameter to consider is that heat transfer through a metal to the caustic solution may accelerate corrosion. This is due to the local increase in concentration at elevated temperature and by erosion caused from gas bubbles formation. Contaminants encountered in sodium hydroxide production and usage may further affect the corrosion resistance. However, it is reported that differences in concentration and temperature are more important than pollutants resulting from varying manufacturing methods (NACE 1971).

Commercially pure nickel, alloy DIN 2.4066, is one of the best metals for resisting corrosion [Anon 1985]. As with stainless-steel, nickel is more severely attacked in hot, concentrated aqueous sodium hydroxide under heat transfer conditions. In the application of evaporation, from 30wt% sodium hydroxide to 50wt% sodium hydroxide in water at a temperature of 81.7°C the corrosion rate of alloy DIN 2.4066 is 0.003mm a^{-1} (Yasuda et al. 1983).

Thus, it is concluded that storage components serving as containment, such as tanks, tubes, valves, etc. can well be built of polypropylene and stainless-steel 1.4404. Nevertheless, the heat and mass exchanger, and more specifically the absorber / desorber is exposed to high chemical stress. Nickel coating may thus be an appropriate approach to minimise this.

5. Study of absorption at bulk scale

The discrepancy between reported material performance to system achievement, as pointed to in chapter 3. “Closed transported liquid absorption heat storage” on page 49, is a prevalent concern in the field of long-term heat storage based on thermochemical materials. A major source of difference was found in the lack of sufficient material characterisation, testing under material ideal conditions outside of application scope on all scales and poor adaptation of components to the actual sorption material and the specific application of long-term heat storage. To date, there has been little data and experience available concerning performance degradation along the scale from milligram absorbent based material analysis to megagram absorbent based demonstrator system application, as well as kinetics of sorption processes under application specific conditions. Evaluation of theoretical performance according to the defined realistic application temperatures has been performed in chapter 4. “Aqueous sodium hydroxide” on page 55.

In order to gain insight in performance in respect to power (heat and mass exchange kinetics) on a bulk material level (up to 100g), a material unspecific experimental chamber was built for sorption testing under application specific conditions. This intermediate step between pure material sample and available material date (provided in appendix A. “Aqueous sodium hydroxide” on page 186) and real-scale demonstrator, imparted understanding of kinetic behaviour and potential performance degradation through increase of bulk material. This enabled better forecast of performance at system level and provided a basis for heat and mass exchanger design.

A bulk scale test bench consisting of two chambers, absorber / desorber and condenser / evaporator was designed and built in house. Figure 13 on page 66 shows a picture of the setup. In respect to process categorisation, this setup functioned as a closed fixed system. The test bench consisted of two closed compartments interconnected with a flexible corrugated stainless-steel tube to enable vapour exchange. The evaporator / condenser

compartment was dimensioned to have a substantially larger evaporating / condensing surface area and thus respective power compared to the active sorbent surface area in the absorber / desorber compartment. This was undertaken in order to be able to keep a constant vapour pressure independent of the absorption / desorption process. The absorber / desorber unit was the main point of interest in this build. It was constructed of a chamber with inner diameter 200mm and height 200mm produced of stainless-steel, and placed on a high resolution scale, as shown in figure 13. The purpose of the setup was to measure mass increase and decrease in sorption and desorption respectively. Inside the pot, on the bottom, large Peltier elements were installed, on which a tray containing the sorbent sample was placed. The Peltier elements were used to heat and cool the sorbent, thus effecting desorption and absorption respectively. Under the pot, a water-cooled copper plate was installed and connected to a heating and cooling water bath. This plate was kept at constant temperature and served to remove heat released from the Peltier devices during cooling operation without effecting change in mass due to varying cooling water density. In operation, water evaporating temperature and sorbent temperature were controlled and change in weight, due to sorbate uptake or release on the sorbent, was measured.

The main challenge in the setup was to obtain stable measurements from the scale due to the various connections to the absorber / desorber pot. Disturbances such as solar radiation, heating plate water density change, room temperature fluctuation and air turbulence were observed to significantly influence the measurement results. For this reason, the setup was operated in a climate-controlled chamber with fixed humidity and temperature levels and no solar radiation. The scale and absorption / desorption pot were placed on a stable table and insulated from the heat produced by the setup.

With this experimental setup it was possible to characterise sorbent materials in terms of sorption kinetics and energy density under semi application specific conditions.

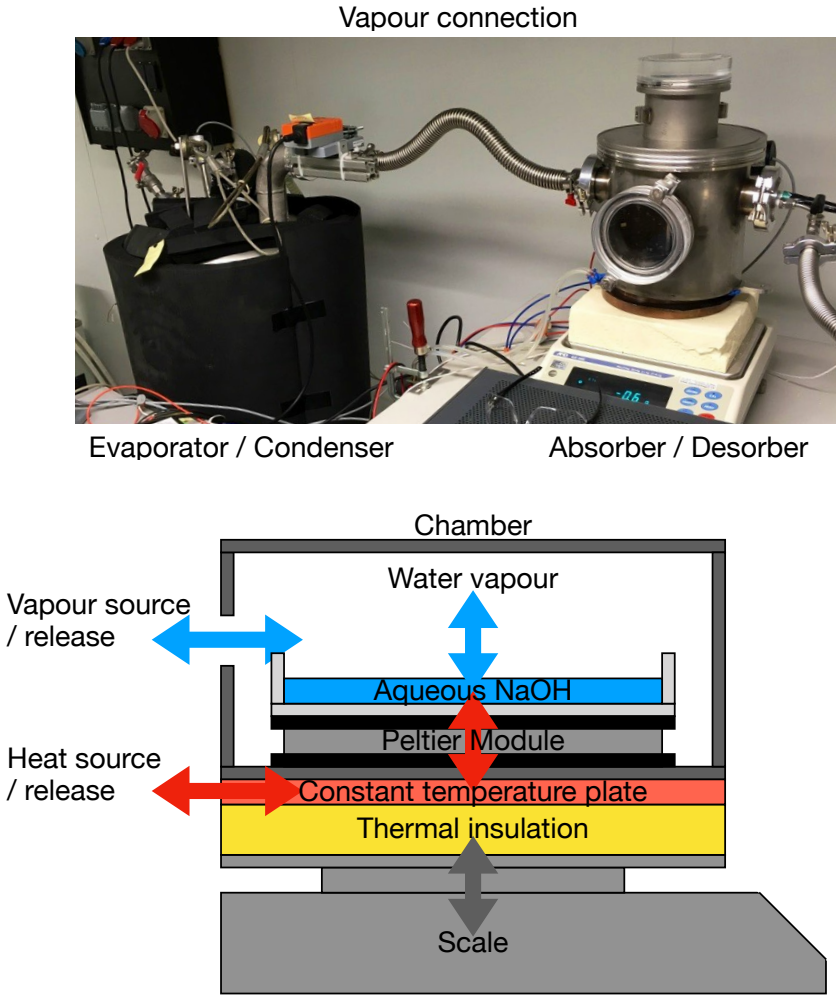

Figure 13: Top: Picture of the bulk scale test bench setup. On the left side is the evaporator and condenser, connected to the absorber and desorber with a semi flexible corrugated stainless steel tube for vapour exchange. Bottom: Illustration of the absorber and desorber unit placed on the mass scale. Vapour is sourced from and released to the evaporator and condenser unit. A Peltier module is employed to heat or cool the aqueous sodium hydroxide in the tray, and heat is sourced from and released to the constant temperature plate from a thermostat machine. Measured is the mass gain and release of water on the sodium hydroxide.

Several testing sequences were performed, governed by the following 4 parameters:

- m_{NaOH}: mass of pure sodium hydroxide in the tray.

- ϑ_v : temperature of the water vapour in the absorber / desorber, as noted in the precess description, this was directly linked to the vapour pressure.
- ϑ_d : temperature of the sorbent solution during desorption.
- ϑ_a : temperature of the sorbent solution during absorption.

The two temperatures ϑ_d and ϑ_a were defined by their difference from the temperature of the water vapour ϑ_v. The standard temperatures relations were:

$$\vartheta_d = \vartheta_v + 45K, \textit{ Equation 17}$$

$$\vartheta_a = \vartheta_v + 25K, \textit{ Equation 18}$$

In addition to the standard settings as shown in equations 17 and 18, the following deviations were also tested:

$$\vartheta_d = \vartheta_v + 55K, \textit{ Equation 19}$$

$$\vartheta_a = \vartheta_v + 15K, \textit{ Equation 20}$$

In this way, measurement tests with temperature difference between desorption and absorption of 20K, 30K and 40K were made. The following table 2 shows the testing conditions. Test are performed at 5°C and 10°C evaporator temperatures. This is slightly higher than the proposed 1°C in chapter 2.4 “Application temperatures” on page 39. 10°C was chosen to provide indication of performance at elevated temperature for comparison to the lower temperature, and 5°C was the minimum temperature reached by the evaporator in the setup.

Table 2: Test settings, deviation from the standard settings are bold.

Test setting	$m_{NaOH}\ [g]$	$\vartheta_v\ [^oC]$	$\vartheta_d\ [^oC]$	$\vartheta_a\ [^oC]$
1	15	10	55	35
2	15	10	65	35
3	15	10	65	25
4	15	5	50	30
5	15	5	60	30
6	15	5	60	20

Each of these tests was run multiple times to ensure consistency in the results and all tests were performed with the same sorbent batch. A single step temperature change was followed between desorption and absorption. Changing from absorption to desorption on the other hand required several intermediate steps due to issues with boiling and consequent splattering of sorbent out of the tray onto the chamber wall, making it inactive (not temperature controlled). For this reason, only the absorption results were further evaluated, since desorption was purposely slowed down to prevent boiling. Both desorption and absorption conditions were kept constant for several hours after each complete temperature change, in order to verify that near equilibrium conditions had been reached. Based on these equilibrium conditions and the mass difference between the absorbed and desorbed state, the concentration was calculated under these steady states, based on the vapour vs. temperature equilibrium curves and equation A5 on page 206 in appendix A.

With the bulk scale test bench, all three performance measures, gross temperature lift, power and energy could be evaluated. Power was recognised the least clear-cut, since specific heat and mass exchanger design substantially influences this. Based on the measured results both the mass diffusion coefficient and the heating power under the semi realistic conditions could be calculated. The operating conditions were realistic in respect to the water vapour atmosphere and the respective operating temperatures both on the evaporator as well as the absorber. Conditions were not as would be expected in the heat and mass exchanger component in respect to the lack of sorbent transport and extended exposure time. In a realistic

transported process exposure time is limited based on flow rate and flow distance. A quiescent film was studied; thus no mass transport acceleration was encountered. The single step temperature change, from ϑ_d to ϑ_a, compared to the continuous temperature gradient encountered on the heat and mass exchanger. This was a parameter that can naturally be followed by respective Peltier control. In future this would be instrumented based on heat and mass exchanger temperature data, in order to measure absorption kinetics under varying conditions along the heat and mass exchanger.

5.1. Diffusion coefficient

The concentration at both absorbed and desorbed equilibrium was calculated according the vapour pressure vs. temperature and concentration equilibrium (see appendix A. “Vapour pressure” on page 204) and based on the initially filled amount of sodium hydroxide.

The weight per cent based concentration was calculated as:

$$X_{NaON} = \frac{m_{NaOH}}{m_{sol}}, \textit{ Equation 21}$$

Where m_{NaOH} [g] is the mass of pure sodium hydroxide, a value kept constant, since the sodium hydroxide was not carried along in the water vapour, and m_{sol} [g] is the mass of sodium hydroxide and water, where the water mass changed.

The diffusion coefficient D [m^2 s^{-1}] is the proportionality factor in Frick’s law of diffusion and is a parallel to the heat transfer coefficient in thermal conductivity. In this particular case, the diffusion coefficient of an absorption process could be determined by using the approximation:

$$D = 0.049\frac{L^2}{\tau}, \textit{ Equation 22 [equation (10.160) in (Crank, 1975)]}$$

where L [m] is the average film height at the half-time, the time it takes to reach half the concentration change, of the absorption process and τ [s] is the respective time to half-time.

Equation 22 is valid for both the absorption process and the desorption process. In this instant only the absorption process was considered, since the desorption process was slowed down to avoid splattering from boiling of the sodium hydroxide aqueous solution.

The time constant of the absorption process τ was calculated as follows:

$$\tau = T_{1/2} - T_0, \text{ Equation 23}$$

where T_0 [s] is the time at which the absorption process is started, and $T_{1/2}$ [s] is the time at which half of the absorption process is completed.

The average film height L [m] can be expressed as:

$$L = \frac{V}{A} = \frac{M}{\rho \cdot A}, \text{ Equation 24}$$

where V [m^3] is the sorbent volume, A [m^2] is the active film area, M [kg] is the sorbent mass, and ρ [kg m^{-3}] is the specific sorbent density (equation A1 on page 188).

5.2. Thermal power

As stated in chapter 4.2. “Temperature and energy density” on page 57, the thermal power consists of both the exothermal process of vapour condensation on the sorbent as well as the exothermic heat of solution:

$$P = P_{PC} + P_{sol}, \text{ Equation 25}$$

Where P [W] is the total power released, P_{PC} [W] is the phase change power from gaseous absorbate to liquid absorbate, and P_{sol} [W] is the power released from mixing absorbate with absorbent.

The heating power released by the phase change from condensation was calculated as follows:

$$P_{PC} = j \cdot A \cdot \Delta H, \text{ Equation 26}$$

Where j [mol m^{-2} s^{-1}] is the chemical current or mass current, A [m^2] is the active absorption area, and ΔH [J mol^{-1}] is the enthalpy of condensation of water in.

The chemical current j is calculated according to:

$$j = \frac{\dot{m}_{H_2O}}{M_{H_2O} \cdot A}, \text{ Equation 27}$$

where $\dot{m}_{H2O}$ [g s^{-1}] is the mass flow rate of water being absorbed, M_{H2O} [g mol^{-1}] is the molar mass of water and A [m^2] is the active film area.

The mass flow rate is determined by dividing the mass difference between two consecutive measures by the time step between these measures:

$$\dot{m}_{H_2O,i} = \frac{m_{i+1} - m_i}{\Delta T}, \text{ Equation 28}$$

Where m_i [g] is the mass at the beginning of the time step, m_{i+1} [g] is the mass at the end of the time step and ΔT [s] is the time step.

The heating power released by mixing was calculated as follows:

$$P_{sol} = \dot{m}_{H_2O} \Delta H, \text{ Equation 29}$$

where ΔH [J g^{-1}] is the heat released from mixing the sodium hydroxide aqueous solution with the absorbed water. The enthalpy of the sodium hydroxide aqueous solution depends on its temperature ϑ_{sol} and its sodium hydroxide concentration X_{NaOH}, See Appendix A. equation A2 on page 191.

5.3. Results and discussion

In the presented tests, 15 g of anhydrous sodium hydroxide was used. Testing cycles were performed by changing the sorbent temperature from absorption to desorption and back at constant vapour pressure. Figure 14 shows the result of test setting 1. Steady state conditions were marked in black. The intermediate temperature increase steps in desorption can be recognised by the wavy form of the Peltier temperature (blue line), with the mass decrease (green line) following a similar slight wave.

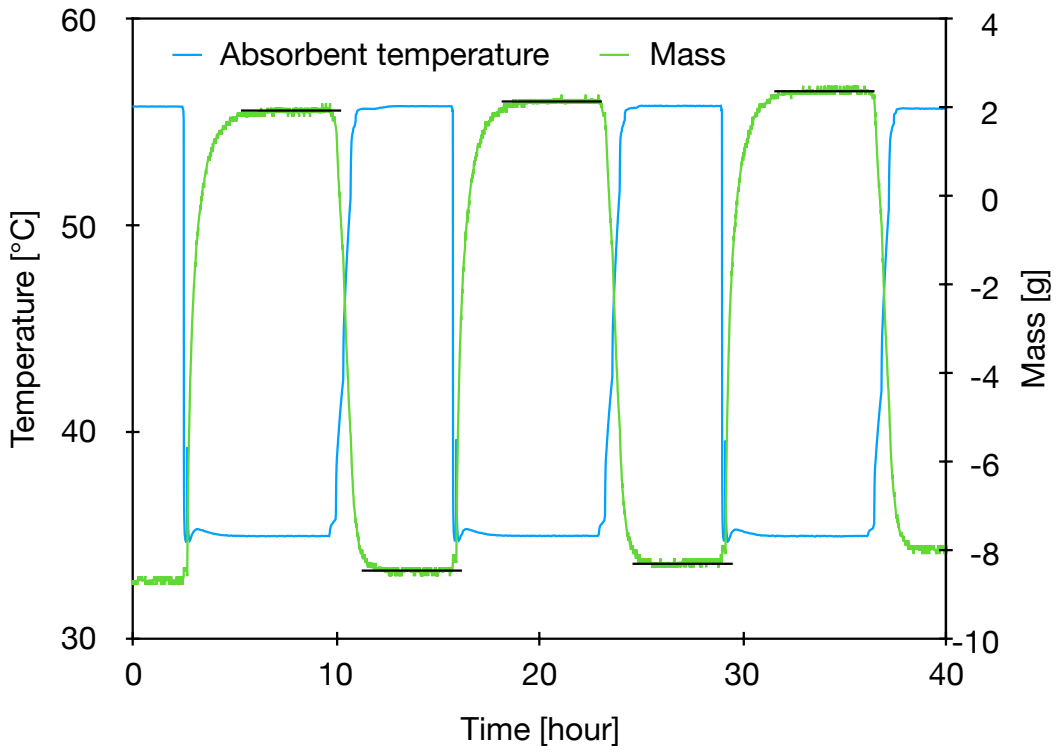

Figure 14: Results from test setting 1, ϑ_v = 10°C, ϑ_d = 55°C and ϑ_a = 35°C.

The measured temperature of ϑ_d was slightly higher than defined, approximately 55.8°C. Thus, a moderately greater concentration resulted, see chapter 4.2. “Temperature and energy density” on page 57. This was accounted for in the further evaluation. While the pressure in the evaporator / condenser, remained close to constant, the pressure measured in the absorber / desorber dropped just prior to absorption. This was due to the testing process. The vapour exchange connecting valve was closed in the process of absorbent temperature change, change from desorption to absorption. A slight increase in mass can be seen during this time, indicating the uptake of part of the water vapour present in the chamber volume, resulting in the pressure drop.

There was a slight increase of mass, in the final desorbed and absorbed state, from one cycle to the next. This was due to a minor relaxation of the connecting tubes. The differences between the final values were small, in the presented case, 10.635g, 10.649g and 10.682g respectively,

and the shift was global, thus this can easily be accounted for in the evaluation.

From the measured mass curve, it was recognised that, as expected, mass flux strongly reduces as the solution proceeds towards temperature, vapour pressure and concentration equilibrium. This result nicely pointed out the substantial difference in the operational requirements of the absorption heat storage optimised heat and mass exchanger compared to the absorption chiller or heat transformer version. While it is adequate to operate these absorption heat pumps in the area of high sorbent mass flux, equivalent to high power, the absorption heat storage must proceed to reach high mass exchange, thus its field of operation is extended to the low mass flux and thus low power area. This can only be reached by extensive exposure time and reduction in volume specific power must be conceded.

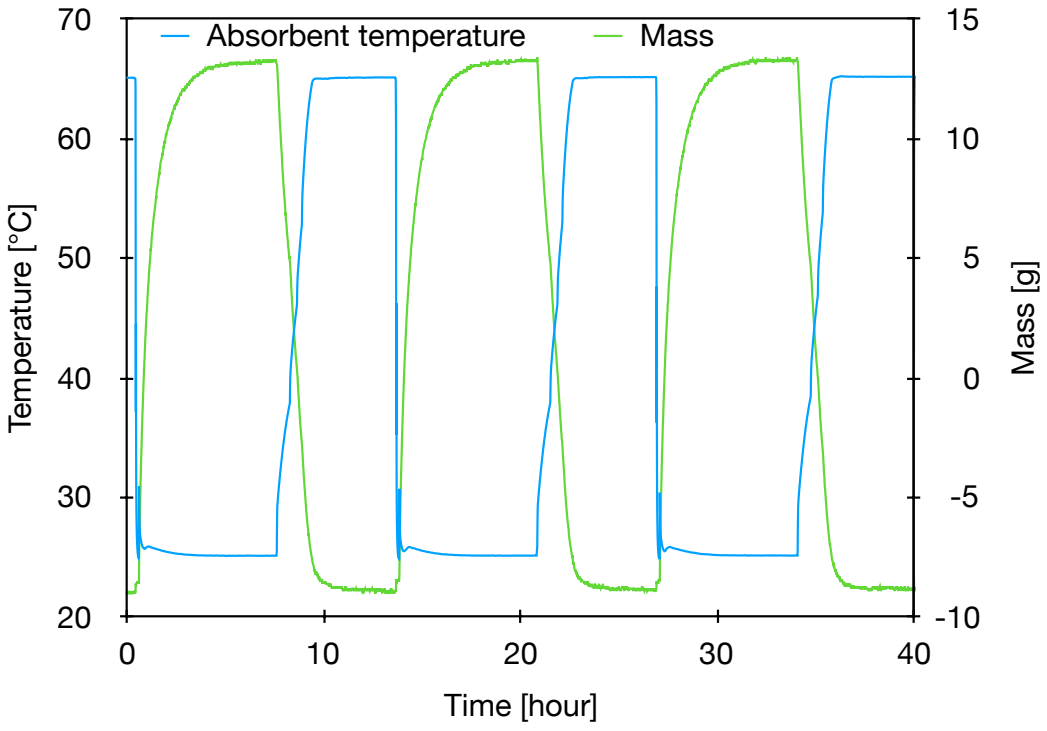

Figure 15: Results from test setting 3, ϑ_v = 10°C, ϑ_d = 65°C and ϑ_a = 25°C.

From the results in figure 14 on page 72 and figure 15 it appeared that the absorption process is slower than the desorption, seen by the slower progress to equilibrium in absorption compared to desorption. In addition, a

difference in the rate of absorption could be seen between the tests at evaporating temperature (ϑ_v) 10 °C compared to those at 5 °C as shown in figure 16. Both these phenomena are linked to the sorbent viscosity (equation 30 on page 76) which is dependent on the sorbent temperature (equation A4 on page 201). Further discussion on this point is found in in chapter 8. “Study of mass transport” on page 112.

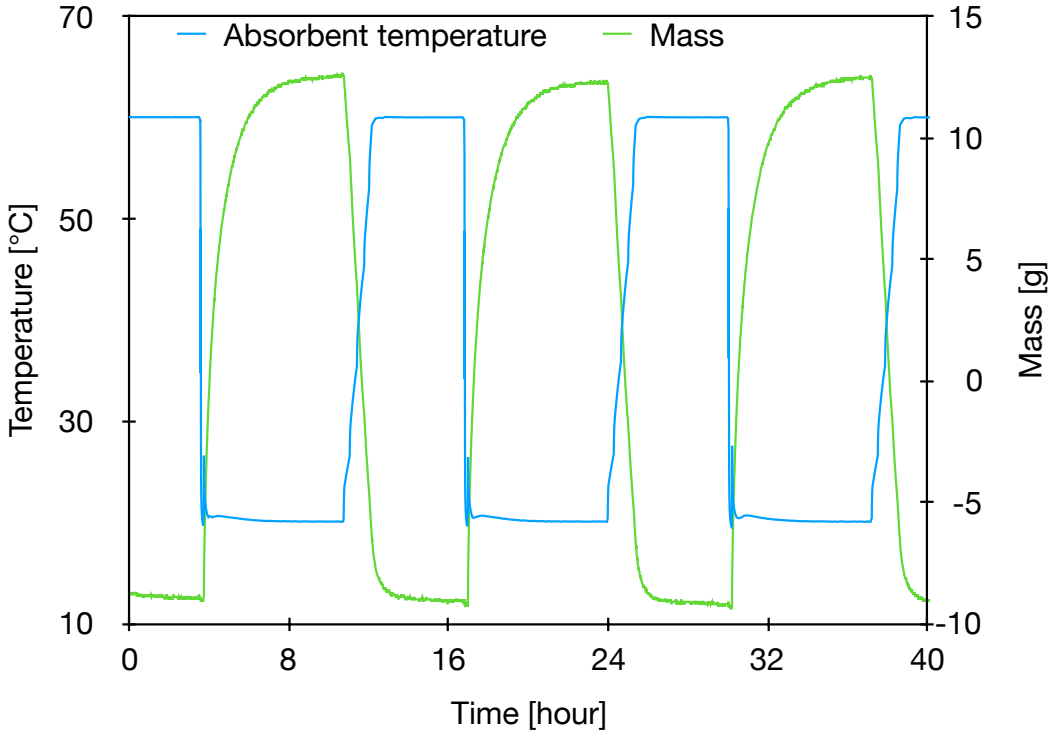

Figure 16: Results from test setting 6, ϑ_v = 5°C, ϑ_d = 60°C and ϑ_a = 20°C.

Based on the measured mass change over time, the change in concentration could be calculated according to equation 27 on page 70. Figure 17 shows the result for test setting 1.

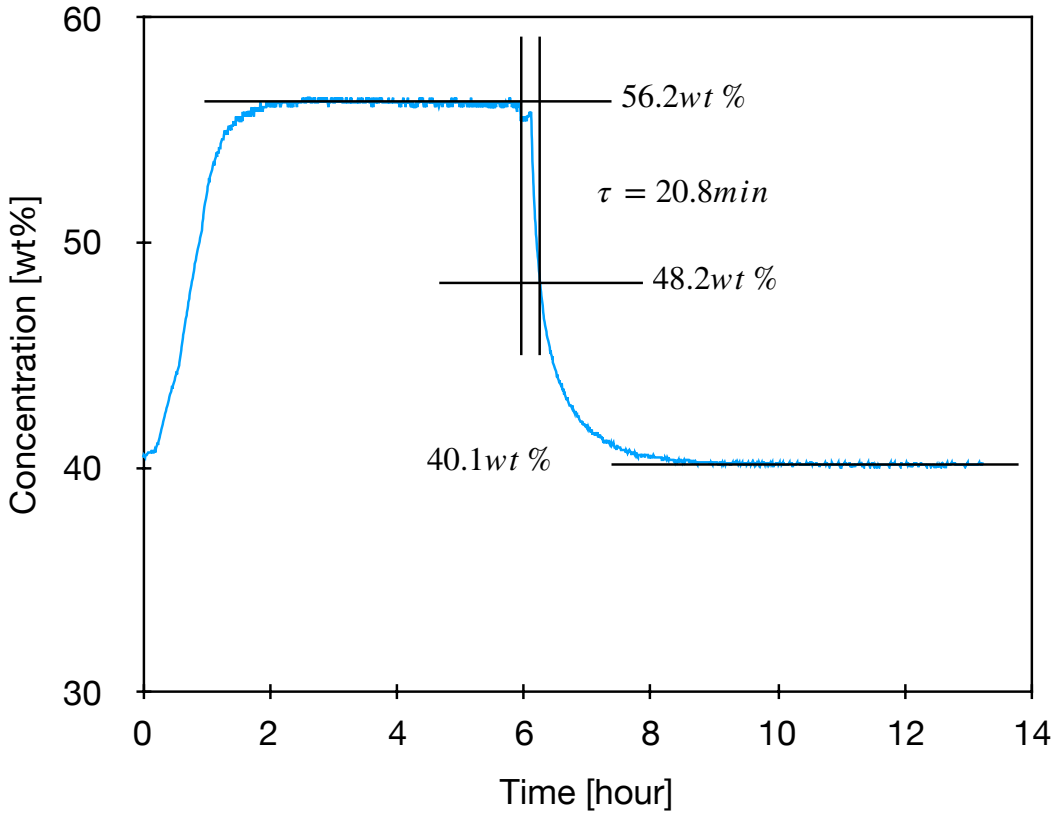

Figure 17: Concentration curve of test setting 1. Indicated is the derivation of the time constant τ.

From the concentration curve, the time constant τ required to calculate the diffusion coefficient according to equation 22 on page 69 was derived. Graphical illustration of the determination of the time constant for Test setting 1 is shown in figure 17. The aqueous sodium hydroxide concentration X_0 is the value at time T_0 at which absorption is initiated. Table 3 shows the obtained values for τ as well as the average film height. With these values, according to equation 22, the diffusion coefficient D_{exp} was calculated. The absorption process takes more time with an extended temperature range and at lower operating temperature.

Table 3: Results of the bulk scale test bench showing average measured temperatures, calculated values for τ (Equation 23 on page 69) and average film height L (Equation 24 on page 69) as well as there from resulting diffusion coefficient D_{exp} (Equation 22 on page 69), compared to the calculated diffusion coefficient based on the Stokes-Einstein equation D_{SE}. (Equation 30).

Test setting	ϑ_v [°C]	ϑ_d [°C]	ϑ_a [°C]	τ [s]	L [µm]	D_{exp} [m^2 s^{-1}]	D_{SE} [m^2 s^{-1}]
1	10.02	55.81	34.94	1246	1136	5.1E-11	9.7E-11
2	10.09	65.24	34.92	1229	1057	4.5E-11	8.6E-11
3	10.0	65.16	25.17	1359	1162	4.9E-11	6.0E-11
4	5.74	50.0	30.01	1325	1283	6.1E-11	1.0E-10
5	6.07	60.0	30.02	1353	1063	4.1E-11	6.4E-11
6	5.70	60.07	20.1	1414	1205	5.0E-11	4.8E-11

The values of experimentally investigated diffusion coefficients D_{exp} were found to be very closely fitting to the values calculated according to the Stokes-Einstein equation (Equation 30). This is a good indication that the bulk scale test setup results are reliable.

The calculation of the Stokes-Einstein equation-based diffusion coefficient (D_{SE}) is as follows:

$$D = \frac{k_B \Theta_{sol}}{b \pi \eta r}, \text{ Equation 30}$$

Where k_B (1.38064352 J K^{-1}) is the Boltzmann constant, Θ_{sol} [K] is the solution temperature, b is a constant dependent on the molecule size, taken to be 4 in this case, η [Pa s]is the dynamic viscosity of the sorbent, see equation A4 on page 201, and r (1.375x10^{-10} m) is the radius of the diffusing molecule, in this case water.

In evaluating the heating power according to equations 25 to 29 on page 70, it was further made clear that there is substantial variation in power over time in respect to equilibrium state. Figure 18 shows the total power change ($P_{PC} + P_{sol}$) in an absorption process under test setting 2. As indicated in the figure, after 30min. of absorption, the power had reduced from the initial 49W to just over 5W, nevertheless, the average concentration had only

reached 44.8wt% and not the possible 40wt%. If the process had been stopped at this point, the resulting energy capacity as shown in figure 12 on page 60, would have been reduced from 208kW h m^{-3} to 115kW h m^{-3}, nearly halved. It was thus recognised that a substantial part of the potential energy capacity is available only at marginal power.

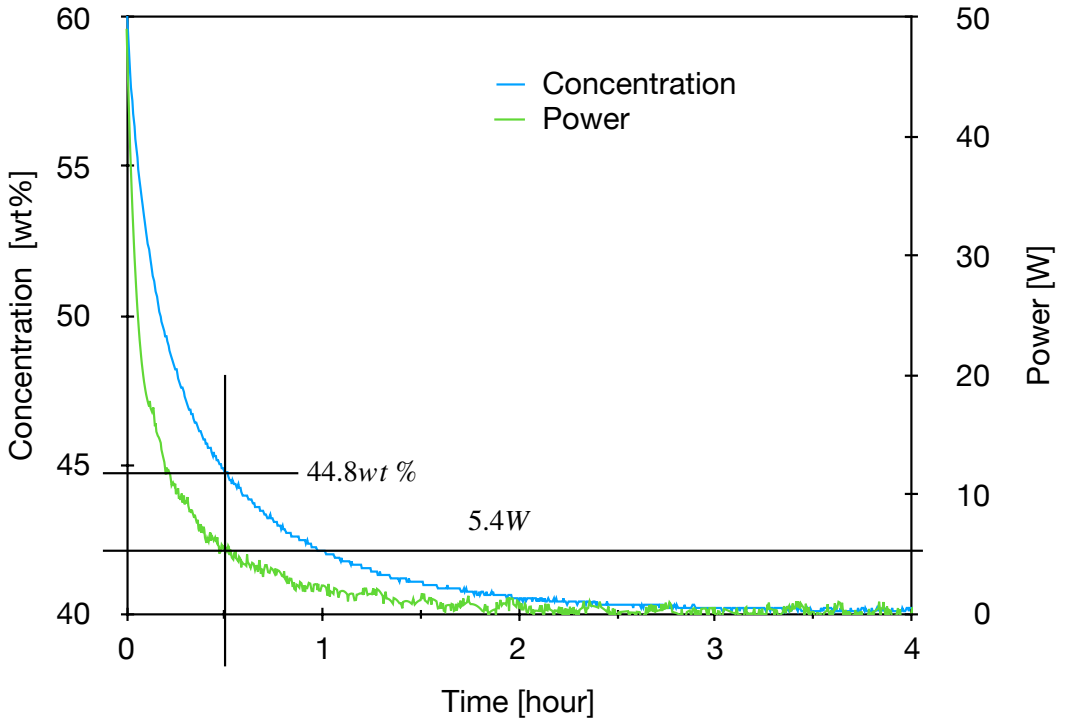

Figure 18: Concentration change and heating power during absorption for test setting 2.

In table 4 it can be recognised that the maximum heating power directly depends on the temperature difference (degree of imbalance) between desorption and absorption, with greater power at larger difference.

Table 4: Shows the maximum power (P_{max}) at the varying operating temperatures .

Test setting	ϑ_v [°C]	ϑ_d [°C]	ϑ_a [°C]	P_{max} [W]
1	10.02	55.81	34.94	43.27
2	10.09	65.24	34.92	49.05
3	10.0	65.16	25.17	61.23
4	5.74	50.0	30.01	37.38
5	6.07	60.0	30.02	52.42
6	5.70	60.07	20.1	61.35

From the bulk scale analysis results it is shown that the absorption kinetic is strongly dependent on the sorbent concentration and the temperature difference. Under the testing conditions, the time to reach equilibrium was in the range of 2 hours. Failure to come close to equilibrium has substantial consequences for the energy capacity. Thus it is confirmed that high exposure time is needed for the absorption heat storage application.

For this reason, it is clear that a heat and mass exchanger design appropriate for sorption heat storage must enable long exposure time of absorbent to absorbate with continuous release of heat, in order to be able to proceed towards equilibrium and thus maximum energy density. The results show a clear discrepancy between energy density (large sorbate uptake) and power. Allowance for volume specific power reduction will be required to improve energy. In the following chapter 6 such a design is proposed.

6. Heat and mass exchanger design[9]

In this chapter work on the design of a heat and mass exchanger for absorption heat storage is presented. Initial experience with a tray type design and a tube bundle heat and mass exchanger is followed by a discussion of parameters affecting absorption performance. From this, an alternative approach to heat and mass exchanger design with a vertically installed spiral finned tube is proposed.

6.1. Tube bundle falling film heat and mass exchanger

Up to now, in the design of liquid absorbent heat storage demonstrators, heat and mass exchanger designs similar to those employed in other heat exchange absorption machines with tube bundle falling film heat and mass exchangers have been followed due to the similarities in absorbate and heat uptake and release (Daguenet-Frick et al. 2017, Daguenet-Frick et al. 2015, Hafsia et al. 2015, Lazcano-Véliz et al. 2016, Zhang et al. 2014, Ibarra-Bahena and Romero 2014). The authors's own experience in this respect was gained in the frame of the (COMTES) project. In this project, a tube bundle falling film heat and mass exchanger for closed liquid absorption heat storage with aqueous sodium hydroxide was designed and built by Daguenet-Frick et al. (2015, 2017). The specific dimensioning can be found in (Daguenet-Frick et al. 2014). The calculated power was 12 kW in the desorption process and 8 kW in the absorption process. Prior to this design, a tray type setup with double walled bottom for heat exchange was followed by Weber and Dorer (2008). In this work, especially the absorption process was completely unsuccessful. The top image in figure 19 shows the tray and the bottom shows the tube bundle heat and mass exchanger.

The trickle bed reactor is another approach discussed in literature. Here, challenge is found in continuous heat release and absorbent streaming

[9] Chapter 6 basis on the authors publication:
Fumey B., Weber R., Baldini L., Sorption based long-term thermal energy storage – Process classification and T analysis of performance limitations: A review, Renewable and Sustainable Energy Reviews 111, 2019, 57–74

due to high viscosity (Niegodajew and Asendrych 2017). Spray absorbers are also discussed, nevertheless, continuous heat release is again not possible (Warnakulasuriya and Worek 2006). Isfahani and Moghaddam (2013) propose an absorption process by superhydrophobic nanofibrous structure constrained absorbent. Again, heat release is challenging.

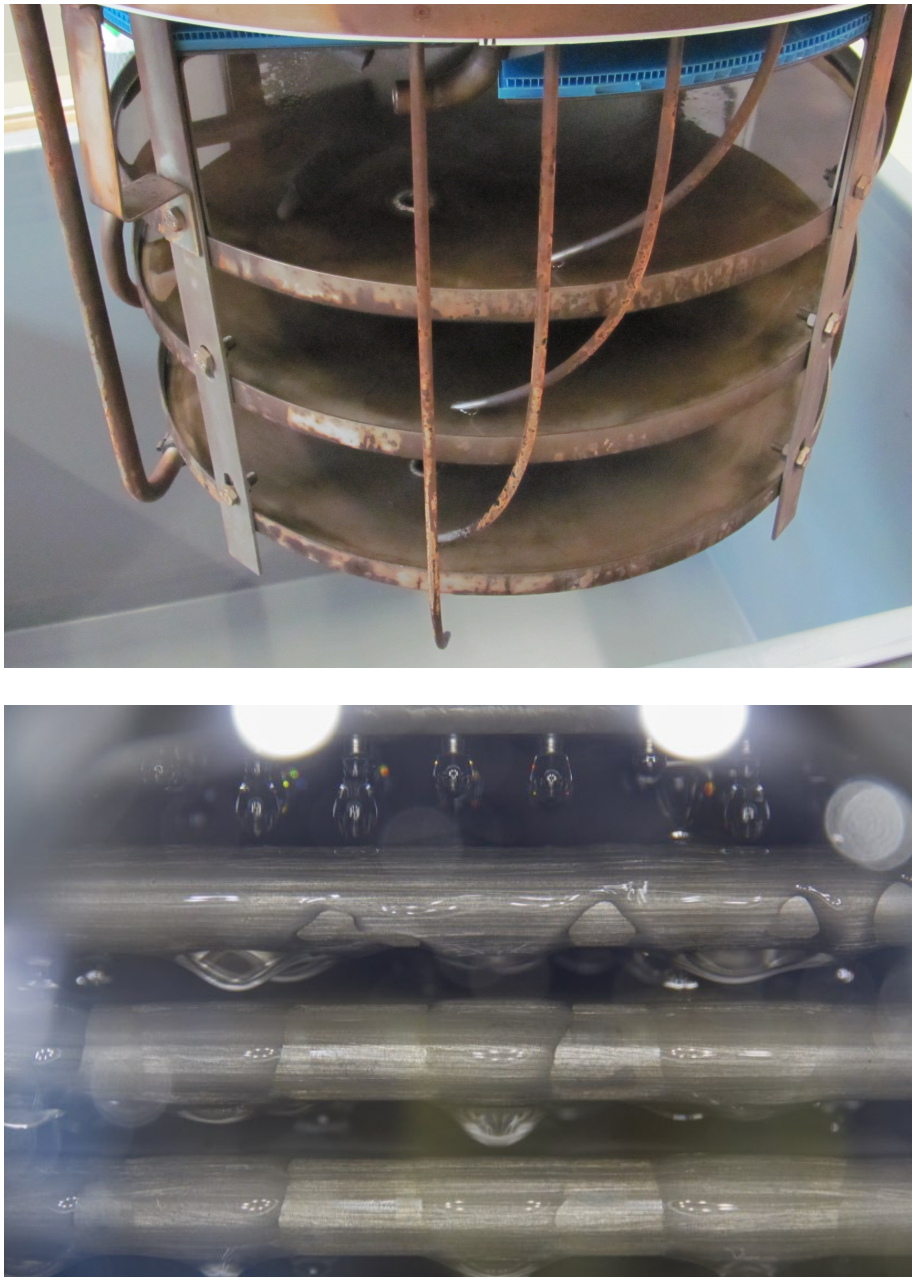

Figure 19: Top: Picture of the tray heat exchanger designed by Weber. Bottom: Picture of the tube bundle falling film heat and mass exchanger from the COMTES project [Fumey et al. 2015c].

Extensive testing of the tube bundle falling film heat and mass exchanger, shown at the bottom in figure 19, was performed in absorption mode (Fumey et al. 2015c, Daguenet-Frick et al. 2016). At high absorbent solution mass flow a continuous power output of approximately 1kW was achieved. Nevertheless, both temperature increase and concentration decrease were marginal. From these results, it was concluded that the conventional heat and mass exchanger as designed in the COMTES project was not fitting for the absorption heat storage process (Fumey et al. 2015c). This was due to poor tube wetting from low absorbent solution flow and high viscosity (see appendix A. viscosity on page 199) of the absorbent aqueous sodium hydroxide leading to regrouping of absorbent solution droplets, reducing both thermal contact to the tubes and the active absorbent solution surface area (Fumey et al. 2015c). In addition, the absorbent solution residence time in the absorber was found to be only approximately 2 s. As shown in the bulk scale tests in chapter 5. “Study of absorption at bulk scale”, this is substantially too low to proceed towards equilibrium state. Figure 19 bottom shows a picture of the droplet flow on the tube bundle heat and mass exchanger. It can be seen that the finely distributed droplets above the first heat exchanger tube, shaped like lightbulbs, grouped after the top-most tube and thus hindered good wetting of the tube for thermal contact, reduced the active absorption area for rapid mass uptake and increased film height, increasing mass transport distance. In figure 20, the performance is shown according to the concentration and gross temperature lift equilibrium line. The achieved gross temperature lift was only approximately 9K, the theoretical limit is 32K. Very minor concentration reduction was noted, thus practically no heat storage capacity was reached. The uniform thermal storage system schematic in figure 20, shows the actual operating temperatures. Herein it can be seen that the output temperature of 26°C was much too low for space heating and the evaporating temperature was much higher than a realistic application would allow. Thus, even though a power performance of approximately 1kW was claimed (Daguenet-Frick et al. 2017), under application specific conditions this heat and mass exchanger would not have function at all.

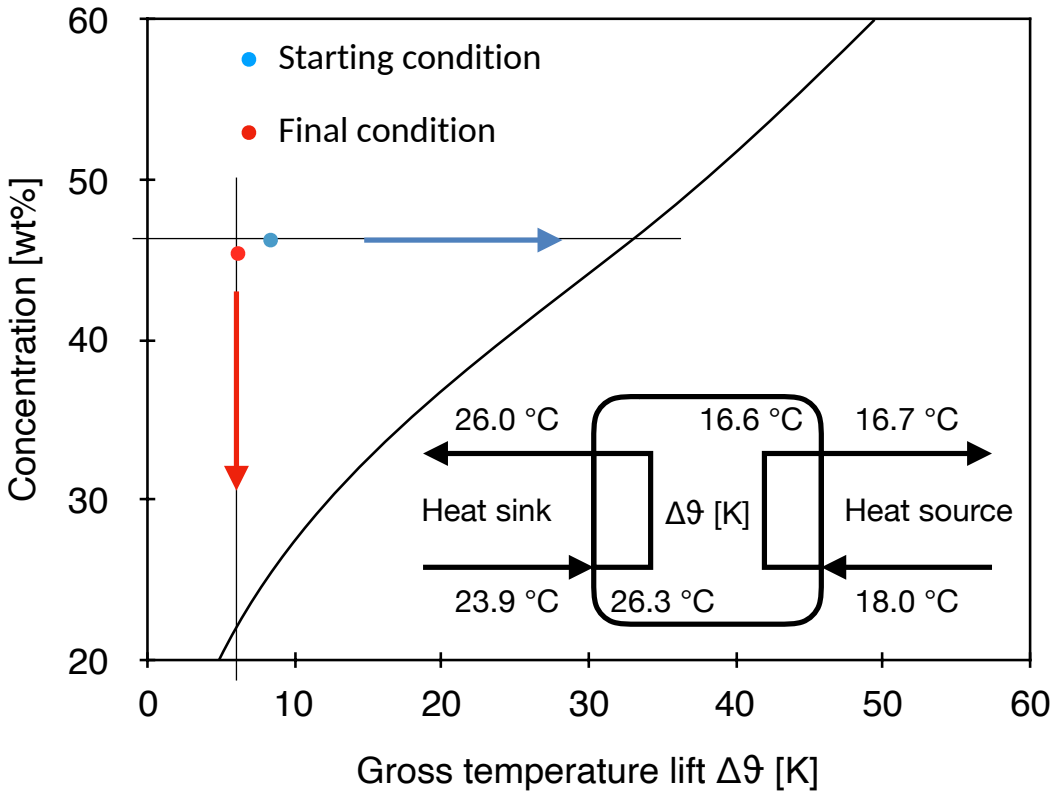

Figure 20: Performance of the tube bundle falling film heat and mass exchanger in the absorption process shown in the equilibrium diagram. The blue dot shows the achieved gross temperature lift, approximately 9K, and the red dot indicates the final concentration, approximately 44wt%.

Others in the field have come to the same conclusion. N'Tsoukpoe et al., (2013) stated that no heat was released in their absorption process with LiBr. Zhang et al. (2014) claimed good operation results nevertheless close look revealed low thermal capacity and non steady state operation with sufficient wetting of the tube bundle reached by recirculation. Thus, having the same limitations as fixed bed processes.

Numerous attempts to improve this heat and mass exchanger design have been followed. Mortazavi et al. (2015) addressed wetting issues for flat plate heat and mass exchanger operating with LiBr. They proposed a finned structure to spread the sorbent on the falling film flat plate heat and mass exchanger. Nevertheless, single pass, recognised as a primary operating condition required for heat storage, was not enabled. Michel et al. (2017) proposed a grooved plate falling film absorber, also not fitting to heat stor-

age application. Further research on novel flat plate falling film designs was reported by Hu et al. (2017) nevertheless they also allowed for recirculation. An alternate heat and mass transfer absorber with staggered tube bundle and M–W corrugated mesh guider was reported by Chen et al. (2016) and Stehlík et al (2014) propose finned surfaces on horizontal tubes, also neglecting focus on single pass. Thus, it was concluded that the basic difference between absorption cooling machine continuous cycle operation and absorption heat storage non continuous cycle operation, namely single pass, was not accounted for.

From the bulk scale reactor results and discussion it was shown that the water vapour absorption on aqueous sodium hydroxide requires substantially more time than that previously assumed or possible with the tube bundle falling film approach, due to the substantial decline in kinetics as equilibrium is approached. For this reason, it was concluded that a novel heat and mass exchanger design specific for absorption heat storage was required. Recognised important criteria were; single pass, adequate exposure time, low absorption solution film thickness, continuous absorbent solution flow and heat release gradient, true counterflow process and good surface wetting at low absorbent flow enabling the absorbent to reach close to true equilibrium and thus maximum specific energy capacity.

In the continuation of this chapter, an alternative heat and mass exchanger proposed by the author is presented.

6.2. Spiral finned tube heat and mass exchanger

The results from the bulk scale heat and mass exchanger tests in chapter 5 “Study of absorption at bulk scale” on page 64 showed that for the extent of the absorption process required in liquid absorption heat storage two basic elements need to be addressed: i) a much greater exposure time and / or ii) a thinner film, reducing mass transport distance. For this reason, it was proposed that a heat and mass exchanger must permit adequate exposure time at a low absorption solution film thickness, while permitting a continuous absorbent solution flow and heat release gradient.

This formulates a substantial challenge, since aqueous sodium hydroxide at the heat storage application specific concentration of around 50wt% has a high viscosity and surface tension, as seen in the droplet accumulation effect in the COMTES (Fumey et al. 2015c) heat and mass exchanger and noted in appendix A. “Viscosity” on page 186. In literature it has been recognised that liquid viscosity has a dominant influence on the Reynolds number and strongly impacts the optimisation of liquid side-controlled mass exchangers (Won and Mills 1982). In conventional heat and mass exchangers, solution is usually sprayed or dripped over the absorber tubes. It has been recognised that, complex surface phenomena and flow instabilities conspire against a uniform thin film flowing downwards over the absorber tubes or sheet surface. For a given Reynolds number, the flow instabilities are more pronounced at reduced tube to tube spacing in a horizontal tube bundle. The same effect is reported for a sheet surface or vertical tube. The film accumulates and flows as a stream of substantially greater film height and much reduced contact area both for mass absorption and thermal conductivity (Tsai and Perez-Blanco 1998). In addition, in literature, it is stated that due to the relatively small mass diffusivities of aqueous solution of liquid sorbents, the mass absorption rates sustained by pure diffusion processes are small. (Sisoeva et al. 2005).

With these challenges in mind, a possible technical solution was fixed on using a vertically mounted spiral fined tube assembly, with the absorbent solution flowing down the spiral fin as a thin narrow film. Film accumulation and development of a thick stream was prevented since the film is narrow from the start. By following the spiral fin, a compact very long flow distance was attained, permitting ample time for absorption and heat release in a continuous temperature and concentration gradient in an absorbent to heat transport fluid true counter flow process.

This proposed alternative heat and mass exchanger was further examined with an initial setup constructed and tests performed in respect to the triple performance criteria. Emphasis was placed on the mass transport parameter of the absorption process kinetics rather than the heat transport.

This was justified since spiral finned tubes are designed for improved thermal conductivity through increased surface area for heat exchange.

6.3. Counterflow heat exchange with absorption

In respect to the counter flow heat exchange process, a consideration with regards to the application in the absorption process needs to be made in order to detect potential limitations. In general, the counter flow heat exchanger benefits from maximum temperature difference between the two heat exchanging fluids. As discussed, in absorption heat storage this is an important criterion, both in order to achieve maximum gross temperature lift as well as maximum energy density through maximum sorbent uptake at reduced temperature dependent vapour pressure, concentration and temperature based equilibrium, see chapter 2.2.4 “Transported process” on page 34. In this sense it was only correct to follow the counter flow heat and mass exchanger design.

As pointed to in chapter 2.1. “Performance parameters” on page 21, the gross temperature lift both in absorption as well as desorption is concentration dependent, with slight variations, conditioned on change in vapour pressure. The energy transfer is based on the mass of water vapour exchanged, multiplied by the liquid to gas phase change enthalpy, as well as the heat of solution, which is a lesser part. Absorbent mass exchange and concentration gradient are far from being linear. Greater mass exchange is required for concentration change at lower concentration. Consequently, the amount of heat exchanged in respect to the temperature difference (J K^{-1}) is nonlinear. This is largely in contrast to a typical counter flow heat exchanger where the heat capacity of both fluids, whilst possibly different, remain practically constant in the process. Figure 21 shows an illustration of the issue. Even though the measurement, change in energy per change in temperature is that of heat capacity, it may be slightly misleading to refer here to the absorbent heat capacity since it involves the uptake and condensation of water vapour and is not the classical fluid characteristic. The specific heat on the

other hand, also changes as concentration of the absorbent alternates, and may lead to efficiency loss. This is not accounted for in this consideration.

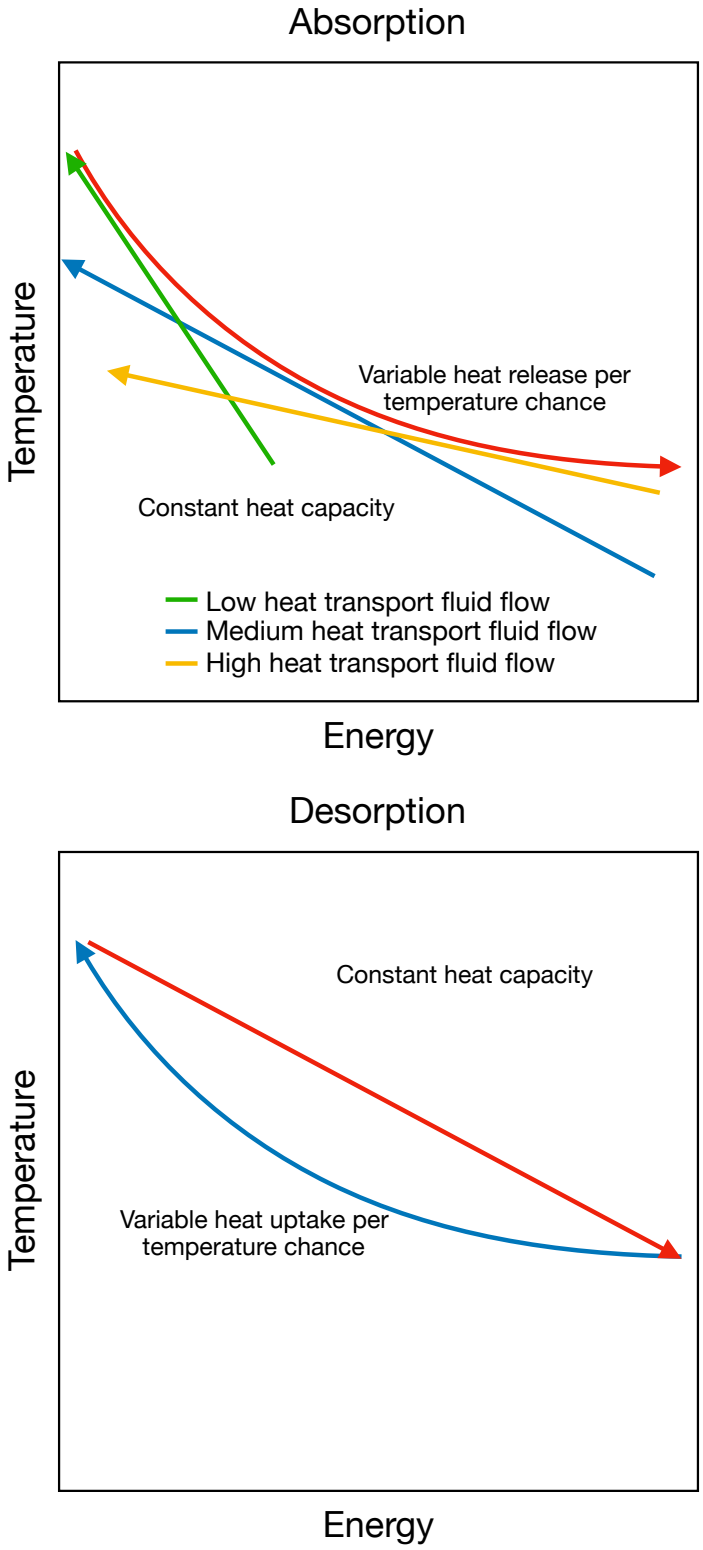

Figure 21: Illustration of the non-constant heat to temperature ratio of the absorbent to the constant thermal capacity of the heat transport fluid.

Due to this nonlinear behaviour, there are limitations in gross temperature lift and volumetric energy capacity to be noted in absorption but not in desorption, as illustrated in figure 21. Since in desorption, the variable heat uptake bellies away from the constant heat capacity line, this curve remains below the line and ends can meet permitting maximum concentration increase at minimum temperature difference. In absorption on the other hand, the variable heat release swells towards the heat transport fluid constant heat capacity. It follows that there is only a single point of coherent heat release and uptake. Depending on the choice of this point, the heat release tends more towards high gross temperature lift but with reduced volumetric energy density and vice versa as illustrated with the green, blue and yellow lines. Choice of the specific heat transport fluid heat capacity depends on the respective flow. At low flow, illustrated in green, high gross temperature lift is reached, but the absorption process stagnates since the heat cannot be released due to lack of sufficient thermal capacity of the heat transport fluid at lower temperatures. The process can be optimised for maximum capacity by sufficient heat transport medium flow at the cost of not reaching maximum gross temperature lift due to the reduced heat capacity at high absorbent concentration. This issue is further discussed on an experimental basis on the lab scale heat and mass exchanger by varying the heat transport fluid in the absorber in chapter 10. “Flooded fin design” on page 157. It is worth noting, that this basic issue of concentration dependent nonlinearity between temperature and heat capacity is not singular to the counterflow heat and mass exchanger, nor specifically to sodium hydroxide as absorbent. This is a general conduct in all sorption processes, strongly emphasised in the heat storage application due to the addition of the performance parameter energy density, substantially broadening the area of operation.

7. Heat and mass exchanger test bench[10]

In order to validate the performance of the proposed spiral finned tube heat and mass exchanger, a test bench was designed built and operated, as shown in figure 23 on page 91 and figure 24 on page 92. The principle process was as follows, absorbent solution was introduced onto the top-most part of the vertically installed spiral finned tube and slowly flowed along the fin channel down the tube by gravitational force. By this method, extended time was given for absorption or desorption and heat exchange with the heat transfer fluid in the tube, running in counter current direction from the bottom to the top. A steady temperature and concentration gradient, steady state, was expected to develop on the fin in a continuous absorbent solution film flow. By adjusting the fin slope and the absorbent solution flow the film thickness and the exposure time could be varied. The design thus gave ample flexibility to adjust to varying absorbent characteristics. The strictly directed flow along the fin was anticipated to prevent large dry areas from evolving, even at very low absorbent solution mass flow. This is much in contrast to the tube bundle falling film approach, which was highly susceptible to dry areas at low absorbent solution flow (Fumey et al. 2015c). In this way, an open channel with low slope was provided by the continuous screw type form of the fin spiralling downwards around the central tube as illustrated in figure 22. For the initial examination, the spiral fin was produced from stainless-steel DIN 1.4571 and the vacuum chamber was made of stainless-steel DIN 1.4404. As pointed to in the previous chapter 4.4. “Corrosion” on page 62, all standard stainless steels are resistant to general corrosion by all concentrations of aqueous sodium hydroxide in water up to about 65°C (LaQue 1963). Due to the thin film and relatively low temperature, it was expected that boiling would not occur and thus corrosion from evaporation would be kept low.

[10] This section basis on the publication:
Fumey B., Weber R., Baldini L., Liquid sorption heat storage – A proof of concept based on lab measurements with a novel spiral fined heat and mass exchanger design, Applied Energy, 200, 2017, 215-25.

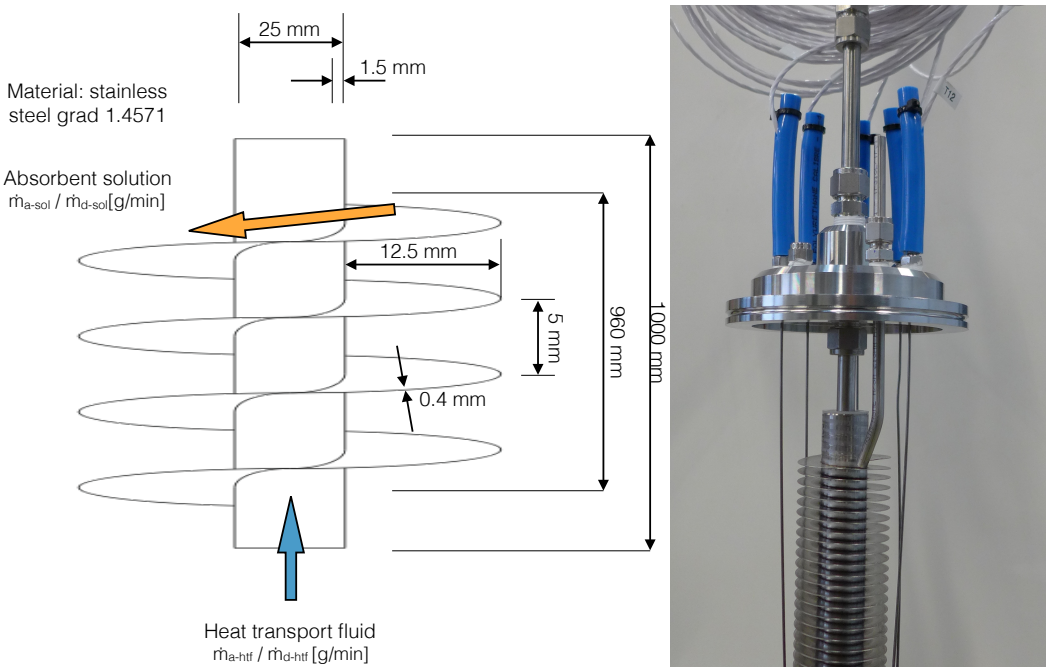

Figure 22: Left: Illustration of the spiral fin tube heat exchanger with absorbent and heat transfer fluid flow. Right: Picture of the heat and mass exchanger with absorbent supply tube and temperature sensors installed. In this initial setup, the spiral fin was slightly bent upwards 'dished' in order to prevent spilling of the fluid over its edge (Fumey et al. 2017).

In the test setup two finned tubes with dimensions as indicated in figure 22 and slightly 'dished' upwards bent fins were installed. Each tube was vertically positioned in a cylindrical vacuum chamber of 1400 mm total length and 100 mm inner diameter, including all sensors and actors, as schematically displayed and pictured in figure 23 on page 91. The spiral finned tubes were supplied with aqueous sodium hydroxide and water respectively by a simple 6 mm stainless steel tube, inserted into the chamber. No special supply nozzle was required. The two heat and mass exchanger chambers serving as absorber and desorber as well as evaporator and condenser respectively were interconnected with two vapour exchange channels of 420 mm length and 100 mm inner diameter. In this way absorbate exchange was enabled at negligible vapour pressure drop between the heat and mass exchangers. This was important due to the temperature and pres-

sure correlation, equilibrium. A drop in vapour pressure would have resulted in a decrease in gross temperature lift.

The heat transfer fluids were circulated to the heat and mass exchangers by gear pumps Px1 and Px2 respectively. The flow of the liquids was regulated by buoyancy flow regulator and additionally periodically measured in respect to mass flow with a scale. Heat and cold were provided from two thermo and cryostat machines.

The absorbent solution was taken from 5 litre polypropylene plastic canisters under atmospheric pressure and was exposed to air, the canister opening was covered but not sealed, in order to reduce air exchange. The approach to storage at ambient pressure was a vital step towards a commercially sound design, replacing low-pressure stainless-steel vessels as followed in the COMTES project. Flow to the absorber / desorber was regulated by tubing pump Px4. Absorbent solution was pumped from atmospheric pressure to the low-pressure heat and mass exchanger vessel. Mass flow was measured by weight loss in the absorbent solution canister. In the absorption process, absorbate (water) was similarly added to the evaporator. A dosing gear pump Px3 was installed for absorbate recirculation, the precise mass flow in the setup was not monitored, since it was not of primary interest in this test. Good wetting of both aqueous sodium hydroxide and water on the heat exchanger fins was confirmed by visual inspection.

Both heat and mass exchangers were each facilitated with a vacuum lock, making it possible to release both absorbent solution as well as liquid absorbate from the heat and mass exchanger composition without introducing air into the system. In this way a continuous operational process was made possible whilst permitting periodic release and sampling of the absorbent concentration without process interruption. The absorbent concentration was calculated in respect to the sample density and temperature according to equation A1 in appendix A “Density” on page 186.

The placement of the sensors is illustrated in figure 24 on page 92. PT100 class A 4-wire thermal sensors were installed on both heat and mass exchangers. On the absorber / desorber heat and mass exchanger the input

ϑ_1 and output ϑ_2 temperatures of the heat transfer fluid was measured as well as five temperatures on the fins: Absorbent solution input temperature ϑ_5, preheating temperature ϑ_6, two temperatures along the heat and mass exchanger ϑ_7 and ϑ_8 and the final absorbent solution temperature ϑ_9. In the evaporator / condenser unit heat transfer fluid input ϑ_3 and output ϑ_4 temperatures were measured as well as the absorbate temperature on the fins at two points ϑ_{10} and ϑ_{11} along the heat and mass exchanger.

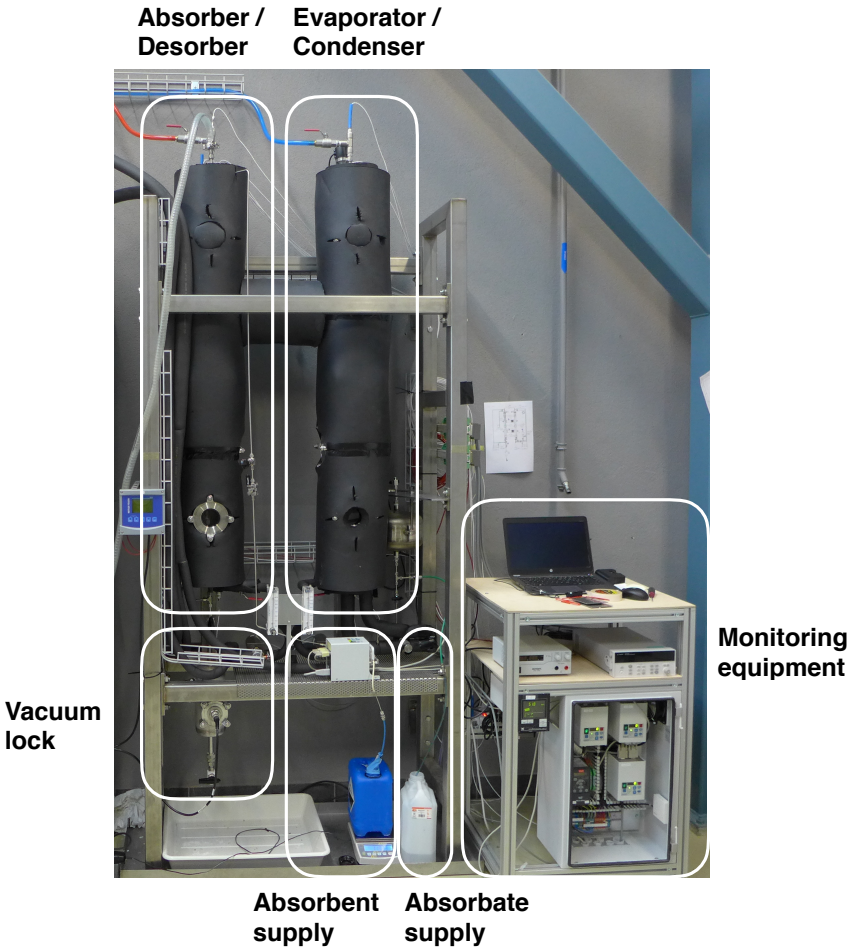

Figure 23: Picture of the lab scale spiral finned tube heat and mass exchanger test bench (Fumey et al. 2017).

In the initial spiral finned tube employed as absorber / desorber, the first 150mm between ϑ_5 and ϑ_6 of spiral fin tube are thermally disconnected from the heat transfer fluid by guiding the fluid through an inner tube of reduced diameter to the finned tube. In this way the absorbent solution is pre-

heated by absorbate uptake without releasing heat to the heat transfer fluid. This approach allows for the absorbent solution to reach maximum temperature gain and prevents reversed heat transport in the initial section of the heat and mass exchanger where the absorbent solution enters at storage temperature.

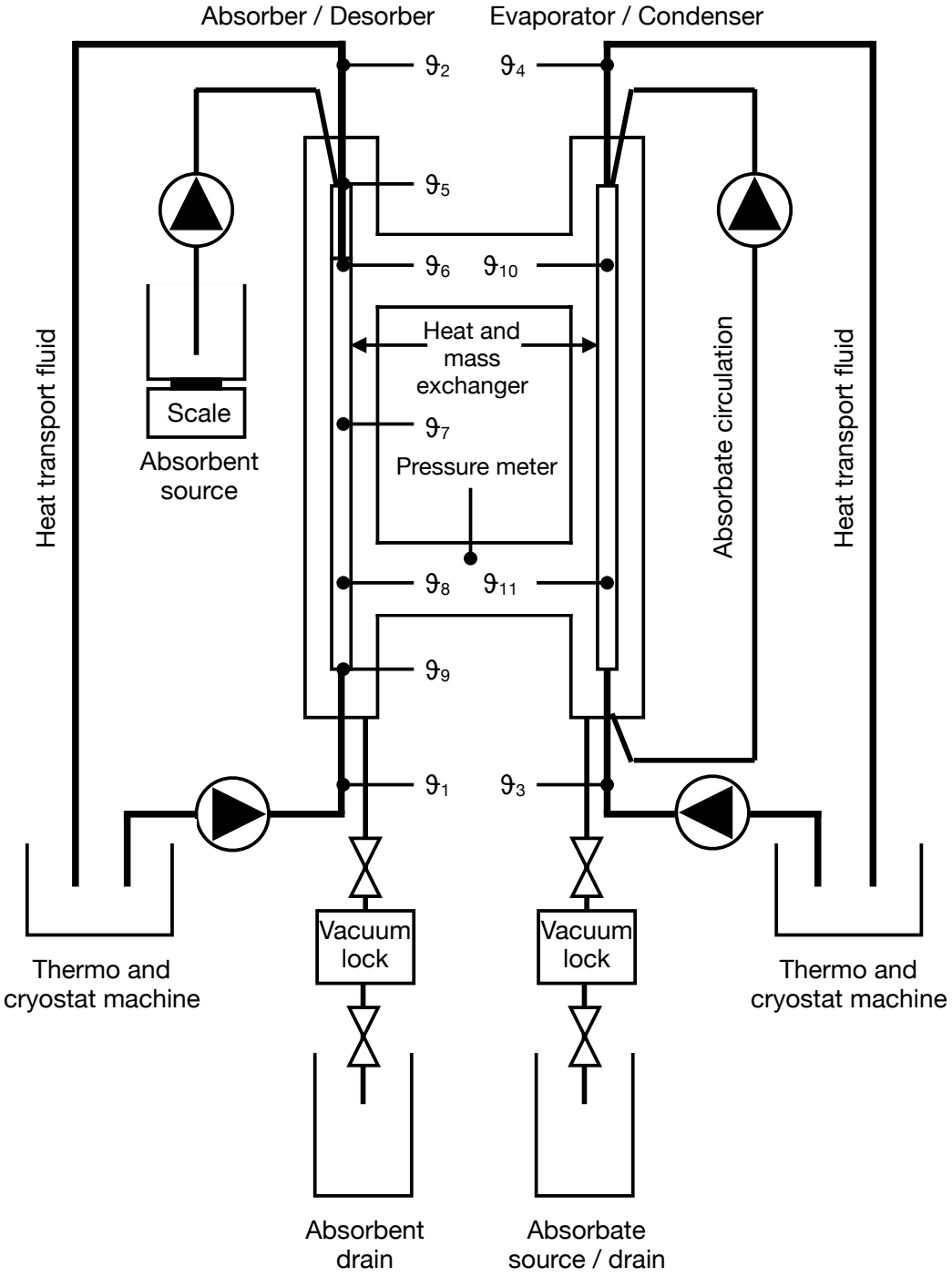

Figure 24: Schematics of the heat and mass exchanger with component placement (Fumey et al. 2017).

Technical grade aqueous sodium hydroxide solution at 50±1wt% sodium hydroxide in water was used as absorbent solution in the absorption process. The solution was not degassed and contained up to 0.1wt% carbonates, 100ppm chloride and sulphate each, 10ppm iron and heavy metals each and 0.1ppm mercury. For the desorption tests, a 25±1wt% sodium hydroxide in water solution was used, sourced by diluting the 50wt% solution with deionised water. In order to verify concentration, ten samples were taken and measured.

All tests were operated for approximately seven hours each, during which temperature values and absorbent solution samples were taken from a sequence of stable operation as shown in figure 25 on page 97.

7.1. Initial test series

The heat and mass exchanger shown in figure 22 on page 89 was tested in both absorption and desorption mode. A vacuum pump was connected in order to remove non condensable gasses prior and during the test period, not continuously, but only when required. Room temperature was recorded to be at approximately 24°C.

In order to investigate the absorption process, 17 individual tests were performed with varying operation settings. A standard test was defined first, with an absorbent mass flow $\dot{m}_{s\text{-}a}$ of 6 g min^{-1}, an absorber to evaporator temperature difference $\Delta\vartheta_{ae\text{-}min}$ between ϑ_9 and ϑ_{10} of 8K, an evaporator temperature $\vartheta_e = \vartheta_{10}$ of 20°C and a heat transport fluid flow in the absorber $\dot{m}_{a\text{-}htf}$ of 200g min^{-1} and in the evaporator $\dot{m}_{e\text{-}htf}$ of 700g min^{-1}. The temperatures of the heat and mass exchangers were adjusted by regulating the heat transfer fluid temperatures measured at ϑ_1 through to ϑ_4. Generally, on a system level the heat transfer fluid temperatures ϑ_1 to ϑ_4 were the most important parameters to demonstrate a successful absorption and desorption process. Even so, in the initial lab scale tests focus was set on the internal

temperature gain of the absorbent and the ability to reach high energy density. Temperature gain of the heat transport fluid was considered as of second priority. It is a matter of further development to minimise the temperature drop of both absorber / desorber and evaporator / condenser in order to reach maximum output temperatures in respect to source temperature. This is very important for final optimised operation. Table 5 on page 95 left shows absorption setting values with standard test settings underlined. All other absorption tests were altered in only one parameter from the standard setting in order to test their effect on the resulting absorbent solution concentration $X_{a\text{-}out}$ in dependence of temperature difference $\Delta\vartheta_{ae\text{-}min}$. Tests were referenced according to their deviation to the standard test. Thus for example the test "$\dot{m}_{a\text{-}htf}$ = 100g min^{-1}" was operated with an absorbent mass flow $\dot{m}_{s\text{-}a}$ of 6 g min^{-1} a temperature difference $\Delta\vartheta_{ae\text{-}min}$ of 8K, an evaporator temperature ϑ_e of 20°C and a heat transport fluid flow $\dot{m}_{a\text{-}htf}$ of 100g min^{-1}and $\dot{m}_{e\text{-}htf}$ = 700g min^{-1}. The standard testing evaporator temperature ϑ_e was set to 20°C, slightly lower than room temperature in order to minimise the effect of ambient temperature while not running the risk of condensation on the vacuum chamber body. The complete setup was insulated with 80mm of flexible synthetic rubber insulation with a specific heat conductivity of 0.03W m^{-1} K^{-1} as shown in figure 23 on page 91. Under realistic application, the evaporating temperature of 20°C is clearly too high, for this reason evaporator temperatures of 5°C, 10°C and 15°C were also measured. It must be noted that these initial tests were performed prior to the definition of realistic operating conditions provided in chapter 2.4. "Application temperatures" on page 39. It was from these tests that the importance for clearly defined temperatures was recognised.

In order to test the desorption process, 11 individual tests were performed. As in the absorption test sequence, a standard test was defined with an absorbent mass flow $\dot{m}_{s\text{-}d}$ of 8g min^{-1}, a temperature difference $\Delta\vartheta_{dc\text{-}max}$ between ϑ_9 and ϑ_{10} of 45K, a condenser temperature $\vartheta_c = \vartheta_{10}$ of 20°C and a heat transport fluid flow $\dot{m}_{d\text{-}htf}$ and $\dot{m}_{c\text{-}htf}$ of 800g min^{-1} in the desorber as well as the condenser respectively. Table 5 right shows desorption setting

values with standard test settings underlined. All other desorption tests were altered in only one parameter from the standard setting in order to test their effect on resulting absorbent solution concentration in dependence of temperature difference $\Delta\vartheta_{dc\text{-}max}$. As in the absorption sequence, tests were referenced according to their deviation to the standard test. Thus for example the test "$\dot{m}_{s\text{-}d}$ = 4g min^{-1}" was operated with an absorbent mass flow $\dot{m}_{s\text{-}d}$ of 4g min^{-1} a temperature difference $\Delta\vartheta_{dc\text{-}max}$ of 45K, a condenser temperature ϑ_c of 20°C and a heat transport fluid flow $\dot{m}_{d\text{-}htf}$ and $\dot{m}_{c\text{-}htf}$ of 800g min^{-1}. The condenser temperature was set to 20°C as in the absorbent sequence in order to reduce the effect of ambient temperature. In real life application, condensing temperatures between 25°C and 35°C are expected (see chapter 2.4. "Application temperatures" on page 39), depending on the heat sink. In this lab scale setting these temperatures above room temperature were difficult to operate, due to unwanted condensation on the system walls.

Table 5: Settings for the absorption as well as the desorption tests (Fumey et al. 2017).

Absorption Parameter	Values
$\dot{m}_{a\text{-}htf}$ [g min^{-1}]	100, <u>200</u>, 400
$\dot{m}_{e\text{-}htf}$ [g min^{-1}]	400, <u>700</u>, 1000
$\Delta\vartheta_{ae\text{-}min}$[K]	5, <u>8</u>, 10, 12, 15, 18
$\dot{m}_{s\text{-}a}$ [g min^{-1}]	2, 4, <u>6</u>, 8, 10
ϑ_e [°C]	5, 10, 15, <u>20</u>
Desorption Parameter	**Values**
$\dot{m}_{d\text{-}htf}$ [g min^{-1}]	400, <u>800</u>, 1200
$\dot{m}_{c\text{-}htf}$ [g min^{-1}]	400, <u>800</u>, 1200
$\Delta\vartheta_{dc\text{-}max}$[K]	35, 40, <u>45</u>
$\dot{m}_{s\text{-}d}$ [g min^{-1}]	4, 6, <u>8</u>, 12
ϑ_c [°C]	<u>20</u>

Operation of the heat and mass exchanger setup was found to be stable. Steady state was reached under all parameter settings. The major source of performance reduction encountered was due to non-condensable gasses in the absorbate atmosphere.

In figure 25 on page 97 a typical testing period is illustrated. It can be seen that after an operation starting period of approximately 10 minutes ϑ_5 and ϑ_6 slowly drop. At flag 1, the vacuum pump was operated for approximately 1 minute to remove non condensable gasses, after which both temperatures rose again and stayed stable for the remaining testing time. An absorption heat storage system may likely require periodic operation of a vacuum pump in order to remove non-condensing gasses. Long term operation of a demonstrator size system will give insight to this. Temperature ϑ_5 showed strong oscillation owing to the drop wise supply of the absorbent solution from the supply nozzle. ϑ_9 showed some instability on account of the fact that the sensor was generally submerged in the collected absorbent solution below the heat and mass exchanger. At flags 2 to 7 absorbent was released to the vacuum lock and the sensor was uncovered. The measured temperature of the sensor was then affected by radiant heat from the absorber up to the point where it was again covered from absorbent solution. The duration of this effect depended on the level of absorbent released. Temperature ϑ_5 tended to show fluctuation coherent to the absorbent release. This may be due to slight pressure differences during the draining process resulting in dissociation of slight non condensable gasses from accumulation at the absorbent supply. Temperatures ϑ_6 through to ϑ_8 showed a continuous reduction of the absorbent solution temperature flowing down the finned tube. The temperature decrease was not-linear due to the non linear concentration reduction as discussed in the absorption based counter flow heat and mass exchanger discussion. Reduced absorbent solution concentrations led to lower temperatures as well as lower affinity of absorbent solution to absorbate, resulting in a decrease in absorption driving force. Thus, for lower concentration, greater absorption surface area or distance along the heat exchanger in respect to temperature decrease is required. ϑ_9 does not follow the general pattern due to its placement below the heat and mass exchanger. ϑ_{10} and ϑ_{11} were nearly equal and showed steady absorbate evaporating temperature.

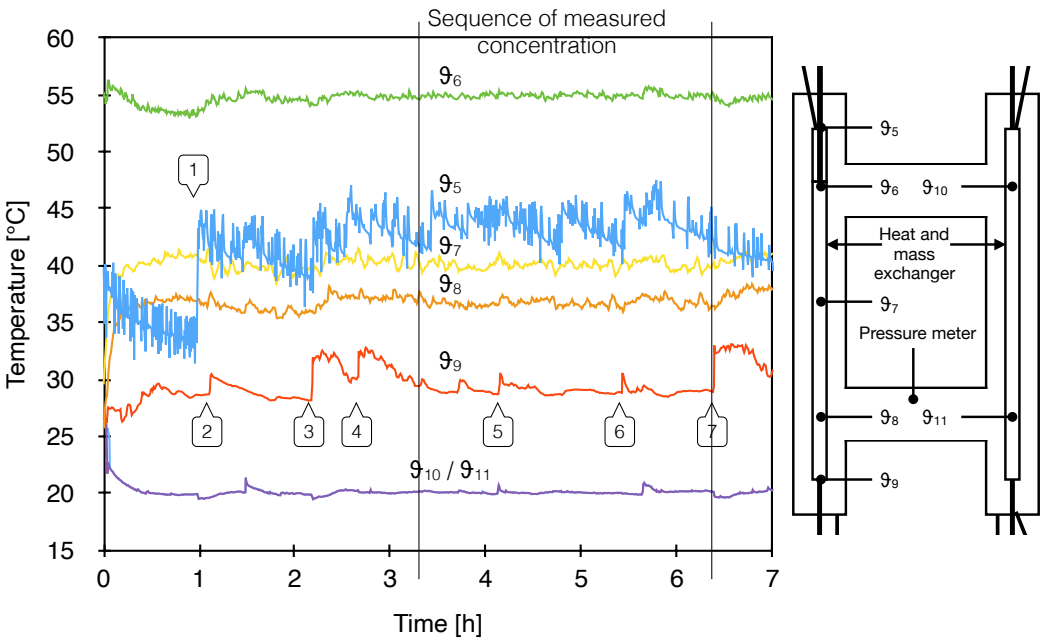

Figure 25: Diagram of a complete testing period in absorption mode showing absorbent temperatures (ϑ_5 to ϑ_9) and absorbate temperatures (ϑ_{10} and ϑ_{11}). For clarity of measurement position, a crop of figure 24 on page 92 is added (Fumey et al. 2017).

The average exposure time of the absorbent solution on the heat and mass exchanger to the absorbate atmosphere was approximately 12 minutes in absorption and 16 minutes in desorption process.

Visual observation showed that as a consequence of the slow mass flow of the absorbent solution a thin film resulted over the whole length of the spiral fin. This was grossly in contrast to the wetting behaviour encountered in the COMTES project tube bundle heat and mass exchange assembly (Fumey et al. 2015c). In addition, the absorbent solution tended to adhere also to the tube wall. This increased the surface area as well as enabled direct heat release to the tube wall, improving contact to the heat transfer fluid.

Table 6: List of the performed tests with setting deviation from the standard test including values of temperature difference and resulting concentration adherent to figure 27 on page 101 (Fumey et al. 2017).

	Setting	$\Delta\vartheta_{ae\text{-}max}$ [K]	$X_{a\text{-}in}$ [wt%]
A-0	Absorption starting point	34.6	50.0
A-1	Standard test	9.6	31.7
A-2	$\dot{m}_{a\text{-}htf}$ = 100g min^{-1}	10.2	33.6
A-3	$\dot{m}_{a\text{-}htf}$ = 400g min^{-1}	9.0	30.6
A-4	$\dot{m}_{e\text{-}htf}$ = 400g min^{-1}	9.1	31.5
A-5	$\dot{m}_{e\text{-}htf}$ = 1000g min^{-1}	9.5	31.8
A-6	$\Delta\vartheta_{ae\text{-}min}$ = 5K	5.8	30.4
A-7	$\Delta\vartheta_{ae\text{-}min}$ = 10K	10.7	33.0
A-8	$\Delta\vartheta_{ae\text{-}min}$ = 12K	12.8	33.6
A-9	$\Delta\vartheta_{ae\text{-}min}$ = 15K	15.4	35.2
A-10	$\Delta\vartheta_{ae\text{-}min}$ = 18K	17.5	36.7
A-11	$\dot{m}_{s\text{-}a}$ = 2g min^{-1}	8.6	26.5
A-12	$\dot{m}_{s\text{-}a}$ = 4g min^{-1}	8.6	29.8
A-13	$\dot{m}_{s\text{-}a}$ = 8g min^{-1}	8.6	34.1
A-14	$\dot{m}_{s\text{-}a}$ = 10g min^{-1}	9.5	35.9
A-15	ϑ_e = 5°C	8.6	34.5
A-16	ϑ_e = 10°C	8.1	33.8
A-17	ϑ_e = 15°C	7.1	32.1

	Setting	$\Delta\vartheta_{dc\text{-}min}$ [K]	$X_{d\text{-}in}$ [wt%]
D-0	Desorption starting point	9.7	25.0
D-1	Standard test	43.2	49.0
D-2	$\dot{m}_{s\text{-}d}$ = 4g min^{-1}	44.2	53.5
D-3	$\dot{m}_{s\text{-}d}$ = 6g min^{-1}	44.2	53.4
D-4	$\dot{m}_{s\text{-}d}$ = 10g min^{-1}	41.3	47.5
D-5	$\dot{m}_{s\text{-}d}$ = 12g min^{-1}	38.7	44.9
D-6	$\Delta\vartheta_{dc\text{-}max}$ = 35K	33.5	45.6
D-7	$\Delta\vartheta_{dc\text{-}max}$ = 40K	38.0	46.4
D-8	$\dot{m}_{d\text{-}htf}$ = 400g min^{-1}	43.2	47.1
D-9	$\dot{m}_{d\text{-}htf}$ = 1200g min^{-1}	42.4	47.7
D-10	$\dot{m}_{c\text{-}htf}$ = 400g min^{-1}	42.1	48.6
D-11	$\dot{m}_{c\text{-}htf}$ = 1200g min^{-1}	43.3	51.6

Table 6 shows the list of all the tests composed with their altered operation parameter to the standard test. A-0 and D-0 refer to the starting conditions of all tests for both absorption and desorption.

In figure 26 average temperatures and power of all absorption and desorption tests are presented. Arithmetic mean values of stable operation sequences are shown including standard deviations.

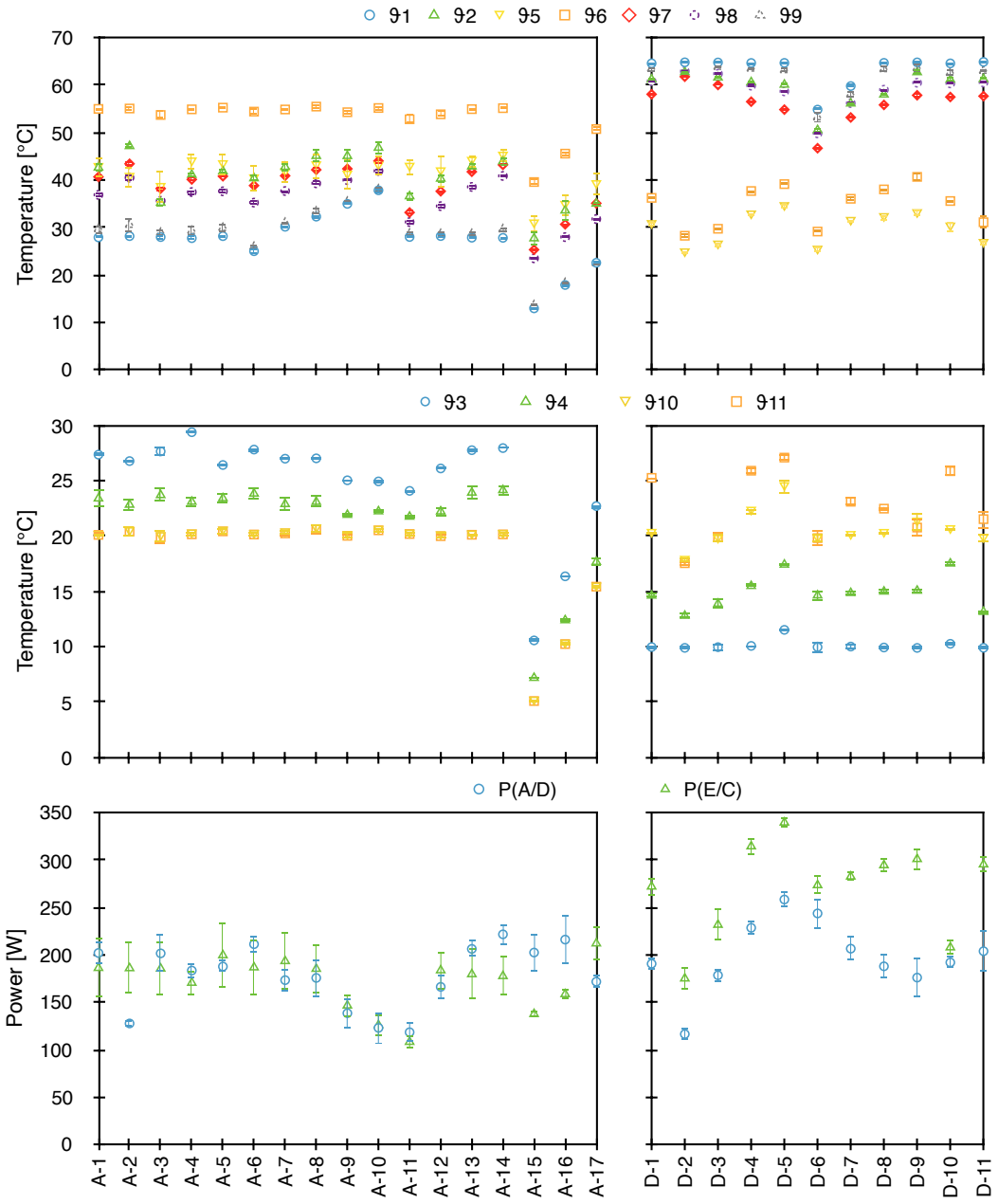

Figure 26: Average temperature and power of the complete absorption and desorption testing series including standard deviation. Temperature sensor allocation is shown in figure 24 on page 92. On the left side the values in absorption are shown and on the right side those from the desorption test (Fumey et al. 2017).

In figure 27 the accumulated results from both absorption and desorption test series, in respect to temperature difference and absorbent solution concentration are presented in a gross temperature lift vs. concentration diagram. The dashed line indicates the theoretical concentration in dependence of the temperature difference equilibrium. For effective heat storage, it is important that in both absorption and desorption, operation is close to this equilibrium. Arithmetic mean values of the test results are shown, taken from a sequence of stable operation as indicated in figure 25 on page 97, standard deviations were omitted for better visibility. *A-0* and *D-0* indicate the starting temperature differences of all absorption and desorption tests respectively. For this reason, maximum and minimum values were indicated. All results were numbered according to table 6 on page 98 where average concentration and temperature values are shown. The diamond shape point *A-0* shows the average temperature increase $\Delta\vartheta_{ae\text{-}max}$ (gross temperature lift) between the maximum absorbent temperature ϑ_6 and the evaporator temperature ϑ_{10} of the absorbent solution in respect to the starting concentration $X_{a\text{-}in}$ of 50wt%. The upside-down triangle points show the resulting absorbent solution concentration $X_{a\text{-}out}$ in the absorption process in respect to the final temperature difference $\Delta\vartheta_{ae\text{-}min}$ (gross temperature lift) between the minimum absorbent temperature ϑ_9 and the evaporation temperature ϑ_{10}. The upright triangle point *D-0* shows the initial temperature difference $\Delta\vartheta_{dc\text{-}min}$ between the temperature of absorbent entering the desorber ϑ_6 and the condenser temperature ϑ_{10} in respect to the starting concentration of $X_{d\text{-}in}$ of 25wt% of all performed desorption tests. The round points show the resulting concentration $X_{d\text{-}out}$ in respect to the temperature difference $\Delta\vartheta_{dc\text{-}max}$ of the maximum desorption temperature ϑ_9 and the condenser temperature ϑ_{10} in desorption.

In general, test results followed the equilibrium line. Values from absorption tests were slightly above and values from desorption tests were below the equilibrium line. This was expected, as a consequence of the continuous absorbent solution flow on the heat and mass exchanger and the

resulting limitations in exposure time. Favourable results in respect to temperature difference $\Delta\vartheta_{ae\text{-}min}$ and $\Delta\vartheta_{dc\text{-}max}$ are close to the equilibrium line. This is due to the minimal temperature difference to the theoretical temperature difference reached. In order to reach a high energy density, a large concentration difference between desorption $X_{d\text{-}out}$ and absorption $X_{a\text{-}out}$ process is required.

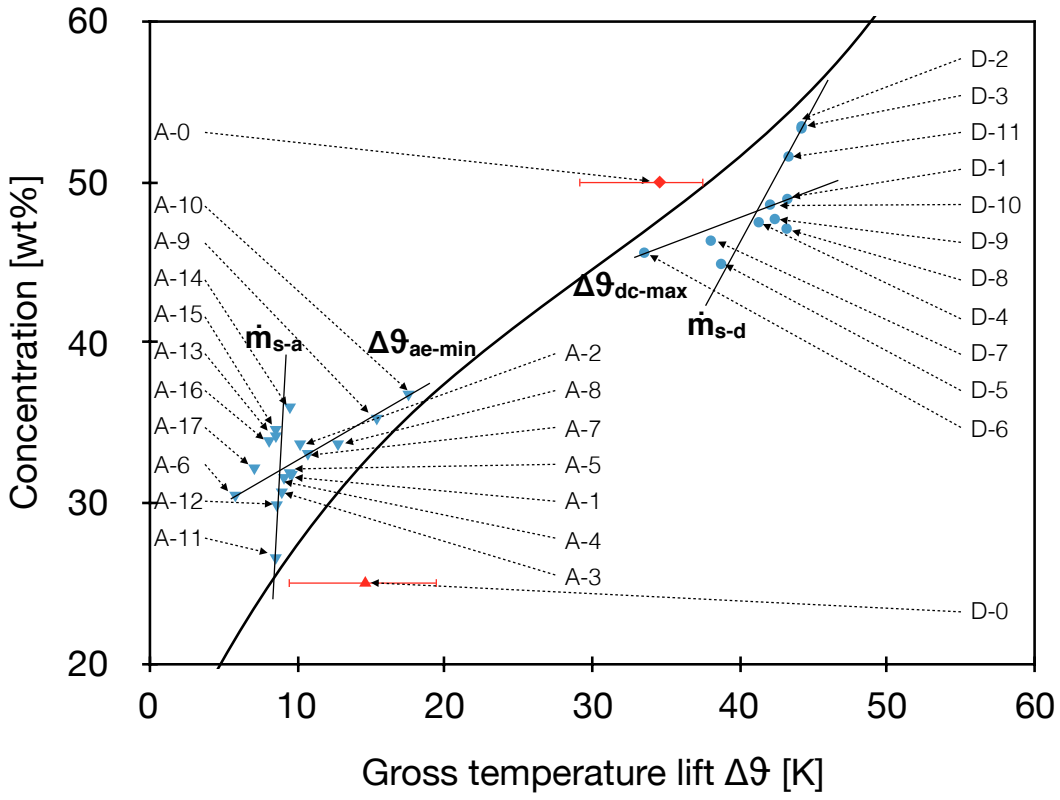

Figure 27: Diagram of the complete testing sequence of both absorption and desorption. Indicated are the effects of change in sorbent mass flow $\dot{m}_s$ and gross temperature lift $\Delta\vartheta$ in absorption as well as desorption. Increase in sorbent mass flow leads to deviation from the equilibrium line, both in absorption and desorption. In absorption, reduction of $\Delta\vartheta_{ae\text{-}min}$ leads to lower concentration but greater diversion from equilibrium, while in desorption the inverse occurs [Fumey et al. 2017].

It can be seen in figure 26, that in absorption, the maximum absorbent temperatures ϑ_6 was directly dependent on the evaporator temperature ϑ_{10} and ϑ_{11}. An average temperature gain $\Delta\vartheta_{ae\text{-}max}$ of 34.6K was reached. The

theoretical temperature gain in respect to the absorbent solution starting concentration $X_{a\text{-}in}$ of 50wt%, would be 38K. A $\Delta\vartheta_{ae\text{-}max}$ of 34.6K corresponds to the equilibrium temperature gain at a concentration $X_{a\text{-}in}$ of 47.5wt%. It is important to recognise that since absorption is required to reach the nominal starting temperature of the absorbent solution, a concentration decrease results and the maximum theoretical temperature gain cannot be reached. It could thus be concluded that the average temperature gain in this absorption test sequence is close to the maximum achievable in practice. Test A-15, A-16 and A-17 illustrate absorber output temperature ϑ_2 dependency on the evaporator input temperature ϑ_3 well. The temperature drop between the maximum absorption temperature ϑ_6 and the heat transport fluid out ϑ_2 varied depending on operation, but was generally high. On the evaporator heat and mass exchanger the same issue of high temperature difference between heat transport input temperature ϑ_3 and evaporator temperatures ϑ_{10} and ϑ_{11} could be seen. Due to the large tube inner diameter of 22mm and the low volumetric flow between 100ml min^{-1} and 1000ml min^{-1}, a laminar flow of the heat transport fluid resulted, leading to increased thermal resistance. In a further development step this may be improved by appropriate design changes and forced turbulence.

The absorber and evaporator power difference varied slightly depending on the test. A closer fit was found at higher temperature difference between absorber and evaporator. In general power output of the heat and mass exchanger was approximately 200W and did not greatly improve at increased absorbent flows in *A-13* and *A-14*. This may indicate absorption limitations in laminar flow due to slow mass diffusion of absorbate into absorbent. In laminar flow, mass transport is solely dependent on the rate of mass diffusion. In turbulent flow on the other hand, mass transport is enhanced by intermixing.

In figure 26 on page 99 results show that, increase in absorber heat transfer fluid flow $\dot{m}_{a\text{-}htf}$ led to a decrease in absorbent solution concentration $X_{a\text{-}out}$ on account of the decrease in temperature on the absorber. Increase in evaporator heat transfer fluid flow $\dot{m}_{e\text{-}htf}$ shows no substantial

change in the concentration $X_{a\text{-}out}$, pointing to sufficient evaporation power. The final absorbent solution concentration $X_{a\text{-}out}$ is most clearly affected by the absorbent solution flow $\dot{m}_{s\text{-}a}$ and temperature difference $\Delta\vartheta_{ae\text{-}min}$. The respective indicated lines in the diagram in figure 27 show the effects. Increase in absorbent solution flow $\dot{m}_{s\text{-}a}$ resulted in an increased final concentration as well as an increased deviation from the equilibrium. This effect points to limitations in mass transport in the absorbent. Higher absorbent solution mass flow led to increased absorbent solution film thickness and higher flow speed, requiring greater time for mass transport and at the same time reduced residence time. For this reason, in order to reach close correlation to the equilibrium line, an absorbent solution flow limitation, or respective power limitation was encountered. Increased gross temperature lift $\Delta\vartheta_{ae\text{-}min}$ resulted in reduced absorbate mass transfer from evaporator to absorber at a constant absorbent solution residence time and surface area given by the heat and mass exchanger design. For this reason, a closer fit to the theoretical equilibrium was measured. A decrease in evaporator temperature ϑ_e at constant $\Delta\vartheta_{ae\text{-}min}$ resulted in greater deviation from the equilibrium line. This may be due to the resulting decrease in absorption pressure, which in turn reduces absorbate contact to the absorbent solution. Due to the lower operating temperature, the aqueous sodium hydroxide viscosity was also lower (see Appendix A. “Viscosity” on page 199), and thus the mass transport flux was reduced (see equation 30 on page 76). Thus, it is recognised that the operating temperature influences kinetics, and in turn, operational energy capacity.

Standard desorption input temperatures ϑ_1 was 65°C and ϑ_3 was 10°C. Temperature difference on the desorber between ϑ_1 and ϑ_9 was approximately 2K. On the condenser on the other hand a temperature difference between ϑ_3 and ϑ_{10} of at least 10K was measured. Again, it can be noted that thermal conductivity needs to be improved.

In desorption, increased heat transfer fluid flow $\dot{m}_{d\text{-}htf}$ in the desorber, showed no clear effect on the final concentration $X_{d\text{-}out}$, see figure 26 on page 99. Increase in condenser heat transfer fluid flow $\dot{m}_{c\text{-}htf}$ showed a slight

increase in the resulting absorbent solution concentration $X_{d\text{-}out}$. As in the absorption test results, the major influence on desorption tests could be seen in respect to absorbent solution flow $\dot{m}_{s\text{-}d}$ and temperature difference $\Delta\vartheta_{dc\text{-}max}$. The respective indicated lines in the diagram in figure 27 on page 101 show the effects. A reduction in $\Delta\vartheta_{dc\text{-}max}$ led to a lower resulting final concentration $X_{d\text{-}out}$ as well as a closer fit to the equilibrium line. This was expected owing to the fact that reducing the maximum gross temperature lift $\Delta\vartheta_{dc\text{-}max}$ led to a reduction in resulting $X_{d\text{-}out}$. That in turn resulted in reducing the absorbate mass transfer from desorber to condenser at a constant absorbent solution residence time and surface area given by the heat and mass exchanger design. Thus a closer fit to the theoretical equilibrium was reached. An increase in absorbent solution flow $\dot{m}_{s\text{-}d}$ resulted in lower concentration $X_{d\text{-}out}$ and greater diversion from the equilibrium line. This is due to the fact that the increase in absorbent solution flow led to a greater film thickness and greater mass transport at constant surface area, requiring greater time to reach respective high concentrations.

On a practical level, it was found that spilling of the aqueous sodium hydroxide over the edge of the spiral fin was no issue. The slightly ‘dished’ upward bent form of the fin was well able to channel the fluid. It was even found that due to the adherence of the fluid to the tube wall, operation was possible with flipped tube, thus downward bent fin, with slightly improved fin wetting.

The concentration difference between D-2 and A-11 resulted in an energy density based on the discharged absorbent solution of approximately 435 kWh m^{-3}. This value naturally needs to be regarded with care, since as mentioned, the operating conditions were not fitting to the application as seasonal heat storage for buildings. However, these initial tests showed that with the novel spiral finned tube heat and mass exchanger, high concentration differences within a continuous absorption process could be achieved. Important parameters in achieving this were, large surface area, good wetting, thin film and sufficient exposure time. This was made possible with the suggested spiral finned tube design but came at the cost of relatively low

thermal power output. Thus, the trade-off between energy storage capacity and specific power output. For absorption heat storage the preferable choice is a reduction of specific power output if high concentration difference is supported. Future work presented in chapter 8. on page 112 and 9. on page 136 therefore focuses on improving volume specific power output through enabling absorbent mixing and enhancing mass transfer rate, without compromising energy density as well as reducing temperature drop. In addition, cycling tests are performed, focussing on both heat and mass exchanger and absorbent material stability.

7.2. Cycling test

In order to gain experience in respect to material stability, both on the component material and absorbent material level, seven absorption and desorption cycles were undertaken using the previously described heat and mass exchanger test bench and performance was compared in terms of deviation of effective temperature difference from the theoretical temperature difference for a given absorbent concentration. Results are again presented in the gross temperature lift vs. concentration diagram and evaluated in respect to the equilibrium curve shown in figure 28. This test distinguished itself from the former tests reported in that both absorbent solution and absorbate were continuously reused. This led to a dependence of absorption performance on the preceding desorption process with the potential of accumulating possible performance degradation. Further, in these test results, reference was made to the heat transfer fluid temperatures and not the working fluid temperatures, a further step towards practical application. In absorption, the absorbent flow was 6g min^{-1}, the absorber / desorber heat transport fluid supply temperature was 28°C at a flow of 200g min^{-1} and the evaporator / condenser supply temperature was 25°C at a flow of 800 g min^{-1}. In desorption the absorbent flow was 8g min^{-1}, the absorber / desorber heat transport fluid supply temperature was 65°C at a flow of 800 g min^{-1} and the evaporator / condenser supply temperature was 10°C at a flow of 1200 g min^{-1}. It must be noted that the evaporator and condenser heat transport fluid temperatures do not follow the realistic temperature guide-

lines and are actually inverse. This is again due to the fact that these tests were performed prior to the definition of the temperature guideline. Even so, the results are valuable for the respective investigation of material stability. The test duration for a single cycle in absorption was approximately 13.5 hours and the desorption duration was 17 hours due to the greater mass of diluted aqueous sodium hydroxide to be transported. No absorbent or absorbate was added or removed from the solution during the test series. Both absorbent and absorbate were stored under atmospheric pressure and exposed to air.

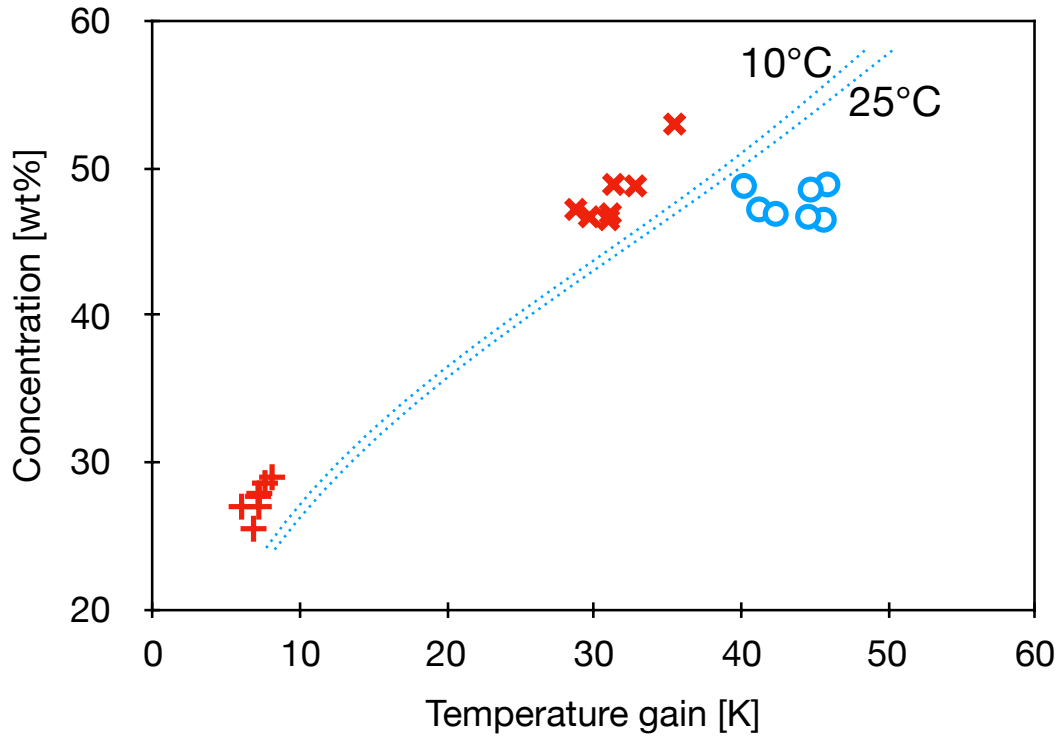

Figure 28: Overview of cycling test shown in the gross temperature lift vs. concentration diagram. Dashed lines are equilibrium conditions at 10°C and 25°C water vapour temperature. Red x representing beginning of absorption, red + end of absorption and blue o end of desorption (beginning of desorption is omitted as initial absorbent concentration do not correspond to charging temperatures) .

In figure 28 the performance is shown by displaying average values of the cycles. The dashed lines show the theoretical equilibrium at 10°C and 25°C water vapour temperature. The red x values show the maximum gross

temperature difference during absorption in dependence of the concentration. Due to the varying concentration in the cycling tests, the maximum absorption temperature varies. Performance is evaluated depending on the horizontal distance from the equilibrium line, as illustrated in figure 29 on page 108. The red + values show the final concentration in the absorption process plotted in respect to the minimum temperature difference between absorber and evaporator. In this case, performance is measured depending on the vertical distance to the equilibrium, shown in figure 30 on page 109. A closer fit to the equilibrium line shows good performance in terms of effective mass transfer (reaching equilibrium at a specific gross temperature difference) and exploited energy density potential. The blue o values show the resulting concentration of the desorption cycles. As with the absorption results, close fit to the equilibrium line is desired, illustrated in figure 31 on page 110.

Figure 29 to 31 show details of the results presented in figure 28 for the different operation regimes, beginning and end of absorption as well as end of desorption process, with indication of cycle number for analysis of cycling performance. Figure 29 shows the maximum temperature increase (gross temperate lift) with respect to concentration in absorption. As expected, the temperatures were lower than the equilibrium. Since the heat transport fluid temperatures are reference to, there are many process steps involved in the temperature drop. These include thermal conductivity of the finned tubes, consisting of temperature difference both on the absorber / desorber and the evaporator / condenser, as well as temperature drop from the finned tube surface to the absorbent and absorbate surface, and the vapour mass transport. The degree of each effect is as yet unclear.

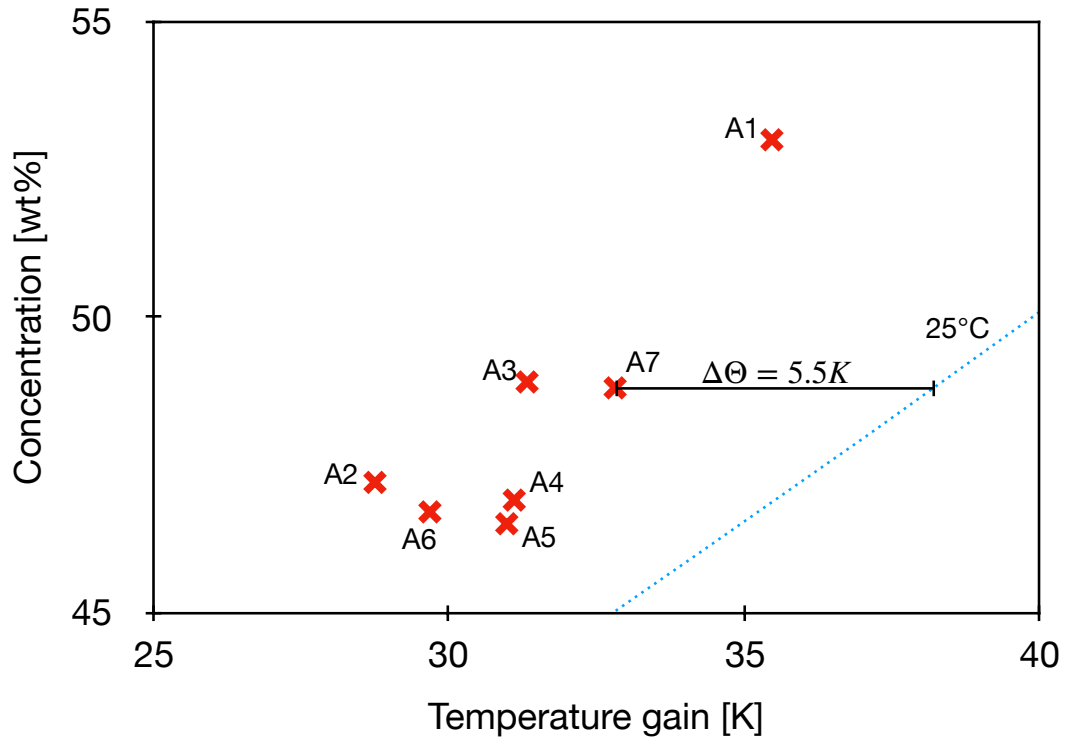

Figure 29: Focus of figure 28 on the maximum temperature increase in respect to the concentration in the absorption process. All values are numbered according to their absorption cycle.

Test *A1* showed a substantially higher temperature gain due to the starting concentration of 53wt%, temperature increase is directly dependent on absorbent concentration. This test also showed a large temperature deviation from equilibrium. This is an interesting combined effect, in part effected due to the greater sorbent temperature, but also due to the non-linearity of the absorbent thermal capacity, as described in chapter 6.3. “Counter flow heat exchange with absorption” on page 85. Interestingly, the first three cycles have a stronger temperature deviation than the following four cycles. Nevertheless, there is no clear tendency observed, highlighting a potential effect of cycling. The least temperature differences were measured at test *A4* and *A5*, with tests *A6* and *A7* again showing an increase. The specific temperature deviation from the equilibrium is illustrated based on the *A7* test result.

Figure 30 shows the resulting concentration in respect to the minimum temperature difference (gross temperature lift) between the absorber and the

evaporator. As in Figure 29 there is no trend of degradation or improvement visible across the cycles. Apart from cycle *A1* and *A6*, all results show similar offset to the equilibrium line. The concentration difference results from the slightly varying temperature difference between the cycles. Specific concentration difference is illustrated based on test *A4* with a *ΔX* of 5.5wt%. In respect to energy capacity this relates to a degradation from 450kWh m^{-3} down to 370kWh m^{-3} under the set operating conditions.

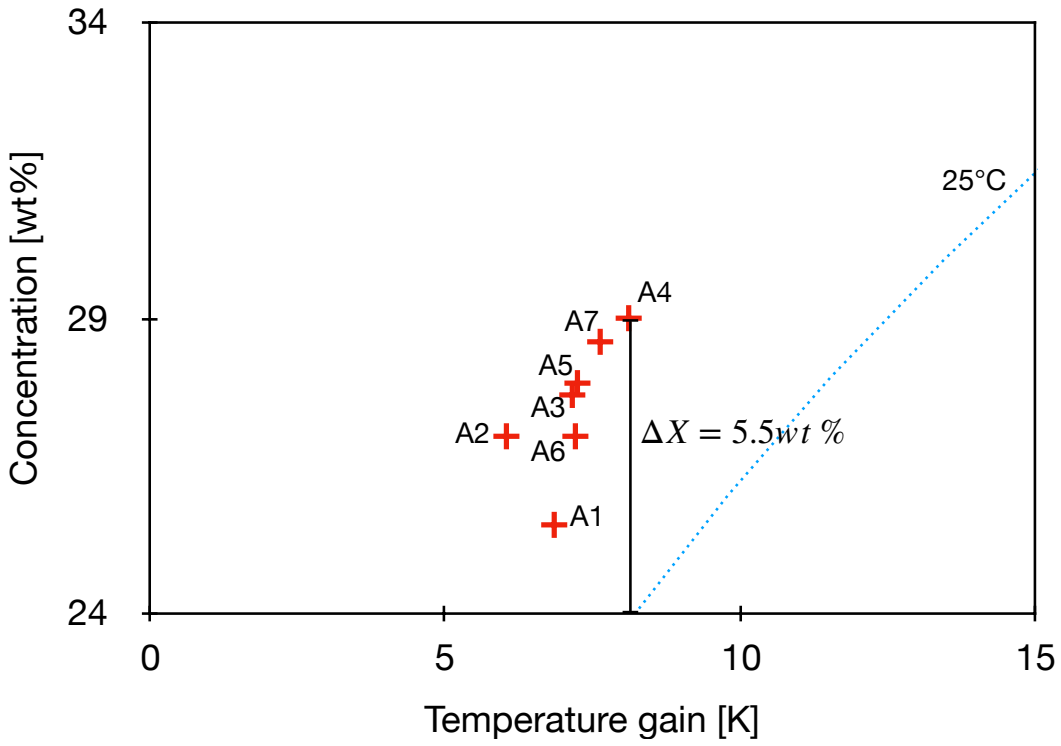

Figure 30: Focus of figure 28 on the minimum concentration reached in absorption modus. All values are numbered according to their cycle.

Figure 31 shows a close up of the resulting concentration in respect to the temperature difference in the desorption process. Concentration deviation is similar as in the absorption process. In general the desorption process is not as critical, since as shown in chapter 2.4. “Application temperatures” on page 39, and discussed in chapter 4.2. “Temperature and energy density”on page 57, sufficient charging temperatures are available. If desorption was powered by a conventional air source heat pump, able to supply only 65°C, this would be more critical.

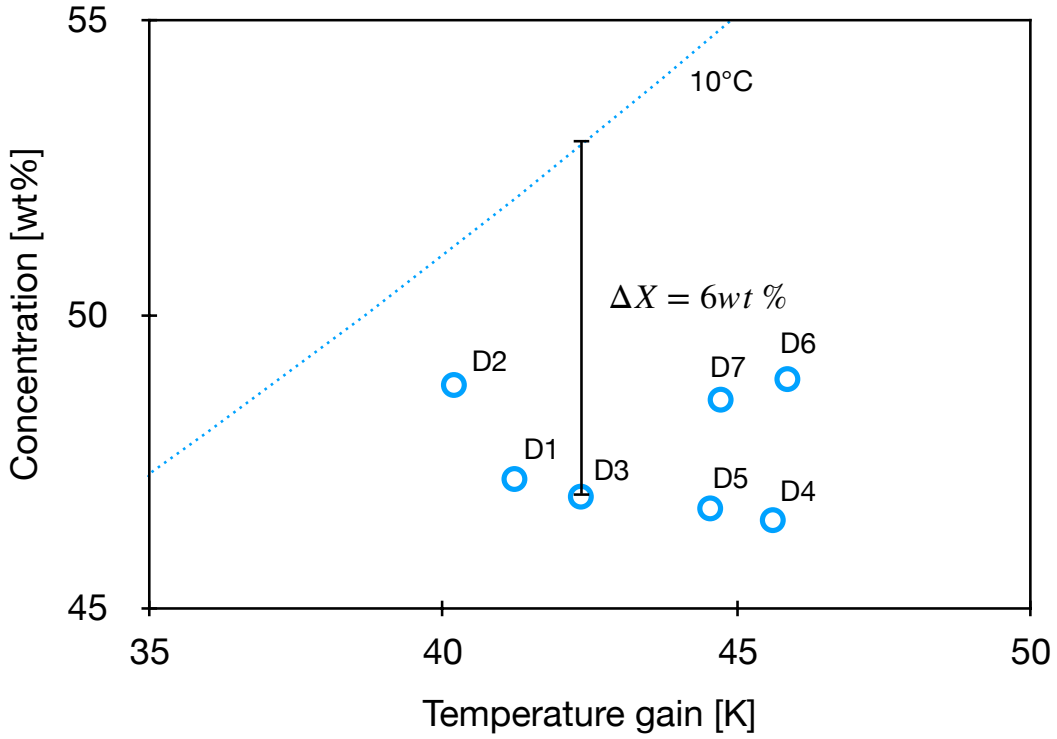

Figure 31: Focus of figure 28 on the maximum concentration reached in desorption modus. All values are numbered according to their cycle.

From the presented results, it was not possible to detect any specific performance degradation. Nevertheless, it can be seen by the general scattering of the results that performance is highly temperature sensitive. In addition to the performance comparison an analysis of the cycled sorbent was undertaken. Visual inspection showed that the aqueous sodium hydroxide with a measured concentration of 47.3wt% had a slight red brown tint.

A sample of the aqueous sodium hydroxide was mixed with a 65wt% hydrochloric acid solution to a pH value of 0 and further diluted at a ratio of 1 to 20 with pure water. After this, the sample was analysed by means of plasma mass spectrometry. Inductively coupled plasma mass spectrometry (ICP-MS) is a type of mass spectrometry used to detect metals in liquid samples at very low concentrations. The following particles were measured.

Table 7: Results of the plasma mass spectrometry analysis of the cycled aqueous sodium hydroxide.

Element	Mass concentration in µg/ml
Iron (Fe)	14
Chromium (Cr)	3.6
Nickel (Ni)	<2
Zinc (Zn)	<2
Phosphorus (P)	<2

In addition, the elements, aluminium (Al), arsenic (As), cobalt (Co), copper (Cu), manganese (Mn), molybdenum (Mo), titanium (Ti), und vanadium (V) were also measured. All values are found to be substantially below 2µg ml^{-1}.

It is concluded that visual analysis is confirmed by the results from the plasma mass spectrometry shown in table 7, there appears to be a slight wash out of iron from the stainless-steel. The precise degree of this activity and the type of corrosion, see chapter 4.4. “Corrosion” on page 62, was not further analysed at this time. For now, it can be stated that even after 4 years of operating the lab scale heat and mass exchanger test bench, no break down due to corrosion has been encountered.

Based on this cycling test of seven cycles, good cycling stability without any clear degradation of the process was concluded. In addition, storage of both absorbent and absorbate at ambient pressure was seen to be a promising system design approach, substantially reducing system complexity and cost. Since the analysis of the sorbent shows slight wash out of iron from the spiral finned tube heat and mass exchanger, it is judged that nickel coating of the tubes may be required for long term operation. Further benefit of nickel coating may be the ability to change to copper as a base material. This may substantially reduce the temperature drop between absorbent and absorbate temperature and the respective heat transport fluid temperature.

8. Study of mass transport

As previously discussed, in the absorption process, the uptake of absorbate by the absorbent results in the release of heat both due to absorbate condensation as well as from mixing the absorbent with absorbate, in as far as this is an exothermic process, which is the case with sodium hydroxide and water. In the process, the absorbent temperature increases and a pseudo equilibrium (steady-state) is established at elevated temperature (gross temperature lift). In desorption, that is absorbate vapour release, the reverse process takes place. Temperature, vapour pressure and concentration in the absorbent are ultimately limited by equilibrium thermodynamics (see chapter 4.2. “Temperature and energy density” on page 57). However, if the process is kinetically limited, the temperature change will not reach the maximum (minimum) adiabatic values, reducing the maximum gross temperature lift, as is shown in chapter 5. “Study of absorption at bulk scale”on page 64 and chapter 7. “Heat and mass exchanger test bench” on page 88. This results in reduced concentration change and therefore diminishes the practicable storage capacity, as shown in the afore mentioned chapters. Thus, a fundamental limitation in liquid absorption storage performance is not due to equilibrium thermodynamics, but due to the kinetics of the heat and mass exchange under application specific conditions, directly affecting gross temperature lift, volumetric power and volumetric energy density.

From the initial testing series, it was recognised that kinetic performance was limited on both levels, heat and mass transport. In operation, there is a respectively high temperature difference between absorbent and absorbate to the corresponding heat transport fluids. This is due to the low thermal conductivity of the stainless-steel as well as to a substantially lower degree, accounted for by the thermal conductivity of the sorbent, since this is generally high (see appendix A. “Thermal conductivity” on page 207). The thermal conductivity issue concerning stainless-steel, can easily be resolved by employing nickel coated copper tubes, as suggested at the end of chapter 7.2 “Cycling test” on page 104, since nickel is recognised as the most

stable metal for all concentrations and temperatures of sodium hydroxide (see chapter 4.4. “Corrosion” on page 62). Thermal conduction from the tube to the heat transport fluid can be improved through internal fins, increasing surface area and possibly enabling turbulent flow. Such products are available from companies such as Schmöle (www.schmoele.de) These improvements are considered to be state of the art and will be applied in an improved heat and mass exchanger design. More interesting and substantially less trivial is the apparent limitations in power, due to mass transport resistance. In this and the following chapter close analysis of mass transport is undertaken.

The vertically installed spiral finned tube counter-flow heat and mass exchanger was designed to resolve particularly the challenge of reaching high concentration change by slow sorbent flows on the fin as a thin film in a downwards spiral motion, long exposure time and low film height (reduced mass transport distance) was reached. Initial tests presented in chapter 7. “Heat and mass exchanger test bench” on page 88 showed that the spiral finned tube design was able to satisfy the requirement for reaching high energy density to a substantially greater degree than the tube bundle falling film design (see chapter 6.1. “Tube bundle falling fin heat and mass exchanger” on page 79). Nevertheless, it was noted that turbulent absorbent flow, and thus absorbent mixing, a frequently followed means for mass transport enhancement, was prevented by the high sorbent viscosity, thin film and respectively slow flow. In order to enhance process kinetics, and so improve the triple performance criteria to achieve commercial viability, it was important to further increase the volume (heat and mass exchanger material) specific power of this design. For this task, it was consequential to understand mass transport phenomena and possible sources of mass transport resistance. This demanded a closer look at the process of mass transport under application specific conditions.

During the bulk scale analysis in chapter 5. “Study of absorption at bulk scale” on page 64, a mean concentration was derived. In this analysis it was important to be able to measure the concentration of the absorbent at

varying depths in the thin film, in the process of absorption and desorption. For this characterisation of the gas-liquid interface and film height, a method enabling both spatially and temporally resolved measurement on the micrometre (thin film) and minutes (time scope comparable to chapter 5. “Study of absorption at bulk scale” on page 64) scale was required. Additional criteria considered included the highly corrosive material aqueous sodium hydroxide, the required pure water vapour atmosphere and the elevated temperatures. Only by enabling all these parameters through dynamic height profiling, was it possible to analyse the mass transport specific rate-limiting steps for water absorption kinetics in aqueous sodium hydroxide thin films under application-specific conditions.

In literature it was found that Raman spectroscopy, though not common, has been utilised to measure concentration of sodium hydroxide (Walrafen and Douglas 2006, Shaffer 1997). However it has not been used spatially and temporally resolved, and thus also not for the analysis of mass transport in the absorption and desorption process, as is the case in this study.

8.1. Fundamentals of the absorption kinetics in liquid thin films

The water vapour pressure in the aqueous sodium hydroxide solution is dependent on the aqueous sodium hydroxide concentration and the temperature of this solution (see chapter 2. “Sorption heat storage for buildings” on page 21 and Appendix A “Vapour pressure” on page 204). Increasing or decreasing the solution temperature leads to a release or uptake of water vapour respectively at the solution surface. This results in the chemical current also referred to as mass current of water molecules:

$$j\left[\frac{mol}{m^2 s}\right] = \frac{\dot{M}}{A}, \textit{ Equation 31}$$

With $\dot{M}$ [mol s^{-1}] being the mass transport and A [m^2] the active area. This current, going into or out of the sorbent, depends on the coupled mass

transport of the gas phase, the uptake and release of sorbate at the gas-liquid interface and the mass transport of the liquid in the film. The thermal power of the heat and mass exchanger relates to the resulting mass current according to equation 26 on page 70 and restated below:

$$P[W] = \dot{q};\ P = jA\Delta H, \text{ Equation 26}$$

In the closed process, as followed in this liquid absorption heat storage design, it was proposed that mass transport in the gas phase can be neglected, under the condition that only water vapour was present. Both in the bulk scale and lab scale heat and mass exchanger tests, it was seen that the slightest presence of non-condensable gas (air) in the setup chambers led to substantial reduction in mass transport due to gas interface mass transport hindrance. The question thus remained whether the kinetic barrier at the gas–liquid interface or the mass transport in the film was rate limiting.

It was found that describing the process of mass transport at the interface is complex [Zhakhovsky et al. 2019]. Persad et al. (2016) proposed a simplified representation by applying the Hertz-Knudsen equation:

$$j_{interface} = \sqrt{\frac{M}{2\pi k_B}}(\sigma_d \frac{p_v}{\sqrt{\theta}_s} - (\sigma_a \frac{p_s}{\sqrt{\theta}_v}), \text{ Equation 32}$$

where, M is mass of the water molecule, k_B is the Boltzmann constant, σ_d and σ_a are desorption and absorption coefficients, p_s is the absorbent equilibrium pressure, p_v is the gas (absorption vapour) pressure, ϑ_s is the temperature of the absorbent and ϑ_v is the temperature of the gas phase.

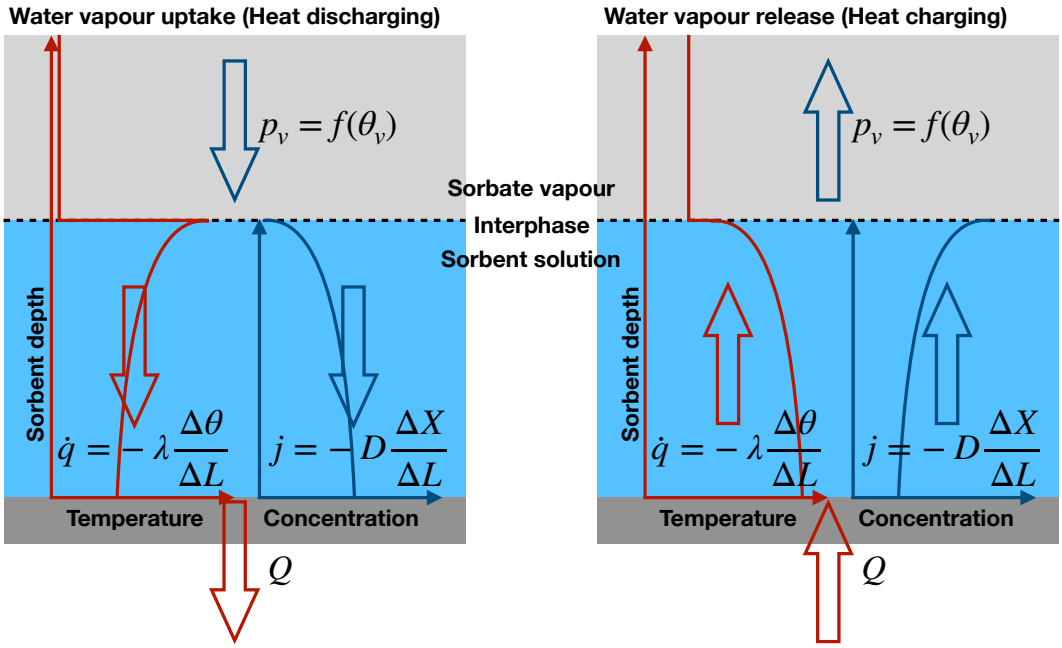

Figure 32: Illustration of the general behaviour of the temperature and sorbent concentration in the sorbent film during water vapour uptake and release.

Moving on to the absorbent film, as previously pointed to, there is potentially both mass and heat transport to be considered. The generally recognised behaviour of the temperature and concentration are shown in figure 32. Both mass and thermal diffusion lead to exponential-like gradients. The discontinuities shown at the gas-liquid interface are a consequence of the interface phenomenon and described by the Herz-Knudsen equation, (Equation 32).

In considering the two possible areas of resistance, interface and film, it was recognised that if the interface was the dominating limitation, close to no concentration gradient should be recognised in the film height. On the other hand, if there was a strong temperature gradient ΔΘ/ΔL or concentration gradient ΔX/ΔL measured, then mass diffusion and / or thermal diffusion was limiting. Thus, in the film, the following equations are of importance:

$$j_{diff} = -D \frac{\Delta X}{\Delta L}, \text{ Equation 33}$$

$$\dot{q} = -\lambda \frac{\Delta\theta}{\Delta L}, \textit{ Equation 34}$$

where λ [$m^2\ s^{-1}$] and D [$m^2\ s^{-1}$] are the thermal diffusion and mass diffusion coefficient respectively, and X [wt%] is the concentration, L [m] the distance and ϑ the temperature.

At this point it was not possible to measure both concentration and temperature at the required spatial resolution. For this reason, further considerations concerning temperature gradient were required. As previously stated, the temperature gradient is expected to be relatively small (see Appendix A. “Thermal conductivity” on page 207). An approximation was followed by combining equations 33 and 34 and assuming a maximum concentration difference of ΔX = 10mol l^{-1} (approximately a concentration difference of 50wt% to 30wt%) over the full film thickness (L):

$$\frac{\Delta\theta}{\Delta L} = \frac{D}{\lambda}\Delta H \frac{\Delta X}{\Delta L} \rightarrow \Delta\theta \approx \frac{2 \cdot 10^{-11}\frac{m^2}{s}\ 5 \cdot 10^4 \frac{J}{mol}}{0.65\frac{J}{(s \cdot K \cdot m)}} 10^4 \frac{mol}{m^3} = 0.015K$$

In consideration of the resulting very small temperature difference, it was concluded that temperature gradient could be negligible, and it was correct to focus on the concentration gradient, or mass transport. Since practically all the material parameters, ΔH, λ, D, σ_d, and σ_a are depended on concentration and temperature and are only partially known, it was recognised that modelling would be associated with a rather large uncertainty value. Consequently, justifying the pragmatic approach towards practical measurement. If a strong concentration gradient in the liquid phase is measured, this gradient is rate limiting, implying that the gas–liquid interface (Equation 32 on page 115) is less relevant. In this case, the empirically determined diffusion coefficients should match the corresponding literature values, providing further verification of the measurement accuracy, as previously followed in chapter 5. “Study of absorption at bulk scale” on page 64. On the other hand, if practically no gradient is detected, the bottleneck is allocated at the gas-liquid interphase.

Understanding allocation of major resistance was considered to be an important step towards finding measures to overcome these restrictions and to be able to improve overall performance of the heat and mass exchanger. Therefore it was considered that if the interface resistance was dominant, surface break-up would be required. This could be solved with surfactants, as suggested by McKenna and McGillis (2004) or light weight magnetic particles driven by external magnetic field, as suggested by Lee (1994). On the other hand if the resistance is found in the film, droplet formation and impingement could be a means of enforcing mixing and breaking up the film gradient, thus accelerating mass transport.

8.2. Raman spectroscopy

The spatial and temporal probing of the concentration gradient of a thin aqueous sodium hydroxide film of approximately 200µm required a method compatible with the corrosive environment able to distinguish material composition at the required spatial and temporal resolution. Since water, aqueous sodium hydroxide and glass, serving as an atmospheric barrier (see chapter 2.2.2. “Closed process” on page 32), are transparent to visible light, Raman spectroscopy was considered to be a good proposition. Raman spectroscopy is commonly used to provide structural fingerprints by which molecules can be identified. For liquids and gases, the corresponding peak intensities (Raman traces) are related to the number of scattering molecules (Li et al. 2017). Raman spectroscopy has been employed for the investigation of microscopic phenomena such as diffusion (Borgschulte eta al. 2010, Borgschulte et al. 2016, Kurt et al. 2000). In this work, the setup and method was adapted to obtain time-resolved measurements of sodium hydroxide concentrations in water, at varying film depths in the process of absorption and desorption, with a time resolution of minutes and a practical spatial resolution of several ten micro-metres using a Bruker Raman SENTERRA Spectrometer (532nm) with a self-built Raman absorption analysis cell as illustrated in figure 36 on page 123 and shown in figure 38 on page 124.

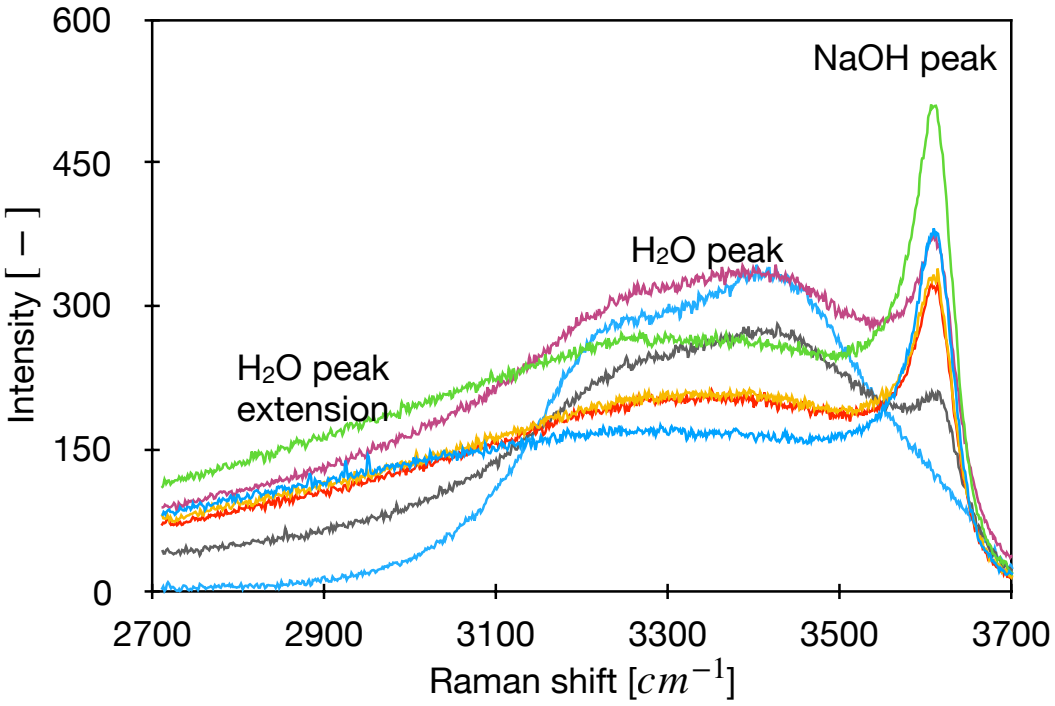

Figure 33: Raman spectra of aqueous sodium hydroxide solutions at various sodium hydroxide concentrations.

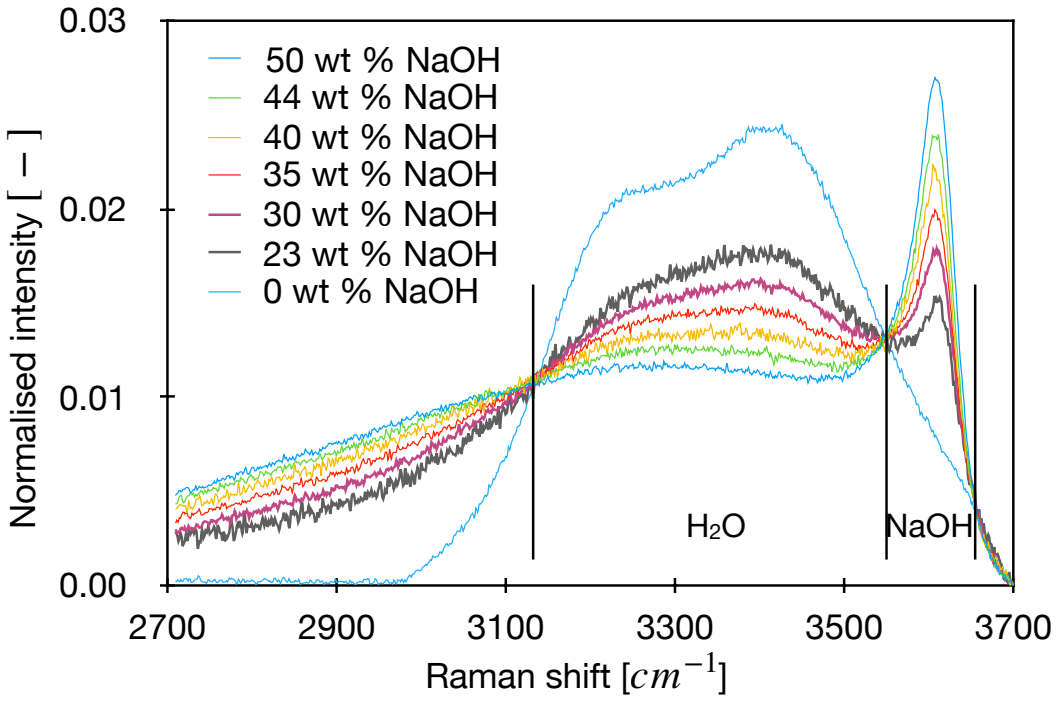

Figure 34: Total-intensity normalised Raman spectra of aqueous sodium hydroxide solutions at various sodium hydroxide concentrations; the lines indicate the isosbestic points which define the integration boundaries for quantification.

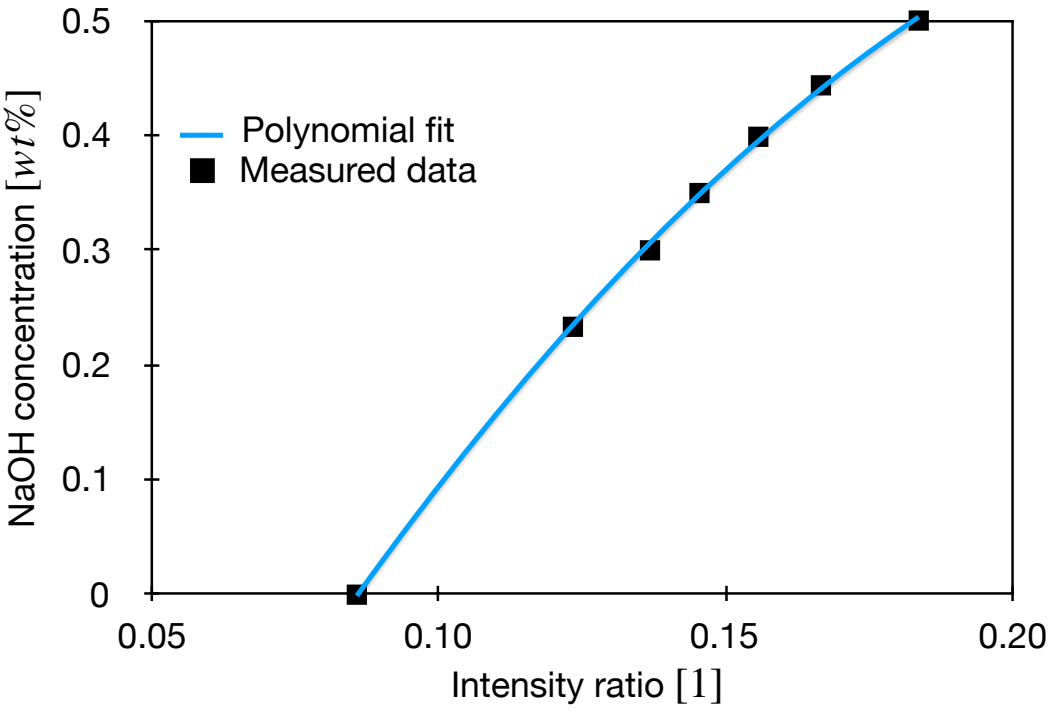

Figure 35: Calibration curve to determine the spatially resolved sodium hydroxide concentration used throughout the analysis, derived from the intensity ratio of the two integration areas indicated in figure 33.

The molecular vibrations used in the aqueous sodium hydroxide concentration probing were OH-stretching vibrations. These occur both in water (H_2O) and sodium hydroxide (NaOH) around Raman shift number 3600cm^{-1} (see figure 33 and 34). In the measurement the slight variation in Raman shift from the solvated OH- ion to the OH in water is made use of. Walrafen and Douglas (2006) note that the local environments of the OH- ions and water molecules depend on the overall concentration. With increasing concentrations, the free water molecules decrease in number until the liquid solidifies (see appendix A. “Solubility” on page 202). The Raman spectra reflects the correlation of the water molecules. The water OH peak broadens and shifts with increase in sodium hydroxide concentration and a peak with centre at wavenumber 3550 develops (Walrafen and Douglas 2006, Shaffer 1997). By normalising the spectra, isosbestic points were defined. These are points where the normalised intensity does not change across various concentrations (see figure 34). This served as border values for the area integration of the water peak and the sodium hydroxide peak, thus solving the difficulty

encountered due to the strongly overlapping peaks, as proposed by Shaffer et al. (1997). Still, the non-linear behaviour is obvious, shown in the calibration curve. This originates from the dynamics of water in aqueous sodium hydroxide. The correlation between the given concentration and the normalised intensity ratios derived from the areas served as the calibration shown in figure 35.

8.3. Experimental setup

To be able to measure the water exchange of the liquid sorbent film under realistic operation conditions, as present in the spiral finned heat and mass exchanger, an optical cell was designed, in which the absorption and desorption into a liquid film of aqueous sodium hydroxide in a water vapour atmosphere at adjustable vapour pressure and absorbent temperatures was operable. The setup diverted from the true operation in that the film was immobile. This was important, in order to prevent turbulences in the liquid, thus measuring solely mass diffusion in the film. Further atypical to the heat and mass exchanger was the rapidly (stepwise) temperature change followed. Again, this was necessary to measure concentration gradient and mass diffusion under strictly defined temperature conditions. Slow temperature change would reduce the rate of absorption and the concentration gradient. Consequently, the absorption and desorption processes in the technical heat and mass exchanger was expected to be slower. The assumption of quiescent film was justified since the viscosity of the aqueous sodium hydroxide solution was high (see appendix A. “Viscosity” on page 199), and the film height was low. Boiling was prevented by keeping a low film height, thus enabling rapid temperature shift also in desorption. This differs to the bulk scale process, where due to the increase film height rapid temperature change in desorption was not possible. The sorbent film temperature was considered constant, this assumption was justified due to the higher thermal conductivity of aqueous sodium hydroxide, see appendix A. “Thermal conductivity” on page 207 and the calculation shown in the previous subchapter.

The test cell consisted of a stainless-steel body with a centre-drilled compartment and a 60mm by 2mm round Suprasil® glass covering window sealed with a rubber o-ring, as illustrated in figure 36. A Peltier element for heating and cooling was placed inside the chamber with a stainless-steel plate as the sample holder. The setup was connected to a water vapour source and vacuum pump for pressure regulation. By moving the xyz-table towards the Raman microscope objective, the Raman focal point was moved into / out of the solution (z-scan). Figure 37 illustrates this process, and in figure 38 a picture of the setup is given.

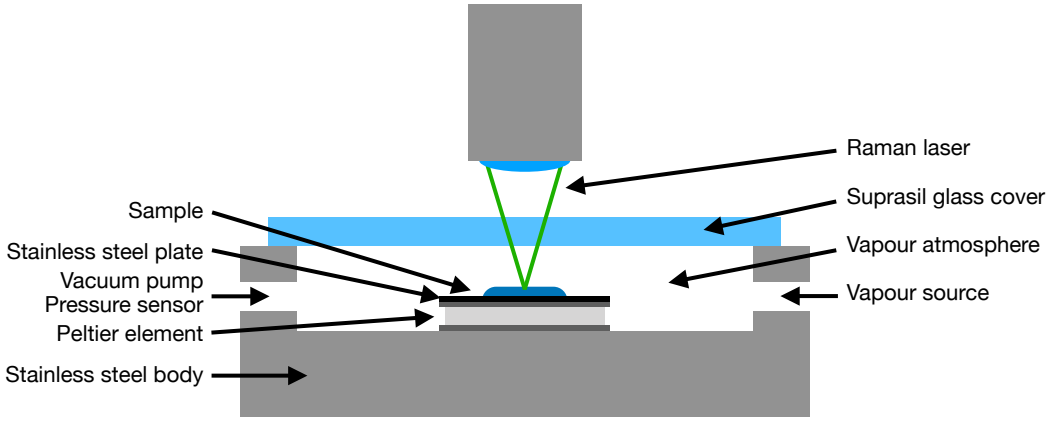

Figure 36: Illustration of the test cell with the Peltier cooler and heater, stainless-steel plate and sample.

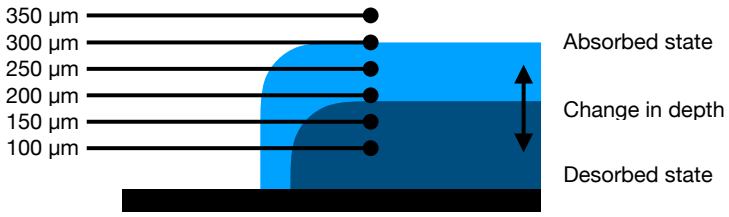

Figure 37: Illustration of the Raman height profiling upon moving the focal point into or out of the aqueous sodium hydroxide film.

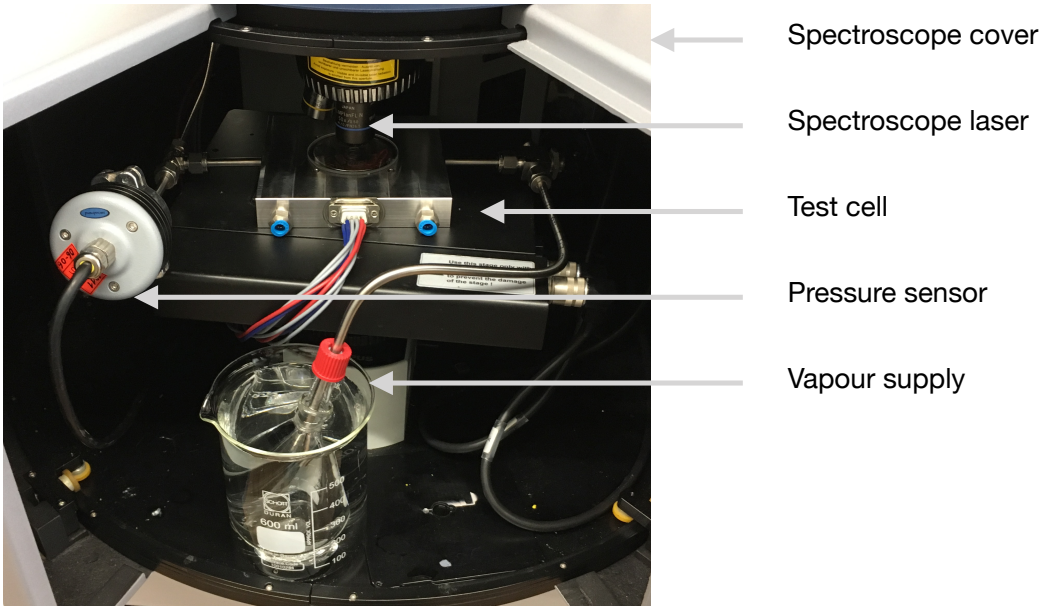

Figure 38: Picture of the test setup installed in the Raman spectroscope.

In preparation for measurement, an aqueous sodium hydroxide droplet was placed on the sample holder situated on top of the Peltier element and slightly smudged to create a thin film. Smudging was required due to the high viscosity and surface tension. After covering the chamber with the glass lid, all non-condensing gases were removed by applying a vacuum. Time was then given for the sorbent droplet to reach the thermodynamic equilibrium based on vapour pressure and absorption temperature. These conditions were set by the Peltier element and the water vapour pressure given by the evaporator temperature. The major challenge faced in the measurement was the allocation of the gas-liquid interface, and the fact that the position of this interface changed during absorption and desorption, thus resulting in a moving target. The movement of the interface was due to the uptake and release of water, as illustrated in figure 37 and noted in literature by Wang et al. (2019). In order to overcome this issue, continuous Raman measurements were performed at a defined distance from the focal point to the bottom of the film (top of the stainless-steel disc) rather than the distance from the interface surface. The measuring point was kept constant through a full cycle, incorporating a temperature change from high to low (absorption) and low to high (desorption). One measurement succession,

consisting of a complete absorption and desorption cycle involved 49 Raman spectral measurements at a single z-axis position with a complete duration of 12 minutes. Thus, the time resolution was approximately ΔT = 15s. A measurement sequence, in turn, consisted of six successions with ΔL = 50µm as illustrated in figure 37 on page 123. The z-position with respect to the gas–liquid interface was then evaluated retrospectively from the measured data. This was possible since the Raman signal markedly changed when the focal point moved out of or into the liquid. Table 8 shows the measurement parameters of 12 measurement sequences performed under varying conditions with the same aqueous sodium hydroxide droplet.

Table 8: Measurement parameters.

Measurement sequence	θ_{ab} [°C]	θ_{de} [°C]	θ_{vap} [°C]	p_{vap} [mbar]	L_{min} [µm]	L_{max} [µm]	L_{avg} [µm]
1	25	45	0	6.5	225	375	300
2	25	45	0	6.5	200	300	250
3	30	50	5	8.7	175	275	225
4	30	50	5	8.7	175	250	213
5	35	55	10	12.2	150	250	200
6	35	55	10	12.2	150	250	200
7	45	65	20	23.3	150	225	188
8	45	65	20	23.3	150	225	188
9	45	65	20	23.3	125	200	163
10	35	55	10	12.2	125	200	163
11	30	50	5	8.7	100	175	138
12	25	45	0	6.5	100	175	138

8.4. Results and discussion

In the measurement campaign, a series of Raman spectral profiles were measured, time resolved in absorption and desorption at a fixed position. The two three dimensional diagrams in figure 39 on page 127 show examples of such sequences. Figure 39a shows a sequence where the measuring point was continuously in the absorbent and figure 39b shows a testing sequence with entrance and drop out of the solution. From these measurements, a series of diagrams on the time-resolved concentration changes during absorption and desorption at varying focal points of the sorbent solu-

tion droplet were derived. Figure 40 on page 128 shows the example of Measurement sequence 4 with the individual curves measured at a defined distance from the film bottom. The blue line, showing concentrations at 100µm above the stainless-steel sample holder was regarded as the concentration at the film bottom. The determination of the concentration at the gas–liquid interface (surface concentration) was derived by considering the intensity of the Raman scattered light, as indicated in figure 39b. The intensities of the measurements near the film bottom did not substantially change, see figure 39a but those at 200µm and above did, as shown in figure 39b. At Measurement 13 the intensities of the measurement series at 200µm (yellow line) increased as the focal point dipped into the solution due to film height increase from water uptake. Two measurements or 30s later the same situation occurred for the measurement series at 250µm (red line) and finally at 300µm (purple line). From these measuring sequences, the concentration at the gas–liquid interface could then be reconstructed based on the entry points. This is shown with the grey line in figure 40. Through this analysis, the concentration changes based on time $\partial X/\partial T$ and the concentration gradient in the film $\partial X/\partial L$, indicated at measuring point 13 were derived.

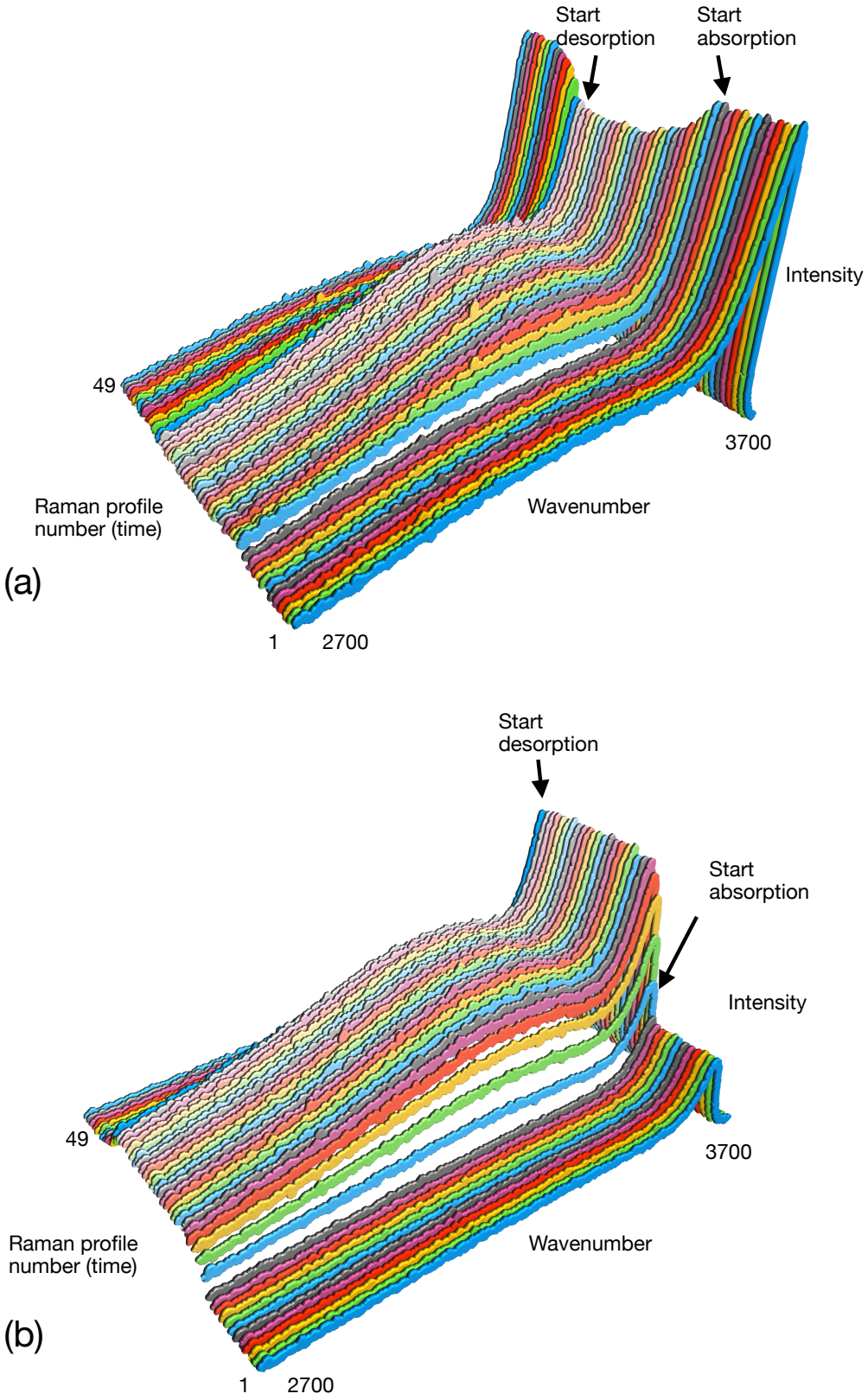

Figure 39: (a) Example of the Raman spectral profiles with constant submersion in the absorbent. (b) Example of the Raman spectral profiles with submersion and drop out of the absorbent.

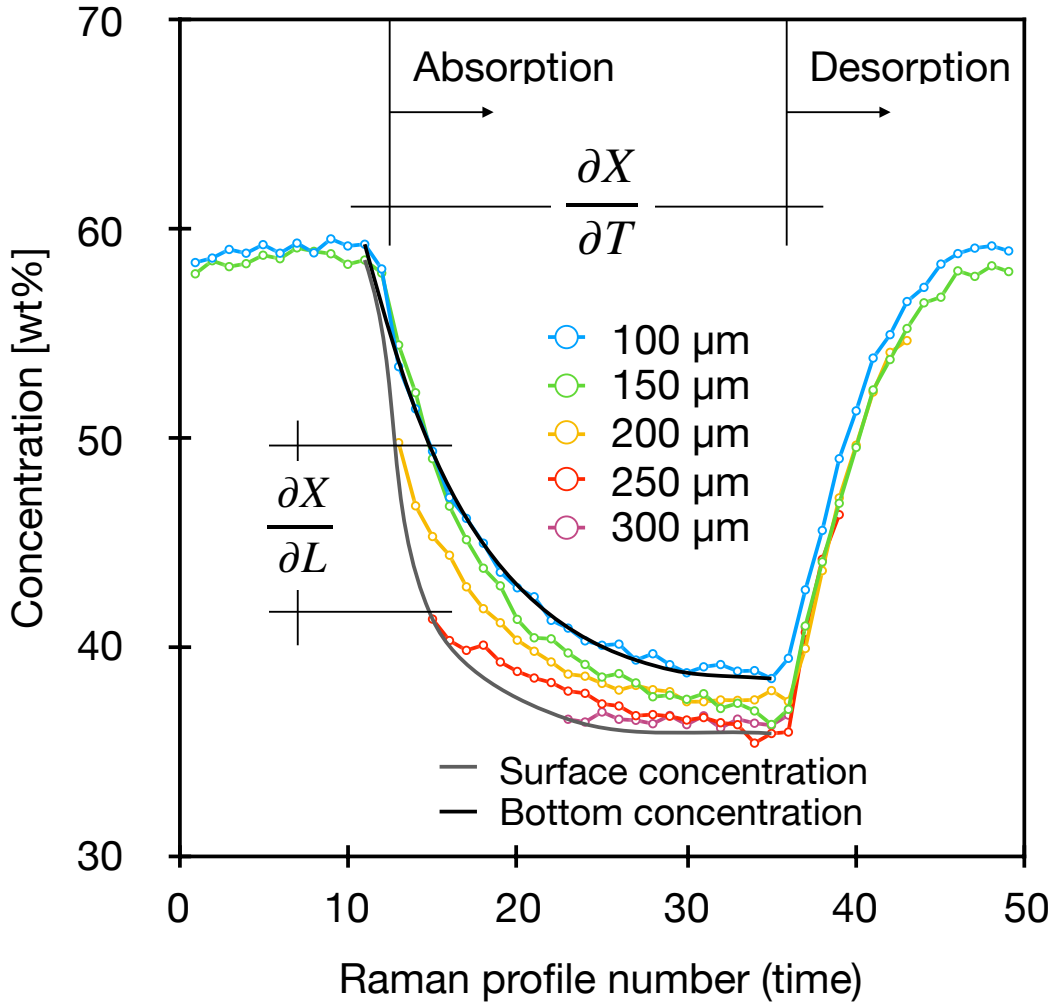

Figure 40: Resulting concentration change or a thin film measured operando during water absorption and desorption at a temperature of 35°C and 55°C, respectively, and a constant vapour pressure of 8.7mbar (measurement sequence 4 in Table 8 on page 125).

The aim of this study was to determine whether the uptake of water vapour on aqueous sodium hydroxide is controlled by surface phenomena or by mass diffusion in the film. It was argued that if a concentration gradient was detected, this would show that diffusion was the dominant resistance.

From the measurement results it was shown that a concentration gradient is established and that with time, this degrades to a lower concentration equilibrium in absorption and to a respective higher concentration steady state in desorption. Thus, it was seen that mass diffusion in the film was the dominant resistance under the measured conditions. The exponen-

tial time dependent concentration decline in absorption, and concentration increase in desorption, were further strong indications in support of a diffusion controlled process. An extended evaluation was followed by comparing the quantitative diffusion parameters from the measurements under the various thermodynamic conditions, as shown in table 8, to the theoretical values. The diffusion coefficient values based on the measurements were calculated according to equation 22 on page 69 and repeated below, by determining the time of the half-uptake τ as followed in chapter 5 “Study of absorption at bulk scale” on page 64:

$$D = 0.049 \times \frac{L^2}{\tau}, \textit{ Equation 22}$$

where *L* is the average film height shown in Table 8 on page 125.

The concentration curve at the 100µm focal point was considered as the mean value. Figure 41, shows an illustration of the evaluation. The average diffusion coefficients obtained from the four varying vapour pressure settings are shown in figure 42 on page 131 in comparison to the calculated values based on the dynamic viscosity of aqueous sodium hydroxide, (appendix A. “Viscosity” on page 199), according to equation 30 on page 76 and repeated below:

$$D = \frac{k_B \Theta}{b \pi \eta r}, \textit{ Equation 30}$$

The reference and measured values were found to be closely fitting, and the slight deviation was taken to be due to measurement uncertainties. The diffusion coefficient values in absorption were consistently slightly higher than the reference values and those in desorption were lower. This may point to a slightly more favourable process in absorption to desorption. This proposition was nevertheless not further examined at this time.

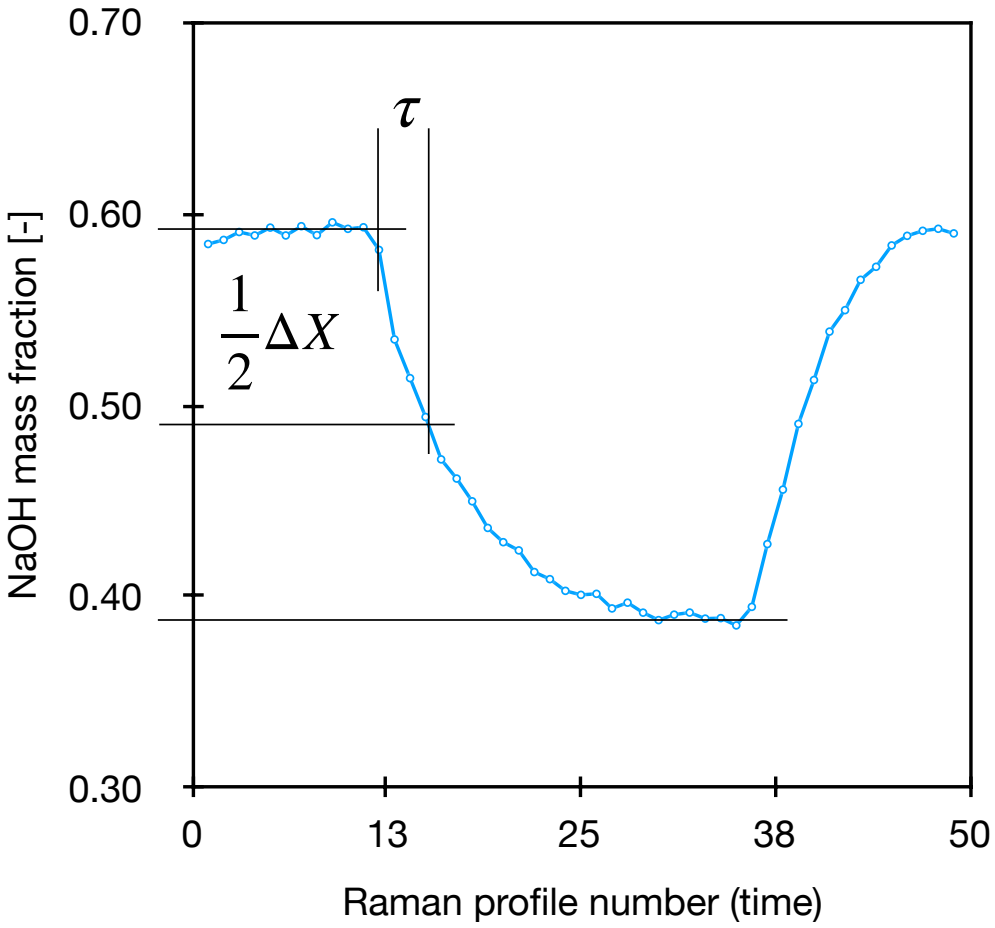

Figure 41: Illustration of the evaluation of τ based on the concentration curve at 100µm.

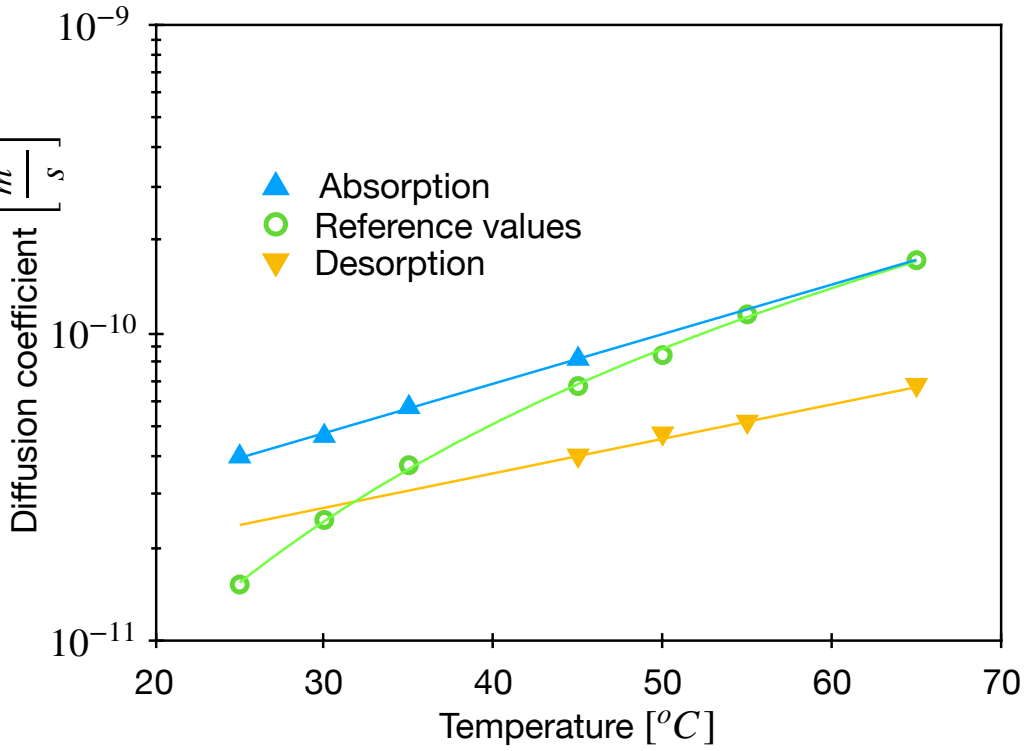

Figure 42: The diffusion coefficient of water in aqueous sodium hydroxide at various temperatures.

An area of uncertainty at the commencement of this research was the coherency of findings from literature to the thin film applied in the spiral finned heat and mass exchanger. This is basically a matter of definition of the gas-liquid interface and the bulk material. In phase transitions of pure substances, such as the evaporation of water where no substance redistribution in the bulk through mass transport takes place, the interface between the gas and liquid alone remains and is thus clearly the mass transfer rate limiting parameter (Gatapova et al. 2017). On the other hand, in deep pools of sorbents, the mass transfer rate may well be the restricting parameter. Now, when proceeding towards a thin film, surface layer and bulk begin to merge. For this reason, no obvious conclusions could be drawn.

A model commonly adopted to describe the physical absorption of a gas into a liquid is the laminar film model given by Whitman et al. (1923) . As discussed by Danckwerts et al. (1954), this model assumes a laminar gas–liquid interface layer as the predominant constriction to mass transfer from the gas into the liquid phase, even under bulk turbulence. Tsai and Perez-

Blanco (1998) relied on similar assumptions, that the surface layer close to the phase boundary determines the mass transfer rate, and a consequent surface-to-bulk mixing is required to increase the transfer rates beyond those achieved by molecular diffusion.

Models for mass transfer from the gas phase to liquid phase, such as the stagnant film model (Whitman 1923), the penetration model (Higbie 1935) and the film-penetration model (Toor 1958), all assume the presence of a well-mixed liquid bulk. In our thin-film application, the issue concerning the absence of a constant concentration and temperature bulk is that the effective driving force for a mass transfer is reduced due to the reduction of the sorbent concentration in the solution contacting the solid interface. This decreases the mass transfer flux and thus also reduces the average flux, as seen in figure 40 on page 128, also shown in the bulk scale absorption analysis (figure 18 on page 77). Therefore, applications of these constant bulk-based models may lead to substantially overly optimistic values for the mass transfer flux found in technical heat and mass exchangers, especially in heat storage application, where operation close to equilibrium is key. For these reasons, a closer investigation of the mass transfer across the thin sorbent film was required.

In the past, many practical studies on water absorption in liquid salt solutions associated with large heat gain, as is the case here, have been carried out (Chiang et al. 1964, Grigoryeva and Nakoryakov 1977, Grossman 1983, Brauner et al. 1989, Andberg and Vliet 1987, Yüksel and Schlündler 1987, Kauai et al. 1989, van der Weaken and Wassenaar 1988, Brauner 1991, Ibrahim and Vinnicombe 1993). These relied on measuring absorption into absorbent pools at a constant concentration and temperature using setups such as stirred cell reactors and pool absorbers or otherwise, absorption in wetted-wall columns and disk columns with turbulence, thus making the evaluation of the individual transport barriers or spatial-resolved measurements unattainable.

With this novel approach to in-situ probing the reversible water absorption in thin aqueous sodium hydroxide films using Raman spectroscopy, it

was clearly shown that the rate-limiting step in this process is the mass diffusion from the gas–liquid interface to the film body. This is the first time that the transient concentration gradients of a thin film absorption process with high temporal and spatial resolutions in application relevant conditions have been measured.

The spatial resolution of several 10µm and temporal resolution of 15s were attributed to the Raman apparatus employed. With this limited resolution, which may be improved using advanced Raman microscopes, and related optical methods such as sum frequency generation (Tarbuck et al. 2006) and high-pressure photoemission (Lam et al. 2017), the existence of a rate-limiting gas–liquid interface barrier could not be ruled out. However, under the respective application specific, realistic testing conditions, including film height, it was possible to show that the major mass transport resistance was due to mass transport in the film bulk.

The influence of the gas–liquid interface barrier is expected to increase with mixing in the bulk of the film as the hindrance by diffusion is reduced. However, due to the high viscosity of the sorbent, great effort will be required for strong mixing of the thin film, as described by the surface renewal model (Danckwerts 1951). Thus, in a practical application, it is expected that diffusion will continue to be the main resistance to kinetics but possibly with a reduced diffusing distance.

In the heat and mass exchanger process, there are two concentration gradient scales to be observed: across the film thickness $\partial X/\partial L$ and along the heat and mass exchanger height (time) $\partial X/\partial T$. The first may be countered by turbulence, as discussed, reducing the concentration gradient in the film to a mean level, thus substantially reducing the mass transport resistance, and emphasising restrictions from the gas-liquid interface barrier. Nevertheless, the concentration gradient in the film diminishes as the mean concentration reduces because of the reduced driving force, as shown in figure 40 on page 128. Thus, the positive effect of film mixing also declines. On the other hand, the mean concentration gradient along the spiral finned tube and the consequent reduction of the driving force for the mass transfer

are principal consequences of the storage application that cannot be resolved. It must thus be recognised that there are fundamental restrictions to the augmentation of power in heat and mass exchangers for absorption heat storage.

Comparing the investigated diffusion coefficient in figure 42 on page 131 to the performance results presented in chapter 7. “Heat and mass exchanger test bench” on page 88, the respective diffusion coefficient of the heat and mass exchanger was calculated based on the power, active area, concentration gradient and film thickness, as per equation 26 on page 70 and equation 31 on page 114. Interestingly, this resulted in an average diffusion coefficient of $7.5 \times 10^{-9} m^2\ s^{-1}$. This was a good order of magnitude, greater than the values measured in the still setup, and suggested that even though a slowly creeping film flow was visually detected, slight bulk turbulence, or other movement must have been involved. This behaviour was further investigated by neutron imaging and reported in the following chapter.

9. Investigation of absorbent mixing

While solid sorbents generally suffer from low thermal conductivity due to the high porosity of the sorbing material, liquid sorbents face the challenge of much lower absorbing surface area and slow mass transport into the liquid. Since liquid sorption for heat storage is performed under absorbate atmosphere, as noted in chapter 4. “Aqueous sodium hydroxide” on page 55 gas phase resistance is largely omitted. Sorbate mass flux to and from the absorbent is based on the absorbate vapour pressure on the absorbent solution, in turn affected by the rate of absorbate mass diffusion into and out-of the absorbent. Once the gas and liquid are in pressure equilibrium at the surface, the resulting concentration gradient to the bulk material controls the rate of absorption by mass diffusion (Danckwerts 1965) and as shown in chapter 8. “Study of mass transport” on page 112, to be the case even for thin films . In order to accelerate absorption rate, mass transport in the absorbent is frequently enhanced by turbulence (mixing) (Perry 2007). In this approach, at best, concentration gradient through mass transport resistance is broken and the respective mean concentration is reached on the liquid / vapour contact surface, increasing rate of absorbate uptake and thus rate of absorption. The increase in mass transport may be achieved by active or passive means. An example of active turbulence is stirring of a pool (Jiru and Eimer 2013, Vaidya and Kenig 2007) and mixing by droplet impingement is an example of a passive process (Behfar et al. 2014). Conventionally, in absorption chilling machines, passive measures are met by high flow rate, consequent turbulent flow and droplet impingement in a tube bundle falling film heat and mass exchanger design. Thus, increase in mass transport in liquid sorption processes is reached by high flow rates and strong turbulence of concentrated absorbent in the tube bundle heat and mass exchanger, readily enabling mixing (Behfar et al. 2014). This is well fitting for chiller or heat pump application, where absorbent solution concentration gradient on the absorber is a parameter largely irrelevant. Nevertheless, this is quite in the contrary in absorption heat storage. As noted in chapter 3. “Liquid absorption heat storage” on page 49, it is recognised that

threefold fundamental parameters govern performance: gross temperature lift, volume specific power, and volumetric energy density. It is now of interest to find a means for mixing while keeping the required high concentration gradient along the spiral finned tube heat and mass exchanger. In this study, a visual analysis of the absorption process under enhanced mixing through droplet impingement is performed. To this purpose, neutron imaging is employed making it possible to detect water content in the absorbent based on the image grey scale. A similar study of water accumulation on zeolite beads has been reported in (Borgschulte et al. 2016).

In the analysis it is seen that the effect of droplet impingement depends strongly on the film height. At low film height there is a pushing movement of the diluted absorbent film to the sides as the droplet distributes on the impinging surface. At greater film height the droplet is absorbed into the film without spreading. Under all conditions clear mixing of the absorbent at various concentrations could not be confirmed. Further examination of droplet impingement into a suspended droplet, adhering to a wire mesh, was also performed. In this case initial mixing was rapidly succeeded by a strong separation of diluted absorbent from concentrated absorbent. It was recognised that buoyancy forces (natural convection) are the grounds for this behaviour and that by effective utilisation of this convective response, improved absorption kinetics could be achieved on the spiral finned heat and mass exchanger.

9.1. Neutron imaging process

Neutron imaging is an area of study followed ever since the availability of neutron sources in about 1938 (Peter 1946). To date, world-wide there are 15 state of the art installations, commonly situated at research reactors (Peter 1946, Trite et al. 2015). It follows that the application of neutron imaging is at present strongly limited. In this study the SINQ facility of the Paul Scherrer Institute (PSI), with the ICON beam line was employed.

In the field of non-destructive materials and component investigation the neutron is a distinctive probe due to its weak interaction to many com-

mon materials attributed to its neutral charge (Banhart 2008, Dobrzynski et al. 1994, Foderaro 1971, Sköld 1986). Strong interaction is found with only a small number of chemical elements, of which hydrogen is the most prominent, providing high sensitivity to water (Lehmann et al. 2004). Temporal and spatial resolution of the images is highly dependent on the beam flux and in general one is optimised on the expense of the other. With the implementation of improved digital detectors, both spatial (Kardjilov et al. 2011, Frei et al. 2009, Lehmann et al. 2007, Tremsin et al. 2009a) and temporal (Tremsin et al. 2009b, Schillinger et al. 2005) resolution has been increased and vast possibilities of digital image processing have been introduced. To date, maximum resolution is in the order of 5μm (Peter 1946), commonly applied resolution is in the range of 20μm to 100μm enabling generally appropriate exposure times. In this study, frames were taken at 0.01s, 0.1s and 1s rates and exposure times. In the data analysis it was found that noise to signal ratio was high at the 0.01s exposure time, for this reason, these frames were averaged at 10 original frames to one average frame, equalling to the 0.1s frame rate. The image resolution was 44μm.

Neutrons are strongly reflected by the hydrogen in both the sodium hydroxide (NaOH) and the water (H_2O) and to a substantially lower degree by sodium (Na) and oxygen (O). In order to improve contrast of absorbent solution to absorbed absorbate, the experiment was followed through with isotopically-enriched absorbent solution, thus a mixture of heavy sodium hydroxide (NaOD) in heavy water (D_2O) rather than NaOH in H_2O is used, while the absorbate vapour was kept as conventional water (H_2O). The change from hydrogen to deuterium brought about a doubling of its standard atomic weight of 1.008 to 2.014. Nevertheless, in respect to the molar mass of NaOH, this was a minor increase from 40g mol^{-1} to 41g mol^{-1} and for water an increase from 18g mol^{-1} to 20g mol^{-1}. It followed that heavy sodium hydroxide at 40wt%, as used in the analysis, has a density of 1.46g ml^{-1} while conventional sodium hydroxide has 1.43g ml^{-1} at the equivalent concentration and 1.53g ml^{-1} at 50wt% as generally employed.

9.2. Experimental Setup

In this study, visual observation of the absorption process of water vapour on aqueous sodium hydroxide was performed under heat storage application specific conditions of absorbent in absorbate atmosphere. Two varying basic testing procedures were followed: droplet impingement of absorbent solution onto an absorbent film resting on a solid plate, comparable to droplet impingement on the spiral fin, and droplet impingement into an absorbent solution droplet suspended by adhering to a wire mesh. The examination was performed under realistic conditions in respect to absorbent exposure to pure absorbate atmosphere. Deviation from the spiral finned tube heat and mass exchanger as followed in the underlying research described in chapter 6. “Heat and mass exchanger design” on page 79 was found in the quiescent absorbent pool, the absence of heat release and the change to isotopically-enriched absorbent solution for contrast purpose. In order to further improve contrast through high absorption rate, investigation was performed at 23.3mbar water vapour pressure (20°C evaporating temperature). This was higher than for the technical application, where evaporating temperatures of 1°C should be considered, as discussed in chapter 2.4 “Application temperature” on page 39.

A test cell was designed and built out of aluminium, as shown in the picture in figure 44 on page 140. Aluminium was considered to be a good material for the cell body, since it is mostly transparent to neutrons and resists the pressure difference from the low vapour pressure in the cell to the atmospheric pressure. In respect to contact with aqueous sodium hydroxide on the other hand, aluminium is highly unsuitable and immediately starts to oxidise under violent foaming, releasing hydrogen. For this reason, inside the aluminium body, a tray manufactured from polytetrafluoroethylene (PTFE) was placed, as shown in figure 43. Polytetrafluoroethylene is also sufficiently transparent for the neutron beam since its composition $(C_2F_4)_n$ does not contain hydrogen. Nevertheless, it would not have been adequately firm to serve as body material.

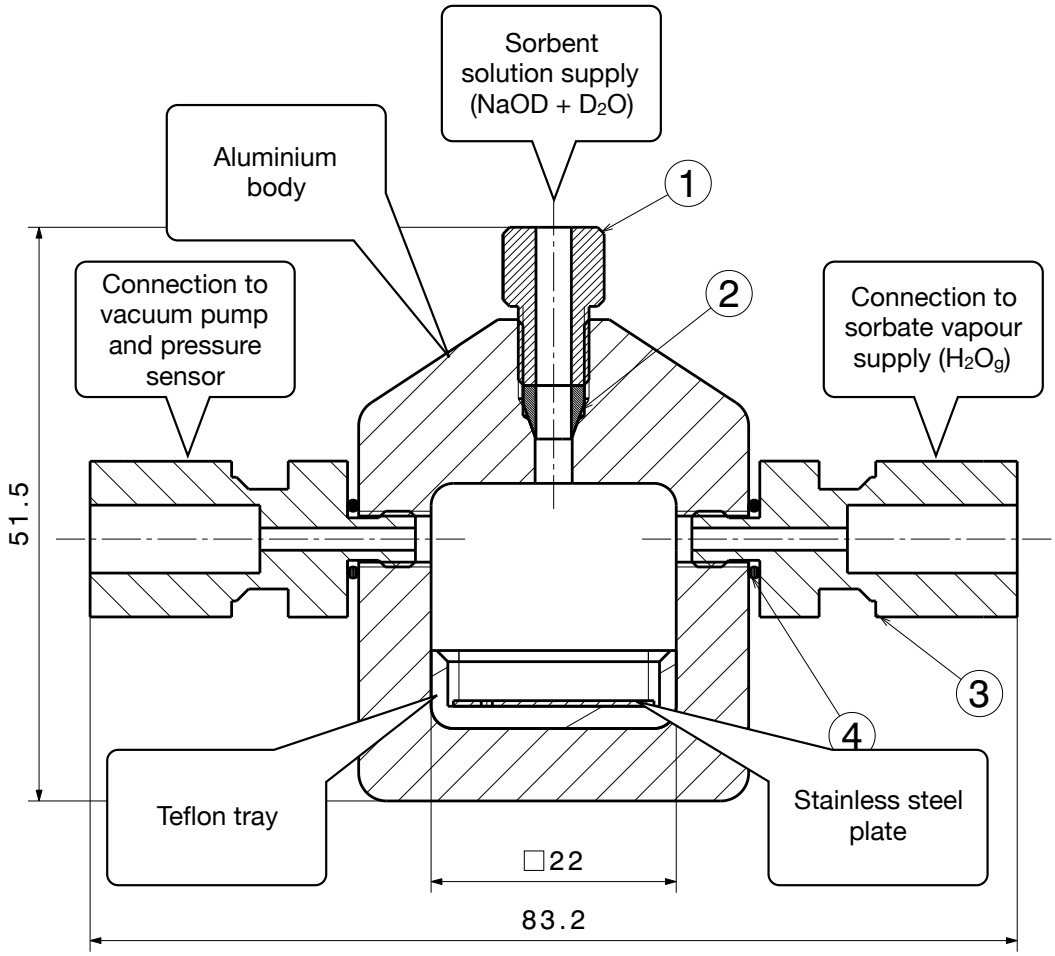

Figure 43: Schematics of the test cell with component indication and dimensions.

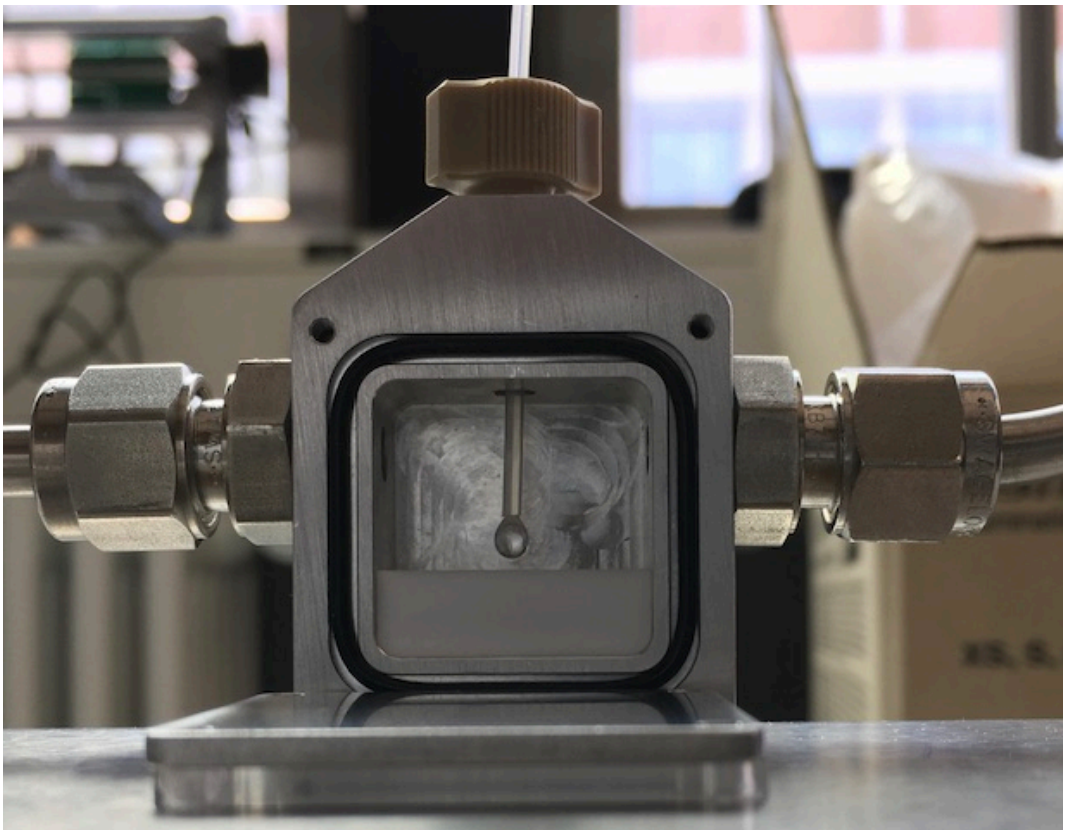

Figure 44: Picture of the uncovered test cell, showing a droplet of absorbent at the end of the supply tube.

A thin PTFE tube was inserted from the top of the cell and positioned above the tray for supply of absorbent solution (NaOD / D_2O) as shown in figure 44. The included side junctions as indicated in figure 43, were connected to the water (H_2O) evaporator, the vacuum pump and pressure sensor. The absorbent supply was regulated by tubing pump. From the neutron beam, a radiographic image was provided, visualising the presence of hydrogen in liquid water (H_2O). Temporal and spatial resolution was not adequate to show water vapour movement in the chamber. For best focal quality very close positioning of the sample to the scintillator screen was followed.

For the droplet impingement tests, a stainless-steel sheet 18mm long, 11mm wide and 0.5mm thickness was placed inside the polytetrafluoroethylene tray for the droplets to fall onto, in order to have realistic conditions in respect to surface wetting. In the process of testing, an absorbent droplet

was formed on the end of the supply tube and impinged onto the lower set stainless-steel inlay which initially contained no absorbent film. It was expected that the absorbent will spread due to impingement and a dark layer of absorbate would form on the film from absorbate uptake. Several droplets in series were impinged, increasing the impinging film height, as droplets accumulated. The layer of absorbate (H_2O) absorbed on the absorbent solution (NaOD / D_2O) was expected to be visible as a dark grey line on the absorbent film. As a succeeding droplet impinged upon the pool, both pool and droplet surface layers were expected to be disturbed and initial mixing as well as formation of a new equilibrium layer on the pool was expected. Trtik et al. (2016) have performed a similar droplet impingement analysis of H_2O impingement in D_2O, not including absorption.

In the droplet suspension tests a strip of stainless-steel wire mesh, bent in the form of an upside-down U, was placed inside the tray instead of the stainless-steel inlay. The absorbent droplets from the supply tube fell onto the sieve and by adhering to the wire mesh, were so suspended in the water vapour atmosphere. A subsequent falling droplet impinged onto the suspended more dilute one and mixing without solid impingement surface was visualised.

9.3. Results

In the droplet impingement analysis, fresh absorbent droplets were impinged on a partly sorbed absorbent film at varying film height. The droplet diameter was 2.8mm on average and approximately 3.5mm above the steel plate. In figure 45 on page 144, a series of exemplary results from the droplet impingement analysis are shown. For every step shown, an illustration is provided on the left, followed by the respective picture in the centre and a contrast enhanced version, emphasising the allocation of diluted and concentrated absorbent, on the right. Due to the contrast enhancement, the intersection between concentrated absorbent in the film and the water vapour is lost, this is visible in the standard picture. The diluted absorbent (NaOD), containing hydrogen from the absorbate (H_2O), is dark (black) and

the fresh absorbent (NaOD in D_2O) not containing any hydrogen is light grey (white). A red line is drawn in the pictures to indicate the top side of the stainless-steel plate. The film height is noted where relevant, after droplet impingement. In pictures *D1* to *D6* the effect of droplet impingement is shown at varying film height with pictures of pre and post droplet release. Time between pre and post droplet impingement is 0.2s. The time between droplet release is approximately 10s. The images were taken with an exposure time of 0.1s.

Droplet *D1* fell directly on the steel plate without an absorbent film and showed rapid distribution with prompt vapour absorption, building a film of height 0.26mm. As the second droplet *D2* impinged, the film of dilute absorbent was pushed to the side forming a pool of concentrated absorbent inside a ring of dilute absorbent. From the formed pattern it appeared that there was little mixing of the diluted and concentrated absorbent. It gives the impression that the droplet broke through the existing film, spread due to impact on the steel and washed the diluted absorbent to the side. The third droplet *D3* confirmed this tendency, by further pushing diluted absorbent from the centre outwards. As the film height increased in *D4* onward, a further pattern began to develop. As fresh absorbent droplets fell through the absorbent film surface and spread due to impact on the stainless-steel, concentrated absorbent moved underneath the diluted absorbent. As the film height increased and the ratio of film height to droplet diameter reduced, the sideways movement of dilute absorbent decreased and the process of impingement and spreading developed more towards a process of braking through the surface allocated semi dilute absorbent, and depositing of the fresh absorbent underneath. Comparing *D4* to *D6*, there is a spreading of the concentrated absorbent underneath the dilute absorbent.

The final sequence of images shown in figure 46 on page 145, does not follow the pre and post droplet pattern as the initial pictures in figure 45 on page 144, but provides a time sequence of images including one droplet impingement. These are images taken directly adherent to the previous droplet sequence. The images were taken at an exposure time of 1s, and

show absorbent film movement and development. The process seen in *D4* to *D6* was further confirmed, concentrated absorbent spread along the sheet metal and diluted absorbent floated above this. From time T = 0s to T = 1s a new pattern developed. By floating over the concentrated absorbent, the dilute absorbent broke loose from the sides, exposing concentrated absorbent directly to the water vapour. At T = 4s the last droplet was added. At this stage no spreading of the absorbent could be recognised, only an increase in film height and thus slight raise of the diluted film above the concentrated absorbent (film height increase from 1.36mm to 1.45mm). From the further images it was seen that interestingly the sideways exposed concentrated absorbent was not covered, but the height of the concentrated absorbent continuously decreased and the diluted absorbent film height respectively increased.

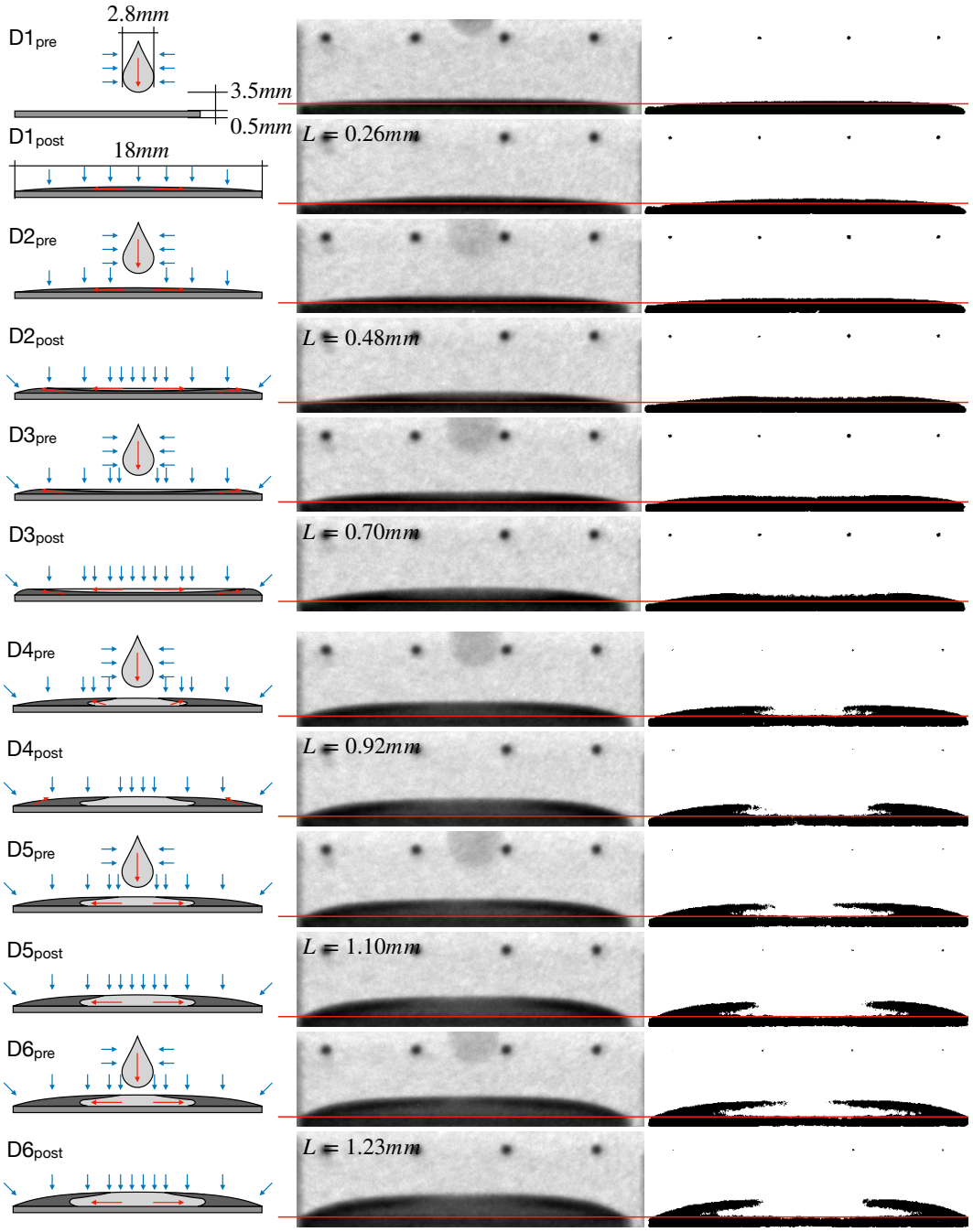

Figure 45: Images of droplet impingement taken at an image exposure time of 0.1s. Each process step consists of a sketch, a regular picture and a contrast enhanced picture emphasising the dilute absorbent (black). The red line indicates separation between stainless-steel plate and absorbent. Dark areas above the red line are regions of diluted absorbent containing absorbed H_2O. "Pre" indicates just before impingement and "post" refers to just after impingement. Time between pre and post was 0.2s. Time between droplets was approximately 10s.

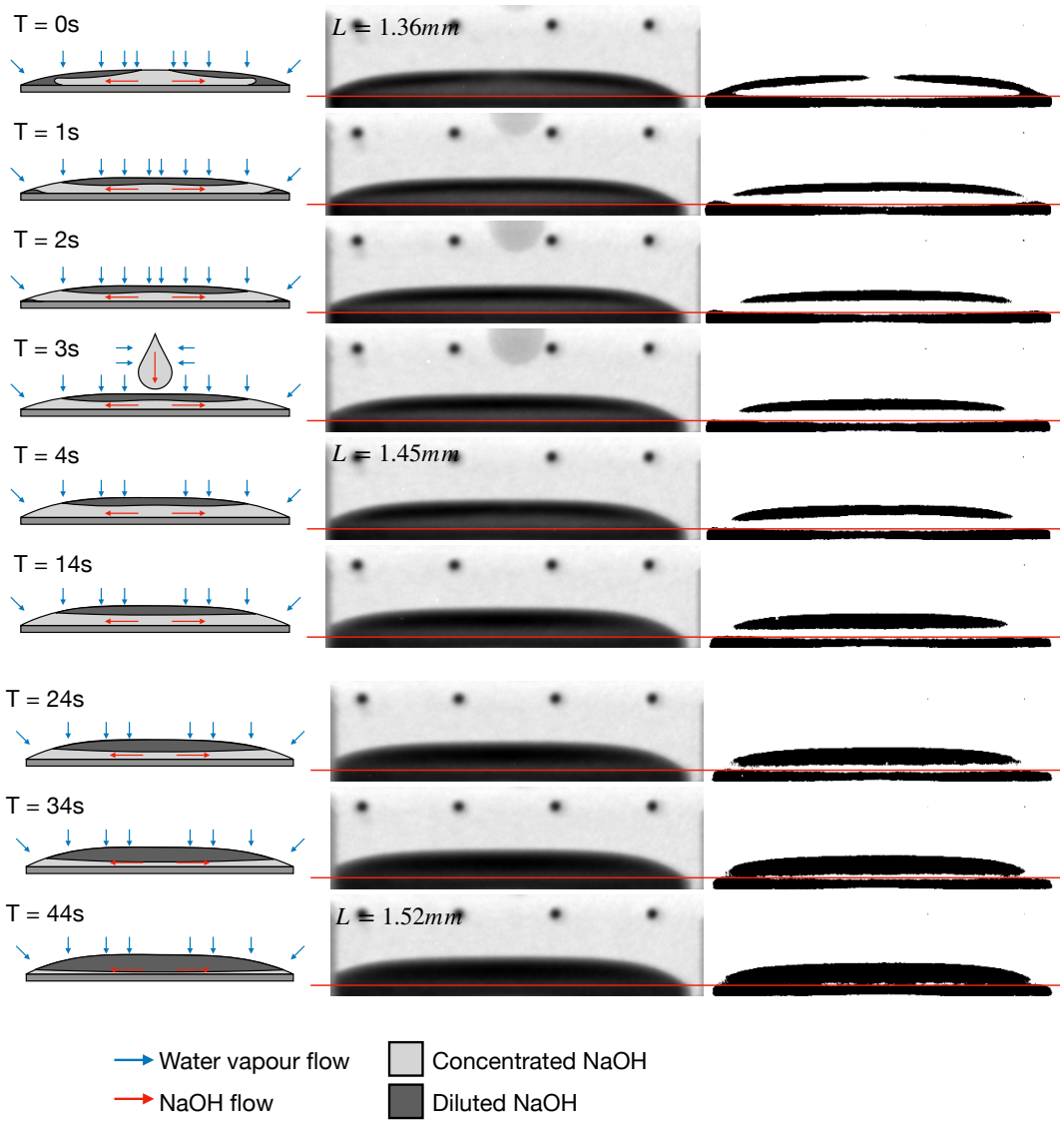

Figure 46: Images of droplet impingement and sorption process taken at an exposure time of 1s. T = x indicates the elapsed time.

In the droplet suspension and impingement inspection, a diluted droplet was suspended from a stainless-steel wire mesh and a fresh absorbent droplet was supplied as with the previous droplet impingement tests, from a tube above the absorbent. Figure 45 exhibits results from this sequence, again with an illustration, regular picture and contrast enhanced image. Images are taken with an exposure time of 0.1s. Picture $T = 0$ shows the initial setting with the dark droplet adhering to the mesh. The fresh droplet before falling could be seen in light grey just above the diluted droplet. At time $T = 0.2$s the fresh droplet had fallen and collided with the metal sieve and the diluted droplet. Interestingly, already just after first impact it could be seen that concentrated, heavy absorbent sunk to the bottom of the droplet. It appears that there was practically no intermixing of dilute and concentrated sorbent. From time $T = 0.4$s on, a separation between diluted and concentrated absorbent developed and already at time $T = 2.4$s, the combined droplets had separated into a concentrated solution on the bottom and a diluted area on the top. Thus, it was shown that rapid strong separating occurred. The droplet suspension has the benefit that the concentrated absorbent is strongly exposed to the absorbate on the lower side of the droplet.

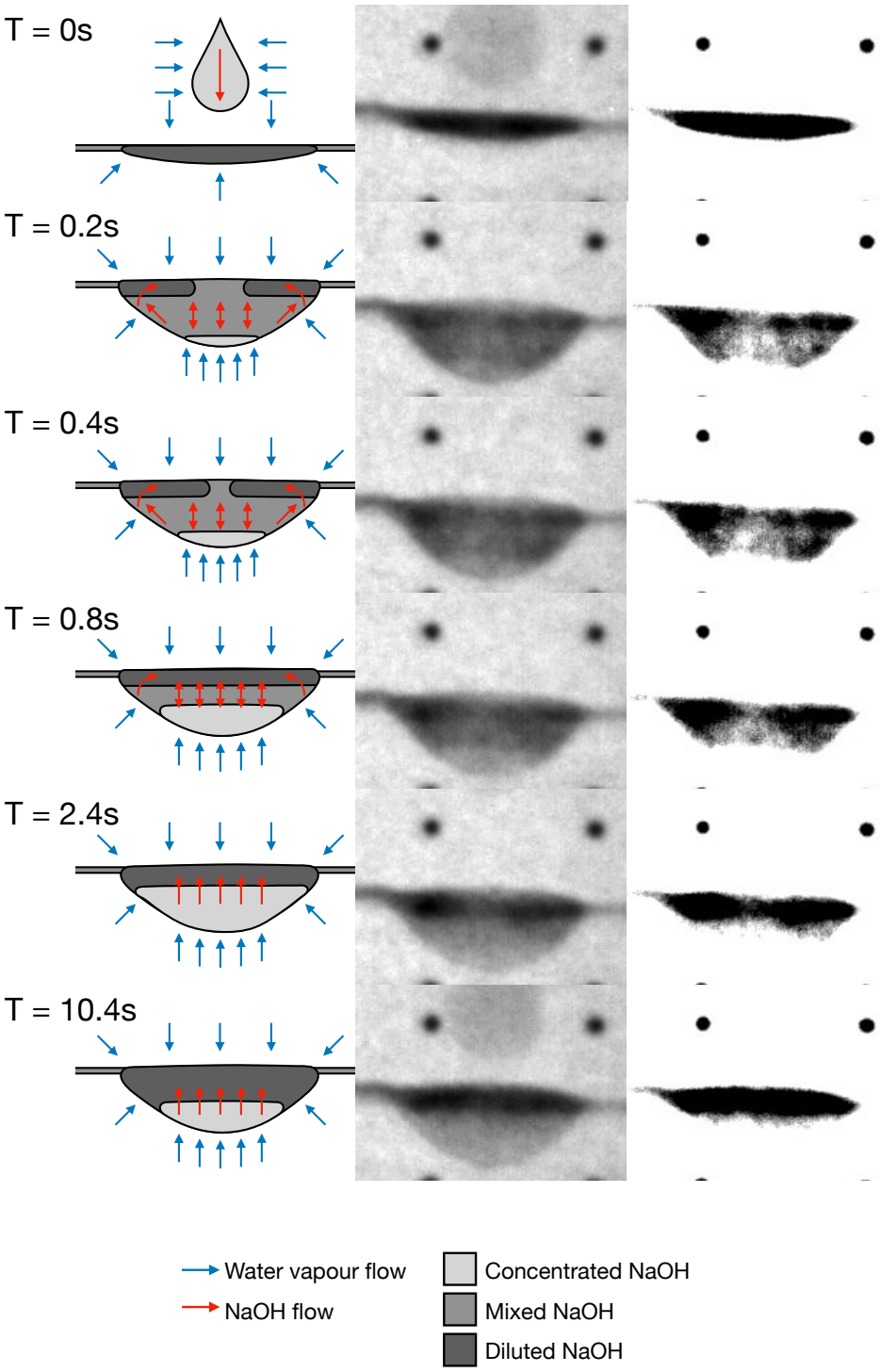

Figure 47: Image sequence of droplet suspension and impingement. Each process step consists of a sketch, a regular picture and a contrast enhanced picture emphasising the dilute absorbent (black). The absorbent is suspended by adhering to a wire mesh. A droplet of fresh absorbent impinges onto the suspended droplet. Initial solution mixing is rapidly followed by separation through stratification.

9.4. Discussion

High heat and mass transport kinetics is a governing criterion for the successful design of a heat and mass exchanger for absorption heat storage, affecting: gross temperature lift, volumetric power and volumetric energy density. In liquid sorbents, mass diffusion is recognised as a primary restrictor in achieving a favourable rate of mass uptake. For this reason, measures are sought to increase mass uptake by improving mass transport in the absorbent, while keeping high concentration difference of absorbent in single pass process, along the heat and mass exchanger. This is a requirement due to the concentration dependent temperature gain. Based on the slow laminar flow of absorbent along the spiral fin, it was expected that a concentration gradient perpendicular to the film flow was established as measured in chapter 8. “Study of mass transport” on page 112. Finding a method to mix the absorbent film as it flows along the fin, in order to break this gradient would thus enhance the rate of mass uptake, while keeping high concentration gradient along the tube. A common approach towards inducing turbulence is droplet impingement. Nevertheless, the images in figures 45 on page 144 and figure 46 on page 145 show that droplet impingement on the sorbent film does not induce mixing. In the first images with only a slight absorbent film (below 1mm), it was seen that the impinging droplet spread from impact on the stainless-steel plate. On the spiral fin, there is a constant film flow of approximately 1mm average height. For this reason, the behaviour of droplet *D4* to *D6* were considered more applicable. In this case the droplet fell through the dilute layer and spread under the surface with no detectable turbulence. Thus, the effect of surface renewal reduced to the area of droplet penetration and was quickly covered again with diluted absorbent with no bulk mixing.

Further indication of the low mixing effect and strong stratification was seen in the droplet suspension tests shown in figure 47. The strong stratification is considered to be due to natural convection driven by absorbent density change. This was caused by concentration change and temperature increase from absorption. The specific mass decrease and temperature in-

crease on the surface of the absorbent lead to a strong buoyancy force, for which its counter force is dependent on the absorbent viscosity. Due to the good thermal conductivity of aqueous sodium hydroxide as shown in chapter 8. “Study of mass transport” on page 112, thermal stratification is considered to be minor to concentration-based effects. As well as the fact that greater reduction of density results from concentration decrease compared to temperature increase, see appendix A. “Density” on page 186. The specific mass varies strongly, between water and aqueous sodium hydroxide, where at 50wt% and 20°C it is 1.53g mm^{-3}.

The onset of natural convection in fluids can be determined by the Rayleigh number (*Ra*).

$$Ra = \frac{\Delta\rho g L^3}{D\eta}, \text{ Equation 35}$$

where, $\Delta\rho$ [g mm^{-3}] is the difference in density between the diluted and concentrated absorbent, g [m s^{-2}] is the local gravitational acceleration, L [m] is the characteristic length-scale of convection, D [m^2 s^{-1}] is the diffusion coefficient, and η [mPa s] is the dynamic viscosity. At low Rayleigh number, there is no buoyancy-initiated flow. In this case, heat transfer is purely by conduction and mass transport by diffusion. At increased Rayleigh number, heat and mass is transferred by natural convection, and depending on the degree and viscosity of the fluid, laminar or turbulent flow results.

In order to quantify the opposing forces, buoyancy force and viscous force the Grashof number (*Gr*) can be used. This is a number analogous to the Reynolds number used in fluid dynamics and heat transfer to approximate the ratio of the buoyancy to viscous force acting on a fluid.

$$Gr = \frac{buoyant\ forces}{viscouse\ forces}, \text{ Equation 36}$$

$$Gr = \frac{g\beta\Delta\Theta L^3}{\nu^2}, \text{ Equation 37}$$

Where, g [m s^{-2}] is the local gravitational acceleration, β is the coefficient of thermal expansion, $\Delta\Theta$ [K] is the temperature difference, L [m] is the characteristic length-scale of convection and ν is the kinematic viscosity v [m^2 s^{-1}], which equals to:

$$\nu = \frac{\eta}{\rho}$$, *Equation 38*

Where, η [mPa s] is the viscosity and ρ [g mm^{-3}] is the density of the fluid

In respect to temperature gradient for vertical flat plates the Grashof number is calculated as:

$$\mathrm{Gr}_L = \frac{g\beta(\theta_{int} - \theta_b)L^3}{\nu^2}$$, *Equation 39*

Where, ϑ_{int} [°C] is the surface temperature and ϑ_b [°C] is the bulk temperature.

In the case of mass transfer, natural convection is caused by concentration gradients rather than temperature gradients. The analogous form of the Grashof number used in this case is:

$$\mathrm{Gr} = \frac{g\beta^*(X_{int} - X_b)L^3}{\nu^2}$$, *Equation 40*

Where, X_{int} [wt%] is the concentration at surface and X_b [wt%] is the ambient medium concentration.

And:

$$\beta^* = -\frac{1}{\rho}\left(\frac{\partial\rho}{\partial X_b}\right)_{\vartheta,p}$$, *Equation 41*

Where, ρ [g mm^{-3}] is the medium density, X_b [wt%] is the bulk medium concentration, ϑ [°C] is the constant temperature and p [Pa] is the constant pressure.

In the following analysis, difference must be made between the observed behaviour in the neutron imaging analysis with sodium deuteroxide solution at 40wt% and the predicted behaviour with aqueous sodium hydroxide solution with starting concentration of 50wt%. The following calculations are made in respect to sodium hydroxide, the more relevant in the application and the deuteroxide results are added in brackets.

Based on the density difference $\Delta\rho$ = 525 kg m^{-3}, the film height of L = 2mm, the mass diffusion coefficient of D = 2x10^{-10}m^2 s^{-1} (taken from chapter 8. “Study of mass transport” on page 112), and the dynamic viscosity η = 30 mPa s, a Rayleigh number of 6.87x10^6 (6.02x10^6) results. This gives clear indication of strong convection, likely without turbulence due to the high viscosity of the absorbent.

In calculating the Grashof number the fluid viscosity is a dominant parameter, which strongly varies dependent on concentration, see appendix A “Viscosity” on page 199. Taking $(\partial\rho/\partial X_b)_{\vartheta,p}$ to be 525kg m^{-3}/50wt%, and ρ to be 1525 kg m^{-3} (density at 50wt% and 20°C), then β^* = 6.9x10^{-3}, and if ΔX = 50wt%, L = 2mm, and η = 0.54mPa s (water at 50°C), then Gr = 2.2x10^5. On the other hand if η = 25.5mPa s (aqueous sodium hydroxide at 50wt% and 40°C), then Gr = 9.7x10^1.

The value of the Rayleigh number points to strong convection. From the discussion on the Grashof number it is clear that the dynamic viscosity of the absorbent has a substantial impact on the ratio of buoyancy force to viscosity force. It follows that the mass flux due to buoyancy force depends on the location of the dilute absorbent, in the absorbent bulk (low Grashof number) or on the sorbent surface (high Grashof number). The Grashof number is substantially greater at the surface due to the concentration gradient, as reported in chapter 8. “Study of mass transport” on page 112.

The lack of turbulence is confirmed both in the droplet impingement and suspension study, by the clear separation of diluted and concentrated absorbent. In a horizontally aligned absorbent film, such as in figure 45 on page 144 and figure 46 on page 145, this strong buoyancy force is in direct counter orientation to mass diffusion from the film top surface. This substantially reduces mass diffusion and thus volumetric power. Nevertheless, since there is a potential for strong movement of diluted absorbent, an effective heat and mass exchanger should be designed to use the buoyancy force in order to improve heat and mass transport in a manner where mass transport and buoyancy force are in equal direction, or buoyancy otherwise supports absorption.

The droplet suspension images provide an indication of a possibility to actively use the buoyancy force in order to increase the rate of absorption. It is clearly visible, that since concentrated absorbent sinks to the bottom of the droplet, and the droplet is suspended under the wire mesh, this stratification exposes concentrated absorbent directly to the absorbate atmosphere, thus successfully increasing rate of absorption and practically obliterating restrictions due to mass diffusion. Furthermore, this is a continuous process, since, as water vapour is absorbed and specific mass of absorbent reduces, this absorbent moves to the top of the droplet by buoyancy force. It can thus be concluded that droplet suspension could eliminate the need for mass enhancement through turbulence. Stratification in droplet suspension is substantially more effective, since highest concentration is exposed to the vapour, not the mean concentration, due to it being the heaviest part of the solution. It can even be concluded that mass transport is counterproductive since like turbulence, it tends towards a mean concentration in the solution. Nevertheless, the transport of diluted absorbent in the droplet suspension, is guided through the concentrated bulk, as illustrated in figure 47 on page 147, thus tending more to low Grashof values due to the high viscosity of concentrated absorbent.

There are also further practical challenges in the design of a technical heat and mass exchanger with droplet suspension such as stable droplet

suspension and thermal conduction to the heat transport fluid. In previous work (Daguenet-Frick et al. 2017) it was recognised that due to the high viscosity and surface tension of the absorbent, there is a strong tendency towards droplet accumulation. This can lead to large heavy droplets which will fall from their suspended position. In order to follow a continuous process of absorbate uptake and heat release with maximum heat gain and maximum concentration gradient, counter flow of absorbent and heat transport fluid is required. This involves droplet mobility in suspension during absorption, an undertaking esteemed highly challenging to attain in a continuous process.

The practical challenge is thus to design a heat and mass exchanger based on true counterflow with vertical absorption surface to enable surface renewal through buoyancy force, with increased rate of surface renewal by reduced viscosity on the absorbent surface.

A possible solution is found in the spiral finned tube heat and mass exchanger with low fin spacing. It is proposed that in the space between the upper and lower fin, concentration stratification occurs as seen in the images in figures 45 to 47. This stratification has the tendency to push concentrated absorbent to the vapour / liquid interface in the lower section of the fin space, as is seen in figure 46 on page 145, where it absorbs vapour and rises to the underside of the upper fin, releasing the resulting heat to the heat transport fluid via finned tube. By using a spiral finned tube, a continuous process of mass uptake and heat release can be followed where due to stratification, constant contact of concentrated absorbent to the vapour is possible in a continuous downward spiral flow.

This approach is substantially different to the functionality of the previous spiral finned tube heat exchanger not in the basic idea of counter flow of absorbent and heat transport fluid or the spiral fin employed for absorbent suspension and sufficient exposure time, but in the concept of absorption. While previously, thin absorbent film on wide fins with adequate fin spacing to prevent flooding was sought in order to compensate slow mass transport, the new approach requires the opposite, narrow fins and low fin spacing for

optimal flooding and best stratification as shown in the picture in figure 49 and illustrated in figure 50 on page 156.

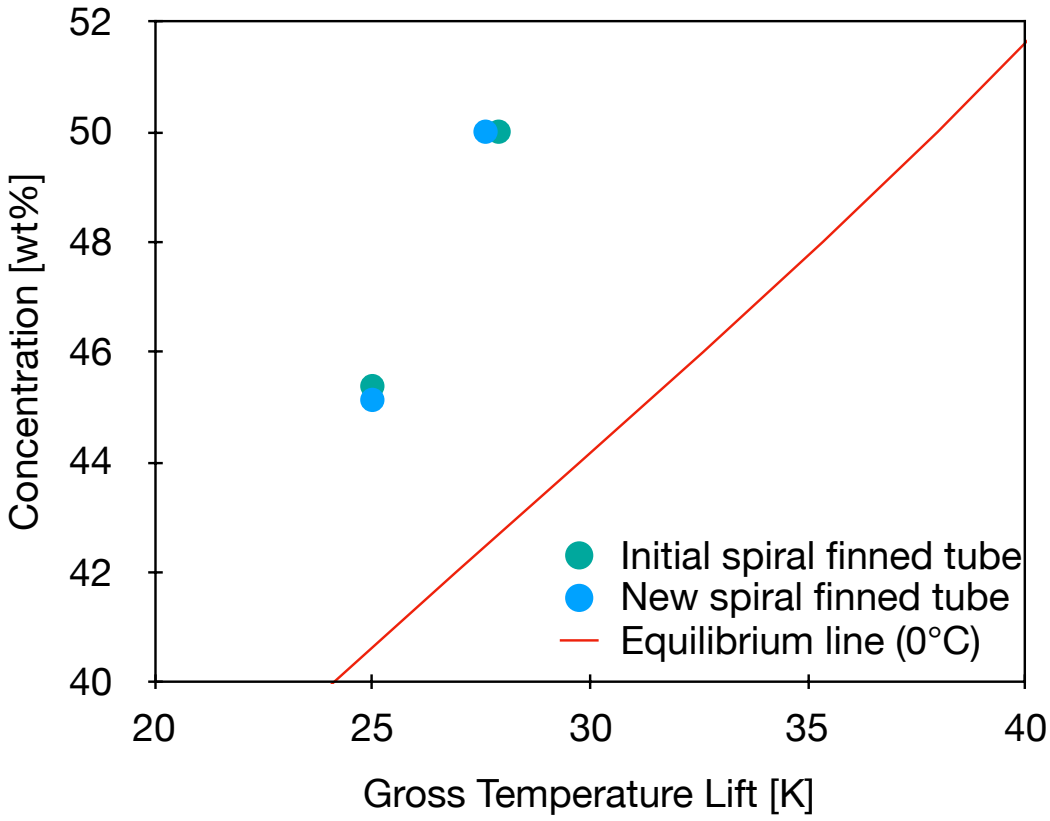

Figure 48: Comparison of the spiral finned tube with outer diameter of 50 and 5 mm fin spacing (turquoise dots) to the version with reduced 21 mm outer diameter and 1.9 mm fin spacing operated with flooded fin (blue dots).

This concept was tested in the lab scale spiral finned tube heat exchanger test bench reported in chapter 7. “Heat and mass exchanger test bench” on page 88. A copper spiral finned tube with a fin outer diameter of 21mm, tube outer diameter of 12mm, length of 960mm, and fin space of 1.9mm was tested, shown in figure 49. In figure 48 a comparison to the initially tested stainless-steel version (see chapter 7. “Heat and mass exchanger test bench”) is made. Test settings were strictly based on realistic temperatures as proposed in chapter 2.4 Application temperatures; absorbent heat transfer input temperature 25°C and evaporating temperature 1°C with absorbent flow 6 g/min and absorbent heat transfer flow 200 g/min. While the output temperature at 50wt% was slightly lower at 27.6°C compared to

27.9°C, the final concentration was also slightly lower 45.13wt% compared to 45.38wt%. Performance of the two tubes was thus quite similar. Nevertheless, the volume specific power of the new tube of 104.5kW m^{-3} is 5 times that of the original, due to the substantially lower finned tube diameter. The active area due to the flooding of the fin is reduced by a factor of 4.4, to $6.3x10^{-2}m^2$ and the diffusion coefficient is increased by a factor of 34, to $2.14x10^{-7}m^2$ s^{-1}. This is an increase of 10^3 times the measurement from the Raman spectroscopy analysis and the bulk scale evaluation.

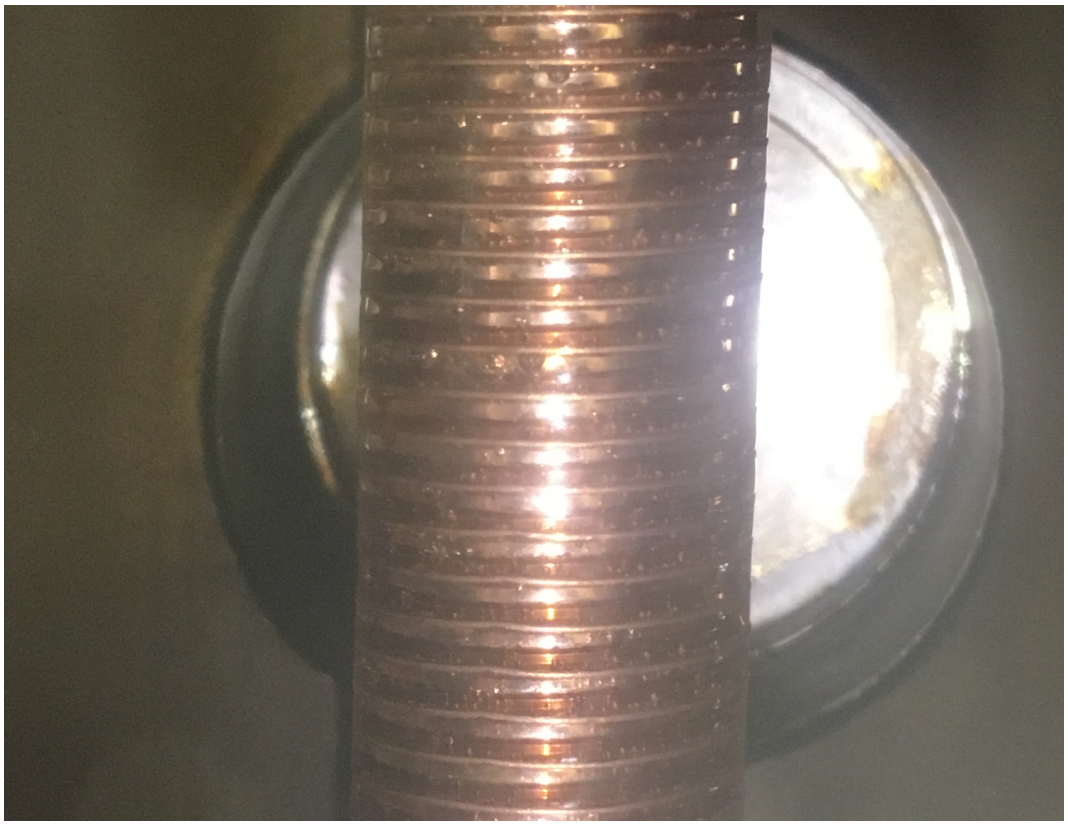

Figure 49: Picture of the flooded spiral finned tube installed in the test bench

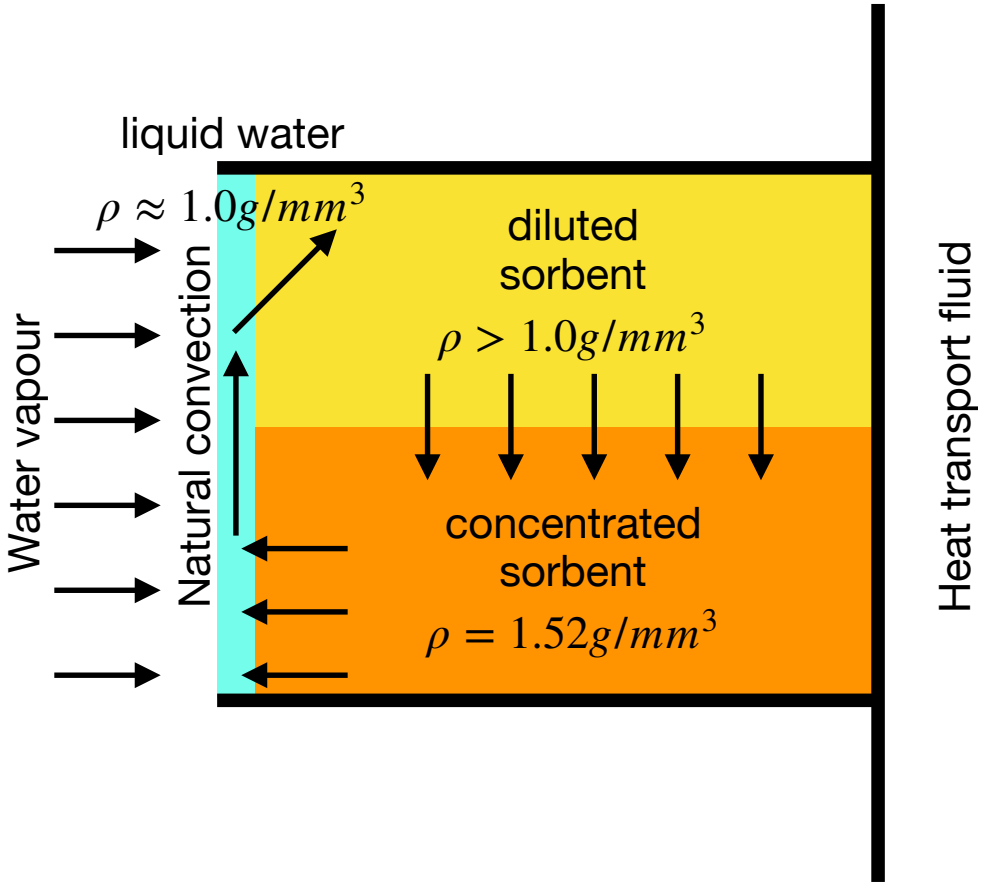

Figure 50: Illustration of the mass transport through buoyancy force.

This result shows that rather than pursuing absorbent mixing, by which at best, a mean concentration is reached, discreetly targeted use of concentration stratification from buoyancy forces can prompt continuous exposure and renewal of concentrated absorbent to the vapour / liquid interface, thus having the potential to augment mass uptake kinetics beyond that of maximum turbulence. Further work must follow to define best fin width and spacing in order to optimise this process.

10. Flooded fin design

Extensive performance testing of the flooded finned tube heat exchanger as shown in figure 49 on page 155 was undertaken, at varying evaporator temperatures and varying absorber heat transfer fluid flow. Tests were performed on a single tube in the lab scale heat and mass exchanger as described in chapter 7. “Heat and mass exchanger test bench” on page 88. In all, 92 tests were performed, all operating at steady state conditions for several hours. As proposed in chapter 2.1 Performance parameters” on page 21 and shown in figure 2 on page 24, results were evaluated by mapping on the concentration versus gross temperature lift diagram. In the diagrams, the performance in respect to the theoretical maximum in respect to gross temperature lift and concentration change, derived from the vapour pressure vs. temperature and concentration diagram (see chapter 4.2. “Temperature and energy density” on page 57 as well as appendix A. “Vapour pressure” on page 204) can easily be evaluated and compared. The evaluation is again illustrated in figure 51a. The points horizontally aligned at the concentration of 50wt% indicate the resulting gross temperature lift and are compared to the actual maximum value given by the adiabatic equilibrium curve. The values vertically aligned at 20K in this figure, are compared in respect to the minimum concentration indicated by the equilibrium curve. The heat transport fluid temperatures were measured and referred to. All presented tests are performed at 25°C absorber input temperature, as proposed in chapter 2.4. “Application temperatures” on page 39. The evaporator input temperatures are taken at 5°C (see figures 51a to c), 10°C (see figure 52a) and 15°C (see figure 52b) in order to provide a span of operation. In reading the diagram, generally close coherence to the equilibrium state is sought, both in maximum temperature gain for high output temperature as well as low concentration for maximum volumetric energy density. The actual absorber input and output temperatures can be calculated from the respective minimum and maximum gross temperature lift by adding the evaporator temperature. An orientation in respect to volumetric power and volumetric energy density can be gained in respect to the final concentration and

the mass flow. Decrease in final concentration at increased absorbent mass flow results in greater power. Energy density on the other hand is only dependant on the final concentration, low concentration gives high energy density. For specific positioning, maximum and minimum volume specific power and energy values are provided in the diagrams. Volumetric power is calculated in respect to the tube volume, not including tube spacing, housing or other system components, and volumetric energy density values are in respect to the volume in charged state, including concentrated absorbent and absorbate.

Figures 51a to c show diagrams of typical operation with heat supplied from a ground source heat exchanger at a supply temperature of 5°C. The reported tests were performed at absorbent flows of 6g min^{-1} (Figure 51a), 4g min^{-1} (Figure 51b) and 2g min^{-1} (Figure 51c). Under all three absorbent flows, a clear pattern of greater temperature gain at low heat transport fluid flow with high final concentration and low temperature gain at high heat transport fluid flow with reduced final concentration was encountered.

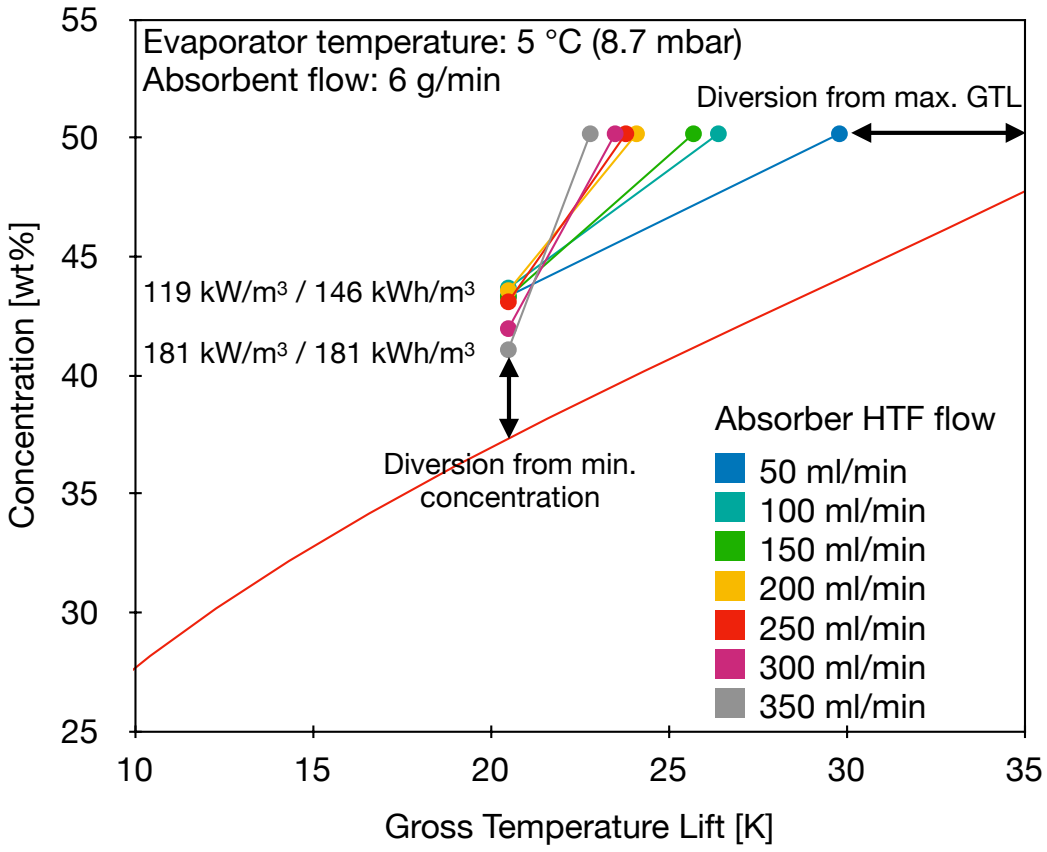

Figure 51a: Diagram showing concentration vs. gross temperature lift for the comparison of performance with 6g min^{-1} absorbent flow, 5°C evaporator temperature and varying heat transport fluid flows, to the respective equilibrium line. Included is the mythology of reading performance deviation in respect to maximum gross temperature lift and minimum concentration.

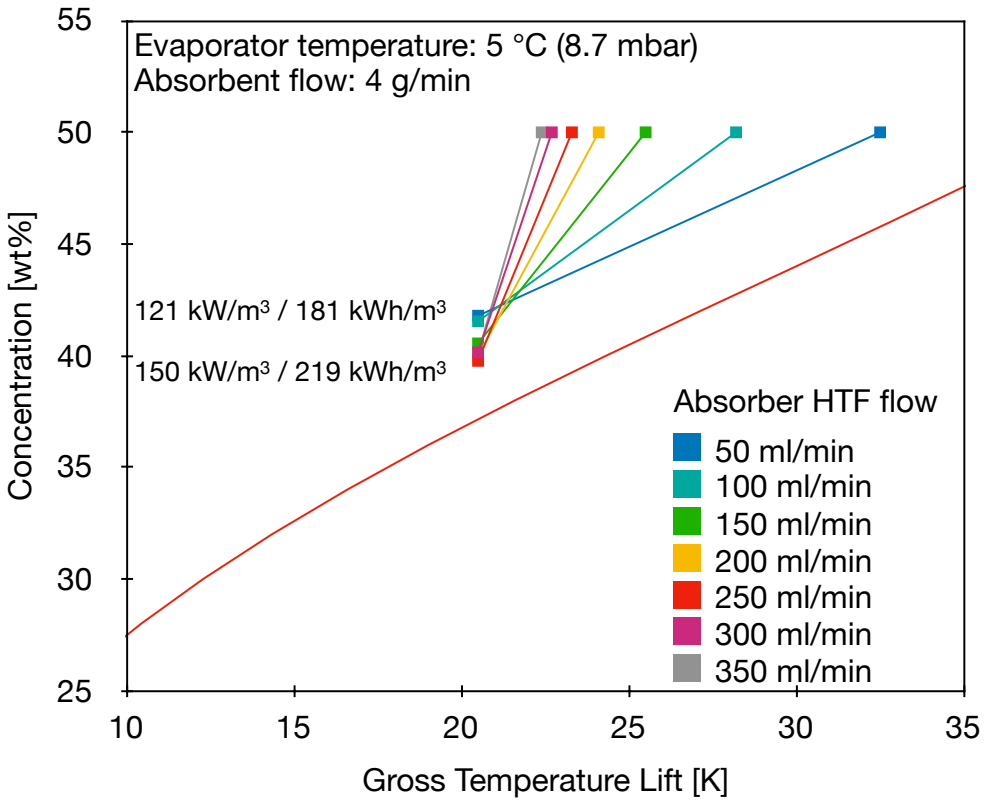

Figure 51b: Diagram showing concentration vs. gross temperature lift for the comparison of performance with 4 g min^{-1} absorbent flow, 5°C evaporator temperature and varying heat transport fluid flows, to the respective equilibrium line.

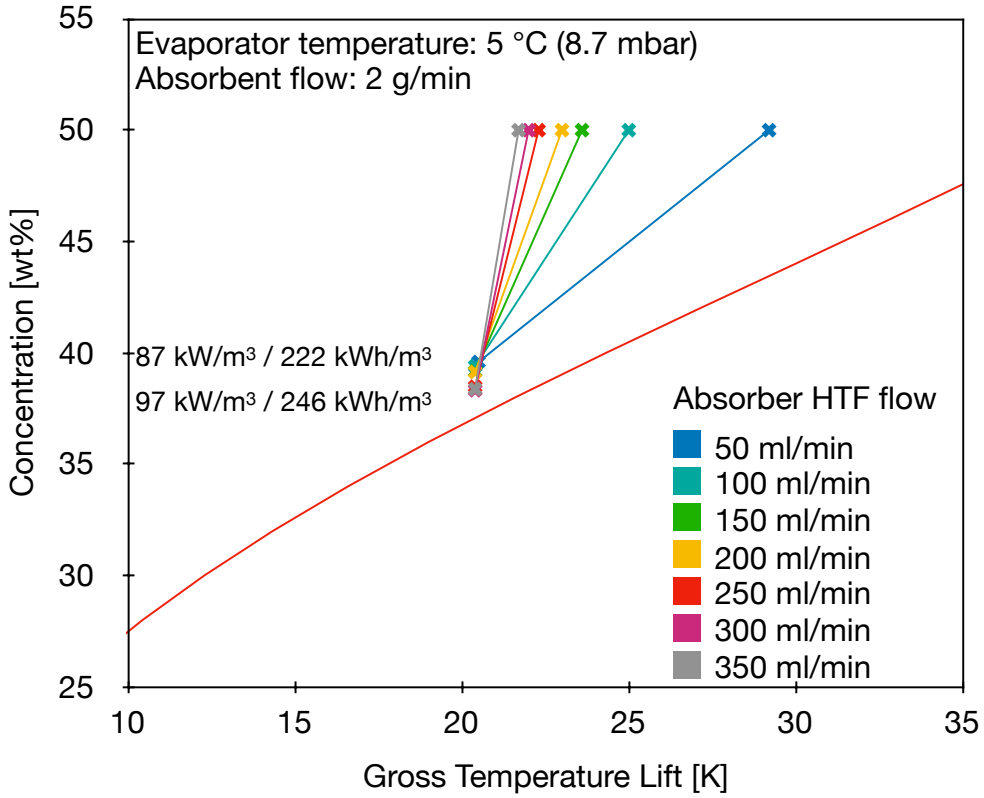

Figure 51c: Diagram showing concentration vs. gross temperature lift for the comparison of performance with 2 g min^{-1} absorbent flow, 5°C evaporator temperature and varying heat transport fluid flows, to the respective equilibrium line.

This emphasises the challenge concerning the non-linear behaviour between heat gain and temperature gain, due to the concentration gradient, arising from the non-linear behaviour of absorbent mass gain to concentration change. For this reason, more heat is available at low temperature gain (concentration decrease at lower initial concentration) than at greater temperature gain (concentration decrease at greater initial concentration). Since the thermal capacity (J kg^{-1}) of the heat transport fluid (water) is practically constant in the application temperature range, high temperature gain can be reached if its specific heat capacity (J kg^{-1} K^{-1}) is in line with the absorbent thermal capacity at high concentration change. On the other hand, low final discharge concentration can only be reached if the heat transport fluid specific heat capacity is adapted to the concentration change at the low concentrations. This issue is not only specific for the counter flow process or

even the general transported process, but present also in the fixed bed process. In the counter flow process, being a refined approach to reach maximum performance the drawback is however more emphasised since other limitations to temperature and energy performance are reduced. The best volumetric power and volumetric energy density thus depends on required gross temperature lift, and this in turn is based on the required output temperature and the evaporator temperature. Figures 52a and b on page 158 and 159 show examples of equal testing conditions as in figures 51a to c, but at varying evaporator temperatures 10°C and 15°C at constant absorbent flow. While the difference between final concentration to theoretical minimum concentration increases as evaporating temperature is increased, due to the increase of heat and mass transport (power) the specific concentration markably reduces at low evaporating temperature. High evaporating temperatures are substantially more favourable for both power and energy-based performance. Gross temperature lift is not as much affected, nevertheless, final output temperate naturally is, since this is the sum of gross temperature lift and evaporating temperature. For this reason, if an output temperature of 35°C is required for a building floor heating system, and a geothermal heat exchanger supplying heat at 5°C is used, then at 4g min^{-1} absorbent flow per tube the heat transport fluid flow would have to be set to between 50ml min^{-1} and 100ml min^{-1} per tube. The volume specific power would then be just over 121kW m^{-3} and the volumetric energy capacity would be slightly more than 181kWh m^{-3}. On the other hand if heat at 15°C is available, a gross temperature lift of only 20°C would be required thus a flow between 150ml min^{-1} and 200ml min^{-1} per tube would be possible, enabling a volume specific power density of 330kW m^{-3} and volume specific energy density of 340kWh m^{-3}. These operating conditions could be made possible if operation in series with an air source heat pump was followed. In this case, a first temperature increase by the air source heat pump is followed by a second step from the absorption heat storage system. This enables operating below 0°C heat source temperature, improves storage capacity and enables the air source heat pump / absorption to reach similar performance to the ground source heat pump.

Figure 52a: Comparison of performance with 6 g min^{-1} to equilibrium line.

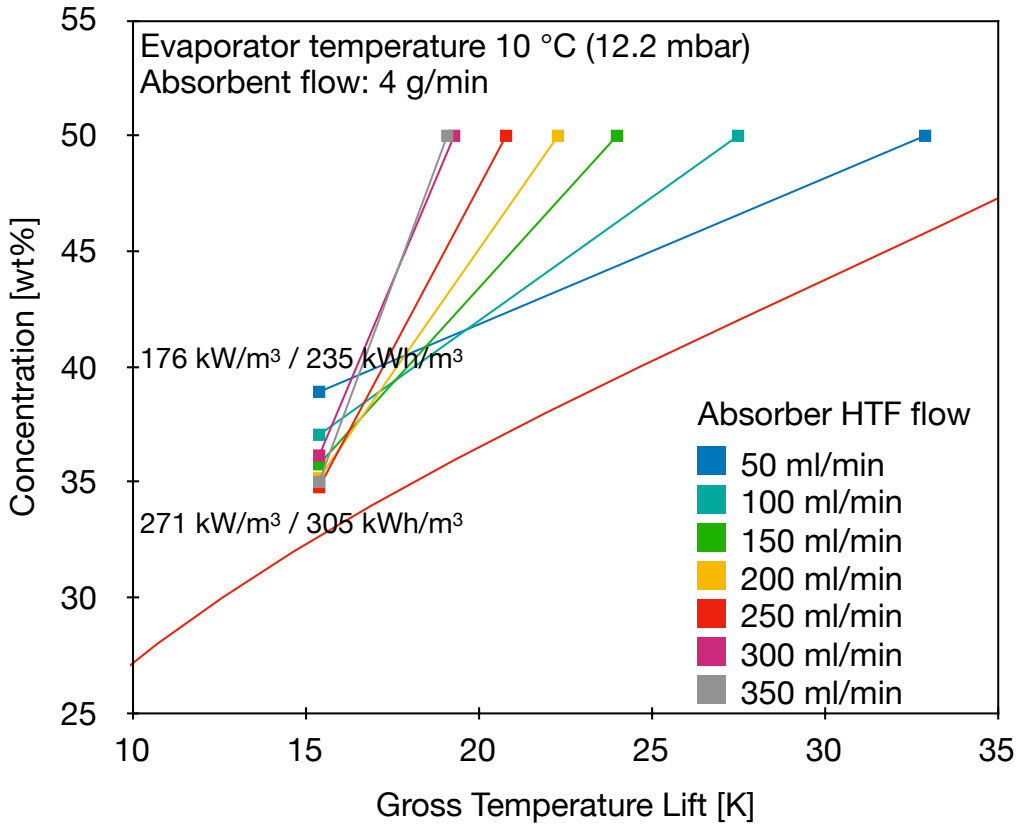

Figure 52a: Diagram showing concentration vs. gross temperature lift for the comparison of performance with 4 g min^{-1} absorbent flow, 10°C evaporator temperature and varying heat transport fluid flows, to the respective equilibrium line.

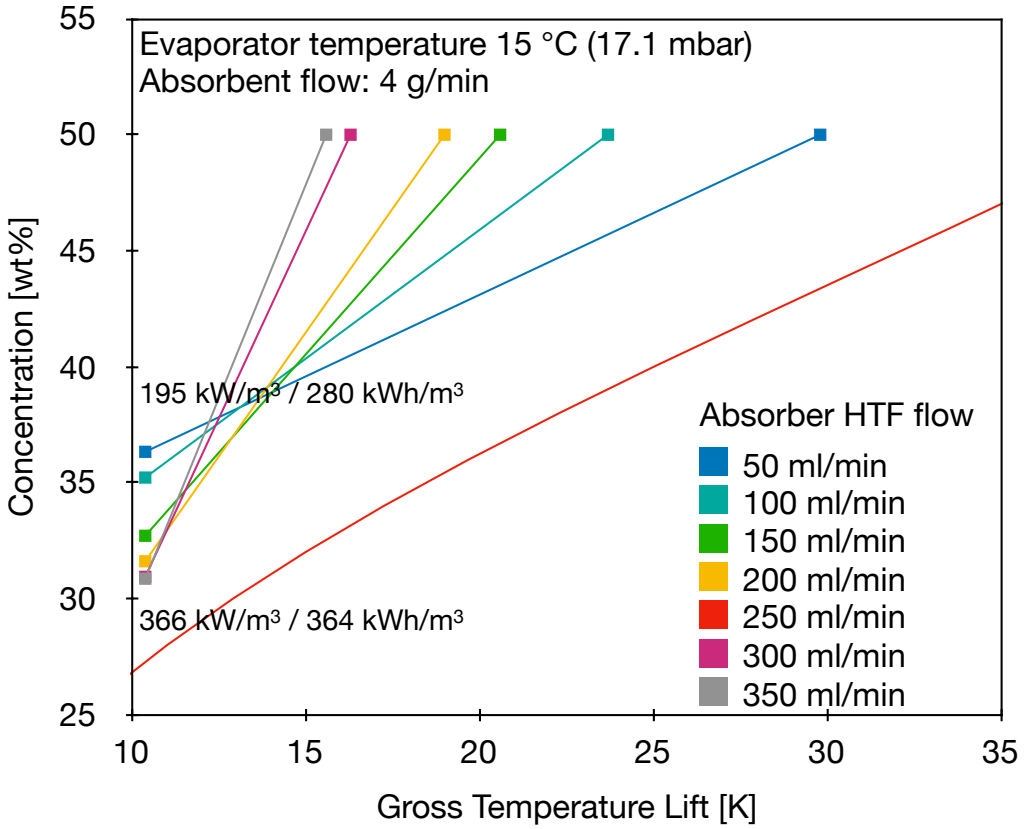

Figure 52b: Diagram showing concentration vs. gross temperature lift for he comparison of performance with 4 g min^{-1} absorbent flow, 15°C evaporator temperature and varying heat transport fluid flows, to the respective equilibrium line.

The presented results nicely emphasises how performance of the heat and mass exchanger is highly dependent on the operating conditions. For this reason, as stated in chapter 2.4. “Application temperatures” on page 39, performance comparison can only be made if clear application specific temperature guidelines are followed.

11. Conclusion

There is a great potential for long term heat storage applications in buildings, bridging seasonally shifted supply and load, to reduce greenhouse gas emission and effectively use carbon free renewable energy, harvested on-sight or off the grid, for space heating and domestic hot water. Work in the field is ongoing, with much research focussed on compact inter-seasonal thermal storage based on sorption processes. In this task, it is key to have a global understanding of both material and component behaviour under application specific requirements and boundaries. Due to the fact that this technology is based on a chemically driven heat pump process, it is highly sensitive to operating conditions, as discussed and clearly shown in the final test in chapter 10. “Flooded fin design” on page 157. A clear course of action in the design as well as performance evaluation, can only be followed if realistic application specific temperatures are defined and followed. For this reason, a set of temperatures for the building space heating and domestic hot water application were defined in chapter 2.4. “Application temperatures” on page 39 as a prerequisite for this work. Upon the basis of these temperature guidelines, performance along the development scale from material to systems and across the landscape of varying system approaches has been possible. The important performance parameters for sorption heat storage systems are; gross temperature lift and volumetric power density, as well as volumetric energy density, as discussed in chapter 2.1. “Performance parameters” on page 21, a parameter irrelevant in other sorption processes such as sorption chillers. This is highly critical to understand, since it exerts a strong influence on component design, operation and evaluation.

The ratio of gross temperatures lift required in charging compared to the resulting gross temperature lift in discharging can be used as a measure of temperature effectiveness, providing a means for comparing system and process performance as followed in chapter 2.3 “Performance evaluation of reported systems” on page 36. Through studying the varying categories of processes, defined in chapter 2.2. “Sorption heat storage system categori-

sation” on page 30, it has been shown that the closed transported approach has the greatest potential for good performance, especially if counterflow of sorbent to heat transport fluid is followed. The single pass, counterflow process is one of the substantial benefits of the transported process, shown in chapter 2.2.4. “Transported process” on page 34. This approach is most easily employed with liquid absorbents. With continuous counterflow, maximum achievable temperature can be reached at maximum concentration difference. This is so, since the absorbent is cooled to a temperature close to the heat transport fluid input temperature, which is lower than the absorber output temperature. The single pass process is necessary for maximum temperature gain, since recirculation of semi discharged sorbent leads to strong reduction in gross temperature lift, as discussed in chapter 2.2. “Sorption heat storage system categorization” on page 30.

The indispensable starting point for an initial performance evaluation is the vapour pressure vs. temperature diagram - in respect to absorbent concentration, founded on the gross temperature lift and energy density. Beyond this, both mass and heat transport flux affect the actual performance on all three performance levels. A further parameters substantially impacting performance of the absorption process is the non-linear behaviour of the absorbent heat capacity. Consequently, there is a balance between gross temperature lift and volumetric energy density and one is optimised at the expense of the other.

Evaluation of the absorption process in the bulk scale test bench showed that there was a substantial gradient in the absorption power along the concentration scale. Long exposure time and continuous heat release are thus two important specifications for the absorption heat storage specific heat and mass exchanger to be able to reach high concentration difference. This is a central point to understand. In the search for a practical method to enable this, the spiral finned tube was fixed upon. With this setup, long exposure time with constant wetting in a continuous counterflow process was made possible. Initial tests showed promising results, see figure 27 on page 101.

In the liquid absorption process, mass transport is generally the limiting parameter, naturally also affected by heat transport. This is different to the solid adsorbent processes, where due to the high porosity of the material mass transport is generally secondary to heat transport limitations. In this work it was considered of significant importance to understand the mass transport of water in aqueous sodium hydroxide to gain further insight in the process and evaluate methods for improvement. For this reason two varying experimental facilities were designed and built to study the mass transport under application specific conditions and temperatures. With Raman spectroscopy the water transport in thin film aqueous sodium hydroxide was analysed, highly temporally and spatially resolved, refer to chapter 8 “Study of mass transport” on page 112 for details. It was shown that mass diffusion and not a possible gas liquid intersectional barrier was process limiting. In order to increase mass transport mixing of the sorbent film bulk was required. A passive approach considered was droplet impingement. With neutron imaging visual inspection of droplet impingement on a sorbent film and impingement on a suspended droplet was carried out. The analysis showed little effect of mixing through impingement. On the other hand, substantial concentration based stratification, due to buoyancy forces from varying absorbent concentration, was recognised and a potential approach to implementing this behaviour for increased mass uptake flux, and thus power, was found, while keeping to the previously achieved benefits of the spiral finned tube heat and mass exchanger, see chapter 9 “Investigation of absorbent mixing” on page 135.

With this new flooded, narrow, spiral finned tube heat and mass exchanger, an approach to increase the diffusion coefficient by a factor of 10^3 was found, by specifically employing the discovered buoyancy force effect in a vertical absorption process. In the design, the resulting vertical wall of absorbent, suspended in the spiral fin, is exposed to the absorbate atmosphere as shown in figure 50 on page 156. From this, it is proposed that a vertical film of diluted absorbent forms, which due to the strong buoyancy force, rises, resulting in exposure of more highly concentrated sorbent from the flow bulk. This tube design was thoroughly tested in the lab scale heat

and mass exchanger under application specific conditions as well as extended conditions for possible combined air source heat pump and absorption storage systems, see chapter 10 “Flooded fin design” on page 157. Steady operation and highly improved performances were achieved under all realistic operation conditions.

As expected, and discussed in detail in chapter 2 “Sorption heat storage for buildings” on page 21, the results show that performance strongly depends on operating conditions. By employing the closed transported process with counterflow heat exchange, many of the limitations of the other three process types are reduced. For this reason the challenge in respect to the non-linear heat capacity of the absorbent is emphasised, see chapter 6.3. “Counterflow heat exchanger with absorption” on page 85. This is a sorption heat storage application specific condition that cannot be resolved. Under a specific temperature profile, best performance in absorption is reached if absorber heat transfer fluid flow is regulated to just reach the required output temperature. Absorbent flow on the other hand can likely be kept constant at approximately 4 g/min per tube in this case.

On a system level, the transported liquid absorption heat storage is separated into the heat and mass exchanger (power unit) and the storage tanks (energy unit). This is a substantial benefit, providing design flexibility. Nevertheless, on the process level power and energy are strongly interconnected. For this reason, the volumetric power density of an absorption heat storage will never reach that of an absorption chiller.

It is concluded, that in this work, based on the establishment of a clear understanding of the application specific boundary conditions and the extensive study of the liquid absorbent working pair aqueous sodium hydroxide and water under these conditions, a heat and mass exchanger was designed, able to fulfil the requirements for sorption heat storage.

The work presented in this thesis is limited to a single tube lab scale heat and mass exchanger. Upscaling will be performed by parallel operation of many spiral finned tubes. One of the challenges in this will be the equal

supply of heat transport fluid and absorbent to all tubes. Failure to reach this will result in a drop of all performance parameters.

11.1. Next steps

Next steps in this work will be to upgrade the single tube testing setup to a nickel coated copper multi tube assembly, in this case consisting of both 100 parallel tubes for the absorber / desorber and the equal number for the evaporator / condenser shown in figure 53. This setup will have a thermal power output of approximately 4 kW to 12 kW depending on the operating conditions.

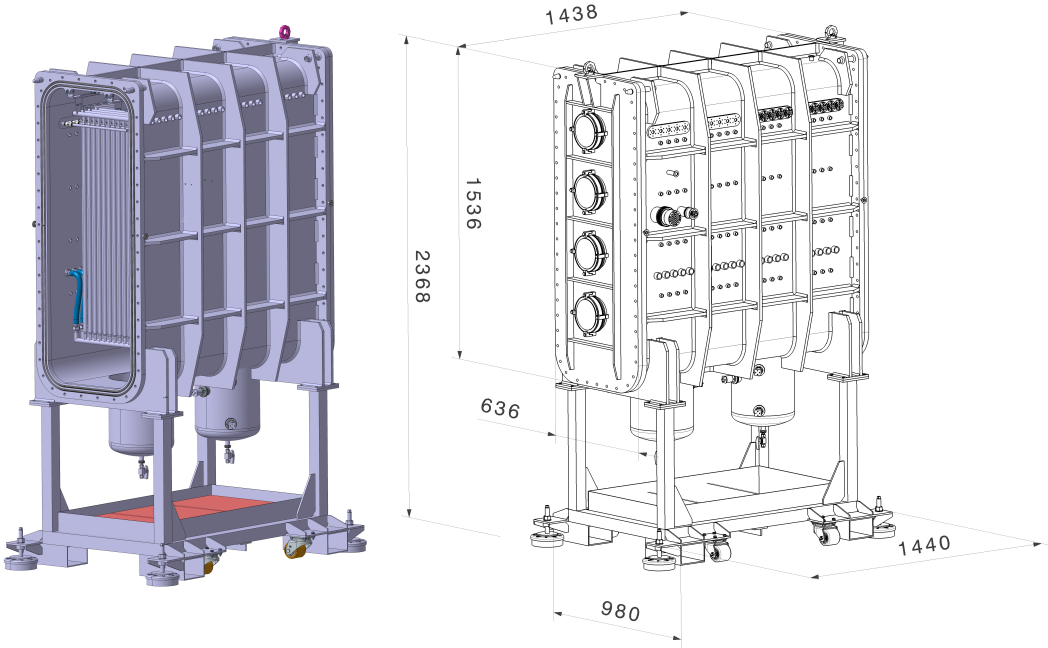

Figure 53: CAD image of the upscaled liquid absorption heat storage heat and mass exchanger unit, holding 200 spiral finned tubes, dimensions are in mm. The vessel outer dimensions are 1536mm / 1438mm / 636mm.

The setup will undergo extensive testing under the defined application specific conditions in chapter 2.4. “Application temperatures” on page 39. Further work will be followed both on the experimental and the simulation level in order to evaluated the buoyancy force based movement in the film and determine best fin width and fin spacing for good and robust operation. On the experimental level this can involve further Raman based concentra-

tion tests on the spiral finned tube in operation with a self built Raman setup, as well as Neutron imaging of fin segments including fin cooling.

Beyond these next steps taken, many areas of further research and engineering emerge from this work. On the material level, a liquid sorbent with an approximately 10K greater average gross temperature lift would be preferable. This is not to be mistaken with charging aqueous NaOH to a concentration beyond 50wt% and finding means of keeping the absorbent liquid, since this benefit is mostly lost to the non-constant heat to temperature ratio of the absorbent. In this material research, material price must be a forefront criterion, generally directly linked to the availability of the specific elements. Potential elements include sodium, magnesium, potassium, and calcium. On the component level there is great potential in reduction of materials and components as well as improvement in compact build. Storage tanks able to simultaneously contain both charged and discharged sorbent, in order to reduce dead volume are required. Much work on the system and system integration level can yet be performed, in order to achieve simple system architecture, compact build and good performance.

References

Abedin, AH. Rosen, MA. (2011). A critical review of thermochemical energy storage systems. The Open Renewable Energy Journal, 4, pp. 42-46.

Abhat, A. (1983). Low temperature latent heat thermal energy storage: Heat storage materials. Solar Energy, 30(4), pp. 313-332.

Alexandrov, AA. (2005). The Equations for Thermophysical Properties of Aqueous Solutions of Sodium Hydroxide. 14th International Conference on the Properties of Water and Steam in Kyoto.

Andberg, J. W. Vliet, G. C. (1987). A simplified model for absorption of vapors into liquid films flowing over horizontal tubes. Proceedings for ASHRAE. 93, pp. 2454–2466

Anon, (1985). Resistance to Corrosion, publication no. 3M8-88 S-37, Huntington, WV: Inco Alloys International. pp. 33.

Aristov, YI. (2013). Challenging offers of material science for adsorption heat transformation: a review. Applied Thermal Engineering. 50(2), pp. 1610–1618.

Armstrong, F. Blundell, K. (2007). Energy ... beyond oil. Oxford University Press.

ASHRAE handbook: fundamentals. (2005). I-P edition Atlanta: American Society of Heating, Refrigerating and Air-Conditioning Engineers. 1.13–1.5.

Aydin, D. Casey, SP. Chen, X. Riffat, S. (2016). Novel “open-sorption pipe” reactor for solar thermal energy storage. Energy Conversion Management. 121, pp. 321–334.

Baghapour, B. Rouhani, M. Sharafian, A. Kalhori, SB. Bahrami, M. (2018). A pressure drop study for packed bed adsorption thermal energy storage. Applied Thermal Engineering. 138, pp. 731–739.

Bales, C. (2005). Thermal Properties of Materials for Thermo-chemical Storage of Solar Heat. A Report of IEA Solar Heating and Cooling programme – Task. 32. 2005.

Bales, C. (2006a). Solar cooling and storage with the thermo-chemical accumulator. Proceedings of Eurosun.

Bales, C. (2006b). Solar energy research center, “Chemical and sorption heat storage”. Proceedings of DANVAK seminar.

Bales, C. (2008). Final report of subtask B chemical and sorption storage the over- view Available from: http://archive.iea-shc.org/ publications/downloads/task32-b7.pdf.

Banhart, J. (2008). Advanced Tomographic Methods in Materials Research and Engineering. Oxford University Press. Oxford, UK (2008)

Bauer, D. Marx, R. Nußbicker-Lux, J. Ochs, F. Heidemann, W. Müller-Steinhagen, H. (2010). German central solar heating plants with seasonal heat storage. Solar Energy. 84, pp. 612-623.

Behfar, A. Shen, Z. Lau, J. Yu, Y. (2014). Heat and mass transfer enhancement potential on falling film absorbers for water-LiBr mixtures via a literature review (RP-1462). HVAC&R Research. 20(5), pp. 570-580.

Boman, BD. Hoysall, DC. Staedter, MA. Goyal, A. Ponkala, MJ. Garimella, S. (2017a). A method for comparison of absorption heat pump working pairs. International Journal of Refrigeration. 77, pp. 149–175.

Boman, DB. Hoysall, DC. Pahinkar, DG. Ponkala, MJ. Garimella, S. (2017b). Screening of working pairs for adsorption heat pumps based on thermodynamic and transport characteristics. Applied Thermal Energy. 123, pp. 422–434.

Borgschulte, A. Delmelle, R. Duarte, RB. Heel, A. Boillatc, P. Lehmann, E. (2016). Water distribution in a sorption enhanced methanation reactor by time resolved neutron imaging. Physical Chemistry Chemical Physics. 18, pp. 17217–17223.

Borgschulte, A. Gremaud, R. Łodziana, Z. Züttel, A. (2010). Hydrogen tracer diffusion in LiBH 4 measured by spatially resolved Raman spectroscopy. Physical Chemistry Chemical Physics. 12, pp. 5061–5066.

Brancato, V. Gordeeva, LG. Sapienza, A. Palomba, V. Vasta, S. Grekova, AD. Frazzica, A. Aristov, YI. (2019). Experimental characterization of the LiCl/vermiculite composite for sorption heat storage applications. International Journal of Refrigeration. 105, pp. 92-100.

Brauner, N. (1991). Non isothermal vapour absorption into falling film. International Journal of Heat and Mass Transfer, 34, pp. 767–784.

Brauner, N. Moalem Maron, D. Meyerson, H. (1989). Coupled heat condensation and mass absorption with comparable concentrations of absorbate and absorbent. International Journal of Heat and Mass Transfer. 32, pp. 1897–1906.

Cabeza, LF. Solé, A. Barreneche, C. (2017). Review on sorption materials and technologies for heat pumps and thermal energy storage. Renewable Energy, 110, pp. 3–39.

Chen, Y. Cao, R. Wu, J. Yi, Z. Ji, G. (2016). Alternate heat and mass transfer absorption performances on staggered tube bundle with M–W corrugated mesh guider inserts,.International Journal of Refrigeration, 66, pp. 10-20,

Chiang, SH. Toor, HL. (1964). Gas absorption accompanied by a large heat effect and volume change of the liquid phase. AIChE, 10, pp.398–402.

Clarke, J. Colclough, S. Griffiths, P. McLeskey, JT. (2014), A passive house with seasonal solar energy store: in situ data and numerical modelling. International Journal of Ambient Energy. 35(1), pp. 37-50.

Colclough, S. Griffiths, PW. Hewitt, NJ (2011). A year in the life of a Passive House with Solar Energy Stores. International Conference on Sustainable Energy Storage, 21st-24th February, Belfast.

COMTES. http://comtes-storage.eu 2020

Crank, J. (1979). The Mathematics of Diffusion. Oxford science publications. ISBN 9780198534112 1980

Daguenet-Frick, X. Gantenbein, P. Frank, E. Fumey, B. Weber, R. (2015). Development of a numerical model for the reaction zone design of an aqueous sodium hydroxide seasonal thermal energy storage. Solar Energy. 121, pp. 17-30,

Daguenet-Frick, X. Gantenbein, P. Frank, E. Fumey, B. Weber, R. Williamson, T. (2014). Reaction zone development for an aqueous sodium hydroxide seasonal thermal energy storage. Energy Procedia. 57, pp. 2426–2435.

Daguenet-Frick, X. Gantenbein, P. Müller, J. Fumey, B. Weber, R. (2017). Seasonal thermochemical energy storage: comparison of the experimental results with the modelling of the falling film tube bundle heat and mass exchanger unit. Renewable Energy. 110, pp. 162-173.

Danckwerts, P. (1965) The absorption of gases in liquids. Pure and Applied Chemistry. 10(4), pp. 625-642.

Danckwerts, PV. (1951). Absorption by simultaneous diffusion and chemical reaction into particles of various shapes and into falling drops. Transactions of the Faraday Society. 47, pp. 1014–1023.

Danckwerts, PV. Kennedy, AM. (1954) Kinetics of liquid-film process in gas absorption. Part I: Models of the absorption process. Chemical Engineering Research and Design. 75, pp. 101–104.

Dannemand, M. Johansen, JB. Kong, W. Furbo, S. (2016). Experimental investigations on cylindrical latent heat storage units with sodium acetate trihydrate composites utilizing supercooling. Applied Energy. 177, pp. 591–601.

Davies, M. (1997). Material Selector for Hazardous Chemicals Ammonia and Caustic Soda“ Materials Technology Institute of the Chemical Process Industries, Inc. ISBN 1-57698-031-6, pp. 106.

de Boer, R. Haije, W. Veldhuis, J. Smeding, S. (2004). Solid sorption cooling with integrated storage: the SWEAT prototype. Proceedings of 3rd international heat powered cycles conference.

de Jong, A.J. Finck, C. Oversloot, H. van ‘t Spijker, H. Cuypers, R. (2014). Thermochemical heat storage (TCS) - system design issues. Energy Procedia. 48, pp. 309 – 319.

de Jong, AJ. van Vliet, L. Hoegaerts, Ch. Roelands, M. Cuypers, R. (2016). Thermochemical heat storage – from reaction storage density to system storage density. Energy Procedia. 91, pp. 128–137.

Dincer, I. Rosen, M. (2002). Thermal Energy Storage – Systems and Applications. John Wiley & Son, New York.

Dobrzynski, L. Blinowski, K. Cooper, M. (1994). Neutrons and solid state physics. Ellis Horwood, New York

Drake Landing Solar Community, 2012. Borehole thermal energy storage (BTES).http://dlsc.ca.

Englmair, G. Furbo, S. Dannemand, M. Fan, J. (2020). Experimental investigation of a tank-in-tank heat storage unit utilizing stable supercooling of sodium acetate trihydrate. Applied Thermal Engineering. 167, pp.-.

Englmair, G. Moser, Ch. Furbo, S. Dannemand, M. Fan, J. (2018). Design and functionality of a segmented heat-storage prototype utilizing stable supercooling of sodium acetate trihydrate in a solar heating system. Applied Energy. 221, pp. 522–534.

essentialchemicalindustry http://www.essentialchemicalindustry.org/chemicals/sodium-hydroxide.html, 01.2020

Faninger, G. (2004). Thermal energy storage. etn.wsr.ac.at.

Farid, MM. Khudhair, AM. Razack, SAK. Al-Hallaj, S. (2004). A review on phase change energy storage: Materials and applications. Energy Conversion and Management. 45, pp. 1597– 1615.

Fernandes, D. Pitié, F. Cáceres, G. Baeyens, J. (2012). Thermal energy storage: “How previous findings determine current research priorities”. Energy. 39(1), pp. 246-257.

Finck, C. Henquet, E. van Soest, C. Oversloot, H. de Jong, AJ. Cuypers, R. van‘t Spijker, H. (2014). Experimental results of a 3 kWh thermochemical heat storage module for space heating application. Energy Procedia. 48, pp. 320–326.

Finck, Ch. Li, R. Kramer, R. Zeiler, W. (2018). Quantifying demand flexibility of power-to-heat and thermal energy storage in the control of building heating systems. Applied Energy. 209, pp. 409–425.

Foderaro, AH. (1971). The elements of neutron interaction theory, MIT Press, Cambridge.

Frei, G. Lehmann, EH. Mannes, D. Boillat, P. (2009). The neutron micro-tomography setup at PSI and its use for research purposes and engineering

applications. Nuclear Instruments and Methods in Physics Research Section A: Accelerators, Spectrometers, Detectors and Associated Equipment. 605(1–2), pp. 111-114.

Fumey, B. Weber, R. Gantenbein, P. Daguenet-Frick, X. Williamson, T. Dorer, V. (2014a). Closed sorption heat storage based on aqueous sodium hydroxide. Energy Procedia. 48, pp. 337-346.

Fumey, B. Weber, R. Gantenbein, P. Daguenet-Frick, X. Williamson, T. Dorer, V. (2014b). Experience on the development of a thermo-chemical storage system based on aqueous sodium hydroxide. Energy Procedia. 57, pp. 2370-2379.

Fumey, B. Weber, R. Gantenbein, P. Daguenet-Frick, X. Williamson, T. Dorer, V. (2014c). Development of a closed sorption heat storage prototype. Energy Procedia. 46, pp. 134-141.

Fumey, B. Weber, R. Gantenbein, P. Daguenet-Frick, X. Hughes, I. Dorer, V. (2015a). Limitations imposed on energy density of sorption materials in seasonal thermal storage systems. Energy Procedia. 70, pp. 203 – 208.

Fumey, B. Stoller, S. Fricker, R. Weber, R. Gantenbein, P. Daguenet-Frick, X. Dorer, V. (2015b) Performance of the absorption process in a seasonal sorption heat storage prototype. Cisbat conference, EPFL, Lausanne, Switzerland.

Fumey, B. Weber, R. Gantenbein, P. Daguenet-Frick, X. Stoller, S. Fricker, R. Dorer, V. (2015c), Operation results of a closed sorption heat storage prototype. Energy Procedia. 73, pp. 324 – 330.

Fumey, B. Weber, R. Gantenbein, P. Daguenet-Frick, X. Baldini, L. (2016). Absorption based seasonal thermal storage with sodium hydroxide, progress and outlook. 19. Status-Seminar, ETHZ, Zürich, Switzerland.

Fumey, B. Weber, R. Baldini, L. (2017) Liquid sorption heat storage – a proof of concept based on lab measurements with a novel spiral fined heat and mass exchanger design. Applied Energy. 200, pp. 215–225.

Fumey, B. Weber, R. Baldini, L. (2019). Sorption based long-term thermal energy storage – Process classification and analysis of performance limitations: A review. Renewable and Sustainable Energy Reviews. 111, pp. 57–74.

Gaeini, M. Javed, MR. Ouwerkerk, H. Zondag, HA. Rindt, CCM. (2017). Realization of a 4kW thermochemical segmented reactor in household scale for seasonal heat storage. Energy Procedia 135, 105–114.

Garg, HP. Mullick, SC. Bhargava, AK. (1985). Solar thermal energy storage. Dordrecht: Reidel Publishing Company.

Gatapova, EY. Graur, IA. Kabov, OA. Aniskin, VM. Filipenko, MA. Sharipov, F. Tadrist, L. (2017). The temperature jump at water – air interface during

evaporation. International Journal of Heat and Mass Transfer. 104, pp. 800–812.

Gmelins (1928a) Handbuch der Anorganischen Chemie - Natrium vol. XXI, p. 226.

Gmelins (1928b) Handbuch der Anorganischen Chemie -T.21, Natrium p. 215 and 213.

Griffiths, PW. and Colclough, S. (2015). Seasonal Thermal Storage, in Handbook of Clean Energy Systems, Vol.5, Wiley, Chichester, UK.

Grigoryeva, NI. Nakoryakov, VE. (1977). Exact solution of combined heat and mass transfer problem during film absorption. Journal of engineering physics. 33, 1349–1353.

Grossman, G. (1983). Simultaneous heat and mass transfer in film absorption under laminar flow. International Journal of Heat and Mass Transfer. 26 pp. 357–371

Hadorn, JC. (2006). IEA solar heating and cooling programme—task 32: advanced storage concepts for solar and low energy buildings. Proceedings of ECO- STOCK.

Hafsia, NB. Chaouachi, B. Gabsi, S. (2015). A study of the coupled heat and mass transfer during absorption process in a spiral tubular absorber, Applied Thermal Engineering. 76, pp. 37-46.

Hasnain, SM. (1998). Review on sustainable thermal energy storage technologies, Part I: heat storage materials and techniques. Energy Conversion and Management. 39(11), 1127-1138.

Hauer, A. (2007). Sorption theory for thermal energy storage. In: Paksoy HÖ., editor. Thermal energy storage for sustainable energy consumption. Netherlands: Springer, pp. 393–408.

Hauer, A. (2008). Sorption storages for solar thermal energy—possibilities and limits. Proceedings of the Eurosun.

Higbie, R. (1935). The Rate of Absorption of a Pure Gas into a Still Liquid during Short Periods of Exposure. AIChE. 31, pp. 365–389.

Hu, T. Xie, X. Jiang, Y. (2017). Design and experimental study of a plate-type falling-film generator for a LiBr/H2O absorption heat pump. International Journal of Refrigeration, 74, pp. 304-312.

Ibarra-Bahena, J. Romero, RJ. (2014). Performance of different experimental absorber designs in absorption heat pump cycle technologies: a review. Energies. 7(2), pp. 751–766.

Ibrahim, GA. Vinnicombe, GA. (1993). A hybrid method to analyse the performance of falling film absorbers. International Journal of Heat and Mass Transfer. 36, pp. 1383–1390.

IEA (2016), "Energy Technology Perspectives 2016", IEA, Paris https://www.iea.org/reports/energy-technology-perspectives-2016

IEA ECES Annex 35 Flexible Sector Coupling. https://iea-eces.org/annexes/flexible-sector-coupling/ 01.2020.

Inglezakis, VJ. and Poulopoulos, S. (2006). Adsorption, ion exchange and catalysis: design of operations and environmental applications. Elsevier.

International Energy Agency. Solar heating and cooling task 32 - advanced storage concepts for solar and low energy buildings. http://task32.iea-shc.org, 01.2019

International Energy Agency. Solar heating and cooling task 42 - compact thermal energy storage. http://task42.iea-shc.org, 01.2019

International Energy Agency. Solar heating and cooling task 58, material and component development for thermal energy storage. http://task58.iea-shc.org, 01.2019

intratec https://www.intratec.us/chemical-markets/caustic-soda-prices, 02.2020

Isfahani, RN. Moghaddam, S. (2013). Absorption characteristics of lithium bromide (LiBr) solution constrained by superhydrophobic nanofibrous structures. International Journal of Heat and Mass Transfer. 63, pp. 82-90.

Jaehnig, D. Hausner, R. Wagner, W. Isaksson, C. (2006). Thermo-chemical storage for solar space heating in single-family house. ECOSTOCK conference.

Jiang, L. Wang, RZ. Wang, LW. Roskilly, AP. Investigation on an innovative resorption system for seasonal thermal energy storage. Energy Conversion and Management. 149, pp. 129–139.

Jiru, Y. Eimer, DA. (2013). A Study of Mass Transfer Kinetics of Carbon Dioxide in (Monoethanolamine + Water) by Stirred Cell, Energy Procedia. 37, pp. 2180-2187.

Johannes, K. Kuznik, F. Hubert, JL. Durier, F. Obrecht, C. (2015). Design and characterisation of a high powered energy dense zeolite thermal energy storage system for buildings. Applied Energy. 159, pp. 80–86.

Kabus, F. and Wolfgramm, M. (2009). Aquifer thermal energy storage in Neubrandenburg -Monitoring throughout three years of regular operation. EFFSTOCK'2009. In: 11th International Conference on Thermal Energy Storage, Stockholm, Sweden.

Kakaç, HFS. Avelino, MR. editors. (2003). Low temperature and cryogenic refrigeration: proceedings of the NATO advanced study institute. Springer Netherlands. pp. 401.

Kardjilov, N. Manke, I. Hilger, A. Strobl, M. Banhart, J. (2011). Neutron imaging in materials science, Materials Today. 14(6), pp. 248-256.

Kato, Y. (2007). Chemical energy conversion technologies for efficient energy use, Thermal energy storage for sustainable energy consumption. Springer Netherlands. pp. 377–91.

Kawae, N. Shigechi, T. Kanemaru, K. Yamada, T. (1989). Water vapor absorption into laminar film flow of a lithium bromide water solution (influence of variable properties and inlet film thickness on absorption mass transfer rate). Journal of the Heat Transfer Society of Japan. 8, pp. 58–70.

Kawasaki, H. Watanabe, T. Kanzawa, A. (1999). Proposal of a chemical heat pump with paraldehyde depolymerization for cooling system. Applied Thermal Energy. 19(2), pp. 133–43.

Kenisarin, MM. (2010). High-temperature phase change materials for thermal energy storage. Renewable and Sustainable Energy Reviews. 14(3), pp. 955-970.

Kerskes, H. Mette, B. Bertsch, F. Asenbeck, S. Drück, H. (2011). Development of a thermochemical energy storage for solar thermal applications. Proceedings of ISES solar world congress.

Kerskes, H. Mette, B. Bertsch, F. Asenbeck, S. Drück, H. (2013). Development of a thermo- chemical energy storage for solar thermal applications. Proceedings of ISES. Solar World Congress.

Kessling, W. Laevemann, E. Kapfhammer, C. (1998a). Energy storage for desiccant cooling systems component development. Solar Energy. 64(4–6), pp. 209–221.

Kessling, W. Laevemann, E. Peltzer, M. (1998b). Energy storage in open cycle liquid desiccant cooling systems. International Journal of Refrigeration. 21(2), pp. 150–156.

Köll, R. van Helden, W. Engel, G. Wagner, W. Dang, B. Jänchen, J. Kerskes, H. Badenhop, T. Herzog, T. (2017). Experimental Investigation of a realistic scale seasonal solar sorption storage system for buildings. Solar Energy. 155, pp. 388–397.

Krönauer, A. Lävemann, E. Brückner, S. Hauer, A. (2015). Mobile sorption heat storage in industrial waste heat recovery. Energy Procedia. 73, pp.272–280.

Kurt, C. and Bittner, J. (2000). Sodium Hydroxide, in Ullmann's Encyclopedia of Industrial Chemistry. Wiley-VCH Verlag GmbH & Co. KGaA.

Kuznik, F. Johannes, K. Obrecht, Ch. David, D. (2018). A review on recent developments in physisorption thermal energy storage for building applications. Renewable and Sustainable Energy Reviews. 94, pp. 576–586.

Lam, RK. Smith, JW. Rizzuto, AM. Karslıoğlu, O. Bluhm, H. Saykally, RJ. (2017) Reversed interfacial fractionation of carbonate and bicarbonate evidenced by X-ray photoemission spectroscopy. The Journal of Chemical Physics 146.

LaQue, FL. and Copson, HR. (1963). Corrosion resistance of metals and alloys. New York (NY): Reinhold Publishers. pp. 365.

Lazcano-Véliz, Y. Siqueiros, J. Juárez-Romero, D. Morales, LI. Torres-Merino, J. (2014). Analysis of effective wetting area of a horizontal generator for an absorption heat transformer. Applied Thermal Engineering. 62(2), pp.845-849.

Lazcano-Véliz, Y. Hernández, JA. Juárez-Romero, D. Huicochea-Rodríguez, A. Álvarez-Gallegos, A. Siqueiros, J. (2016). Improved of effective wetting area and film thickness on a concentric helical bank of a generator for an absorption heat transformer, Applied Thermal Engineering. 106, pp. 1319-1328.

Le Pierrès, N. Huaylla, F. Stutz, B. Perraud, J. (2017). Long-term solar heat storage process by absorption with the KCOOH/H2O couple: experimental investigation. Energy. 141, pp. 1313–1323.

Le Pierrès, N. Liu, H. Luo, L. (2011). CaCl2/H2O absorption seasonal storage of solar heat. In: Proceedings of the international conference for sustainable energy storage, Ulster, Belfast. Feb. 21–25.

Lee, S. (1994). Heat and mass transfer enhancement in an absorber using active particles. München Discussion Meeting.

Lehmann, EH. Frei, G. Kühne, G. Boillat, P. (2007). The micro-setup for neutron imaging: A major step forward to improve the spatial resolution. Nuclear Instruments and Methods in Physics Research Section A: Accelerators, Spectrometers, Detectors and Associated Equipment. 576(2–3), pp. 389-396.

Lehmann, EH. Vontobel, P. Kardjilov, N. (2004). Hydrogen distribution measurements by neutrons. Applied Radiation and Isotopes. 61(4), pp. 503-509.

Li, F. Li, Z. Wang, S. Li, S. Men, Z. Ouyang, S. Sun, C. (2017). Structure of water molecules from Raman measurements of cooling different concentrations of NaOH solutions. Spectrochimica Acta Part A: Molecular and Biomolecular Spectroscopy. 183, pp. 425–430.

Lottner, V. Schulz, ME. Hahne, E. (2000). Solar-assisted district heating plants: status of the german programme solarthermie-2000. Solar Energy. 69, pp.449–459.

McKenna, SP. and McGillis, WR. (2004). The role of free-surface turbulence and surfactants in air– water gas transfer. International Journal of Heat and Mass Transfer. 47(3), pp. 539-553.

McCabe, WL. and Wilson, HR. (1942). Specific Heats and Heats of Dilution of Concentrated Sodium Hydroxide Solutions. Industrial & Engineering Chemistry. 34(5), pp. 558-566

Mette, B. Kerskes, H. Drück, H. (2012a). Concepts of long-term thermochemical energy storage for solar thermal applications – selected examples. Energy Procedia. 30 pp. 321–330.

Mette, B. Kerskes, H. Drück, H. (2012b). New high efficient regeneration process for thermo- chemical energy stores. Proceedings of innostock.

Michel, B. Mazet, N. Neveu, P. (2014). Experimental investigation of an innovative thermo- chemical process operating with a hydrate salt and moist air for thermal storage of solar energy: global performance. Applied Energy. 129, pp. 177–186.

Mortazavi, M. Isfahani, RN. Bigham, S. Moghaddam, S. (2015). Absorption characteristics of falling film LiBr (lithium bromide) solution over a finned structure. Energy. 87, pp. 270-278,

N'Tsoukpoe, KE. Le Pierrès, N. Luo, L. (2013). Experimentation of a LiBr-H2O absorption process for long-term solar thermal storage: prototype design and first results. Energy 53, pp. 179–98.

N'Tsoukpoe, KE. Liu, H. Le Pierrès, N. Luo, L. (2009). A review on long-term sorption solar energy storage. Renewable and Sustainable Energy Reviews. 13(9), pp. 2385–2396.

NACE (1971) Task Group T5-A report, Materials Protection and Performance 10, 7. pp. 39.

National Research Council. 1928. International Critical Tables of Numerical Data, Physics, Chemistry and Technology vol.III. pp. 79. Washington, DC: The National Academies Press. https://doi.org/10.17226/20230.

Niegodajew, P. Asendrych, D. (2017). An interfacial heat transfer in a countercurrent gas–liquid flow in a trickle bed reactor. International Journal of Heat and Mass Transfer. 108(A), pp. 703-711.

Nielsen, K. (2003). Thermal energy storage—a state-of-the-art. A report within the research program Smart Energy-Efficient Buildings at the Norwegian University of Science and Technology and SINTEF.

Nonnen, T. Beckert, S. Gleichmann, K. Brandt, A. Unger, B. Kerskes, H. Mette, B. Bonk, S. Badenhop, T. Salg, F. Gläser, R. (2016). A Thermochemical long-term heat storage system based on a salt/zeolite composite. Chemical Engineering and Technology. 39, pp. 2427–2434.

Olsson, J. Jernqvist, Å. Aly, G. (1997). Thermophysical properties of aqueous NaOHH2O solutions at high concentrations. International Journal of Thermophysics. 18, pp. 779–793.

Palomba, V. and Frazzica, A. (2018). Recent advancements in sorption technology for solar thermal energy storage applications. Solar Energy. 192, pp. 69-105.

Palomba, V. Vasta, S. Freni, A. (2017). Experimental testing of AQSOA FAM Z02/water ad- sorption system for heat and cold storage. Applied Thermal Engineering. 124, pp. 967–974.

Perry, RH. (2007) Perry's chemical engineers' handbook. eighth ed. McGraw-hill.

Persad, AH. and Ward, CA. (2016) Expressions for the Evaporation and Condensation Coefficients in the Hertz-Knudsen Relation. Chemical Reviews. 116 pp. 7727–7767

Peter, O. (1946). Neutronen-Durchleuchtung. Zeitschrift für Naturforschung A, 1(10), pp. 557-559.

Quinnell, JA. Davidson, JH. Burch, J. (2011) Liquid calcium chloride solar storage: concept and analysis. Journal of Solar Energy Engineering. 133. 10.1115/ES2010-90181.

Raab, S. Mangold, D. Heidemann, W. Müller-Steinhagen, H. (2004). Solar assisted district heating system with seasonal hot water heat store in Friedrichshafen (Germany). In: The 5th ISES Europe Solar Conference, Freiburg, Germany (20–23 June).

Rathgeber, Ch. Hiebler, S. Lävemann, E. Dolado, P. Lazaro, A. Gasia, J. de Gracia, A. Miró, L. Cabeza, LF. König-Haagen, A. Brüggemann, D. Campos-Celador, A. Franquet, E. Fumey, B. Dannemand, M. Badenhop, T. Diriken, J. Nielsen, JE. Hauer, A. (2016). IEA SHC task 42/ECES Annex 29 – a simple tool for the economic evaluation of thermal energy storages. Energy Procedia. 91, pp. 197–206.

Reddy, KS. Mudgal, V. Mallick, TK. (2018). Review of latent heat thermal energy storage for improved material stability and effective load management. Journal of Energy Storage. 15, pp. 205-227

Regin, AF. Solanki, SC. Saini, JS. (2008). Heat transfer characteristics of thermal energy storage system using PCM capsules: A review, Renewable and Sustainable Energy Reviews. 12(9), pp. 2438-2458.

Roelands, M. Cuypers, R. Kruit, K. Oversloot, H. de Jong, A.J. van ‘t Spijker, H. Duvalois, W. van Vliet, L. Hoegaerts, C. (2015). Preparation & characterization of sodium sulfide hydrates for application in thermochemical storage systems. Energy Procedia. 70, pp. 257 – 266.

Rommel, M. Hauer, A. van Helden, W. (2016). IEA SHC task 42/ECES Annex 29 compact thermal energy storage. Energy Procedia. 91, pp. 226–230.

Rossini, FD. Wagman, DD. Evans, WH. Levine, S. Jaffe, I. (1952). Circular of the Bureau of Standards no. 500: selected values of chemical thermodynamic properties. National Bureau of Standards.

Scapino, L. Zondag, HA. van Bael, J. Diriken, J. Rindt, CCM. (2017a). Energy density and storage capacity cost comparison of conceptual solid and liquid sorption seasonal heat storage systems for low-temperature space heating. Renewable and Sustainable Energy Reviews. 76, pp. 1314–1331.

Scapino, L. Zondag, HA. van Bael, J. Diriken, J. Rindt, CCM. (2017b) Sorption heat storage for long-term low-temperature applications: a review on the advancements at material and prototype scale. Applied Energy. 190, pp. 920–948.

Schillinger, B. Abele, H. Brunner, J. Frei, G. Gähler, R. Gildemeister, A. Hillenbach, A. Lehmann, E. Vontobel, P. (2005). Detection systems for short-time stroboscopic neutron imaging and measurements on a rotating engine. Nuclear Instruments and Methods in Physics Research Section A: Accelerators, Spectrometers, Detectors and Associated Equipment. 542(1–3), pp. 142-147.

Schmidt, T. Mangold, D. Müller-Steinhagen, H. (2004). Central solar heating plants with seasonal storage in Germany. Solar Energy. 76, pp. 165– 174.

Shaffer, CD. (1997). Quantification of hydroxide in aqueous solutions by Raman spectroscopy. article, West Mifflin, Pennsylvania.

Sisoev, GM. Matar, OK. Lawrence, ChJ. (1986). Absorption of gas into a wavy falling film, Chemical Engineering Science. 60(3), pp. 827-838.

Sköld, K. and Price, DL. (1986). Neutron scattering, Academic Press, Orlando.

Solé, A. Martorell, I. Cabeza, LF. (2015). State of the art on gas–solid thermochemical energy storage systems and reactors for building applications. Renewable and Sustainable Energy Reviews. 47, pp. 386–398.

SOLVAY (1967) Technical and Engineering Service, Caustic Soda - Bulletin N° 6

Srikhirin, P. Aphornratana, S. Chungpaibulpatana, S. (2001), A review of absorption refrigeration technologies. Renewable and Sustainable Energy Reviews. 5, pp. 343–372.

Srivastava, NC. Eames, IW. (1998). A review of adsorbents and adsorbates in solid- vapour adsorption heat pump systems. Applied Thermal Engineering. 18(9–10), pp. 707–714.

Stehlík, P. Jegla, Z. Kilkovský, B. (2014). Possibilities of intensifying heat transfer through finned surfaces in heat exchangers for high temperature applications. Applied Thermal Engineering. 70(2), pp. 1283-1287.

Tarbuck, TL. Ota, ST. Richmond, GL. (2006). Spectroscopic Studies of Solvated Hydrogen and Hydroxide Ions at Aqueous Surfaces. Journal of the American Chemical Society 128, 14519–14527.

Tatsidjodoung, P. Le Pierrès, N. Heintz, J. Lagre, D. Luo, L. Durier, F. (2016). Experimental and numerical investigations of a zeolite 13X/water reactor for solar heat storage in buildings. Energy Conversion and Management. 108, pp. 488–500.

Toor, HL. and Marchello, JM. (1958) Film-penetration model for mass and heat transfer. AIChE. 4, pp. 97–101.

Trausel, F. de Jong, A.J. Cuypers, R. (2014) A review on properties of salt hydrates for thermochemical storage. Energy Procedia. 48, pp. 447 – 452.

Tremsin, AS. McPhate, JB. Vallerga, JV. Siegmund, OHW. Hull, JS. Feller, WB. Lehmann, E. (2009a). Detection efficiency, spatial and timing resolution of thermal and cold neutron counting MCP detectors. Nuclear Instruments and Methods in Physics Research Section A: Accelerators, Spectrometers, Detectors and Associated Equipment. 604(1–2), pp. 140-143.

Tremsin, AS. McPhate, JB. Vallerga, JV. Siegmund, OHW. Hull, JS. Feller, WB. Lehmann E. (2009b) High-resolution neutron radiography with microchannel plates: Proof-of-principle experiments at PSI. Nuclear Instruments and Methods in Physics Research Section A: Accelerators, Spectrometers, Detectors and Associated Equipment. 605(1–2), pp. 103-106.

Trtik, P. Hovind, J. Grünzweig, C. Bollhalder, A. Thominet, V. David, C. Kaestner, A. Lehmann, EH. (2015). Improving the Spatial Resolution of Neutron Imaging at Paul Scherrer Institut – The Neutron Microscope Project. Physics Procedia. 69, pp. 169-176,

Trtik, P. Morgano, M. Bentz, R. Lehmann, E. (2016). 100Hz neutron radiography at the BOA beamline using a parabolic focussing guide. MethodsX. 3, pp. 535-41

Tsai, BB. and Perez-Blanco, H. (1998). Limits of mass transfer enhancement in lithium bromide-water absorbers by active techniques. International journal of heat and mass transfer. 41, pp. 2409–16.

Vaidya, PD. and Kenig, EY. (2007). Gas–Liquid Reaction Kinetics: A Review of Determination Methods. Chemical Engineering Communications. 194. pp. 1543–1565.

van Alebeek, R. Scapino, L. Beving, MAJM. Gaeini, M. Rindt, CCM. Zondag, HA. (2018). Investigation of a household-scale open sorption energy storage system based on the zeolite 13X/water reacting pair. Applied Thermal Engineering. 139, pp. 325–33.

van der Wekken, BJC. and Wassenaar, RH. (1988). Simultaneous heat and mass transfer accompanying absorption in laminar flow over a cooled wall. International Journal of Refrigeration. 11, pp. 70–77.

van Helden, W. Yamaha, M. Rathgeber, Ch. Hauer, A. Huaylla, F. Le Pierrès, N. Stutz, B. Mette, B. Dolado, P. Lazaro, A. Mazo, J. Dannemand, M. Furbo, S. Campos-Celador, A. Diarce, G. Cuypers, R. König-Haagen, A. Höhlein, S. Brüggemann, D. Fumey, B. Weber, R. Köll, R. Wagner, W. Daguenet-Frick, X. Gantenbein, P. Kuznik, F. (2016). IEA SHC task 42/ ECES Annex 29 – working group B: applications of compact thermal energy storage. Energy Procedia. 91, pp. 231–45.

Vasiliev, LL. and Kulakov, AG. (2003). Heat Pipe Applications in Sorption Refrigerators. In: Kakaç S., Smirnov H.F., Avelino M.R. (eds) Low Temperature and Cryogenic Refrigeration. NATO Science Series (Series II: Mathematics, Physics and Chemistry), vol 99. Springer, Dordrecht.

Walrafen, GE. and Douglas RT. (2006). Raman spectra from very concentrated aqueous NaOH and from wet and dry, solid, and anhydrous molten, LiOH, NaOH, and KOH. The Journal of Chemical Physics. 124(11).

Wang, LW. Wang, RZ. Oliveira, RG. (2009). A review on adsorption working pairs for refrigeration. Renewable and Sustainable Energy Reviews. 13(3), pp. 518–534.

Wang, Z. Orejon, D. Sefianec, K. Takata, Y. (2019). Water vapor uptake into hygroscopic lithium bromide desiccant droplets: mechanisms of droplet growth and spreading. Physical Chemistry Chemical Physics. 21, pp. 1046-1058.

Warnakulasuriya, FSK. Worek, WM. (2006) Adiabatic water absorption properties of an aqueous absorbent at very low pressures in a spray absorber. International Journal of Heat and Mass Transfer. 49(9-10), pp. 1592-1602.

Weber, R. (2010). Long-term heat storage with NaOH. EUROSUN, Graz, Austria, Sep 28 to Oct 1.

Weber, R. and Dorer, V. (2008) Long-term heat storage with NaOH. Vacuum. 82, pp. 708–716.

Weber, R. Asenbeck, S. Kerskes, H. Drück, H. (2016). SolSpaces – testing and performance analysis of a segmented sorption store for solar thermal space heating. Energy Procedia, 91, pp. 250–258.

Whitman, WG. (1923). Preliminary experimental confirmation of the two-film theory of gas absorption. Chem. Met. Eng. 29, pp. 146–148.

Won, YS. and Mills, AF. (1982). Correlation of the effects of viscosity and surface tension on gas absorption rates into freely falling turbulent liquid films. International Journal of Heat and Mass Transfer. 25(2), pp. 223-229.

Wongsuwan, W. Kumar, S. Neveu, P. Meunier, F. (2001). A review of chemical heat pump technology and applications. Applied Thermal Engineering. 21(15), pp. 1489–519.

Yan, T. Wang, RZ. Li, TX. (2018). Experimental investigation on thermochemical heat storage using manganese chloride/ammonia. Energy. 143, pp. 562–574.

Yasuda, M. Takeya, F. Hine, F. (1983). Corrosion Behavior of Nickel in Concentrated NaOH Solutions under Heat Transfer Conditions. Corrosion 39(10), pp. 399-406.

Yosemite. https://yosemite.epa.gov/sab/sabproduct.nsf/953CCBEB820F047085257 7 920076316D/$File/NaOH+Practicality+Study.pdf, sourced 01.2020

Yu, N. Wang, RZ. Wang, LW. (2013). Sorption thermal storage for solar energy. Progress in Energy and Combustion Science. 39, pp. 489–514.

Yüksel, ML. and Schlündler, EU. (1987). Heat and mass transfer in non isothermal absorption of gases in falling liquid films part I: theoretical description and numerical calculation of turbulent falling film heat and mass transfer. Chemical Engineering and Processing. 22, pp. 203–213

Zalba, B. Marin, JM. Cabeza, LF. Mehling, H. (2003). Review on thermal energy storage with phase change: materials, heat transfer analysis and applications. Applied Thermal Engineering. 23, pp. 251–283.

Zettl, B. and Lachner, M. (2015). An Advanced Desorption Concept for TES-Materials, Proc. International Conference on Solar Heating and Cooling for Buildings and Industry. SHC 2015, 2-4 Dec 2015, Istanbul.

Zhakhovsky, VV. Kryukov, AP. Levashov, VY. Shishkova, IN. Anisimov, SI. (2019). Mass and heat transfer between evaporation and condensation surfaces: Atomistic simulation and solution of Boltzmann kinetic equation. Proceedings of the National Academy of Sciences of the United States of America. 116, pp. 18209–18217.

Zhang, X. Li, M. Shi, W. Wang, B. Li, X. (2014). Experimental investigation on charging and discharging performance of absorption thermal energy storage system. Energy Conversion and Management. 85, pp. 425–434.

Zhang, YN. Wang, RZ. Li, TX. (2017). Experimental investigation on an open sorption thermal storage system for space heating. Energy. 141, pp. 2421–2433.

Zhao, DL. Li, Y. Dai, YJ. Wang, RZ. (2011). Optimal study of a solar air heating system with pebble bed energy storage. Energy Conversion and Management. 52, pp. 2392–2400.

Zhao, YJ. Wang, RZ. Li, TX. Nomura, Y. (2016). Investigation of a 10 kWh sorption heat storage device for effective utilization of low-grade thermal energy. Energy. 113, pp. 739–747.

Zondag, H. Kalbasenka, A. van Essen, M. (2008). First studies in reactor concepts for thermochemical storage. Proceedings of the Eurosun.

Zondag, H. Kikkert, B. Smeding, S. de Boer, R. Bakker, M. (2013). Prototype thermochemical heat storage with open reactor system. Applied Energy. 109, pp. 360–265.

Zondag, HA. (2015). Chapter 6 - Sorption Heat Storage, Editor(s): Bent Sørensen, Solar Energy Storage, Academic Press. pp. 135-154.

Appendix A: Aqueous sodium hydroxide

In the following appendix, important attributes of aqueous sodium hydroxide are listed. Where available, a table, diagram and equation is provided. Reference to some of the equations is made in the text.

Density

Concentration $[g_{NaOH}/g_{sol}]$	Temperature $[^{o}C]$										
	0	**10**	**20**	**30**	**40**	**50**	**60**	**70**	**80**	**90**	**100**
0.00	999.9	999.8	998.2	995.7	992.2	988.1	983.2	977.9	971.8	965.3	958.4
0.02	1024.4	1023.0	1020.7	1017.7	1013.9	1009.5	1004.5	998.9	992.9	986.8	979.7
0.04	1048.2	1045.9	1042.8	1039.3	1035.2	1030.5	1025.4	1019.8	1013.9	1007.5	1000.9
0.06	1071.3	1068.3	1064.8	1060.9	1056.4	1051.7	1046.3	1040.7	1034.7	1028.4	1022.0
0.08	1094.3	1090.8	1086.9	1082.6	1078.0	1073.0	1067.6	1061.9	1056.0	1049.7	1043.2
0.10	1117.1	1113.2	1108.9	1104.3	1099.5	1094.2	1088.9	1083.1	1077.1	1070.8	1064.3
0.12	1139.9	1135.5	1130.9	1126.1	1121.0	1115.7	1110.1	1104.3	1098.3	1092.0	1085.5
0.14	1162.4	1157.8	1153.0	1148.0	1142.8	1137.3	1131.6	1125.7	1119.5	1113.2	1106.6
0.16	1184.9	1180.1	1175.1	1169.9	1164.5	1158.8	1153.1	1147.1	1140.8	1134.3	1127.7
0.18	1207.3	1202.3	1197.2	1191.8	1186.3	1180.5	1174.6	1168.5	1162.1	1155.6	1148.9
0.20	1229.6	1224.4	1219.1	1213.6	1207.9	1202.0	1196.0	1189.8	1183.3	1176.8	1170.0
0.22	1251.9	1246.5	1241.1	1235.4	1229.6	1223.6	1217.4	1211.1	1204.6	1198.0	1191.2
0.24	1274.1	1268.6	1262.9	1257.1	1251.2	1245.1	1238.8	1232.4	1225.9	1219.2	1212.4
0.26	1296.3	1290.6	1284.8	1278.9	1272.8	1266.6	1260.3	1253.8	1247.2	1240.5	1233.6
0.28	1318.2	1312.4	1306.4	1300.2	1294.2	1287.8	1281.4	1275.0	1268.2	1261.5	1254.6
0.30	1340.0 *	1334.0	1327.9	1321.7	1315.4	1309.0	1302.5	1295.9	1289.2	1282.4	1275.5
0.32	1361.4*	1355.2	1349.0	1342.7	1336.2	1329.8	1323.2	1316.5	1309.7	1302.9	1296.0
0.34	1382.3*	1376.0*	1369.6	1363.2	1356.6	1350.1	1343.4	1336.7	1329.9	1323.0	1316.1
0.36	1403.0*	1396.5*	1390.0	1383.5	1376.8	1370.2	1363.4	1356.7	1349.8	1342.9	1336.0
0.38	1423.4*	1416.8*	1401.1	1403.5	1396.7	1390.0	1383.2	1376.3	1369.5	1362.6	1355.6
0.40	1443.5*	1436.7*	1430.0	1423.2	1416.4	1409.5	1402.7	1395.8	1388.9	1382.0	1375.0
0.42	1463.2*	1456.1*	1449.4	1442.5	1435.6	1428.7	1421.7	1414.8	1407.9	1400.9	1394.0
0.44	1482.5*	1475.5*	1468.5	1461.5	1454.5	1447.5	1440.5	1433.5	1426.6	1419.6	1412.7
0.46	1501.8*	1494.7	1487.3	1480.5	1473.4	1466.3	1459.3	1452.3	1445.4	1438.4	1431.5
0.48	1521.0*	1513.8	1506.5	1499.4	1492.2	1485.1	1478.1	1471.1	1464.1	1457.2	1450.3
0.50	1540.0*	1532.6*	1525.3	1518.1	1510.9	1503.8	1496.7	1489.7	1482.7	1475.9	1469.0

(*) saturated solutions

Source: National Research Council (1928).

Density of Aqueous Solutions of NaOH

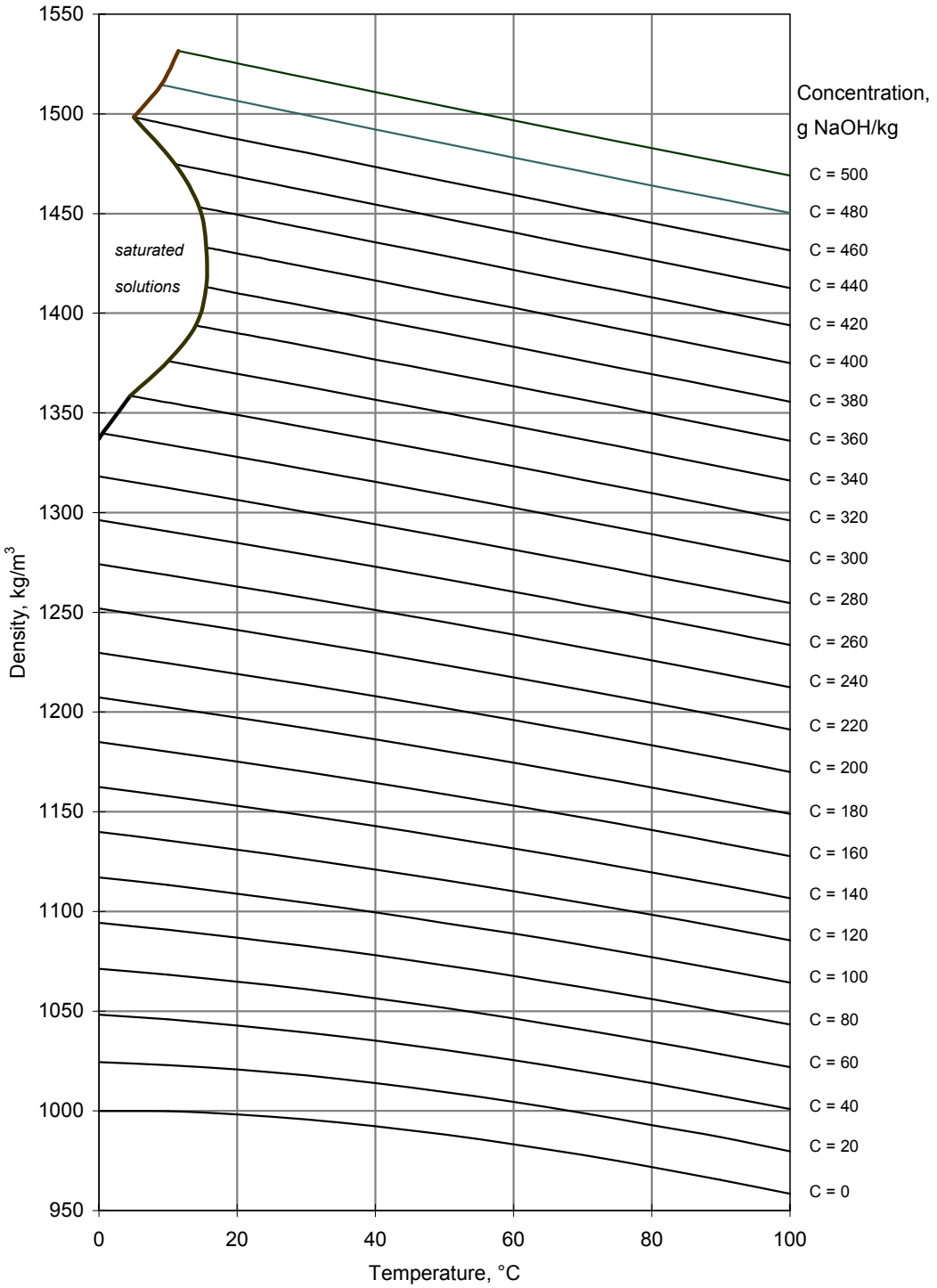

Source: National Research Council (1928).

$$\rho = b_1 + b_2\vartheta_{sol} + b_3\vartheta_{sol}^2, \text{ Equation A1}$$

$$b_1 = k_{D0} + k_{D1}X_w^{0.5} + k_{D2}X_w + k_{D3}X_w^{1.5} + k_{D4}X_w^2 + k_{D5}X_w^{2.5}$$

$$b_2 = l_{D0} + l_{D1}X_w^{0.5} + l_{D2}X_w + l_{D3}X_w^{1.5} + l_{D4}X_w^2 + l_{D5}X_w^{2.5}$$

$$b_3 = m_{D0} + m_{D1}X_w^{0.5} + m_{D2}X_w + m_{D3}X_w^{1.5} + m_{D4}X_w^2 + m_{D5}X_w^{2.5}$$

Where ρ is the density in $[kg/m^3]$, ϑ_{sol} is the temperature in $[^oC]$and X_w is the mass fraction in $[g_{H_2O}/g_{sol}]$.

numerical values of k		numerical values of m		numerical values of l	
k_{D0}	5007.2279636	m_{D0}	0.24436776978	l_{D0}	-64.786269079
k_{D1}	-25131.164248	m_{D1}	-1.9737722344	l_{D1}	525.34360564
k_{D2}	74107.692582	m_{D2}	6.04601497138	l_{D2}	-1608.4471903
k_{D3}	-104657.48684	m_{D3}	-8.9090614947	l_{D3}	2350.9753235
k_{D4}	69821.773186	m_{D4}	6.37146769397	l_{D4}	-1660.9035108
k_{D5}	-18145.91181	m_{D5}	-1.7816083111	l_{D5}	457.64374355

The correlation is valid within the temperature and concentration ranges indicated.

Temperature range	Concentration range
$[^oC]$	$[g_{NaOH}/g_{sol}]$
$0 \le \vartheta_{sol} < 10$	$0 \le X_{NaOH} \le 0.200$
$10 \le \vartheta_{sol} < 20$	$0 \le X_{NaOH} \le 0.300$
$20 \le \vartheta_{sol} < 60$	$0 \le X_{NaOH} \le 0.500$
$60 \le \vartheta_{sol} < 70$	$0 \le X_{NaOH} \le 0.600$
$70 \le \vartheta_{sol} < 150$	$0 \le X_{NaOH} \le 0.700$
$150 \le \vartheta_{sol} < 200$	$0 \le X_{NaOH} \le 0.800$

Source: Olsson et all (1997)

Enthalpy

(Basis : Liquid Water and NaOH at Infinite Dilution at 20°C)

Concentration $[g_{NaOH}/g_{sol}]$	Temperature $[^{O}C]$																				
	0	10	20	30	40	50	60	70	80	90	100	110	120	130	140	150	160	170	180	190	200
0.00	0.0	41.8	84.6	126.8	168.9	211.1	254.6	299.5	341.5	383.0	424.6	466.8	508.7	550.6	592.7	635.0	677.5	720.1	763.1	806.4	849.9
0.02	1.2	41.9	82.3	123.0	163.8	204.6	245.6	287.3	328.4	369.5	410.6	452.0	493.4	534.8	576.4	618.1	660.0	702.1	744.4	786.9	829.7
0.04	1.4	41.1	79.7	119.2	158.8	198.5	237.5	276.5	316.9	357.5	398.2	439.0	479.8	520.8	561.9	603.0	644.4	685.8	727.5	769.3	811.4
0.06	1.0	39.7	76.9	115.5	154.1	192.9	230.4	267.3	307.0	347.2	387.5	427.6	468.0	508.5	549.0	589.7	630.5	671.4	712.4	753.6	795.0
0.08	0.0	37.9	74.2	111.9	149.9	187.9	224.3	259.6	298.7	338.5	378.3	417.8	457.8	497.8	538.0	578.1	618.4	658.7	699.2	739.8	780.5
0.10	-1.3	36.0	71.6	108.8	146.1	183.6	219.2	253.4	292.0	331.4	370.8	409.7	449.3	488.9	528.6	568.3	608.0	647.8	687.8	727.8	767.9
0.12	-2.7	34.0	69.3	106.1	143.0	180.1	215.2	248.7	286.8	325.8	364.8	403.3	442.5	481.6	520.8	560.1	599.4	638.7	678.1	717.6	757.1
0.14	-3.9	32.2	67.5	104.0	140.6	177.4	212.3	245.5	283.2	321.8	360.4	398.5	437.2	476.0	514.8	553.6	592.4	631.3	670.2	709.1	748.1
0.16	-4.9	30.8	66.3	102.6	139.1	175.7	210.7	243.8	281.1	319.4	357.6	395.3	433.6	472.0	510.3	548.7	587.1	625.5	663.9	702.4	740.8
0.18	-5.3	30.1	65.9	102.1	138.5	175.0	210.2	243.5	280.6	318.5	356.4	393.7	431.6	469.6	507.5	545.5	583.5	621.4	659.4	697.3	735.3
0.20	-5.1	30.2	66.4	102.5	138.9	175.4	211.0	244.8	281.6	319.1	356.6	393.6	431.2	468.8	506.3	543.9	581.4	619.0	656.5	694.0	731.5
0.22	-3.9	31.3	67.9	104.1	140.5	177.0	213.1	247.5	284.1	321.3	358.5	395.2	432.4	469.6	506.7	543.9	581.0	618.2	655.3	692.3	729.4
0.24	-1.5	33.6	70.7	106.9	143.3	179.9	216.6	251.7	288.1	325.0	361.8	398.2	435.1	471.9	508.7	545.4	582.2	618.9	655.6	692.3	728.9
0.26	2.2	37.4	74.8	111.1	147.6	184.2	221.5	257.5	293.7	330.2	366.6	402.9	439.3	475.7	512.2	548.6	584.9	621.3	657.6	693.8	730.0
0.28	7.4	42.8	80.5	116.7	153.3	190.0	227.8	264.7	300.7	336.9	373.0	409.0	445.1	481.1	517.2	553.2	589.2	625.2	661.1	696.9	732.8
0.30		50.0	87.8	124.0	160.6	197.3	235.6	273.3	309.2	345.1	380.8	416.6	452.3	488.0	523.7	559.4	595.0	630.6	666.1	701.6	737.0
0.32		59.3	96.9	133.0	169.5	206.2	244.9	283.5	319.3	354.7	390.2	425.7	461.1	496.4	531.7	567.0	602.3	637.5	672.7	707.8	742.8
0.34		70.8	107.9	143.9	180.3	216.9	255.8	295.2	330.7	365.9	401.0	436.3	471.3	506.3	541.2	576.1	611.0	645.9	680.7	715.4	750.2
0.36			121.1	156.9	193.0	229.4	268.4	308.3	343.7	378.5	413.2	448.3	482.9	517.6	552.1	586.7	621.2	655.7	690.2	724.6	758.9
0.38			136.6	171.9	207.7	243.7	282.6	322.9	358.1	392.5	426.9	461.8	496.0	530.3	564.5	598.7	632.9	667.0	701.1	735.1	769.1
0.40			154.4	189.2	224.4	260.1	298.5	339.0	374.0	408.1	442.1	476.6	510.5	544.4	578.3	612.1	645.9	679.7	713.4	747.1	780.7
0.42			174.8	208.9	243.5	278.5	316.1	356.5	391.3	425.0	458.7	492.9	526.5	560.0	593.5	626.9	660.3	693.7	727.1	760.4	793.7
0.44			197.9	231.1	264.8	299.0	335.6	375.6	410.0	443.4	476.6	510.6	543.8	576.9	610.0	643.1	676.1	709.2	742.2	775.1	808.0
0.46			223.9	256.0	288.6	321.8	356.9	396.1	430.2	463.1	496.0	529.7	562.4	595.2	627.9	660.6	693.3	725.9	758.5	791.1	823.7
0.48			252.9	283.6	314.9	346.9	380.0	418.0	451.8	484.3	516.8	550.1	582.5	614.8	647.1	679.5	711.7	744.0	776.2	808.4	840.6
0.50			285.1	314.1	343.9	374.5	405.1	441.5	474.8	506.9	539.0	571.9	603.8	635.8	667.7	699.6	731.5	763.4	795.2	827.0	858.8
0.52			320.5	347.7	375.6	404.5	432.2	466.4	499.1	530.9	562.6	594.9	626.5	658.0	689.6	721.1	752.5	784.0	815.4	846.8	878.2
0.54				384.4	410.2	437.1	461.3	492.8	524.9	556.2	587.5	619.4	650.5	681.6	712.7	743.8	774.8	805.8	836.9	867.9	898.8
0.56					447.8	472.4	492.5	520.6	552.1	583.0	613.8	645.1	675.8	706.4	737.1	767.7	798.3	828.9	859.5	890.1	920.6
0.58						510.4	525.7	549.9	580.6	611.0	641.4	672.0	702.3	732.5	762.7	792.9	823.1	853.2	883.3	913.4	943.5
0.60							561.1	580.7	610.5	640.5	670.4	700.3	730.1	759.8	789.6	819.3	849.0	878.6	908.3	937.9	967.5
0.62							598.7	613.0	641.8	671.3	700.6	729.8	759.1	788.4	817.6	846.9	876.1	905.2	934.4	963.5	992.6
0.64							638.5	646.7	674.4	703.4	732.2	760.5	789.4	818.1	846.9	875.6	904.3	933.0	961.6	990.2	1018.8
0.66								681.8	708.4	736.8	765.1	792.5	820.8	849.1	877.3	905.5	933.7	961.8	989.9	1017.9	1045.9
0.68								718.4	743.7	771.5	799.3	825.6	853.4	881.2	908.9	936.5	964.1	991.7	1019.2	1046.6	1074.0
0.70								756.5	780.3	807.6	834.8	860.0	887.2	914.4	941.6	968.6	995.7	1022.6	1049.5	1076.4	1103.1
0.72								796.0	818.2	844.9	871.5	895.5	922.2	948.8	975.4	1001.8	1028.3	1054.6	1080.9	1107.0	1133.1
0.74								837.0	857.5	883.5	909.5	932.2	958.3	984.3	1010.3	1036.1	1061.9	1087.6	1113.2	1138.7	1164.1
0.76									898.0	923.4	948.7	970.0	995.5	1020.9	1046.2	1071.4	1096.5	1121.5	1146.4	1171.2	1195.8
0.78												1009.0	1033.8	1058.6	1083.2	1107.8	1132.2	1156.5	1180.6	1204.6	1228.4

Source: McCabe and Wilson (1942).

Enthalpy of Aqueous Solutions of NaOH

(Basis: Liquid Water and NaOH at Infinite Dilution at 20°C)

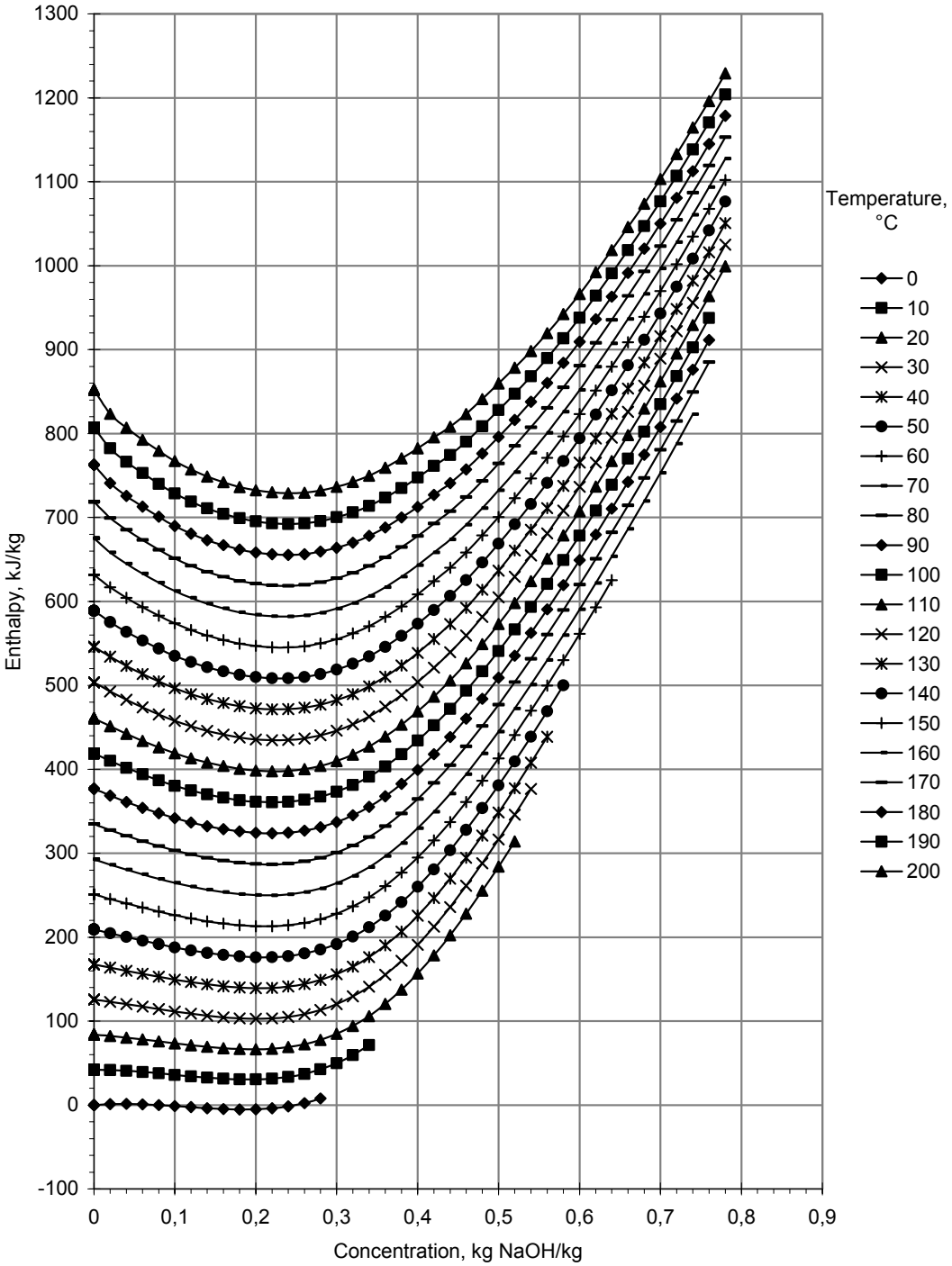

Source: McCabe and Wilson (1942).

$$H = c_1 + c_2\vartheta_{sol} + c_3\vartheta_{sol}^2 + c_4\vartheta_{sol}^3, \textit{ Equation A2}$$

$$c_1 = \frac{k_{H0} + k_{H2}X_w + k_{H4}X_w^2 + k_{H6}X_w^3}{1 + k_{H1}X_w + Hk_{H3}X_w^2 + k_{H5}X_w^3 + k_{H7}X_w^4}$$

$$c_2 = l_{H0} + l_{H1}X_w + \ldots + l_{H8}X_w^8$$

$$c_3 = m_{H0} + m_{H1}X_w + \ldots + m_{H7}X_w^7$$

$$c_4 = n_{H0} + n_{H1}X_w + \ldots + n_{H7}X_w^7$$

Where H is the enthalpy in $[kJ/kg]$, ϑ is the temperature in $[^oC]$and X_w is the mass fraction in $[g_{H_2O}/g_{sol}]$.

numerical values of k		numerical values of l		numerical values of m		numerical values of n	
k_{H0}	1288.4485	l_{H0}	2.3087919	m_{H0}	0.02302860	n_{H0}	-8.5131313E-05
k_{H1}	-0.49649131	l_{H1}	-9.0004252	m_{H1}	-0.37866056	n_{H1}	1.3652823E-03
k_{H2}	-4387.8908	l_{H2}	167.59914	m_{H2}	2.4529593	n_{H2}	-8.7568741E-03
k_{H3}	-4.0915144	l_{H3}	-1051.6368	m_{H3}	-8.2693542	n_{H3}	2.9200398E-02
k_{H4}	4938.2298	l_{H4}	3394.3378	m_{H4}	15.728833	n_{H4}	-5.4882983E-02
k_{H5}	7.2887292	l_{H5}	-6115.0986	m_{H5}	-16.944427	n_{H5}	5.8418034E-02
k_{H6}	-1841.1890	l_{H6}	6220.8249	m_{H6}	9.6254192	n_{H6}	-3.2787483E-02
k_{H7}	-3.0202651	l_{H7}	-3348.8098	m_{H7}	-2.2410628	n_{H7}	7.5445993E-03
		l_{H8}	743.87432				

The correlation is valid within the temperature and concentration ranges indicated.

Temperature range	Concentration range
$[^oC]$	$[g_{NaOH}/g_{sol}]$
$0 \le \vartheta_{sol} \le 4$	$0 \le X_{NaOH} \le 0.220$
$4 \le \vartheta_{sol} \le 10$	$0 \le X_{NaOH} \le 0.320$
$10 \le \vartheta_{sol} \le 15$	$0 \le X_{NaOH} \le 0.420$
$15 \le \vartheta_{sol} \le 26$	$0 \le X_{NaOH} \le 0.460$
$26 \le \vartheta_{sol} \le 37$	$0 \le X_{NaOH} \le 0.560$
$37 \le \vartheta_{sol} \le 48$	$0 \le X_{NaOH} \le 0.600$
$48 \le \vartheta_{sol} \le 60$	$0 \le X_{NaOH} \le 0.660$
$60 \le \vartheta_{sol} \le 71$	$0 \le X_{NaOH} \le 0.700$
$71 \le \vartheta_{sol} \le 82$	$0 \le X_{NaOH} \le 0.720$
$82 \le \vartheta_{sol} \le 93$	$0 \le X_{NaOH} \le 0.760$
$93 \le \vartheta_{sol} \le 204$	$0 \le X_{NaOH} \le 0.780$

Source: Olsson et all (1997)

Heat of solution

The table shows the heat of solution of NaOH at 25 °C.

Final Concentration $[g_{NaOH}/g_{sol}]$	Heat of Solution $[J/g_{NaOH}]$
0.000	1071.8
0.002	1062.8
0.004	1060.8
0.006	1059.7
0.010	1059.6
0.015	1059.7
0.020	1059.9
0.025	1060.3
0.030	1060.8
0.035	1061.5
0.040	1062.2
0.060	1065.7
0.080	1069.4
0.100	1072.5
0.150	1072.9
0.200	1056.5
0.250	1018.6
0.300	958.1
0.350	876.5
0.400	777.6
0.450	666.6
0.500	550.0

Source: Rossini et al. (1952)

Heat of Solution of NaOH at 25°C

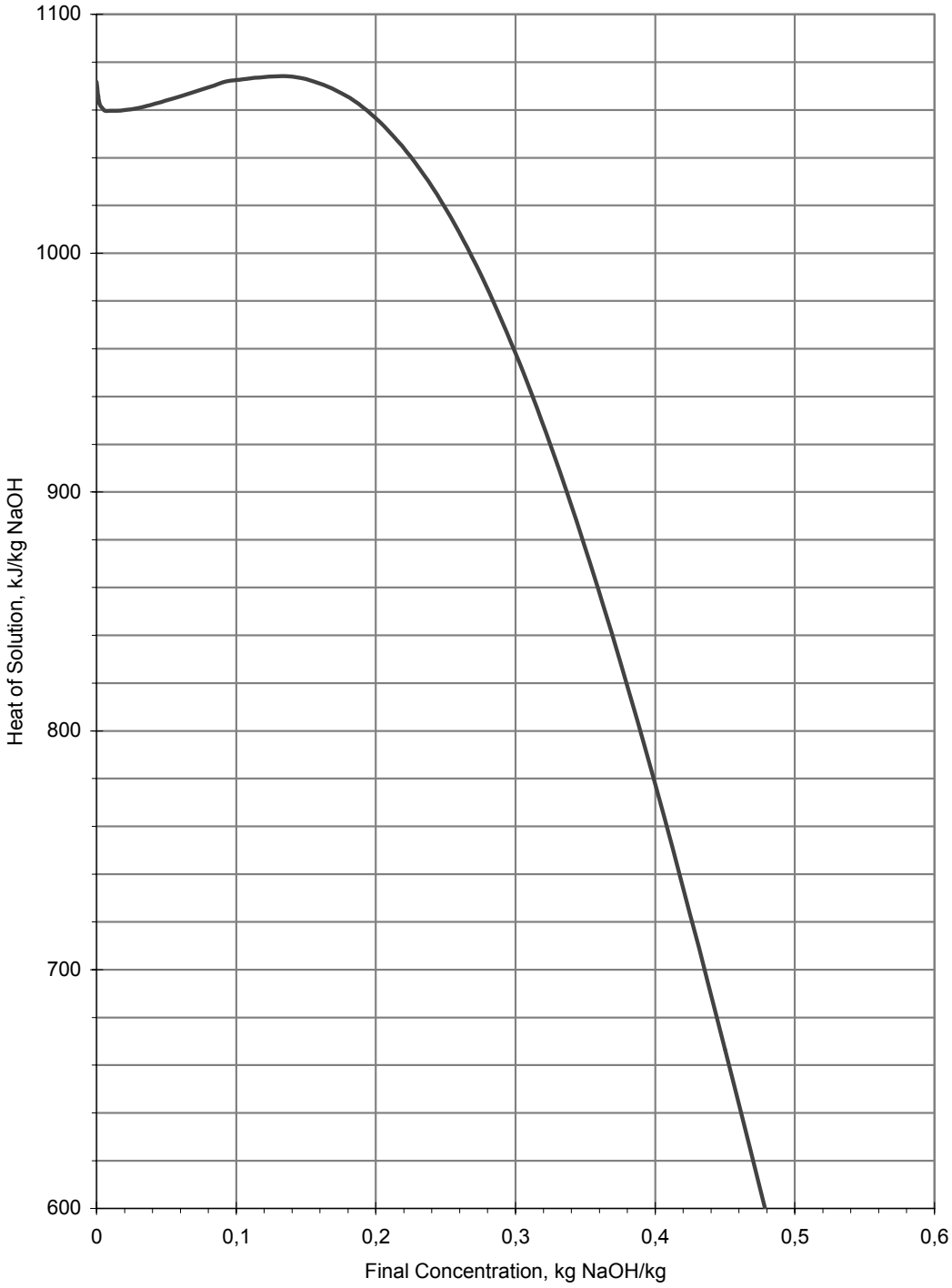

Source: Rossini et al. (1952)

Specific heat

Mass fraction	Temperature [^oC]													
[g_{NaOH}/kg_{sol}]	0	10	20	30	40	50	60	70	80	90	100	110	120	130
0.00	4204	4190	4181	4177	4176	4177	4182	4187	4194	4201	4207			
0.02	4041	4053	4063	4072	4080	4088	4096	4104	4113	4124	4137			
0.04	3921	3947	3969	3985	3999	4010	4019	4027	4035	4043	4053			
0.06	3831	3867	3894	3915	3931	3943	3951	3959	3966	3975	3986			
0.08	3757	3796	3827	3851	3869	3883	3893	3901	3909	3916	3926			
0.10	3695	3738	3772	3798	3819	3834	3845	3852	3858	3863	3868			
0.12	3647	3692	3728	3756	3778	3794	3805	3813	3818	3822	3825			
0.14	3610	3656	3692	3721	3743	3759	3770	3777	3782	3784	3786			
0.16	3575	3624	3663	3693	3716	3732	3743	3750	3754	3756	3758			
0.18	3550	3598	3637	3667	3690	3707	3718	3725	3729	3731	3732			
0.20	3527	3574	3613	3645	3669	3687	3699	3708	3712	3713	3714			
0.22	3508	3554	3593	3624	3649	3669	3682	3691	3696	3696	3697			
0.24	3534	3572	3605	3632	3654	3670	3680	3685	3685	3685				
0.26	3517	3556	3589	3617	3639	3656	3666	3670	3670	3670				
0.28	3499	3539	3573	3602	3624	3641	3651	3656	3656	3656				
0.30	3482	3522	3556	3585	3608	3625	3635	3640	3640	3640				
0.32	3465	3504	3538	3566	3588	3605	3615	3620	3620	3620				
0.34	3444	3484	3517	3545	3566	3581	3590	3594	3594	3594				
0.36	3428	3465	3496	3520	3539	3552	3560	3564	3564	3564				
0.38	3416	3446	3471	3491	3507	3518	3525	3528	3528	3529				
0.40	3398	3424	3445	3460	3472	3479	3483	3485	3484	3484				
0.42	3378	3395	3409	3419	3426	3431	3433	3434	3433	3433				
0.44	3362	3369	3375	3379	3380	3379	3375	3369	3360					
0.46	3322	3326	3327	3326	3324	3320	3314	3306	3297					
0.48	3280	3277	3274	3270	3266	3261	3256	3250	3245					
0.50	3231	3225	3220	3215	3210	3206	3202	3199	3196	3193	3191	3189	3187	3185
0.52	3181	3175	3169	3164	3158	3153	3148	3144	3139	3135	3131	3126	3122	3118
0.54	3120	3111	3104	3098	3093	3088	3084	3079	3074	3068	3062	3054	3045	
0.56	3065	3055	3046	3039	3034	3028	3024	3019	3014	3008	3001	2993	2983	
0.58	3016	3009	3001	2994	2986	2978	2971	2963	2956	2949	2942	2936	2931	
0.60	2955	2950	2943	2936	2929	2921	2913	2906	2898	2892	2886	2881		
0.62	2913	2905	2897	2890	2883	2877	2870	2864	2857	2849	2842	2833		
0.64	2863	2857	2851	2844	2837	2829	2822	2815	2808	2802	2797			
0.66	2825	2818	2811	2804	2797	2791	2784	2777	2770	2762	2753			
0.68	2777	2771	2764	2758	2751	2745	2738	2731	2724	2717				
0.70	2743	2734	2727	2720	2713	2707	2700	2694	2687	2679				
0.72	2701	2694	2686	2678	2671	2664	2658	2652	2646					
0.74	2661	2652	2645	2638	2632	2626	2619	2612						
0.76	2630	2626	2620	2613	2605	2597	2590	2583						
0.78	2599	2590	2583	2578	2572	2565	2557							

Source: McCabe and Wilson (1942).

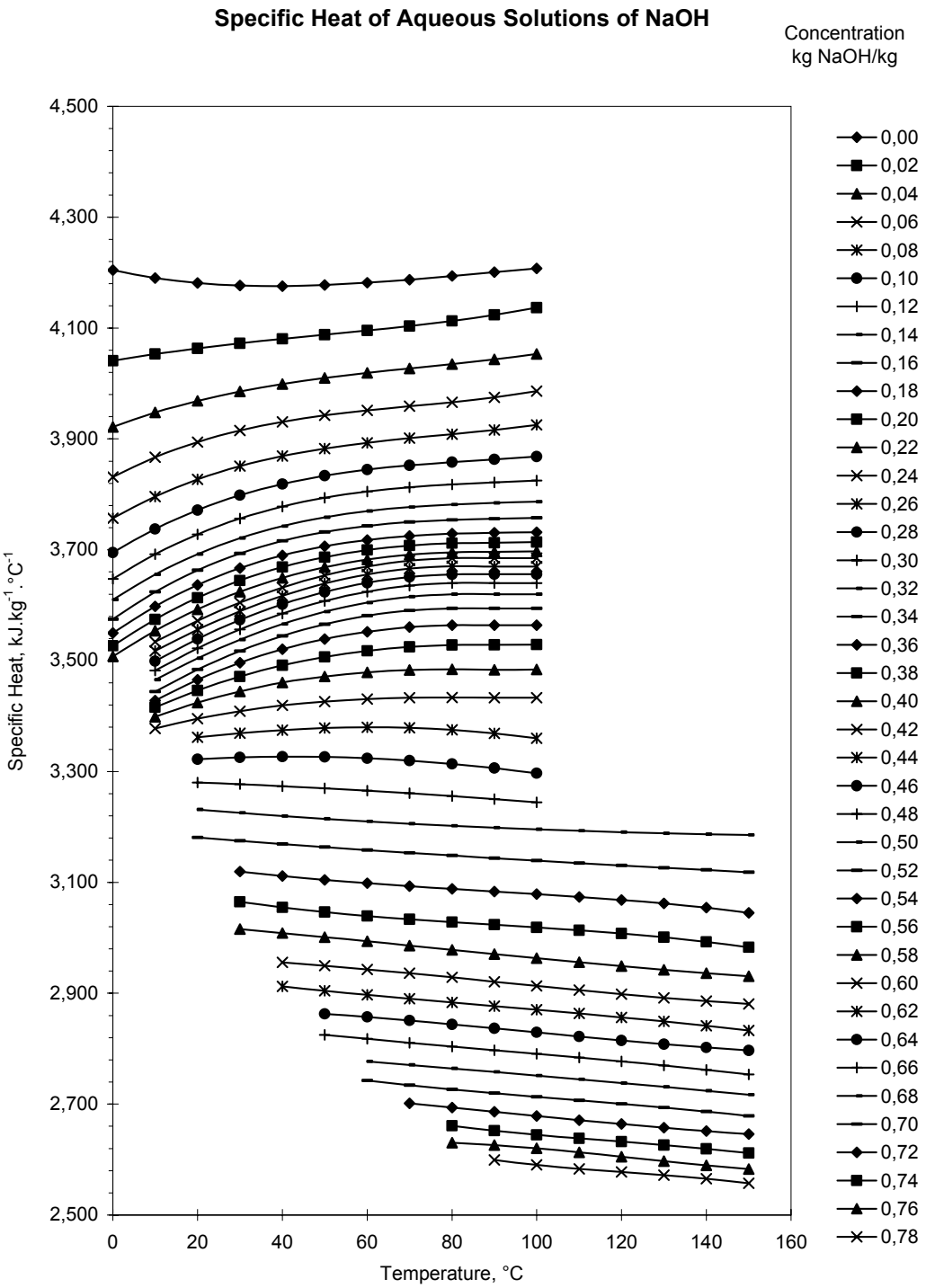

Source: McCabe and Wilson (1942).

$$c_p = c_{p,w} - \sum_{j=1}^{j=5} \sum_{i=1}^{i=5} a_{ij} \tau^i m^j, \text{ Equation A3}$$

Where c_p is the heat capacity of the solution in $[kJ/(kg \cdot K)]$, $c_{p,w}$ is the heat capacity of water in $[kJ/(kg \cdot K)]$, $\tau = \theta_{sol}/\theta_0$ $[-]$ where θ_0 is 273.15 K and θ_{sol} is the solution temperature in $[K]$, and m is the molality of the solution in $[mol/kg]$.

a_{01}	9.8555259E+01	a_{02}	-3.4357815E+01	a_{03}	1.9791083	a_{14}	8.5936388E-02
a_{11}	-3.4501318E+02	a_{12}	1.1674552E+02	a_{13}	-5.3828966	a_{24}	-1.6966718E-02
a_{21}	4.8180532E+02	a_{22}	-1.5776854E+02	a_{23}	5.5124212	a_{34}	-1.4864492E-02
a_{31}	-3.3440616E+02	a_{32}	1.0577045E+02	a_{33}	-2.5430046	a_{05}	7.9944152E-03
a_{41}	1.1516735E+02	a_{42}	-3.5099188E+01	a_{43}	4.5943595E-01	a_{15}	-1.5444457E-02
a_{51}	-1.5708814E+01	a_{52}	4.5935013	a_{04}	-5.6191575E-02	a_{25}	7.5030322E-03

Source: Alexandrov, 2005.

Boiling point

Concentration $[g_{NaOH}/g_{sol}]$	Boiling Point $[^oC]$
0.050	100.2
0.100	101.6
0.150	104.3
0.200	108.0
0.250	112.5
0.300	117.5
0.350	123.1
0.400	129.1
0.450	135.5
0.500	142.5
0.550	150.1
0.600	158.8
0.650	169.0
0.700	181.5
0.750	197.1
0.800	217.5
0.850	244.9
0.900	282.8
0.950	336.7
0.975	372.4
0.987	392.3

Source: Gmelins (1928)

Boiling Point of Aqueous Solutions of NaOH

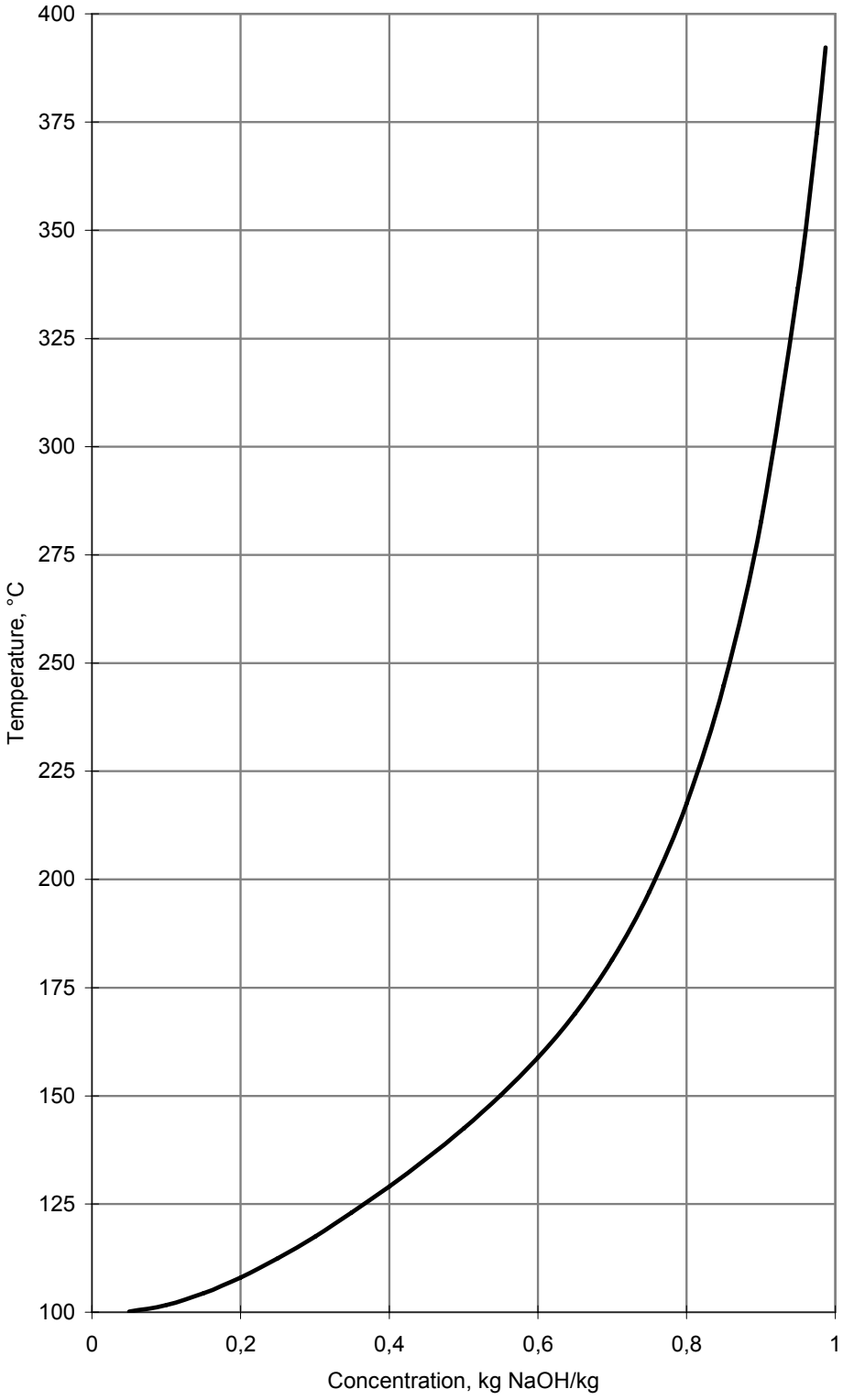

Source: Gmelins (1928)

Viscosity

Mass fraction $[g_{NaOH}/g_{sol}]$	Temperature $[^oC]$								
	0	10	20	30	40	50	60	70	80
0.00	0.97	0.78	0.64	0.54	0.46	0.40	0.35	0.32	0.28
0.05	1.31	1.03	0.83	0.69	0.58	0.50	0.43	0.38	0.33
0.10	1.86	1.43	1.14	0.93	0.78	0.66	0.55	0.47	0.40
0.15	2.78	2.07	1.62	1.31	1.08	0.90	0.73	0.62	0.51
0.20	4.43	3.17	2.43	1.93	1.57	1.26	1.03	0.84	0.68
0.25	7.45	5.15	3.76	2.87	2.26	1.80	1.44	1.16	0.94
0.30	12.60	8.43	5.99	4.38	3.28	2.55	2.02	1.62	1.28
0.35	21.60	13.40	9.23	6.41	4.71	3.57	2.79	2.20	1.75
0.40	38.10	21.80	13.50	9.00	6.36	4.76	3.69	2.89	2.29
0.45	68.00	32.80	18.90	12.10	8.37	6.13	4.62	3.63	2.85
0.50	120.00	47.70	25.50	15.80	10.40	7.60	5.60	4.36	3.41

Source: SOLVAY (1967)

Viscosity of Aqueous Solutions of NaOH

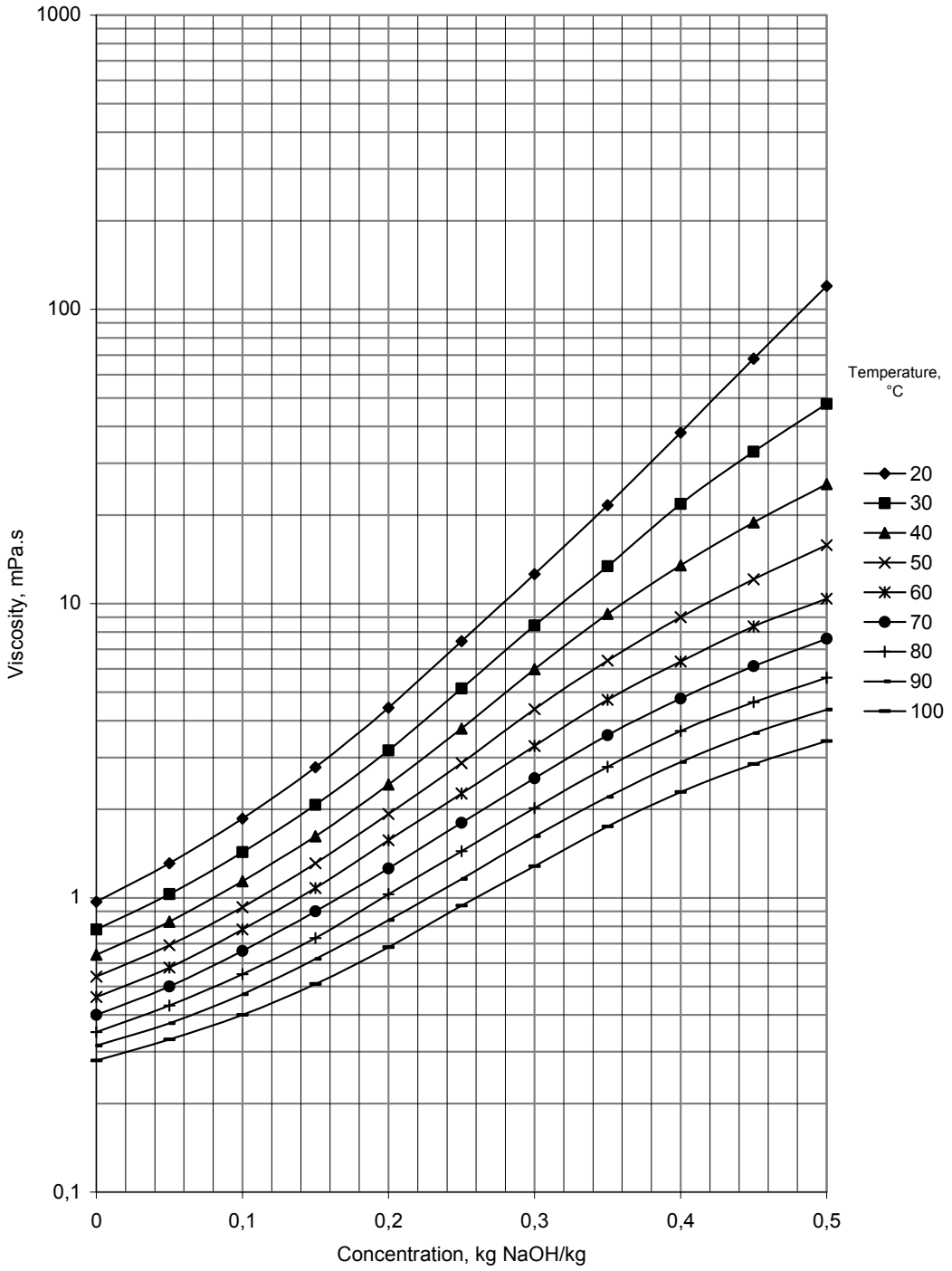

Source: SOLVAY (1967)

$$ln\left(\frac{\eta_{sol}}{\eta_w}\right)_{\vartheta} = d_1 + d_2\vartheta_{sol}^{0.5} + d_3\vartheta_{sol}^{1}, \textit{ Equation A4}$$

$$d_1 = k_{\eta 1}(1 - X_w) + \ldots + k_{\eta 4}(1 - X_w)^4$$

$$d_1 = l_{\eta 1}(1 - X_w x) + \ldots + l_{\eta 5}(1 - X_w)^5$$

$$d_1 = m_{\eta 1}(1 - X_w) + \ldots + m_{\eta 5}(1 - X_w)^5$$

Where η_{sol} is the viscosity of the solution in $[mPa \cdot s]$, η_w is the viscosity of water in $[mPa \cdot s]$, ϑ_{sol} is the temperature of the solution in $[^oC]$ and X_w is the concentration of water in the solution in $[g_{H_2O}/g_{sol}]$

$k_{\eta 1}$	-6.1420727	$l_{\eta 1}$	2.3171396	$m_{\eta 1}$	-0.1152143	$n_{\eta 1}$	-3.98182E-02
$k_{\eta 2}$	124.64849	$l_{\eta 2}$	-23.153644	$m_{\eta 2}$	1.0543467	$n_{\eta 2}$	2.47793E-03
$k_{\eta 3}$	-247.08170	$l_{\eta 3}$	49.267937	$m_{\eta 3}$	-2.3693277	$n_{\eta 3}$	-4.9427E-06
$k_{\eta 4}$	147.73585	$l_{\eta 4}$	-36.970260	$m_{\eta 4}$	2.0099091	$n_{\eta 4}$	1.48701E-07
		$l_{\eta 5}$	6.5882887	$m_{\eta 5}$	-0.5257284		

The correlation is valid within the temperature and concentration ranges indicated.

Temperature range [°C]	Concentration range [g NaOH/g solution]
$20 \leq \vartheta_{sol} < 30$	$0 \leq X_{NaOH} \leq 0.40$
$30 \leq \vartheta_{sol} < 50$	$0 \leq X_{NaOH} \leq 0.45$
$50 \leq \vartheta_{sol} < 70$	$0 \leq X_{NaOH} \leq 0.55$
$70 \leq \vartheta_{sol} < 150$	$0 \leq X_{NaOH} \leq 0.70$
$150 \leq \vartheta_{sol} < 200$	$0 \leq X_{NaOH} \leq 0.80$

Source: Olsson et all (1997)

Solubility

Area	State of NaOH and H_20 mixture
0	Solution
1	Ice + Solution
2	Solution + NaOH . 7 H_2O
3	Solution + NaOH . 5 H_2O
4	Solution + NaOH . 4 H_2O
5	Solution + NaOH . 3.5 H_2O
6	Solution + NaOH . 2 H_2O
7	Solution + NaOH . H_2O
8	Ice + NaOH . 7 H_2O
9	NaOH . 7 H_2O + NaOH . 5 H_2O
10	NaOH . 5 H_2O + NaOH . 4 H_2O
11	NaOH . 4 H_2O + NaOH . 3.5 H_2O
12	NaOH . 3.5 H_2O + NaOH . 2 H_2O
13	NaOH . 2 H_2O + NaOH . H_2O
14	NaOH . H_2O + NaOH

Eutectic Point	Temperature $[^oC]$	Saturated Solution Concentration $[g_{NaOH}/g_{sol}]$
A	-28.4	0.1896
B	-24.2	0.2211
C	-17.85	0.2473
D	5.4	0.3225
E	5.2	0.4590
F	12.2	0.5080
G	62.3	0.7430

Source: Gmelins (1928b)

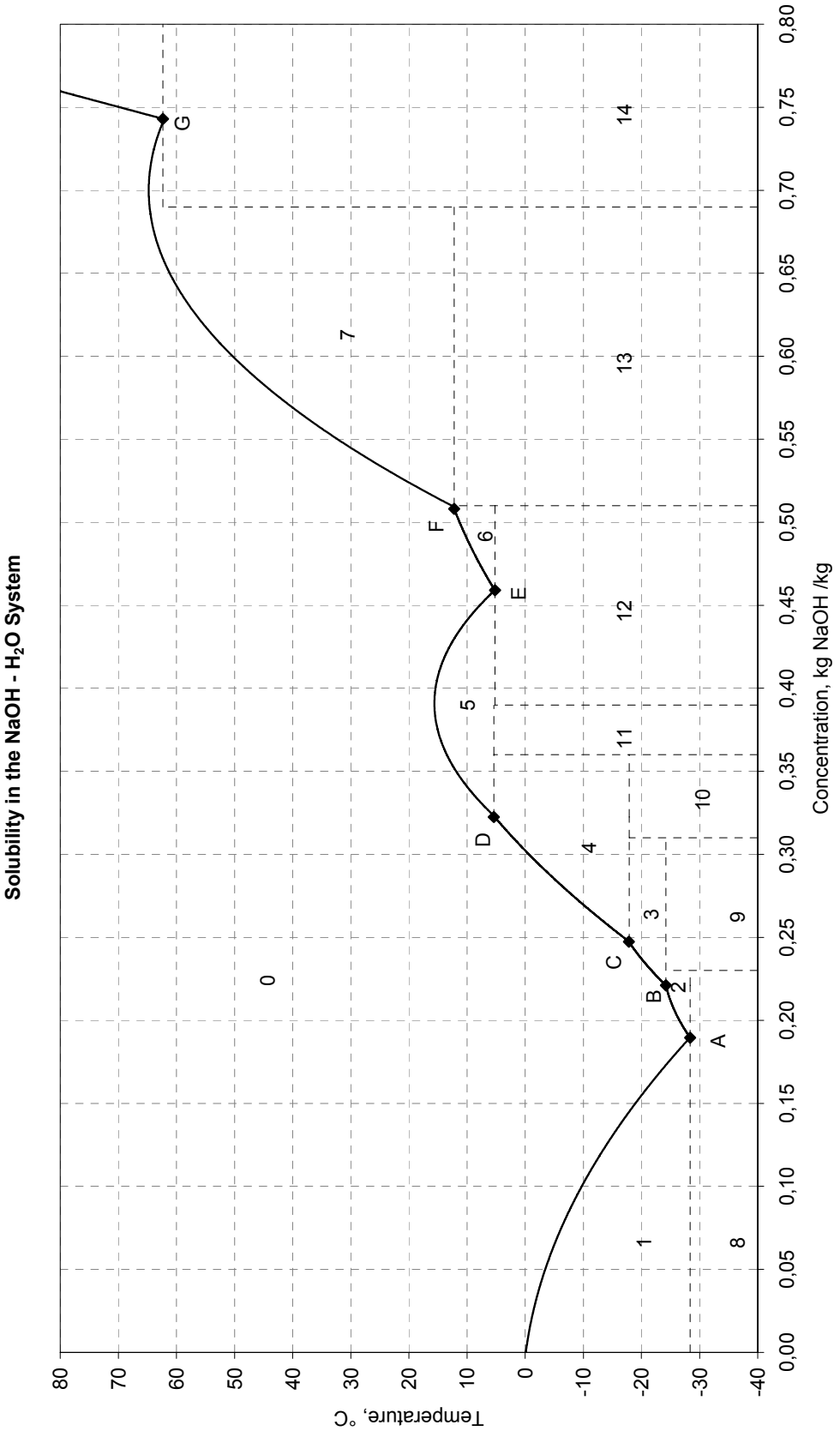

Source: Gmelins (1928b)

Vapour pressure

Concentration $[g_{NaOH}/g_{sol}]$	Temperature $[^oC]$											
	0.55	0.5	0.45	0.4	0.35	0.3	0.25	0.2	0.15	0.1	0.05	0
0.00			0.05	0.10	0.17	0.25	0.35	0.43	0.50	0.55	0.59	0.61
0.02			0.06	0.12	0.19	0.29	0.40	0.50	0.58	0.64	0.68	0.70
0.04			0.07	0.14	0.23	0.34	0.46	0.57	0.67	0.73	0.78	0.81
0.06			0.09	0.16	0.27	0.40	0.53	0.66	0.77	0.84	0.90	0.93
0.08			0.11	0.19	0.31	0.46	0.62	0.76	0.88	0.97	1.03	1.07
0.10			0.12	0.22	0.36	0.53	0.71	0.87	1.01	1.11	1.18	1.23
0.12			0.15	0.25	0.41	0.61	0.81	1.00	1.16	1.27	1.35	1.40
0.14			0.17	0.30	0.48	0.70	0.93	1.14	1.32	1.45	1.54	1.60
0.16			0.20	0.34	0.55	0.80	1.06	1.30	1.50	1.65	1.75	1.82
0.18			0.23	0.40	0.63	0.91	1.20	1.48	1.71	1.87	1.98	2.07
0.20			0.27	0.46	0.72	1.04	1.37	1.68	1.94	2.12	2.25	2.35
0.22		0.19	0.32	0.53	0.82	1.18	1.55	1.90	2.19	2.40	2.54	2.66
0.24		0.22	0.37	0.61	0.94	1.34	1.76	2.15	2.47	2.71	2.87	3.00
0.26		0.26	0.42	0.70	1.07	1.52	1.99	2.43	2.79	3.05	3.23	3.39
0.28		0.30	0.49	0.80	1.22	1.72	2.24	2.73	3.14	3.43	3.63	3.81
0.30		0.35	0.56	0.91	1.38	1.94	2.52	3.07	3.53	3.85	4.08	4.28
0.32		0.40	0.65	1.03	1.56	2.19	2.84	3.45	3.95	4.32	4.57	4.80
0.34		0.46	0.74	1.18	1.77	2.46	3.18	3.86	4.43	4.83	5.11	5.37
0.36		0.53	0.85	1.33	1.99	2.76	3.57	4.32	4.95	5.40	5.71	6.00
0.38		0.61	0.96	1.51	2.24	3.10	3.99	4.83	5.52	6.02	6.36	6.69
0.40		0.70	1.10	1.71	2.52	3.47	4.45	5.38	6.15	6.70	7.08	7.45
0.42		0.80	1.24	1.93	2.83	3.88	4.96	5.99	6.84	7.45	7.87	8.28
0.44		0.91	1.41	2.17	3.17	4.32	5.53	6.65	7.59	8.27	8.73	9.19
0.46		1.04	1.60	2.44	3.54	4.82	6.14	7.38	8.42	9.16	9.67	10.18
0.48		1.18	1.80	2.74	3.96	5.36	6.81	8.18	9.32	10.14	10.70	11.27
0.50		1.33	2.03	3.07	4.41	5.95	7.55	9.05	10.30	11.20	11.82	12.45
0.52		1.50	2.28	3.43	4.91	6.60	8.36	10.00	11.37	12.36	13.04	13.74
0.54		1.70	2.56	3.83	5.46	7.31	9.23	11.04	12.54	13.62	14.37	15.14
0.56		1.91	2.87	4.27	6.06	8.09	10.19	12.16	13.80	14.98	15.81	16.66
0.58		2.15	3.21	4.75	6.71	8.93	11.23	13.38	15.17	16.47	17.37	18.31
0.60		2.41	3.59	5.28	7.43	9.85	12.36	14.70	16.66	18.07	19.06	20.09
0.62	1.87	2.70	4.01	5.86	8.21	10.85	13.58	16.14	18.27	19.81	20.89	22.02
0.64	2.10	3.02	4.46	6.50	9.06	11.94	14.91	17.69	20.01	21.69	22.86	24.10
0.66	2.35	3.38	4.96	7.19	9.99	13.12	16.35	19.37	21.89	23.71	25.00	26.35
0.68	2.62	3.76	5.51	7.95	10.99	14.40	17.90	21.18	23.91	25.89	27.30	28.77
0.70	2.93	4.19	6.10	8.77	12.09	15.79	19.58	23.13	26.09	28.25	29.77	31.38
0.72	3.26	4.66	6.76	9.67	13.27	17.28	21.39	25.24	28.44	30.78	32.44	34.19
0.74	3.63	5.17	7.47	10.65	14.55	18.90	23.34	27.50	30.97	33.50	35.30	37.20
0.76	4.03	5.73	8.25	11.70	15.94	20.64	25.45	29.94	33.68	36.42	38.37	40.44
0.78	4.47	6.34	9.09	12.85	17.44	22.52	27.71	32.55	36.59	39.55	41.67	43.91

Source: Olsson et all (1997)

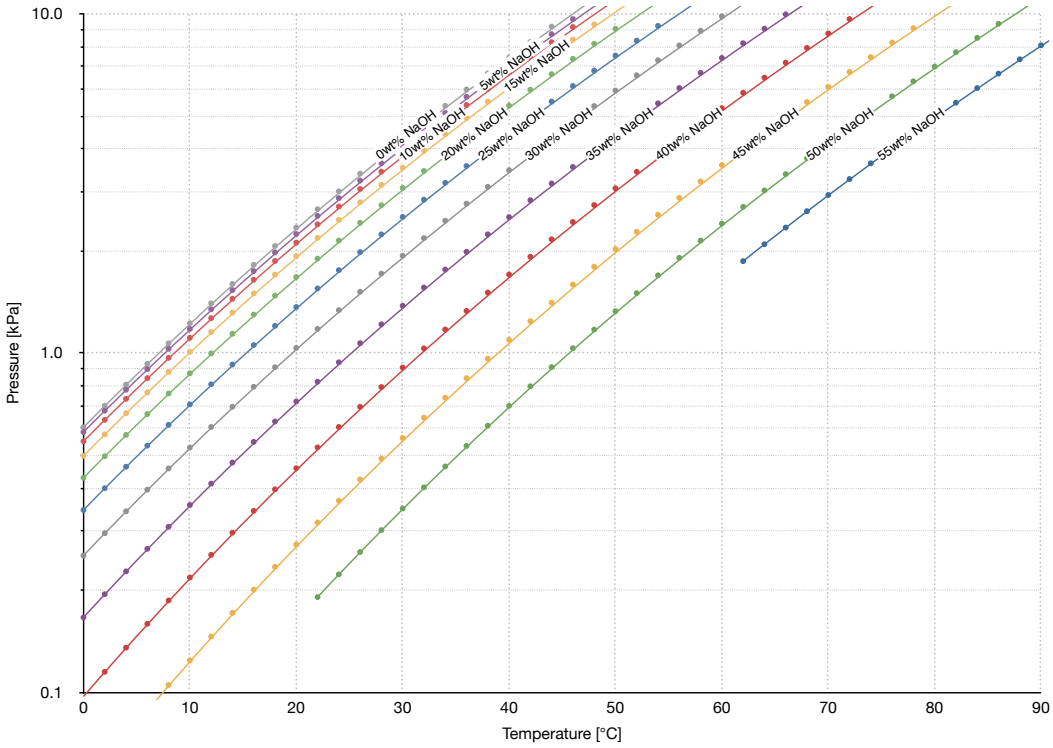

Source: Olsson et all (1997)

$$a_1 + a_2 \cdot \vartheta_{sol} + a_3 \cdot ln(p_{vap}) = \vartheta_{sol} \cdot ln(p_{vap}),\ \textit{Equation A5}$$

$$a_1 = k_{P0} + k_{P1} ln(X_w) + k_{P2} ln(X_w)^2 + \ldots + k_{P8} ln(X_w)^8$$

$$a_2 = l_{P0} + l_{P1} ln(X_w) + l_{P2} ln(X_w)^2 + \ldots + l_{P10} ln(X_w)^{10}$$

$$a_3 = m_{P0} + m_{P1} ln(X_w) + m_{P2} ln(X_w)^2 + \ldots + m_{P10} ln(X_w)^{10}$$

Where ϑ_{sol} is the solution temperature in $[^oC]$, p_{vap} is the vapour pressure in $[kPa]$ and X_w is the weight concentration in respect to the water content in the solution in $[g_{H_2O}/g_{sol}]$.

numerical values of k		**numerical values of l**		**numerical values of m**	
k_{P0}	-113.93947	l_{P0}	16.240074	m_{P0}	-226.80157
k_{P1}	209.82305	l_{P1}	-11.864008	m_{P1}	293.17155
k_{P2}	494.77153	l_{P2}	-223.473050	m_{P2}	5081.87910
k_{P3}	6860.83300	l_{P3}	-1650.399700	m_{P3}	36752.12600
k_{P4}	2676.64330	l_{P4}	-5997.311800	m_{P4}	131262.00000
k_{P5}	-21740.32800	l_{P5}	-12318.744000	m_{P5}	259399.54000
k_{P6}	-34750.87200	l_{P6}	-15303.153000	m_{P6}	301696.22000
k_{P7}	-20122.15700	l_{P7}	-11707.480000	m_{P7}	208617.90000
k_{P8}	-4102.98900	l_{P8}	-5364.955400	m_{P8}	81774.02400
		l_{P9}	-1338.541200	m_{P9}	15648.52600
		l_{P10}	-137.968890	m_{P10}	906.29769

The correlation is valid within the temperature and concentration ranges indicated.

Temperature range [°C]	Concentration range [g NaOH/g solution]
$0 \leq \vartheta_{sol} < 20$	$0 \leq X_{NaOH} \leq 0.418$
$20 \leq \vartheta_{sol} < 60$	$0 \leq X_{NaOH} \leq 0.500$
$60 \leq \vartheta_{sol} < 70$	$0 \leq X_{NaOH} \leq 0.647$
$70 \leq \vartheta_{sol} < 150$	$0 \leq X_{NaOH} \leq 0.700$
$150 \leq \vartheta_{sol} < 200$	$0 \leq X_{NaOH} \leq 0.800$

Source: Olsson et all (1997)

Thermal conductivity

$$\lambda_{sol} = \lambda_w + \sum_{j=1}^{j=3} \sum_{i=0}^{i=3} e_{ij} (\Theta_{sol}/\Theta_0)^i m^j, \text{ Equation A6}$$

Where λ_{sol} is the thermal conductivity of the solution in $[W/(m \cdot K)]$, λ_w is the thermal conductivity of the water in $[W/(m \cdot K)]$, Θ_0 = 403.0 K, Θ_{sol} is the temperature of the solution in $[K]$ and m is the molality of solution in $[mol/kg]$.

e_{01}	3.2900544E-01	e_{12}	5.9100989E-02
e_{11}	-1.1048583	e_{22}	-4.4407173E-02
e_{21}	1.2503803	e_{03}	1.5069324E-03
e_{31}	-4.4228179E-01	e_{13}	-4.3273501E-03
e_{02}	-2.1990820E-02	e_{23}	3.3763248E-03

$$\lambda_w = \sum_{i=0}^{i=9} g_i \tau^i + \pi \sum_{i=?0}^{i=9} q_i \tau^i$$

Where $\lambda_w$is the thermal conductivity in $[W/(m \cdot K)]$, $\tau = \Theta_0/\Theta_{sol}$, Θ_0 =293.15 K and Θ_{sol} is the temperature of the solution, $\pi = p_{sol} - p_s$, where p_{sol}p- is the presume of the solution in $[MPa]$ and p_s is the saturation pressure in $[MPa]$.

i	g_i	q_i
0	5.99454842E-01	5.31492446E-04
1	-4.82554378E-01	3.46658996E-04
2	-4.31229616E-01	1.23050434E-02
3	-8.62555022E-01	1.27873471E-01
4	-3.80050418E-01	-7.40820487E-01
5	4.85828450E+01	-1.93072528E+01
6	3.35400696E+02	-1.22835056E+02
7	1.08007806E+03	-3.66150909E+02
8	1.67727081E+03	-5.31321978E+02
9	1.04225629E+03	-3.03153185E+02

Equation A6 is valid in region of pressures up to 15 MPa and temperatures from 273 to 405 K for solutions with concentration up to 5 mol/kg.

Source: Alexandrov, 2005.

Appendix B: Publications

This list includes the author's presentations, publications and International Energy Agency participation in the area of sorption heat storage from 2014 until 2019.

Conference presentations:

1. Parameters effecting economy and heat density of sorption heat storage systems, Eurotherm Seminar #99 Advances in Thermal Energy Storage, Lleida, Spain, 2014
2. Limitations imposed on energy density of sorption materials in seasonal thermal storage systems, International Conference on Solar Heating and Cooling for Buildings and Industry, SHC Bejing, China, 2014
3. Development of a closed sorption heat storage prototype, Swiss Symposium Thermal Energy Storage, Luzern, Switzerland, 2014.
4. Performance of the absorption process in a seasonal sorption heat storage prototype, Cisbat conference, EPFL, Lausanne, Switzerland, 2015
5. Operation results of a closed sorption heat storage prototype, 9th International Renewable Energy Storage Conference IRES, Dusseldorf, Germany, 2015.
6. Seasonal absorption based heat storage with sodium hydroxide, IEEE ICE International Technology Management Conference, Belfast, Northern Irland, 2015
7. Absorption based seasonal thermal storage with sodium hydroxide, progress and outlook, 19. Status-Seminar, ETHZ, Zürich, Switzerland 2016.
8. Seasonal absorption based heat storage with sodium hydroxide, Heat storage workshop, Danish Technical University, Copenhagen, Denmark, 2016.

9. Cycling test of liquid sorption thermal energy storage using sodium hydroxide, SWC/SHC Abu Dhabi United Arab Emirates, 2017.
10. Liquid sorption heat storage spiral fin heat and mass exchanger, steps towards increased rate of absorption, 12th International Renewable Energy Storage Conference IRES, Dusseldorf, Germany, 2018.
11. Einblick in die Entwicklung von Wärmespeicher mit flüssigen Sorbentien, Fachforum Thermische Energiespeicher, Meerbusch / Düsseldorf, Germany, 2019
12. Thermochemical material testing under semi-real conditions: A lab-scale bulk reactor to support optimised component design for long-term thermal energy storage, 13th International Renewable Energy Storage Conference IRES, Dusseldorf, Germany, 2019.
13. Component development for a liquid sorption TES system, ISES SHC webinar, 2019.

Conference publications:

1. Fumey B., Weber R., Gantenbein P., Daguenet-Frick X., Williamson T., Dorer V., Parameters effecting economy and heat density of sorption heat storage systems, Eurotherm Seminar #99 Advances in Thermal Energy Storage, Lleida 2014
2. Fumey B., Weber R., Gantenbein P., Daguenet-Frick X., Hughes I., Dorer V., Limitations imposed on energy density of sorption materials in seasonal thermal storage systems, Energy Procedia 70 (2015) 203 – 208
3. Fumey B., Weber R., Gantenbein P., Daguenet-Frick X., Sorption based heat storage demonstrator, 18. Status-Seminar, ETHZ, Zürich, Switzerland 2014
4. Fumey B., Stoller S., Fricker R., Weber R., Gantenbein P., Daguenet-Frick X., Dorer V., Performance of the absorption process in a seasonal sorption heat storage prototype, Cisbat conference, EPFL, Lausanne, Switzerland, 2015

5. Fumey B., Weber R., Gantenbein P., Daguenet-Frick X., Stoller S., Fricker R., Dorer V., Operation results of a closed sorption heat storage prototype, Energy Procedia 73 (2015) 324 – 330.
6. Fumey B., Weber R., Gantenbein P., Daguenet-Frick X., Baldini L., Absorption based seasonal thermal storage with sodium hydroxide, progress and outlook, 19. Status-Seminar, **ETHZ**, Zürich, Switzerland 2016.
7. Fumey B., Weber R., Baldini L., Cycling test of liquid sorption thermal energy storage using sodium hydroxide, SWC/SHC Abu Dhabi United Arab Emirates, 2017.

Journal publications:

1. Fumey B., Weber R., Baldini L., Liquid sorption heat storage – A proof of concept based on lab measurements with a novel spiral fined heat and mass exchanger design, Applied Energy, Volume 200, 2017, 215-225
2. Fumey B., Weber R., Baldini L., Sorption based long-term thermal energy storage – Process classification and T analysis of performance limitations: A review, Renewable and Sustainable Energy Reviews 111, 2019, 57–74

Journal publications under progress:

3. Fumey B., et al. Building application specific temperatures for the testing of phase change and thermo chemical materials, components and systems, Renewable and Sustainable Energy Reviews
4. Fumey B., Baldini L., Borgschulte A., Water Transport in Aqueous Sodium Hydroxide Films for Liquid Sorption Heat Storage, Energy and Environmental Science
5. Fumey B., Baldini L., Borgschulte A., Neutron imaging of water vapour uptake in aqueous sodium hydroxide, Nature Energy

International Energy Agency activities:

SHC Task 42: Compact Thermal Energy Storage

1. 10th Experts Meeting, October 2-4, 2013, Ljubljana, Slovenia
2. 11th Experts Meeting, April 28-30, 2014, Lyon, France
3. 12th Experts Meeting, October 8-10, 2014, Nagoya, Japan
4. 13th Experts Meeting, February 9-11, 2015, Vienna, Austria
5. 14th Experts Meeting, October 5-7, 2015, Zaragoza, Spain
6. Definition meeting Task 58, April 6-8, 2016, Graz, Austria
7. Definition meeting Task 58, September 15-16, 2016 Vienna, Austria

SHC Task 58: Material and Component Development for Thermal Energy Storage, serving as Leader for Subtask 4T “Component design for Thermo Chemical Materials”

8. 1st Experts Meeting, April 5-7, 2017, Lyon, France
9. 2nd Experts Meeting, October 4-6, 2017, Dubendorf, Switzerland
10. 3rd Experts Meeting, April 9-11, 2018, Ljubljana, Slovenia
11. 4th Experts Meeting, October 1-2, 2018, Graz, Austria
12. 5th Experts Meeting + Public Seminar, May 1-3, 2019, Otttawa, ON, Canada
13. 6th Experts Meeting, October 9-11, 2019, Messina, Italy